ABSTRACT

Title of Dissertation: DEVELOPMENT OF A PHYSICS OF FAILURE MODEL AND QUANTITATIVE ASSESSMENT OF THE FIRE FATALITY RISKS OF COMPRESSED NATURAL GAS BUS CYLINDERS

Samuel Seamore Chamberlain, Doctor of Philosophy, 2004

Dissertation directed by: Professor Mohammad Modarres
Department of Mechanical Engineering

The research presented in this dissertation details the development of a new probabilistic fracture mechanics model of corrosion fatigue failure of steel CNG bus cylinders. This model was used to estimate the frequency of leakage or catastrophic rupture, due to the propagation of a micro-crack on the inside, outside or transition surface, of hemispherical and flat-bottom cylinder designs, in assessing the fire and explosion fatality risks associated with a typical CNG bus. Quantitative assessment of the fire and explosion fatality risk was completed by analytically modeling the postulated fire scenarios from initial release of natural gas from a failed cylinder. The

frequency of the initiating events, likelihood of subsequent events leading to a fire or explosive event was combined with the consequence of each event in a Probabilistic Risk Assessment (PRA) model to estimate the overall risk. Epistemic and aleatory uncertainties in the approach was evaluated using a combination of parametric modeling, conservative estimation and engineering judgment.

Direct computation of the fire fatality risk associated with diesel powered buses is possible because these are mature technologies for which historical performance data are available. Due to the limited experience, fatal incident data for CNG buses fleets are minimal. This study therefore had to rely on analytical modeling of failures, dynamics of fire initiation and propagation along with the subsequent events in this PRA approach. The new methodology provides guidance on performing risk assessment of other novel technologies presently being developed or for which actuarial performance data is not available.

This study predicts that the mean fire fatality risk for a typical CNG bus is approximately 23 fatalities per 100-million miles for all persons involved, including bus passengers. Estimated CNG bus passengers mean risk is 14.4 fatalities per 100-million miles or 63% of fire fatalities. Based on historical data, diesel school bus mean fire fatality risk is 0.091 and 0.0007 per 100-million miles for all people and bus-passengers respectively. One can therefore reasonably conclude that CNG school buses are expected to be more prone to fire fatality by 250 times that of diesel buses, with the bus passengers being more at risk by over four orders of magnitude.

Explosion due to detonation and deflagration of a flammable vapor cloud within a bus or building, for which there is some historical events, is a major contributor, to this increased risk, a phenomenon not normally associated with diesel fuel.

The overall mean fire risk frequency has also been estimated at 2.23×10^{-3} fatalities/bus/year. The 5% and 95% uncertainty bounds are 1.18×10^{-4} and 8.83×10^{-3} respectively. These results provide the foundation for doing comparative analysis of CNG with other technologies by combining the estimated mean fire fatality risk, with the expected health and environmental benefits of using CNG powered buses.

DEVELOPMENT OF A PHYSICS OF FAILURE MODEL
AND
QUANTITATIVE ASSESSMENT OF FIRE FATALITY RISKS
OF
COMPRESSED NATURAL GAS BUS CYLINDERS

by

Samuel Seamore Chamberlain

**Dissertation Submitted to the Faculty of the Graduate School of the
University of Maryland, College Park in partial fulfillment
of the requirements for the degree of
Doctor of Philosophy
2004**

Advisory Committee:

Professor Mohammad Modarres, Chair/Advisor
Dr. Marjorie-Ann Erickson-Kirk
Dr. Paul Hoffman
Associate Professor Frederick Mowrer
Professor Emeritus Marvin Roush

PREFACE

A previous study to assess the fire safety risk associated with Compressed Natural Gas (CNG) vehicle system, comprising primarily of a typical school bus and supporting fuel infrastructure was conducted by the Center for Technology Risk Studies (CTRS) at the University of Maryland, in 2002. The intention of this study was to assess the fire safety risks of CNG buses notwithstanding their significant potential environmental and health benefits. A qualitative evaluation of the hazards associated with the system, using a system safety scenario driven technique was conducted as a precursor. All important fire scenarios originate from component failures, excepting fires from electro-static discharge. This informed a subsequent failure mode and effects analysis using the MIL-STD-1629 standard which provided the initiating events used in the quantitative risk assessment. The quantitative study utilized probabilistic assessment methods as practiced in nuclear, process and aerospace industries. Computation of the frequency of occurrence of the initiating events was done using published generic failure data for similar components. The likelihood of subsequent events to the postulated release of natural gas was estimated using actuarial data, generic data and engineering judgment. Analytical modeling of fuel dispersion and mixing was outside the scope of that study. Consequence of the fire scenarios considered, were computed by assuming fatality would occur if an individual was subjected to 25kW/m^2 of heat flux for 1 minute. Simplified approaches were used to compute the heat flux produced and the likelihood of ignition of a natural gas vapor cloud.

The CTRS study predicted that mean fire fatality risk for a typical CNG bus was approximately 0.23 fatalities per 100-million miles for passengers and non-passengers.

Mean estimates of 0.16 fatalities per 100-million miles for bus passengers was more than two orders of magnitude greater than for a similar diesel bus. Overall predicted fire fatality risk was 2.5 times greater for CNG buses than diesel buses. The component that contributed most to the frequency of gradual and catastrophic release of natural gas was the failure rate of the CNG cylinder with the integral pressure relief device. The cylinder was also the component that contributed most to risk reduction based on the Birnbaum reliability importance measures. Additionally failure of the cylinder contributed most to the creation of a fireball or a large unconfined vapor cloud flash fire, with estimated completely lethal effects in the exposure zones.

Intuitively the PRA results agreed with the very small amount of historical data available on CNG vehicle fires. The sensitivity of these results to the generic failure rate data, along with the need to develop a robust methodology for computing CNG vehicle risk, prompted this research. A physics of failure approach to estimate mean time to failure of cylinders from which a frequency of failure could be derived was considered most appropriate. Analytical methods for estimating consequence of fire scenarios were also considered necessary to improve on the simplified approaches used in the previous study. Overall this new methodology of computing the risk of CNG buses serves as a template for conducting risk assessment for novel technologies such as hydrogen fuel cells, gasoline-electric hybrids, liquid natural gas, and others that may be contemplated in the future. The results from this risk assessment could be combined with the environmental and health benefits to be gained in order to arrive at an assessment of the suitability of each technology based on the overall risk. The methods developed in this new study could also help to guide

design standards and maintenance practices in reducing the fire and explosion risks associated with existing CNG buses.

Major funding for the initial study, which was published in report CTRS-MC1-02 by the Center for Technical Risk Studies, was provide by International Truck and Engine Corporation, of Chicago, Illinois.

DEDICATION

To my parents, Mazelin and Joscelyn Chamberlain

and

my family for your understanding and support throughout

ACKNOWLEDGEMENTS

I am honored and privileged for having the opportunity to work and learn with my advisor and mentor, Professor Mohammad Modarres. I am thankful to him for his patience with me, technical guidance, academic stimulation, insightful comments and interest in my personal welfare throughout the course of my graduate study at the University of Maryland.

I am grateful to the members of my dissertation committee for consenting to serve. Your time and comments have shaped the final version of my dissertation. A special thanks to Dr. Paul Hoffman from NAVAIR Structures Division Code 4.3.3, who is serving as a special member. Dr. Marjorie Erickson-Kirk has been very supportive throughout and have contributed significantly in understanding the crack growth phenomenon. Professor Fredrick Mowrer provided guidance in analytic modeling of fires and valuable insights in completing the initial study which provided the basis for the dissertation research. I am grateful to Professor Emeritus Marvin Roush for being a mentor throughout my graduate work.

Special thanks too to Dr. Ivis Forrester-Anderson of Morgan State University whose technical and editorial comments improved the quality of my dissertation. The support of her family throughout is greatly appreciated. So too is the support of my fellow Research Assistants of the Center for Technology Risk studies, in the Reliability Engineering program at the University of Maryland. Special thanks to Mohammad Reza Azarkhail for his help in coding the routines in MatLab. Miss Willie Webb from the Reliability Engineering department offered professional help in completing the dissertation, for which I am grateful.

Lastly to God whose goodness and love enabled me to achieve this important milestone. My family prayed for me throughout and the difficulties that we have faced have made us stronger. To my children I love you all and look forward to playing a more fulsome role in your lives once again.

TABLE OF CONTENTS

LIST OF TABLES

LIST OF FIGURES

LIST OF ACRONYMS

CNG:	Compressed Natural Gas
NGV:	Natural Gas Vehicle
CNGV:	Compressed Natural Gas Vehicle
FMEA:	Failure Modes and Effect Analysis
FMECA:	Failure Modes and Effect Criticality Analysis
MIF:	Mechanically-Induced Failures
PRF:	Pressure-Related Failures
IRF:	Impact-Related Failures
OMF:	Other Mechanically-Induced Failure
CIF:	Chemically-Induced Failure
EIF:	Electrically-Induced Failure
CARB:	California Air Resources Board
CTRS:	Center of Technology Risk Studies
NHTSA:	The National Highway Traffic Safety Administration
PRD:	Pressure Relief Device
GRI:	Gas Research Institute
DOT:	Department of Transportation
LNG:	Liquefied Natural Gas
SCC:	Stress Corrosion Cracking
LEFM:	Linear Elastic Fracture Mechanics
EPFM:	Elastic-Plastic Fracture Mechanics

CTOD:	Crack Tip Opening Displacement
CVE:	Charpy V-notch Energy
CVN:	Charpy V-notch
ASTM:	American Society of Testing and Materials
ASME:	American Society of Mechanical Engineers
NDT:	Non-Destructive Testing
PNNL:	Pacific Northwest National Laboratory
PRD:	Pressure Relief Device
PDF:	Probability Density Function
PRA:	Probabilistic Risk Assessment
PFM:	Probabilistic Fracture Mechanics

PART 1

PHYSICS OF FAILURE MODELING AND FREQUENCY OF CYLINDER LEAKAGE AND CATASTROPHIC RUPTURE DETERMINATION

CHAPTER 1: INTRODUCTION

1.1 Objective and Scope of Study

Analytical modeling of reliability and comprehensive risk analysis of compressed natural gas (CNG) fueled vehicles and systems have never been attempted because of the sparsity of failure and accidental data. This is largely due to the small number of such vehicles in operation, and the technology being relatively new when compared with diesel and gasoline engines. Where such data exist, estimation of the failure frequencies of system components is not possible. This is due in part to the lack of applicable models that can combine actuarial data and operational experience with expert opinions, while reducing aleatory and epistemic uncertainties.

The primary objective of this research is to develop an analytical model of the predominant failure mechanisms and to estimate the fire safety risks associated with a typical CNG bus, with its associated fuel infrastructure. A secondary objective is to provide a methodology for conducting risk analysis of vehicular systems using alternative fuels being contemplated for mass transit. Finally, once absolute risk of CNG buses can be established, the societal risk can be compared with other similar technology to help guide the development of applicable regulations. This includes physics based inspection intervals, safe operating life and replacement plan.

Compressed natural gas bus fuel system components are subject to degradation from stress corrosion cracking and corrosion fatigue. Previous research [1] has identified

the storage cylinder to be the component with the highest risk. This also is the most vulnerable component in the system, due to the presence of corrosive constituents in the CNG and frequent charging at high pressures in a filling station and discharging the cylinders as the fuel is consumed. Physics of failure modeling is used to estimate the frequency of leakage and rupture of the CNG cylinders.

This analytical model features probabilistic facture mechanics modeling of the associated failure mechanisms. The result of which is the determination of the distribution of the frequency of occurrence of cylinder failure leading to a release of CNG, while incorporating impact of manufacturing process, material properties and inspection methodology in a typical bus. A risk model is subsequently developed by combining the frequency of occurrence of gas release scenarios along with the likelihood of subsequence events leading to a fire, and the consequence of the resulting fire. The output from this model is the absolute risk of individual CNG bus fire events.

Consequence of a cylinder failure is modeled analytically by evaluating the thermodynamics of the discharge of fuel into the air and the chemical kinetics of each scenario leading to a premixed or diffusion fire. The hazards associated with gaseous release of CNG are evaluated using thermo-chemistry of methane which is the predominant constituent in CNG. The ignition, burning rates and plume formation is evaluated and the heat flux generated is used to determine the vulnerability of selected targets. Compressibility effects above sonic velocity leading to detonation are considered as well as deflagrations effects at reaction-front speeds below sonic speed. Fatality as a

consequence is determined to occur when the heat flux incident on persons exceed that required to cause serious injury and death. Deaths due to explosions are caused by whole body translation resulting in injuries as well as overpressure effects on body tissue.

The determination of the total risk will be achieved by combining the frequency of occurrence of events leading to the gaseous release, the probabilities associated with subsequent scenarios and the consequence of each fire scenario.

1.2 Background

The growing use of natural gas as a fuel for vehicles is due in part to economic and environmental benefits. Compressed natural gas on an energy-equivalent basis is lower in price than the conventional diesel and gasoline fuels. The emission levels are much lower affording cleaner air quality than conventional diesel and gasoline fuels.

Compressed natural gas has to be stored at high pressures in cylinders to increase the specific energy of the fuel, for reasonable mileage efficiency between refueling. The working pressure of the CNG cylinders has not been defined although the existing standard, NGV 2, specifies a service pressure of between 2400 and 4350 psi [2]. The storage of gas at this high pressure has implications for fatality risk and presents challenges for the safety and reliability of the CNG cylinders throughout their anticipated long service life.

A recent research effort [1] undertaken by the Center for Technology Risk Studies (CTRS) at the University of Maryland has determined that the fire fatality Risk of CNG

powered school buses is between 2-3 times more than diesel buses for all fatalities (those inside and outside the bus) and more than two orders of magnitude for bus passengers. Ensuring the continued safe and reliable operation of Natural Gas Vehicles (NGV) is important to their economic viability and public acceptance.

In the NGV the CNG cylinder is the most critical in addressing fatality risk, since it stores gas at high pressures. The fuel cylinder failure, researched and documented in [1] was also found to be one of the major contributors to the absolute risk computed and uncertainty in the risk results. There are many different types of cylinders such as all metal, over wrapped, consisting of a metal liner and composite over-wrap, or all composite cylinders consisting of a polymer liner and composite over-wrap. Recent studies [3,4] have detected significant degradation defects in cylinders. Incidents involving CNG failures are summarized in [1] which also includes fatalities.

Steel cylinders are currently more widely used (over 90%) and are therefore the focus of this study. These cylinders are the heaviest components of the fuel system and are unlikely to be a viable long-term option in the automotive market. Notwithstanding this, steel cylinders have advantages relative to the more advanced designs inasmuch as they are a well established technology and have complied with most of the regulations relating to CNG cylinders. These cylinders are covered by the U.S. Department of Transportation specification [5]. This specification allows a thinner and more highly stressed wall than the ASME boiler and pressure vessel code [6]. Periodic hydrostatic

testing every five (5) years is the only test specified in the governing regulations [2] as being mandatory, in order to guarantee reliability and fail safe operations.

Hydrostatic testing is costly since it requires removal of the cylinder from the vehicle and shipment to a certified laboratory for testing. The limitation of hydrostatic testing in ensuring the safety of cylinders is highlighted when one considers the expected failure mechanisms of the cylinders. Recent research [3,4], [7] has shown that the existing provisions are inadequate to detect the expected forms of damage that could lead to failure. General corrosion which hydrostatic testing is designed to detect is a probable degradation mechanism. However, it does not significantly reduce the wall thickness to make it detectable with hydrostatic testing. Hydrostatic testing will therefore not detect failure mechanisms that have significant impact on the life of a typical cylinder, or provide adequate indication of the degradation that has occurred.

Catastrophic ruptures will result from localized damage such as that which occurs from the growth of cracks, which originate at either corrosion pits or pre-existing manufacturing defects. Leakage will occur when such cracks grow until they penetrate the cylinder wall without the crack becoming unstable. The existence of cracks or the growth process cannot be detected using the standard hydrostatic test.

It is therefore imperative that in the absence of adequate testing procedures, analytical methods must be developed that are physics based and which can be used to estimate safe operating life. A physics of failure model which incorporates the

significant failure mechanisms is required in order to determine the frequency of occurrence of cylinder failure. Determination of the rate of propagation of defects to failure will facilitate the development of appropriate non-destructive examination (NDE) inspection methodologies and intervals. The results of inspections could also be used to project remaining life from which cylinder replacement plans can be developed or inspection interval revised accordingly.

1.3 Design and Construction of CNG Cylinders

Compressed natural gas cylinders have been designed to satisfy a variety of needs: They must be capable of storing gas at high pressures in order to reach a high specific energy content of the fuel; Weight must be kept to a minimum, and demonstratively safe over the required life, and cost must not be more than a small fraction of the vehicle overall cost. There are four types of cylinders in use for NGV.

They are designated as follows:

- Type 1 - All-metal construction
- Type 2 - Metal liner reinforced with hoop-wrapped filaments in a resin matrix.
- Type 3 - Metal liner reinforced with full-wrapped filament in a resin matrix.
- Type 4 - Plastic liner reinforced with full-wrapped filaments in a resin matrix.

1.3.1 Steel Type 1 Cylinders

These are the most widely used design (91.7 %) and have been in NGV service, since 1974 with an estimated 1.5 million in service. Steel cylinders are usually manufactured from AISI 4130X alloy steel. The higher the strength of this steel the

thinner the wall and the lighter the cylinder. Susceptibility to sulphide stress corrosion cracking due to small amounts of H_2S present in the natural gas increases with increasing strength. In the U.S., cylinders having hardness of R_C 22 (Rockwell C scale) are used. In other countries, cylinders with hardness numbers as high as R_C 33 are permitted. Typical mechanical properties associated with these hardness numbers are shown in Table 1.

Table 1.1 Typical Mechanical Properties of Cylinder Alloy Steels

Rockwell Hardness RC	0.2% Yield MPa (ksi)	UTS MPa (ksi)	% Elongation
22	654 (95)	759 (110)	-
33	862 (125)	952 (138)	20

Six types of steels are permitted for use as material in the manufacturing of NGV fuel cylinders under the Department of Transportation's governing standard, DOT-3AA. Most cylinders are however made from the highly alloyed AISI 4130X steel, containing Chromium and Molybdenum. Fined grained steel such as 15B30 containing higher manganese content micro-alloyed with Boron as well as marageing steels have been experimented with in the past, but without widespread success. Research has focused on two micro structural variations of the 4130X alloyed steel. These are:

- 4130-M, Martensitic micro-structure achieved in the rapidly quenched regions of the cylinder such as the sidewalls.
- 4130-B, Bainitic micro-structure typical of regions of the cylinder where inadequate quenching is achieved such as the transition regions and ends.

The chemical composition of steels used to manufacture cylinders is shown in Table1.2.

Table 1.2 Chemical Composition Limits for DOT-3AA Alloyed Steels

Steel Designation	Chemical Composition in Weight (%)								
	C	Mn	P	S	Si	Cr	Mo	B	Fe
4130X	0.25-0.35	0.40-0.90	0.04 max	0.05 max	0.15-0.35	0.80-1.10	0.15-0.25	-	Balance
15B30	0.27-0.37	0.80-1.40	0.035 max	0.045 max	0.30 max	-	-	0.005-0.0030	Balance

Because of the prevalence of the AISI 4130X steel in service and the extensive fracture analysis research done on the two-micro structure variations (4130-M and 4130-B), only the failure mechanisms of this type is considered in this research.

1.3.2 Aluminum Type 1 Cylinders

All-aluminum cylinders have historically been made from AA 6061-T6 and AA 7032. Only a fraction of these, when compared with steel cylinders, are in service so they will not be considered further in this analysis or model development.

1.3.3 Type 2 Hoop-Wrapped Cylinders

Hoop wrapped cylinders are the second most widely used design and were introduced in 1983. There are estimated an 80,000 units in service or approximately 4.9 % of NGV cylinders. This design is based on the ability of the liner (without the hoop-wrapping) to contain the maximum fill pressure, allowing for the use of higher fiber stress levels than is employed in fully wrapped designs. The design philosophy of hoop wrapped cylinders is based on the fact that a sphere will contain twice as high a pressure

as a long cylinder of the same diameter and wall thickness. The weaker cylindrical portion of a thinner-walled cylinder is wrapped to achieve a comparable pressure retaining capability as in the nearly hemispherical ends. Further consideration will not be given to this design in the ensuing analysis and modeling.

1.3.4 Type 3 Full-Wrapped Cylinders

This design was introduced in 1992 and there are about 40,000 units in service or approximately 2.4 % of CNG cylinders. It consists of a metal liner wrapped with continuous filaments in a resin matrix. In this design, partial load sharing takes place between the metal liner and the composite wrap. Due to this load sharing, the long-term integrity of the composite is more critical to the cylinder durability and safety. No further consideration will be given in the modeling and analysis.

1.3.5 Type 4 Full-Wrapped Cylinders

Composite cylinders were introduced into the NGV market in 1993 with about 15,000 units in service, representing approximately 0.9 % of usage. The liner is non-load-bearing plastic, making them very lightweight. The composite bears the entire load and therefore the cylinder's safety relies on the durability of the composite. Composite cylinders while, offering substantially improved performance on a pressure per weight basis, can fail in a multiplicity of modes that are accounted for through accelerated life testing and conservatism in design. These modes will not be evaluated in this research.

In a report on compressed natural gas safety [8] evaluations of CNG cylinders were made on the basis of cylinder designs, material of construction and inspection measures utilized during production. The risk assessments were based on failure history of the cylinders,

the observed degradation of certain materials while in service and the likelihood that such degradation could occur. The results of the risk assessments show that:

- Steel is generally safer than aluminum due to the superior impact, fire and corrosion performance.
- Type 1 cylinders are generally safer than composite-designs as Type 1 designs are highly resistant to external damage.
- Hoop-wrapped designs are generally safer than full-wrapped designs due to the redundancy of the liner design.
- Carbon fiber is generally safer than other fiber types due to the superior resistance to stress rupture, fatigue, environment attack and thermal stresses.
- Type 3 designs offer advantage over Type 4 designs because the metal liner offers more resistance to leak and liner-boss interface concerns.

From this analysis it was assumed that the physical modeling of the failure mechanisms of Type 1 steel cylinders would give the lower bound representation of the risk of the entire CNG cylinder population due to its superior performance. The risk determined from this modeling approach would be the lower limit of the expected absolute risk of using CNG cylinders.

1.4 Manufacture of Steel CNG Cylinders from Stock Material

The three main fabrication technologies [8] for all steel cylinders is well established. The processes involve forming the stock metal, spinning to form the neck, then drilling and tapping to accommodate the valve. Quenching and tempering follows in

a heat treatment processing. This section describes the manufacturing processes used in the fabrication of CNG steel cylinders. The three different methods are a result of the differences in the form of the raw material employed.

1.4.1 Billet Stock Process

The billet pierce method which is shown schematically in Figure 1.1 is capable of producing high pressure gas storage cylinders with diameters of up to 20 inches. The raw material is a solid steel billet ranging in size from 14 to 20 inches square and from 40 to 60 inches long. After heating to a temperature of about 2,300 F, the billet is formed into a solid cylindrical shape by forging in a closed die forging press. A hole is subsequently pierced in the center of the billet. Currently, this technology is used to produce cylinders in the 8 to 11 inches diameter range.

The drawing process involves the re-heating of the pierced billet to 2,300 F which is subsequently placed on a mandrel in a horizontal draw bench. The mandrel moves the piece through a series of ring dies which progressively reduce the outside diameter and elongate it on the mandrel. Further reduction and elongation are possible using the same type of equipment.

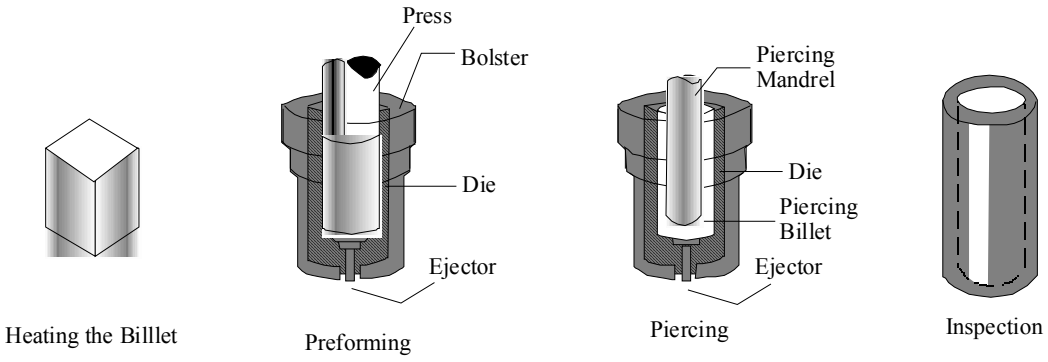

Figure 1.1 Schematic Diagram of Billet Stock Process

As the drawing operations induced high stresses in the work piece, intermediate heat treating or annealing is required. The annealing process involves heating the steel to 1,800 °F and cooling it in air. Annealing not only removes stresses, but also softens the work piece by altering the mechanical properties and refining the grain structure of the steel through re-crystallization. Shot Blasting is sometimes used to relieve stress in the newly formed cylinder. At the completion of the drawing operations, the cylinder is inspected using ultra-sonic and other NDE techniques to determine the wall thickness and surface quality.

The Spinning operation involves square cutting the open end of the newly formed cylinder and heating it to a dull red color. It is then inserted in the hollow spindle of a lathe-type machine and rotated at speeds of 600 to 1,200 rpm. A spinning tool is fed against the cylinder and moved in a sweeping motion from the outside diameter to form the neck and end of the cylinder. Heat generated from the friction of the tool against the

work piece is sufficient to form a weld and completely close the open end. The process of spinning is shown in Figure 1.2.

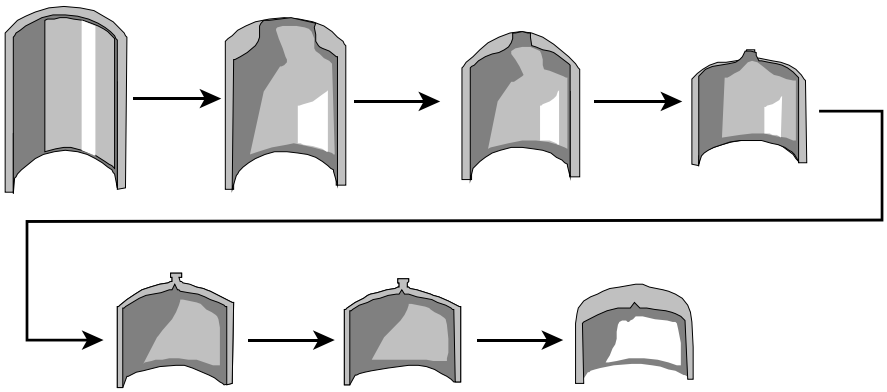

Figure 1.2 Schematic of Steel Cylinder Neck Formation and End Closing

The fabricated cylinder is quenched and tempered to achieve the desired strength, hardness and toughness. The steel is first heated to above the critical reform temperature, approximately 1,500 to 1,600°F and then cooled rapidly by immersion in an oil or water bath. The resulting Martensitic micro-structure is extremely hard and brittle. The cylinder is then tempered to reduce the hardness and increase the toughness or fracture resistance of the steel. The tempering process is accomplished by heating the cylinder to an intermediate temperature of about 1,000°F, holding it at this temperature for an appropriate length of time, allowing the transformation of the grain structure, and then slowly cooling it.

The neck region of the cylinder is ported and threaded to accommodate the valve, after the heat treatment. This valve has a pressure relief valve integrated into it. The interior surface is first shot blasted to remove all scale from the heat treatment and then chemically washed. The cylinder is then tested for hardness and ultrasonic inspection done to check for cracks and other defects. Hydrostatic testing is also done following which an external coating is applied.

1.4.2 Plate Stock Process

The manufacture of steel cylinders using the plate stock process starts with steel plates as stock material. The steel coils are prepared by first drawing in stages in a vertical press followed by deep drawing as shown in Figure 1.3, and ironing in a horizontal press to flatten. The steel coils are cut into blanks from which the cylinders are formed. Intermediate annealing between the drawing operations is critical to ensure a relatively stress-free and malleable work-piece. Chemical treatment and lubrication is applied to facilitate the deep drawing operations.

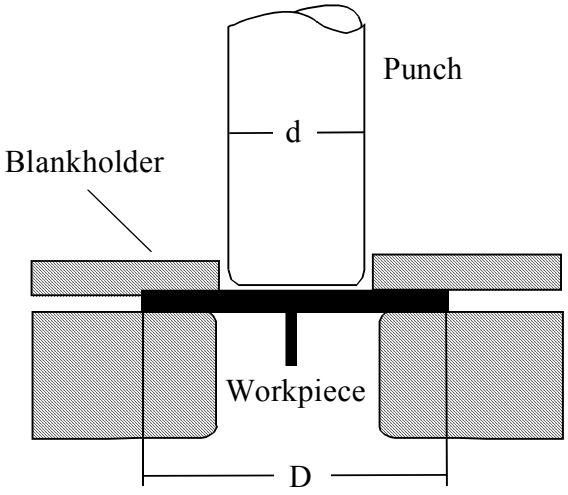

Figure 1.3a Schematic of the Deep Drawing Process

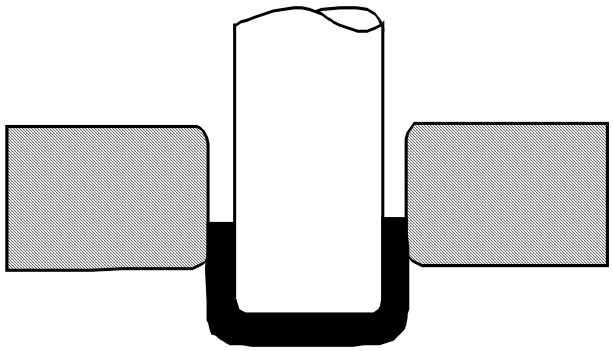

Figure 1.3b Schematic of the Deep Drawing Process

Following the formation of the cylindrical shape, the spinning operation is then undertaken to form the neck and close the cylindrical end. It is similar to the one employed for the neck fabrication of cylinders from billet stock. The ends are ported and threaded and the cylinders are subsequently quenched and tempered in a similar process to the one detailed in the Billet Stock process and shown in Figure 1.2.

The cylinder walls are inspected visually and with ultrasonic methods at the end of the deep drawing process. After heat treatment the material is checked for tensile and hardness properties. Hydrostatic testing is the final procedure following which an external coating is applied to the cylinders as was the case for the Billet Stock process.

1.4.3 Tube Stock Process

The process of manufacturing cylinders from tube stock is less costly than the two processes detailed above. The starting stock is seamless tubes of about 15 inches diameter and 0.300 to 0.400 inches wall thickness. The first part of the process involves

spinning one end of the cut tube until it is closed. The tube is then subject to a series of deep drawing and intermediate annealing cycles to thin the wall and elongate the cylinder.

Base shaping operations is used to form the flat bottom and hemi-spherical end of the cylinders. This operation is conducted with precision, ensuring that there is uniformity throughout the thickness. Final spinning, porting, threading, heat treatment, inspection, testing and painting are performed in a manner similar to the process previously described for the other two manufacturing methods mentioned previously.

1.5 Cylinder Inspection and Testing Procedures

There are three routine inspection or testing procedures that are done on NGV cylinders. Visual inspection is mandatory under the ANSI/NGV2 standard [2], every three years, following manufacturing and deployment of the cylinder. Non-Destructive Examination is recommended by the same standard for all cylinders manufactured and hydrostatic testing every five years. Both tests are intended to ensure the structural integrity of each cylinder. Other tests have been developed and used to examine cylinders especially during routine inspection but none of these tests have been found to be a sufficiently reliable in detecting and characterizing flaws. The testing methods are now reviewed for their effectiveness, in detecting crack-like flaws that originate during the manufacturing process, or cause by general degradation of the cylinder material while in normal use.

1.5.1 Hydrostatic Testing

Hydrostatic testing is required for re-certification of compressed gas (e.g., air and nitrogen) cylinders. The effectiveness and appropriateness of this practice for CNG cylinders are open to some questions. As a result this testing procedure has been withdrawn as a required test since it was determined to be inadequate for detecting cracks and crack growth in the cylinder wall [2]. This is the most likely degradation process leading to the observed failure modes of CNG cylinders [7]. Hydrostatic testing is more suitable to detect section thinning due to localized corrosion which is not one of the failure mechanisms being considered for CNG cylinders.

1.5.2 Non-Destructive/Acoustic Emissions Testing

Acoustic Emissions (AE) testing is a non-destructive testing (NDT) technique used in various industries for evaluating the fitness of structures including tubes and cylinders. Neither existing DOT-3AA [9] specified cylinders, nor existing NGV2-2000 [2] cylinders have regulations that identify AE or other NDT methods as an approved in-service inspection techniques. Therefore, the use of AE in place of detailed visual inspection is only done with approval of the cylinder manufacturer.

AE and other NDT techniques were approved by the revised NGV2-2000 standard in production tests. This is to qualify a cylinder as being free from defects that exceed a specific fracture significant size. The application of these techniques is in accordance with ASTM E647 [10] and other applicable standards. Research currently being undertaken and pending revisions to the ANSI/NGV2 standard opens the potential for AE NDT as an inspection technique. However, in all cases, the use of AE or other

NDT inspection techniques in place of detailed visual inspection requires the approval of the cylinder manufacturer. The Gas Research Institute (GRI) recommends that users consult the cylinder manufacturer for guidance on the use of AE or other NDT techniques.

1.5.3 Visual Inspection

Research indicates that periodic general and detailed visual inspections of CNG cylinders are a prudent and cost-effective means of addressing cylinder safety. General visual inspection, recommended by GRI, describes how to evaluate the visible areas of the cylinder for signs of external damage or abuse. Owner and operators are encouraged to develop awareness among vehicle drivers and mechanics on warning signs to look for when undertaking general visual inspection of NGV cylinders. The NGV2-2000 standard has some guideline for performing such inspections and the qualification of inspectors. Warning signs of damage or abuse that may compromise cylinder integrity includes: cuts, gouges, abrasions, discoloration, broken fibers, loose brackets, damaged gaskets, and heat damage. The general inspections are part of a normal preventive maintenance protocol.

Presently, NGV2 states that a detailed visual inspection should be conducted every three years. FMVSS 304-designed cylinders [11] require this examination every three years or 36,000 miles. This procedure involves a trained and experienced third-party or in-house individual who possesses a thorough understanding of CNG cylinders and knows what evidence to look for when investigating a cylinder and its mounting system.

General visual inspection on a periodic basis by fleet vehicle operators and / or mechanics who have some general training, coupled with detailed visual inspection on a three-year basis, as referred to in the ANSI/NGV2 standard could constitute a suitable program for inspection of compressed gas cylinders for NGVs, providing that all defects were visible to the naked eye. This however is the not the case and continued degradation of cylinders between inspections will lead to failures in service which has been the experience.

1.6 Motivation for This Research

The description of the manufacturing process highlights its potential to introduce defects. These defects, if they continue to grow after leaving the inspection process when the cylinder is manufactured, will very likely go undetected by the existing testing procedure mandated by the NGV-2 standard. This is unless they are on the outside of a cylinder and easily detectible with visual inspection. Even if a crack or crack like defect is detected there is no basis for determining its effect on the remaining life of a cylinder.

The existing state of affairs as it relates to CNG cylinders is that there is a high probability that defects can grow undetected from a sub-critical crack size through the sidewall of a cylinder causing leakage. Unstable crack growth can also occur leading to catastrophic failure of a defective cylinder. Even if a defect is found on the surface of a cylinder using present inspection methods, there are no analytical methods developed and available that can be used to estimate the remaining life of a typical CNG cylinder.

In the foregoing it has been demonstrated that a physics based model that can analytically model the predominant failure mechanisms of a typical CNG cylinder is necessary. This is the motivation for conducting this research. The rationale is that once such a model is developed the frequency of occurrence of failures due to the un-detected degradation of cylinder and the attendant consequences, including fire fatality, can be determined.

Additionally the analytical model will provide a method to fleet owners and operators for estimating the remaining life of a cylinder when defects have been found during the inspection process. The method of developing this physics of failure model and establishing the absolute risk is now expounded.

CHAPTER 2: PHYSICS OF CYLINDER FAILURE

2.1 Factor Contributing to Cylinder Failure

The primary factors that contribute most in determining CNG cylinder life is diagrammatically represented in the conceptual model shown in Figure 2.1. The factors including material property, operating profile, environmental conditions, cylinder geometry and manufacturing process significantly impact the degradation process and ultimately the time or the number of cycles to failure. Their influence is incorporated in the physics of failure model either in development of the mathematical model that best describes the failure mechanisms, or the rate at which the degradation process occurs leading to cylinder failure.

Some factors such as cylinder geometry and operating profile have been analyzed in the past within the context of fracture mechanics in order to develop deterministic models of the growth of preexisting cracks in the material [3 – 4]. Other research efforts have assessed the effects of environmental conditions in determining the degradation process and its effect on the material properties in defining an appropriate criterion for unstable crack growth leading to catastrophic failures such as cylinder rupture [12 – 13].

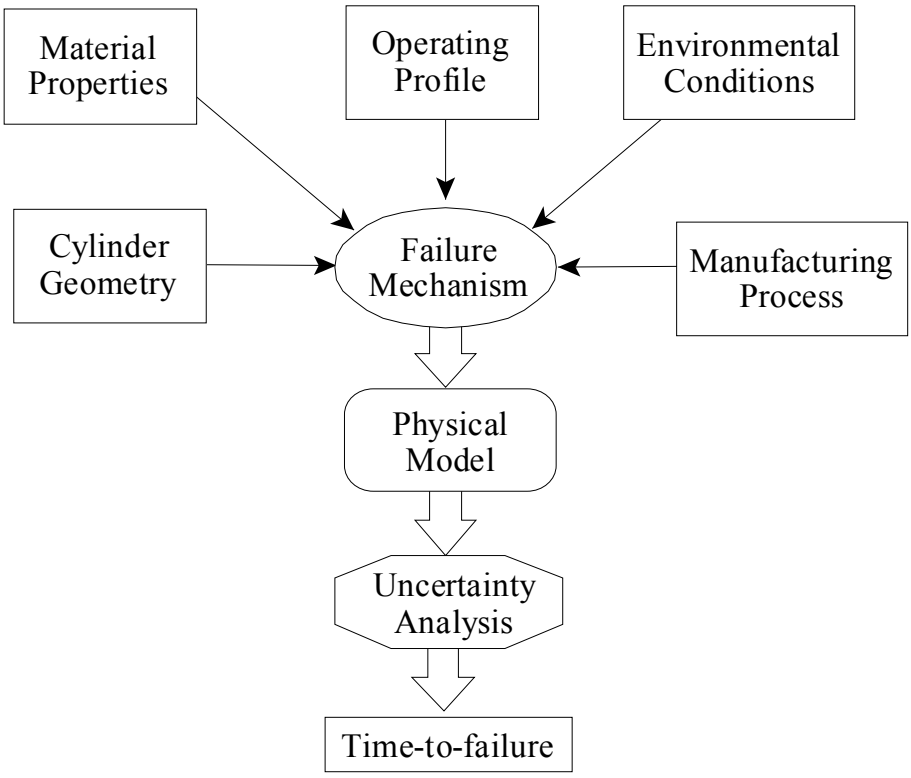

Figure 2.1 Conceptual Cylinder Life Modeling

A combination of approaches will be used to incorporate the effects of these factors in analyzing the physics of cylinder failure, and developing a completely new model of CNG cylinder life. Some of these factors will contribute to or determine the basic input parameters to this model. Other factors such as operating profile and material properties combined to define the cylinder failure criterion.

In developing the physical model, it is assumed that the predominant degradation mechanism could be reduced to a single model with uncertain parameters. The physical life model chosen for the cylinder is a probabilistic model of crack growth due to the

influence of the input parameters shown in Figure 2.1. It has a foundation based on deterministic fracture mechanics. The life of the cylinder is determined by the rate of degradation and the material fracture behavior. The parameters of the deterministic model and the material properties that are used to assess when failure is likely to occur are considered to be random variables, which could be fitted to a parametric distribution. Once the deterministic fracture mechanics model is available and the distribution of the random variables defined, then the failure probability as a function of time, cycles or load can be evaluated.

Determination of the failure frequency is subjected to two well established types of uncertainty: epistemic and aleatory.

Aleatory uncertainty arises as a result of:

1. Inherent randomness in the physical processes that result in cylinder failure such as existence of flaws and fracture toughness of the material.
2. Variability due to incomplete life distribution models selected to represent the crack growth phenomenon.
3. Incompleteness in the parameter selection to define corrosion fatigue phenomenon.
4. Inadequate definition of the inter-relation between the parameters in the complex process of crack propagation to instability.
5. Other human factors.

Epistemic uncertainties exist because of:

1. Statistical uncertainties due to the use of limited information to estimate the parameters of the fracture mechanics model.
2. Simplifying assumptions made in preparation of the mathematical model.

By quantifying the uncertainties, for a given operating profile imposed on the physical model, we are able to determine the expected life of each cylinder in a robust procedure with some measure of confidence. The influence of the input factors in defining the failure mechanism of a CNG cylinder is now detailed below.

2.1.1 Manufacturing Process

Folds, cracks and other defects may be introduced during the manufacturing process. Nucleation and growth of these defects under the influence of cyclic stresses and contaminants in the CNG are the life limiting processes that produce the failure mechanisms in all steel cylinders [12].

Additionally the spinning operations shown in Figure 1.2 and Figure 1.3, creates a large bending moment in the sidewall-bottom transition region as well as the sidewall-neck region. This can promote growth of circumferential crack, initiating on either the inside or the outside surface of each cylinder. Because this crack would be driven by

bending stresses and these stresses are higher at the surface of the metal than at the root of the crack, the crack can grow very long and uniform in depth.

2.1.2 Environmental Condition

The principal corrosion contaminant in U.S. natural gas supplied to gas compression stations are carbon dioxide (CO_2), hydrogen sulphide (H_2S), other sulphur species, oxygen and water [12 - 13]. Natural gas suppliers in the U.S do not routinely analyze their product for H_2S, other sulphur species and water. It has been demonstrated that water is the key constituent since none of the other contaminants produced significant corrosion of cylinder materials in the absence of liquid water or vapor.

Available analyses of the U.S. natural gases from transmission pipelines and distribution systems indicate that corrosive contaminants in natural gas generally are well within limits set by transmission companies and by the U.S. Department of Transportation. These limits apply to natural gas entering transmission pipelines and natural gas used in CNG services, respectively. The only exception is water vapor which is very high in some distribution lines [12]. The maximum water vapor limit allowed by the NFPA standard (7 lbs/mmcf) enables liquid water to form in compressed gas cylinders under certain condition of temperature and pressure. Furthermore, it must also be pointed out that the formation of liquid water within the cylinder is facilitated by the presence of cracks, or crack like defects, due to capillary condensation [14].

2.1.3 Operating Profile

Natural gas vehicle cylinders typically experiences a large number of pressure cycles (from filling at a CNG station to emptying during gas use), than cylinders used in industrial compressed gas service. For example, a 3000 psig service pressure cylinder design is required to provide 15,000 pressure cycles from 300 psig to 3,750 psig for a 15 to 20 years life in NGV service [15 – 17]. This amounts to approximately a refueling history of 2 cycles/day for 365 days/year.

Pressure cycling exceeding the service life will eventually cause cracks in the cylinder walls to grow due to fatigue that may extend through the thickness. When the cracks grow through the cylinder wall they will either result in leak or rupture, the failure mode is usually dependent on the length of the fatigue crack, fracture toughness of the material, internal pressure at the time of failure and the cylinder wall thickness.

The upper pressure limit to which CNG cylinders are filled can exceed the 3750 psig stated above depending on the filling temperature of the gas. Since a fixed volume of gas is usually supplied through the dispensing system, in hot climates the final pressure in the CNG cylinder could be significantly higher assuming ideal gas behavior.

Ambient temperature plays a major role due to the possibility of ductile to brittle transition of the cylinder material. Changes in fracture toughness in very cold climates will cause catastrophic rupture of the cylinders.

2.1.4 Material Properties

The National Association of Corrosion Engineers (NACE) has determined that corrosion of steels will occur irrespective of the threshold limit of hydrogen sulphide, one of the impurities in CNG. The material specified by NACE standard MR-01-75, [18] as being acceptable for service in a gaseous environment where the partial pressure of hydrogen sulphide exceeds 0.05 psia, which is typical for CNG, include carbon and low alloy steels with a minimum hardness of 22 on the Rockwell "C" scale. Quenched and tempered AISI 4130X steels up to a maximum hardness of 26 is also allowed.

The higher the strength of this steel the thinner the wall and the lighter the cylinder. This is a desirable property as not only does it allow the design of lighter cylinders but the higher the strength of the cylinder the more resistant it would be to crack growth and fracture. The corrosive environment limits the use of steels with hardness exceeding 26 HRC, which limits the fracture toughness of the steel used to make CNG cylinders.

2.1.5 Cylinder Geometry

Mode I fatigue cracking occurs more rapidly on the inside walls of a cylinder due to the cylinder geometry, which facilitates higher crack driving force on the inside surface of the cylinder. Cracks tend to grow outwards in a semi-elliptical shape. For most types of CNG cylinders the critical crack length is the length where the crack

becomes unstable and causes the vessel to fail. This critical crack size is a function of the geometry of the cylinder, geometry of the crack and the material properties [7].

For the plane strain fracture toughness K_{IC} to be a valid failure prediction criterion for any CNG cylinder, plane strain conditions must exist at the crack tip. That is, the material must be thick enough to ensure plane strain conditions [19]. It has been estimated empirically that for plane strain conditions the minimum material thickness must be given by:

$$t \geq 2.5\left(\frac{K_{IC}}{\sigma_{yp}}\right)^2 \tag{2.1}$$

Where material thickness is *t*, which is typically from 0.25 - 0.35 inches for CNG cylinders.

A typical CNG cylinder has the following physical parameters:

K_{IC} = 93 ksi
σ_{yp} = 125 ksi

The condition of plane strain is not achieved and plane stress condition exists (right hand side of inequality in Equation 2.1 is 1.38). Linear Elastic Fracture Mechanics (LEFM) criterion using K_{IC} fracture toughness is not valid if the plastic zone around the crack tip is large. If the plastic zone size ahead of the crack tip shown in Figure 2.2 is so large that

small scale yielding conditions are no longer valid then this approach is not valid. If this is so then Elastic Plastic Fracture Mechanics (EPFM) procedures should be employed. This may also affect using available LEFM crack growth models, which have been predicated on plasticity not significantly influencing the growth of cracks.

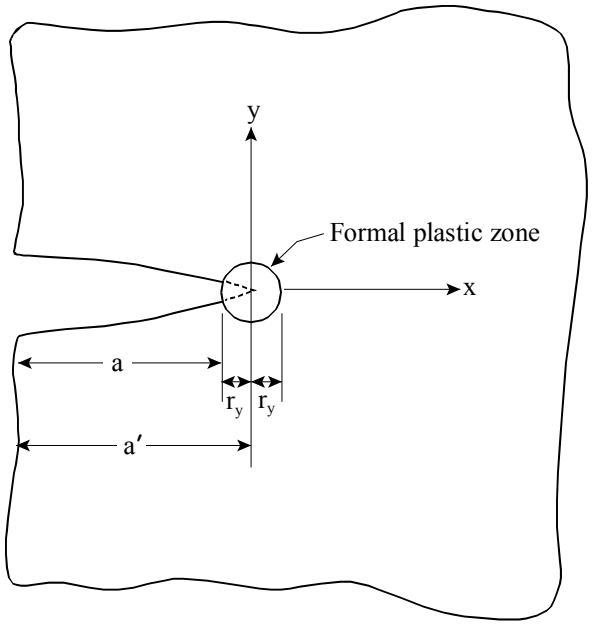

Figure 2.2 Definition of Formal Plastic Zone at Crack Tip

Cylinders that are manufactured with hemi-spherical heads and flat-bottoms, are designed for catastrophic failure to occur in the middle cylindrical portions. This is the area with the highest operating stress. The transition regions are subject to bending moment in the sidewall-bottom and neck transition region. This sets up areas for high stress concentrations if any folds, cracks or other defects are found in this region and would therefore become the weakest part of the cylinder.

2.2 Steel Cylinders Failure Mechanisms

Material properties, cylinder geometry, operating profile, environmental conditions and manufacturing process all contribute to determine the failure mechanisms that are responsible for the degradation process and subsequent failure of a typical CNG cylinder. The combined effect of these factors is more important than any one of them. The manufacturing of thin walled cylinders is a mature technology with the defect limiting procedures well documented. Materials and cylinder profile are selected according to existing good engineering standards to limit the possibility of premature failures. Unlike the other factors less control exist over the operating profile and the environment to which the cylinder is exposed. Undoubtedly therefore, the dominant two factors that determine the mechanism of cylinder degradation leading to failure, are pressure cycling at low frequency in the presence of a corrosive products contained in CNG. The rate of progression of the mechanisms to failure is influenced most by the material properties of the steels and the cylinder geometry. The significant mechanism that results in the degradation of a typical CNG cylinder is now examined.

2.2.1 Stress Corrosion Cracking (SCC)

There is no threshold limit for hydrogen sulphide below which corrosion of steel does not occur [20]. The partial pressure of hydrogen sulphide that could cause sulphide induced stress corrosion cracking (SCC) in CNG cylinders depends primarily on the following factors:

- Micro structure of the AISI 4130X steel

- Applied stress on the cylinder wall
- Time of exposure to the SCC environment

Hydrogen sulphide induced stress corrosion cracking of steels is essentially a hydrogen embrittlement phenomenon [21], [13]. Dissolution of H_2S in water produces an acidic solution according to the reaction in Equation 2.2.

$$H_2S \Leftrightarrow H^+ + HS^- \quad (2.2)$$

Steel in contact with such a solution corrodes to form atomic hydrogen and iron sulphide according to Equation 2.3.

$$Fe + H^+ + HS^- \Leftrightarrow FeS + 2H° \quad (2.3)$$

If the iron sulphide formed is adherent, it acts as a barrier and reduces the corrosion rate to a low level, which is further reduced with additional build up of corrosion products. If the sulphide corrosion products do not adhere to the surface, corrosion continues at a rate determined by the concentration of H_2S, the solution pH, and other factors such as temperature. If iron sulphide covers only part of the metal surface, the corrosion rate of the uncovered part may be accelerated and pitting may occur.

Most of the hydrogen generated in the corrosion reaction shown in Equation 2.3 combines to form molecular hydrogen, H_2, which is evolved from the surface as a gas. However, a part of the atomic hydrogen diffuses into the steel and may recombine to

form molecular hydrogen within the metal which reduces the ductility and fracture toughness of the steel. Under conditions of high stress localized sulfide-induced stress corrosion cracking may occur.

When a cylinder is filled, the material is in tension. The equilibrium concentration of hydrogen at microscopic crack tips is greatly increased by the hydrostatic tension. During the slow filling operations the hydrogen has time to diffuse to any existing crack tips while filling is still in progress; thus, embrittlement results and additional crack propagation occurs during the filling process which is representative of a loading cycle. When the cylinder is fully pressurized, the diffusion of hydrogen to the crack tip still occurs, however the hydrogen cannot cause cracking during the utilization of CNG or the unloading cycle. This is because of the reduction of the partial pressure of hydrogen sulphide in the remaining CNG due to corrosion reactions and the utilization of the fuel. When the pressure in the cylinder is reduced and held at low pressures SCC does not occur as the hydrogen diffuses away from the crack tip because of the reduction of hydrostatic tension.

The propensity is for SCC to increase with increasing material hardness (or strength) and hydrogen sulphide content [21]. Typically, as the strength of the steel increases, less hydrogen is required to promote cracking [20]. Both AISI 4130X and 15B30 steel alloys are susceptible to SCC in liquid water environments saturated with

H_2S. However, it was found that 15B30 steel, which is harder was more susceptible to general corrosion than was 4130X and the corrosion rate was higher [13].

Other sulfur-containing species such as mercaptans contributes to stress corrosion cracking. Mercaptans are common contaminants containing sulfur which may occur naturally in natural gas or which may be added as an odorant. Mercaptans are chemically similar to H_2S and attack steels similarly, forming hydrogen and iron sulfides. Other water soluble sulfur species may be expected to behave similarly to H_2S and mercaptans.

Evaluation of various cylinders, with up to 5 years in service [13], [20] through burst testing, pressure cycling to failure, inspection by acoustic emission, ultrasonic and visual examination has not shown any significant loss of integrity or surface corrosion. No noticeable crack growth from large fabrication flaws found in several of the cylinders was detected during this detailed inspection. These results are not consistent with the previously described failure mechanism of stress corrosion cracking. A possible explanation for this is that a thin film of oil typically found coating the internal surfaces of cylinders, coming from the compressor, acts as an inhibitor contributing to the absence of corrosion. Additionally most of the water in the gas supplied to the compression station is removed by the transmission gas drying system. The distribution and dispensing systems also reduces the water vapor concentration of the CNG fuel.

Because of this finding from extensive research stress corrosion cracking due to hydrogen embrittlement irrespective of the partial pressure of H_2S and CO_2 in the CNG fuel will not be considered by itself to degrade CNG cylinders to be a life limiting failure mechanism. Its contribution to modeling cylinder life is however significant. The elimination of stress corrosion cracking could lead to errors in the results especially for catastrophic failures or rupture of CNG cylinders. This becomes more apparent when one considers the fact that higher strength steels are more susceptible to SCC. It could become an important failure mechanism in the future, with the current research suggesting that significant weight reductions can be achieved without any increased risk of cylinder failure, by switching to higher strength steels.

2.2.2 Corrosion - Fatigue

The most damaging form of cylinder degradation is corrosion fatigue. Corrosion-fatigue occurs as a result of the combined action of cyclic re-pressurization and corrosion of the cylinders due to the presence of impurities in the CNG. The corrosion process is exactly as has been described for hydrogen sulfide induced stress corrosion cracking detailed in the previous section. This failure mechanism is expected to originate at corrosion pits formed on the inside surface of the cylinder or pre-existing manufacturing defects. The corrosion process accelerates fatigue failure by producing pits and surface discontinuities which acts as stress raisers and therefore sites for further crack growth. Additionally cracks in the areas affected by corrosion which are usually brittle acts as fatigue crack nuclei that propagate into the base metal. Crack propagation will occur as a

result of cyclic fluctuation of the internal pressure of the CNG during normal bus operations in the presence of a corrosive environment. The cyclic loads or strain causes cracking and flaking of the corrosion layer, which exposes parent metal to the corrosive medium. Each process will compliment the other thereby accelerating the crack growth phenomenon and making the result disproportionately more significant than would normally be obtained if either mechanism acted independently. Unlike SCC, corrosion fatigue crack growth is expected to occur, the rate of which will be determined by the initial crack size, the cyclic frequency of the loading and the environment.

These cracks will propagate from sub-critical dimensions to a critical size, following which rapid tearing of the cylinder material will occur resulting in a catastrophic burst fracture. Alternatively, the crack could propagate through the sidewall of the cylinder without plastic tearing occurring. The occurrence of one failure mode or another is dependent on the fracture toughness of the material, temperature and the maximum stress intensity factor as the crack penetrates the wall of the cylinder.

Information on the interaction between the environment and the metal surface at the crack tip is necessary in order to model corrosion fatigue and to predict service life of cylinders subject to this failure mechanism. The corrosion process was detailed in the previous section and shows how localized pitting or cracking can occur due to hydrogen embrittlement. The results of the first investigation into the effect of the frequency of sinusoidal cyclic stress fluctuations on the mechanism of corrosion-fatigue were reported

in [22 – 24]. From the data it was concluded that acceleration of fatigue crack growth in a corrosive environment does occur, below the stress intensity factor for unstable crack growth due to stress corrosion cracking, K_{ISCC}. It also showed that for the high strength steel used in the experimentation (12Ni-5Cr-3Mo maraging steel) at ambient temperature in air and 3% sodium chloride solution, the fatigue crack growth rate can be represented by Equation 2.4 [21].

$$\frac{da}{dN} = D(N)\Delta K^{m(N)} \tag{2.4}$$

Where *D(N)* is the constant of proportionality between the rate of crack growth and ΔK, the stress intensity factor. *D(N)* is dependent on the steel and the composition of the corrosive environment and the sinusoidal cyclic stress frequency. The stress intensity factor exponent, *m(N)*, on the other hand is dependent on the rate of increase of the stress level and on the maximum and minimum stress levels. It remains constant with different materials and environment, between stress intensity factor levels where stable or Stage II crack growth is occurring.

Barson found [22 -23] that in air and in sodium chloride solutions at high frequencies (greater than 600 cpm), *D(N)* was a constant. This suggested that the corrosive environment at stress cycling above this frequency had negligible effect on fatigue crack growth rate. In sodium chloride solution at 6 cpm, *D(N)* was found to be three times higher than the value obtained in air. This is an indication that corrosion

accelerated the fatigue crack growth rate. It is further inferred [21] that the corrosion fatigue crack growth rate of this high strength steel in a corrosive environment increases to a maximum value then decrease as the sinusoidal cyclic stress frequency decrease from 600 cpm to frequencies below 6 cpm.

It has been shown in reference [21] that in addition to frequency of load cycling, *D(N)* is dependent on the form of the cyclic loading and the corrosion resistance of the material. Since high strength steel is not strain rate sensitive, then *D(N)* at high frequency loading approaches a constant value characteristic of fatigue crack growth rate in a benign environment. In a corrosive environment at low frequency the shape of the fatigue crack growth curve remains the same and can be represented by Equation 2.4. The shift in the curve from a purely fatigue stable crack growth process, is represented by a multiplicative constant. The same applies to other steels.

Fractographic analysis of the fracture surface [24] of specimens that have failed due to corrosion-fatigue crack growth, indicated that the primary mechanism responsible for accelerating the fatigue crack growth in high strength steel in a corrosive environment (3% sodium chloride) was hydrogen embrittlement [24]. A phenomenological analysis of corrosion-assisted fatigue below K_{ISCC}, shows that crack growth occur primarily while the material at the crack tip is being plastically deformed during the loading cycle and that the environment has little effect during the constant load portion of the cyclic wave. This was deduced from tests during different load profile (square, sinusoidal and

triangular). The load profile of a typical CNG cylinder is somewhere between a square and sinusoidal loading and therefore this crack growth phenomenon would apply. In [24] it has also been shows that the magnitude of environmental is effects dependent on the time within each cycle during which the metal is being plastically strained.

Hydrogen is generated in the crack tip neighborhood by the interaction between the corrosive environment and the fresh metal surface exposed in each cycle as occurs in the SCC process. The hydrogen then diffuses into the plastic zone region where the material has undergone relatively few cycles of plastic strain. Acceleration in the rate of fatigue crack growth in the corrosive environment then occurs by hydrogen embrittlement of the cyclically strained material. No indication of corroding away of ligament left behind the crack tip by the corrosion products have been reported [24].

2.2.3 Generalized Corrosion - Fatigue Crack Growth

The generalized fatigue behavior of various metals can be obtained from experimental research conducted on fatigue crack growth. Fatigue crack growth behavior of steel can be divided into three regions as shown in Figure 2.3. The behavior in Region I exhibit a threshold for cyclic stress intensity factor fluctuation, ΔK_{th}, below which cracks do not propagate under cyclic stress fluctuations [25] or the crack growth rate is immeasurably slow. ASTM [26] has defined the threshold ΔK_{th} to correspond to a fatigue crack growth rate of 10^{-10} m/cycle. The value of ΔK_{th} for CNG cylinder steels has been reported to be between 10-14 ksi $\sqrt{}$inch. Region 1 corresponds to a period

where microscopic defects in the metal nucleate resulting in significantly increased crack growth rate with small changes in the applied stress intensity factor.

Region II is characterized by steady growth of the fatigue crack under the influence of increased stress intensity factor cycling. This represents the most significant part of the corrosion fatigue life of a CNG cylinder. Modeling the growth of a crack through Regions I and II will give adequate representation for the fatigue life of a typical CNG cylinder.

The corrosion-fatigue crack growth rates above ΔK_{th}, in Region II, can in general be described by Equation 2.5 [27 – 28]:

$$\frac{da}{dN} = f(\Delta K) \tag{2.5}$$

where:

a = crack length (inches),

N = number of cycles,

ΔK = stress intensity factor fluctuation (ksi $\sqrt{}$inch), and

$f(\Delta K)$ = functional relationship between the stress intensity factor fluctuations and the rate of crack growth.

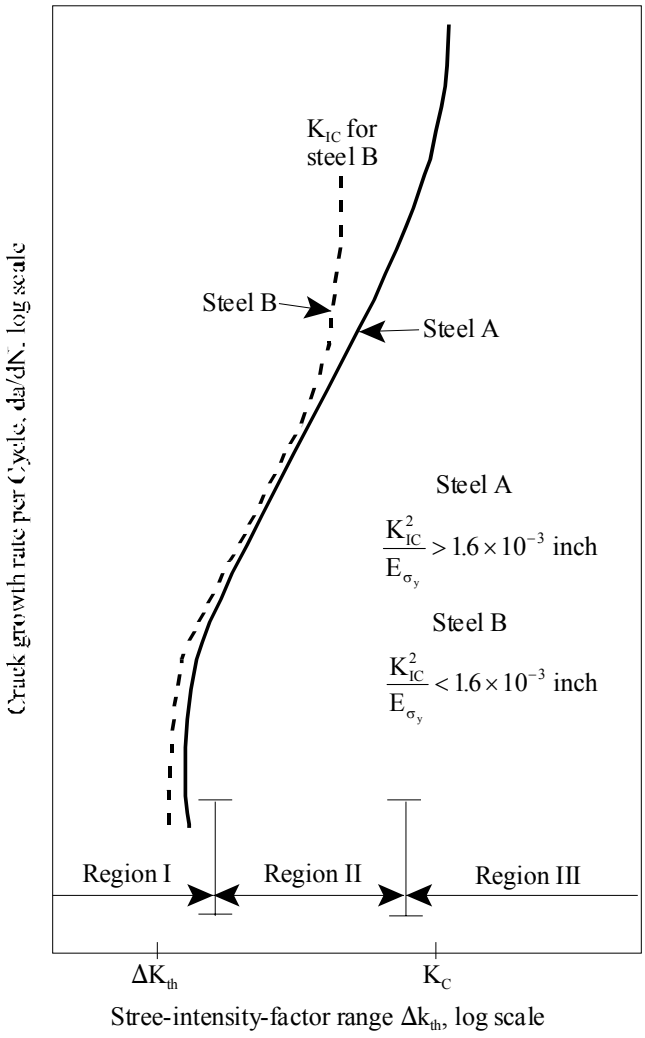

Figure 2.3 Schematic Representation of Fatigue Crack Growth In Steel.

Crack growth behavior is generally modeled using Linear Elastic Fracture Mechanics (LEFM) concepts. LEFM is used because of the availability of stress intensity factor solutions which relate rate of crack growth to loading on the crack surface. Most of these solutions were developed using numerical methods. LEFM methods are most frequently applied to describe crack growth behavior associated with

Region II. In this region the slope of the log *da/dN* versus log *ΔK* curve is approximately linear and lies roughly between 10^{-6} and 10^{-3} in/cycle. Many curve fits to this region have been suggested. The Paris equation [29], shown in Equation 2.6, which was proposed in the early 1960's, is the most widely accepted.

$$\frac{da}{dN} = C(\Delta K)^m \tag{2.6}$$

where

a = crack length (inches)

N = number of cycles

ΔK = stress intensity factor range $(K_{max} - K_{min})$ (ksi $\sqrt{}$inch)

C, m = material constants

ASTM E647 sets guidelines for performing tests in order to determine values of the exponent, m and constant C.

Region III corresponds to the transition into instability and rapid crack extension leading to cleavage fracture typically along a particular crystallographic plane. In this region the fatigue crack growth per cycle is higher than predicted by Equation 2.6. Research has shown [28], [30] that the rate of fatigue crack growth increases and that under zero to tension loading, ($\Delta K = K_{max}$), this increase occurs at a stress intensity factor value given by the equation:

$$\frac{K^2}{E\sigma_y} = 1.6\times10^{-3} \text{ inches} \quad (2.7)$$

where

E = Young's modulus and

σ_y = yield strength (0.2% offset)

Equation 2.7 is used to calculate the stress intensity factor corresponding to the onset of fatigue transition, K_C, for materials where the fracture toughness, K_{IC} is higher than the transition stress intensity factor [21]. This applies to all high strength cylinder steel materials.

Acceleration in the rate of fatigue crack growth occurs at a value slightly below the critical stress intensity factor when the fracture toughness, K_{IC}, of the material is less than the Region III transition stress intensity factor K_T. Most important is the acceleration in the rate of fatigue crack growth, below K_T when the K_{ISCC} for the cylinder exposed to a corrosive environment is less than the stress intensity factor at the onset of fatigue rate transition, K_T. This applies to all DOT 3AA cylinder materials.

The fatigue life in Region III is insignificant compared to the overall life, as the fatigue life is measured by the steady growth of a crack from a small to a critical crack size. Crack growth in this region occurs at high stress intensity factor cycling, $\Delta K's$ and therefore more indicative of imminent failure. The criterion for such failure is when the K_{1C} and J_{1C} material properties are exceeded by the applied K and J.

CHAPTER 3: PHYSICS OF FAILURE MODELING OF SUB-CRITICAL CRACK GROWTH

3.1 Approaches to Cylinder Physical Life Modeling

The major components of the physical life model incorporating deterministic and probabilistic fracture mechanics analysis of corrosion fatigue crack growth is summarized in Figure 3.1 This schematic representation of the model shows the fundamental considerations in modeling and prediction of crack growth to instability in a CNG cylinder.

Overall the failure characteristics are determined by the following from the model:

- Fatigue important cracks and other flaws that originate in the cylinder at the time of manufacture and their location in the cylinder walls.
- Inspection methods used and the probability of detection of fatigue flaws.
- Physical properties of the AISI 4130X material used to construct the cylinders.
- Sub-critical and fast corrosion fatigue crack growth characteristics of the alloy.
- Applicability of the crack driving force solution adopted based on the influence of plasticity at the crack tip.
- Operating profile and stress history of the cylinder while in service.
- The failure criterion used whether elasticity is assumed to dominate the fracture (LEFM) or to include plasticity effects (EPFM).

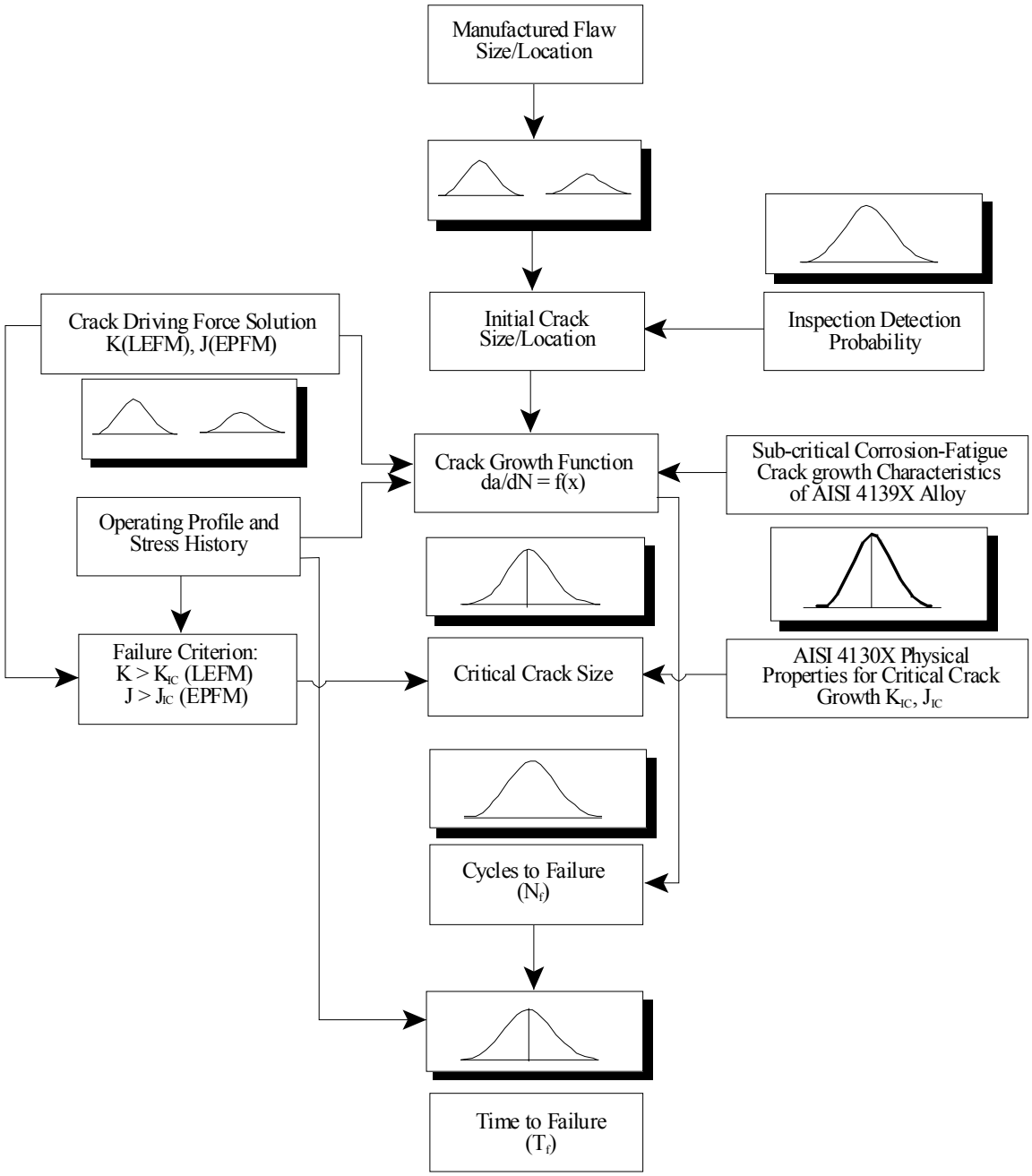

Figure 3.1 Physics of Failure Model of CNG Cylinder Failure Characteristics

The elements of the model and their effects are derived from the factors that have been determined to impact significantly on the degradation and failure of a typical CNG cylinder. The distribution of the parameters representing each element is required in order to analytically model the degradation and the point at which failure is deemed to occur. Calculation of the probabilistic fracture mechanics sub-critical crack growth and the fast crack growth at the onset of fracture can be undertaken by inputting the distributions in the appropriate crack growth model.

The sub-critical crack growth will be assumed to occur as a result of fatigue crack growth which will be accelerated by environmental influences such as the presence of water vapor and corrosive compounds in the CNG. The factors or their influence on the failure characteristics of a cylinder is distributed in nature and as such the cycles to failure and time to failure will be distributed quantities. The model to be developed and the method to evaluate them will be consistent with accepted probabilistic fracture mechanics methods.

A probabilistic model of crack growth will now be developed and its propagation to failure as a result of the characteristics discussed above will be evaluated. The type of crack to be analyzed and necessary assumptions adopted, allow for tractable fracture mechanics analysis of the DOT 3AA materials under consideration, without loss of accuracy in the results. This is consistent with similar analysis done for pressure vessels in the nuclear and other industries. There are no probabilistic models available for crack

growth in CNG cylinders. Comparisons will be made to this model and a deterministic model developed at South West Research Institute (SWRI), to show the superiority of this probabilistic fracture mechanics method of modeling corrosion fatigue crack growth to previous research done.

3.2 Discussion of Fundamental Assumptions

The major assumptions employed in the physical modeling of cylinder life are discussed in this section. Some of the assumptions are inherent in probabilistic fracture mechanics analysis of the CNG cylinders while others are more germane to the specific type of analysis. Throughout the analysis other assumptions more specific to the different sections will be presented. Uncertainties due to these assumptions are not quantified and should be analyzed in future research. The assumptions made are not expected to significantly alter the results of the probabilistic modeling of the corrosion-fatigue crack growth phenomenon.

The following are the major assumptions:

- Cylinder failure due to corrosion fatigue occurs due to the growth of cracks introduced during manufacturing or through normal use. Other failures due to design, manufacturing, assembly or errors in use are omitted. All other failures which are stochastic in nature such as accidental impact are also omitted. These should be considered in future studies.

- All cracks are assumed to be located on the inside or the outside surface of the cylinder wall for both the cylindrical portion and the transition regions which include the ends. Embedded cracks were not considered because it was felt that for a given crack size and stress level, a surface crack will be more severe, because it will have a larger stress intensity factor. The crack driving force will be much greater making the inside and outside the most likely failure sites. Furthermore it has been documented that only surface cracks grow in fatigue.

- In the transitional regions of the cylinder principal stresses are determined and used in finite element solutions of a flat plate subject to bending and tension. This is a simplified approach but the best within the framework of current fracture mechanics techniques and available stress intensity factor solutions.

- Manufacturing flaws in the cylinders are independently and identically distributed in size. In other words the initial crack size distribution is taken to be the same in each section of the cylinder. The density of cracks (number per unit area) will vary for each section consistent with the manufacturing process and the stress distribution in the cylinder. A homogenous Poisson process can therefore be used to model manufacturing flaw distribution and crack depth exponentially distributed.

- Only cracks which are fracture important are considered. Three aspect ratios are considered, 0.2, 0.4 and 1.0 representing a diverse crack shapes that are expected to grow in fatigue.

- The sub-critical growth of cracks due to corrosion fatigue are similar to fatigue crack growth and can be predicted from linear elastic fracture mechanics or elastic plastic fracture mechanics analysis.

- The stress history defined by cycling from filling the cylinder and emptying during the use of CNG, controls corrosion fatigue crack growth. Filling raises the internal pressure to 3000 psig and emptying reduces the pressure to 300 psig.

- If more than one crack exists in each section of the cylinder then the cracks will not interact with each other or nucleate to form larger cracks. The critical condition for unstable crack propagation is dependent only on the size of the largest crack present on the surface of the cylinder.

- Catastrophic cylinder failure from unstable corrosion-fatigue crack growth is determined either by $K_{applied} > K_{1C}$ (cleavage fracture), net section instability (excedence of a critical net section stress) or tearing instability, $T_{applied} > T_{mat}$ (ductile rupture) whichever results in the smallest critical crack size at a given stress level.

- The applied stress used in the failure criterion will not be significantly relaxed by crack extension, instead remains constant even during incremental crack growth. Initial pressure is only relaxed when crack breaches through wall.

- Cracks are elliptical or semi-elliptical in shape and retain that profile during crack growth until they grow through the walls of the cylinder. Once a crack grows through the cylinder wall, the outside and inside surface lengths are equal.

- The crack growth is controlled by the stress intensity factor arising from the stress intensity created by the pressure in the cylinder and the stress distribution at the crack tip.

- Cracks are found during the testing phase after manufacturing or periodic testing using NDE techniques. The probability that a crack will be detected depends only on the size and not on the skill of the equipment operator.

- Cracks detected, if their sizes are fracture significant, are weld-repaired or the cylinder is removed from service. The crack population is not affected by any other maintenance procedure. Cracks can be introduced during the weld repair process consistent with the Chapman model [31].

3.3 Characterizing Corrosion - Fatigue Crack Growth

Crack growth and fracture behavior of CNG cylinders can be evaluated by the two well established fracture mechanics modeling techniques, namely Linear Elastic Fracture Mechanics (LEFM) and Elastic Plastic Fracture Mechanics (EPFM). The growth of cracks due to corrosion-fatigue has to be modeled from the initial crack size until the crack grows through the wall of a typical CNG cylinder, or for rupture of the cylinder material to occur. Both failure modes are considered and constitute the fatigue life of the cylinder.

The rate of crack growth is dependent on the initial crack size, stress distribution at the crack tip and the material resistance to crack growth. Fracture on the other hand is dependent on the resistance of the material to plastic tearing in the vicinity of the crack and fracture toughness. It is therefore evident that the failure modes under consideration are dependent on the number and size of fracture significant flaws generated during manufacturing, operating profile as well as the material properties. Cracks generated during the weld-repair during inspection or after manufacturing are considered separately in their impact on the fatigue life.

Research work conducted on behalf of the Gas Research Institute at South West Research Institute (SWRI), have characterized corrosion-fatigue crack growth and fracture behavior of cylinder steels, within the framework of linear elastic fracture mechanics [4]. This was done by studying the crack growth phenomenon in Region II until transition into Region III where accelerated crack growth will occur. This has been used to define the useful life of the cylinder.

The research results highlighted in Figure 3.2 show that the crack growth rate increased with decreasing frequency of cycling and showed a saturation point of about 0.05 Hz. Below this cyclic loading there was no enhancement in crack growth rate. The significance of this is that the deterministic models developed for corrosion-fatigue testing of CNG cylinders at frequencies below this saturation point, are applicable to much lower cyclic frequencies. The results are therefore valid for the cyclic frequencies expected during re-fueling of CNG cylinders.

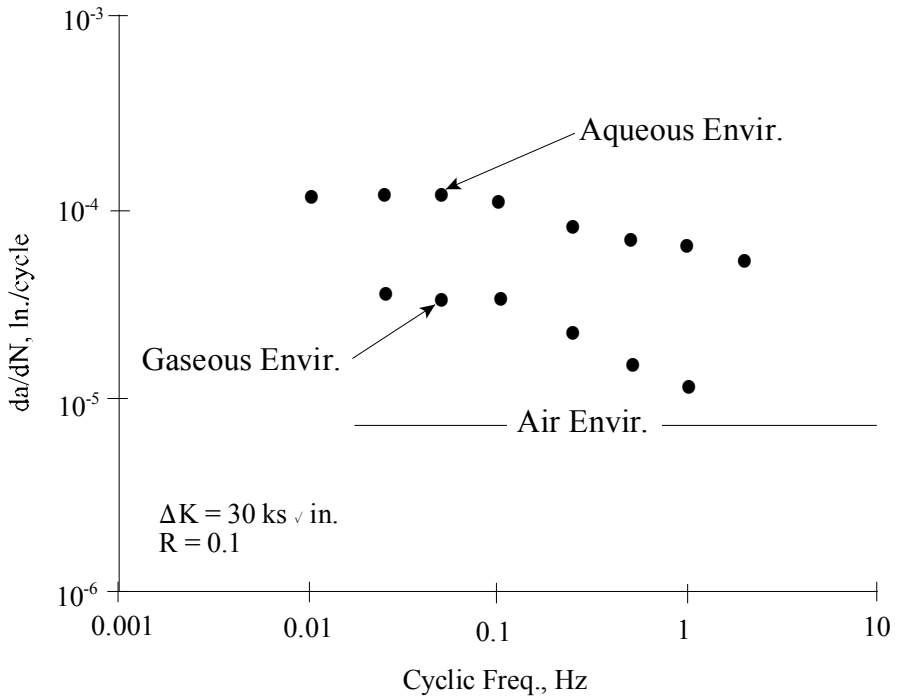

Figure 3.2 Corrosion-Fatigue Crack Growth Dependence on Cyclic Frequency [3]

The stress-strain field near a crack tip in a linear elastic body is controlled by the stress intensity factor, *K*. It is therefore reasonable to assume that the rate of growth of a crack under cyclic loading conditions is controlled by the cyclic value of the stress intensity factor. This can be expressed as follows:

$$\frac{da}{dN} = f(\Delta K) \tag{3.1}$$

where

$$\Delta K = K_{MAX} - K_{MIN} \tag{3.2}$$

This relationship between the cyclic stress intensity factor and the rate of growth of a crack in a material undergoing fatigue cracking, has been experimentally demonstrated since it was first suggested by Paris, Gomez and Anderson [32] and standard exist for such measurements. Many functional relationships have been suggested and correlated with experimental data for fatigue crack growth. Under similar environmental conditions, the growth relationships have been shown [33] to be remarkably insensitive to micro structural variables, with generic values of material constants being applicable to a wide class of materials, such as ferritic steels, martensitic steels, etc., [34]. This is because the growth relationship is most impacted by the lattice structure of the material. At extremes of crack growth rates more material dependencies are seen and more sophisticated models have been developed to account for this. These models have all improved on the original Paris law which states:

$$\frac{da}{dN} = C\,\Delta K^{n_f} \tag{3.3}$$

There are no crack growth models that explicitly accounts for the non-linearity inside the plastic zone which surrounds the crack tip. Unlike stress intensity factor solutions, the number of fully plastic crack driving force solutions available are very limited and are generally confined to simple specimen geometries and a few planar and axisymmetric bodies [35]. A conservative approach will be adopted where all corrosion fatigue crack growth modeling will be limited to consideration of the stress strain field near the crack tip in a linear elastic body.

For Type I cylinders, the critical crack length is the crack length at which point the crack becomes unstable and cause the vessel to fail. This critical crack size is a function of the geometry of the cylinder, geometry of the crack and the material properties. LEFM and EPFM methods will be used to analyze final fracture behavior of CNG cylinders. Research at Powertech Laboratories [7], has found that EPFM methods are more appropriate for characterizing final fracture. This is consistent with what has been determined in Section 2.1.5. Since plain strain conditions do not exist, the uncertainties as a result of the effect of the plastic zone cannot be accounted for in existing LEFM models.

3.4 Corrosion-Fatigue Crack Growth Modeling

Corrosion fatigue crack growth in the CNG cylinder will occur under the influence of the stress intensity factor as the crack driving force. The stress intensity factor represents the combination of far field or bulk stresses and crack length. An increase in either of these will result in an increase in the stress intensity factor. The growths of these cracks are also influenced by the amount of moisture present in the CNG as shown in Figure 3.3. Crack growth in the sidewall region is different from crack growth in the transition region because of the different crack driving force. As will be shown later in Section 3.4 and Section 3.5, the stress intensity factor for the transition region is much greater and as such fracture is likely to occur here first.

3.4.1 Deterministic Crack Growth Modeling

Research on crack growth modeling in pressurized CNG cylinders is sparse, with the most notable conducted at SWRI [3 - 4]. The corrosion-fatigue crack growth model developed from this research is a deterministic model developed empirically from data. This work was conducted on AISI 4130X steels in aqueous, wet and dry gas environments at cyclic frequencies of 0.05, 0.1 and 1.0 Hz. The crack growth behavior at 0.05 Hz is applicable to corrosion fatigue crack growth at the expected much lower frequencies of cyclic filling and emptying of CNG cylinders at use level. Experimentation has shown that the rate of crack growth is greater at the lower cyclic frequency and remains a source of uncertainty when performance is extrapolated to the use level.

The mathematical representation of the phenomenon covers the three crack growth regimes and describes the experimental data over a range of stress intensity factors from the very low near-threshold behavior to the crack growth rates at high ΔK's when failure is eminent. This expression describes the results well for the three environmental effects that were investigated. The mathematical expression is a modified form of the Foreman relation [36] and includes threshold effects and the influence of load ratio, R. It is written in a form to represent the materials resistance to crack growth instead of the rate of crack growth and is given as:

$$\frac{1}{da/dN} = \frac{A_1}{\Delta K^{n_1}} + \frac{A_2}{\Delta K^{n_2}} - \frac{A_1}{\left[(1-R)K_c\right]^{n_2}} \tag{3.4}$$

where

$$\Delta K = K_{MAX} - K_{MIN} \tag{3.5}$$

and

$$R = \frac{K_{min}}{K_{max}} \tag{3.6}$$

$A_1, n_1, A_2, n_2,$ and K_c are empirical constants obtained from the experimental data and R is the ratio of the minimum to maximum loads in each fatigue cycle. R also characterizes the mean stress level. The variability of the constant terms in the expression was not accounted for in the crack growth modeling as the data was not available to develop distributions for these terms. This is a source of uncertainty in the frequency of cylinder failure which should be evaluated.

The first two terms in the equation describe the crack behavior in the first two stages of crack growth before the onset of unstable crack growth. The third term which describes unstable crack growth just prior to ductile tearing and fracture is not needed to describe the cylinder life as this region only contributes to crack growth rate (da/dN) at very high ΔK's, when most of the life has already been expended. The first two terms of the expression describe the fatigue crack growth during what can be called the fatigue life of the cylinder. Because of the uncertainty associated with the on-set of ductile tearing,

the third expression is important to define the fracture point. This was not included in the calculations for the number of cycles to failure that was done.

The values of the parameters shown in Table 3.1 were evaluated by fitting Equation 3.4 to the experimental data obtained by fatigue testing in three gas environments [4]. The parameters represent two different portions of the curve as shown in Figure 3.3. One portion of the curve represents the behavior of the lower ΔK's in the near threshold region, and the other at the higher ΔK's above the threshold. Crack growth tests were conducted on cracked ISI 4130X steel specimens in corrosive environments described as aqueous and wet gas as follows:

1. Aqueous environment consists of H_2S and CO_2 in water with the specimen fully immersed. The partial pressures of H_2S and CO_2 levels were designed to be greater than NFPA 52 Regulation in order to simulate worst case situation.

2. The gaseous environment consists of H_2S and CO_2 gas and water vapor. The partial pressure of water vapor was limited to ensure than condensation did not occur even though capillary condensation of water vapor was observed to occur during the test.

3. Dry gas was the gaseous conditions with contaminants in dry air.

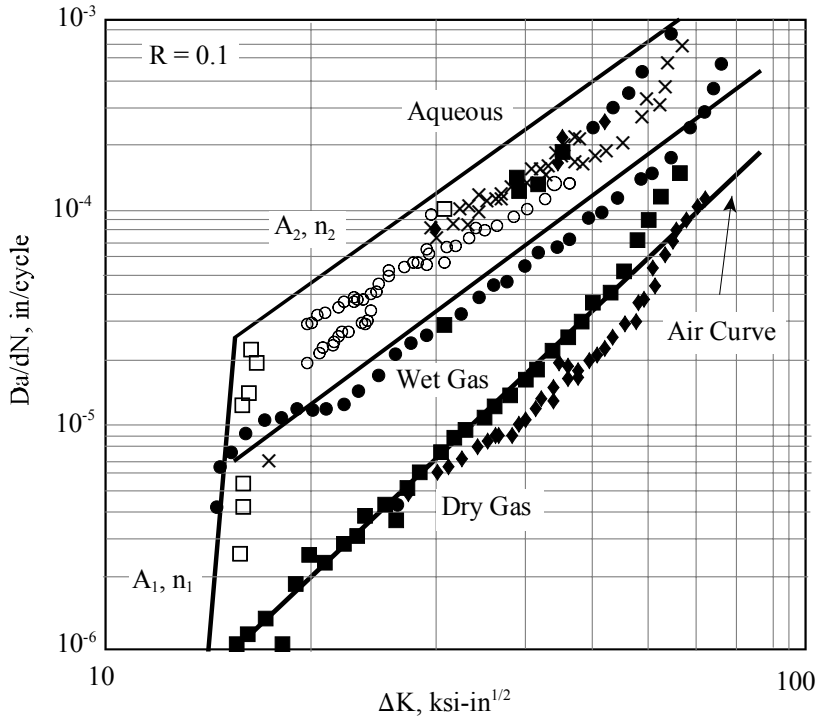

Figure 3.3 Fatigue Crack Growths for CNG Materials in Different Environments [4]

Table 3.1 Fatigue Crack Growth Rate Parameters in Different Gas Environments [4]

Environment	Model Parameters			
	A_1	n_1	A_2	n_2
Aqueous	8.3×10^{60}	48	2.0×10^{7}	2.3
Wet Gas	8.3×10^{60}	48	7.7×10^{7}	2.3
Dry Gas			1.0×10^{10}	3.30

The corrosion fatigue crack growth rates in the aqueous and wet gas environment falls off markedly as the stress intensity factor decreases as shown in Figure 3.3 [4]. This

precipitous drop in the crack growth rates at the lower frequency is a result of the crack flanks being wedged open due to the build up of corrosion products within the crack as well as increasing contact of crack face asperities due to the rough surfaces produced by crack growth in the aggressive environment. This wedging action effectively relieves the high stresses at the crack tip and produces an increase in crack closure with concomitant drop in crack growth rates. This drop in the crack growth rates effectively defines a threshold below which cracks will not grow in an aqueous environment.

3.4.2 Probabilistic Crack Growth Modeling

A probabilistic model was developed for corrosion fatigue crack growth based on the data generated in the experimentation that was used to develop the deterministic model. The uncertainties highlighted in Section 3.3.1 as well as the inability of the model to account for the stress intensity factor threshold below which crack growth will not occur is the primary reason for developing this probabilistic model. The deterministic model did not adequately represent the different mechanism of crack progression from crack blunting to unstable growth and was one of the rationales for the development of this model. The evaluation of the sensitivity of the crack growth relation to the empirical constants is possible using the probabilistic model.

3.4.2.1 Crack Growth Relationship

Fatigue crack growth rate as shown in Equations 3.1 and 3.3 is a strong function of cyclic stress intensity factor. The crack growth rate can be adequately characterized by the following empirical relation [37 - 38]:

$$\frac{da}{dN} = C\left|\frac{\Delta K}{\sqrt{1-R}}\right|^{m} \tag{3.7}$$

Expressing in a simplified format

$$\frac{da}{dN} = C\left(K'\right)^{m} \tag{3.8a}$$

$$K' = \frac{\Delta K}{\sqrt{1-R}} \tag{3.8b}$$

where

da/dN is the fatigue crack growth rate in *inches/cycle*

ΔK is the cyclic stress intensity factor (K_{max} -K_{min}) in *ksi-in*$^{1/2}$

R is the load ratio, K_{min}/K_{max}

C and *m* are empirical material constants

K′ is the effective stress intensity factor that accounts for the effect of cyclic stress intensity, *ΔK* and the load ratio, *R*, on fatigue crack growth rate. It has been shown by

Bamford, Hale and James [37 – 39] that using an exponent of ½ as shown in Equation 3.7 is a good value to use for the steels and environment under consideration. Once we have obtained the distributions of the material constants *C* and *m*, we can assume the form and compute the parameters of the distribution of fatigue crack growth as a function of stress intensity. The effect of load ratio for the AISI 4130X material and corrosive environment created by the CNG contaminants would also be included in the distribution. The material constants will now be determined from the data used to generate the deterministic model discussed in Section 3.3.1 and the method of Maximum Likelihood Estimation (MLE).

From Equations 3.3 and 3.8 and considering the resistance of the CNG cylinder material to crack growth, we can write this resistance to cracking as the inverse of the crack growth rate. The resulting expression is:

$$\frac{1}{da/dN} = \frac{1}{C(K')^m} \tag{3.9}$$

If we let the effective stress intensity factor be represented by *V* and the crack resistance by *L*, then the crack resistance as a function of the stress intensity factor is given by:

$$L(V) = \frac{1}{C V^m} \tag{3.10}$$

From equation 3.10 we see that an inverse power model relationship exists between the resistance to crack growth and with the effective stress intensity factor. If we take the natural log of the crack resistance relationship we get,

$$\ln L = -\ln C - m \ln V \tag{3.11}$$

We could plot the data of crack resistance with effective stress intensity factor to estimate the parameters. One parameter would be evaluated from the slope of the line and the other from the intercept. This is not the approach that will be used however as there are obvious scatter in the effective stress intensity factor as shown by the results in the graph in Figure 3.3. Instead the parameters will be assumed to be randomly distributed and the uncertainty associated with each evaluated from the available data on Figure 3.3.

Two types of uncertainties arise. Firstly, aleatory or Class A uncertainties arising from the inherent variability of the stress intensity factor due to the interaction of the stress distribution at the crack tip, material response and the plasticity effects. Epistemic or reducible uncertainties are represented by the measured variation in crack resistance for the same effective stress intensity factor. Both types of uncertainties are reflected in the randomness of the data in Figure 3.3. Only epistemic uncertainties will be considered in this analysis as no acceptable methodology has been identified which can evaluate aleatory uncertainties.

We will use a lognormal model to represent the epistemic or reducible uncertainties in the rate of crack growth. Lognormal distribution is a good model for fatigue crack growth since the random variable cannot take negative values and the realizations can be orders of magnitude different [40]. The choice of lognormal distribution is itself an epistemic uncertainty. Weibull distribution is also a good model for characterizing the uncertainty in crack growth. Preliminary analysis using the data showed that the lognormal distribution was a better fit than the Weibull distribution.

The choice of lognormal distribution to model the uncertainties of parameter *C* has intuitive appeal. The reason is that such a distribution results in symmetric distribution of the crack growth rate, da/dN for a given K' when plotted with log scales. Such an assumption appears justified for the stable crack growth region of the fatigue phenomenon, denoted as Region II in Chapter 2, Figure 2.3

Recall Equations 3.3, 3.8 and 3.9. Let random variable representing crack resistance be represented by *T*.

$$f(T) = \frac{1}{T\,\sigma_{T'}\sqrt{2\pi}} \exp\left[-\frac{1}{2}\left(\frac{T' - \overline{T'}}{\sigma_{T'}}\right)^2\right] \tag{3.12}$$

where

T' = the natural log of random variable representing crack resistance, *T*.

$\overline{T'}$ = the mean of the natural logarithms of the crack resistance

$\sigma_{T'}$ = the standard deviation of the natural logarithms of the crack growth resistance.

The median of crack resistance based on the lognormal distribution of the crack resistance can be set to be equal to the effective stress intensity factor function. From Equation 3.11 we get:

$$\overline{T'} = -\ln C - m \ln V \tag{3.13}$$

The function for crack resistance, taking into account the dependence on the effective stress intensity factor can be written as:

$$f(T, V) = \frac{1}{T \sigma_{T'} \sqrt{2\pi}} \exp\left[-\frac{1}{2} \left(\frac{T' + \ln C + m \ln V}{\sigma_{T'}} \right)^2 \right] \tag{3.14}$$

The parameters of the inverse power model can be evaluated using the method of maximum likelihood estimation. The likelihood of each data point on the graph in Figure 3.3 can be determined by inputting the values of the crack resistance and the effective stress intensity factor. From the individual likelihood functions the total log likelihood function, Λ, can be shown to be equal to

$$\Lambda = \sum_{i=1}^{F} \ln\left(\frac{1}{T_i \sigma_{T'}} \right) \phi\left(\frac{\ln T_i + \ln C + m \ln V_i}{\sigma_{T'}} \right) \tag{3.15}$$

where

$\phi(x)$ = Standard normal distribution function,

$$\phi(x) = \frac{1}{\sqrt{2\pi}} \exp\left[-\frac{1}{2}(x)^2 \right], \tag{3.16}$$

F is the number of data points on the effective stress intensity factor vs. crack resistance curve,

$\sigma_{T'}$ is the standard deviation of the natural logarithm of the crack resistance and one of the three parameters that have to be estimated,

C is the material constant and is the second parameter to be estimated,

m is the exponent in the inverse power model. This is the third parameter to be estimated,

V_i is the effective stress intensity factor at the i^{th} data point, and

T_i is the exact crack resistance value at the i^{th} data point.

The parameters can be estimated by solving for the maximum likelihood estimators (MLE). The MLE's, $\hat{\sigma}_{T'}, \hat{C}, \hat{m}$ are the values of the parameters such that the partial differential of the log-likelihood function with respect to each parameter would be equal to zero. That is

$$\frac{\partial \Lambda}{\partial \sigma_{T'}} = 0, \quad \frac{\partial \Lambda}{\partial C} = 0, \text{ and } \quad \frac{\partial \Lambda}{\partial m} = 0 \tag{3.17}$$

The partial differential for each parameter is evaluated to be

$$\frac{\partial \Lambda}{\partial \sigma_{T'}} = \sum_{i=1}^{F} \left[\frac{\left(\ln T_i + \ln C + m \ln V_i\right)^2}{\sigma_{T'}^3} - \frac{1}{\sigma_{T'}} \right] \tag{3.18}$$

$$\frac{\partial \Lambda}{\partial C} = -\frac{1}{C \sigma_{T'}^2} \sum_{i=1}^{F} \left(\ln T_i + \ln C + m \ln V_i\right) \tag{3.19}$$

$$\frac{\partial \Lambda}{\partial M} = -\frac{1}{\sigma_{T'}^2} \sum_{i=1}^{F} \ln V_i \left(\ln T_i + \ln C + m \ln V_i\right) \tag{3.20}$$

The standard deviation estimator, $\hat{\sigma}_{T'}$, and the material constant estimator, $\hat{C}$ are positive parameters. We will assume that the natural logs of these estimators are normally distributed in order to estimate the bounds. This assumption fits with the inverse power law model and that the resistance to crack growth being lognormally distributed. Let the number of standard deviations from the mean corresponding to 1-α confidence level be equal to Z_α. The respective upper and lower bounds of the parameters can be estimated from:

$$\sigma_U = \hat{\sigma}_{T'} \exp\left[\frac{Z_\alpha \sqrt{\mathrm{Var}\left(\hat{\sigma}_{T'}\right)}}{\hat{\sigma}_{T'}} \right] \tag{3.21}$$

$$\sigma_L = \frac{\hat{\sigma}_{T'}}{\exp\left[\frac{Z_\alpha \sqrt{\mathrm{Var}\left(\hat{\sigma}_{T'}\right)}}{\hat{\sigma}_{T'}} \right]} \tag{3.22}$$

$$C_U = \hat{C} \exp\left[\frac{Z_\alpha \sqrt{Var\left(\hat{C}\right)}}{\hat{C}}\right] \tag{3.23}$$

$$C_L = \frac{\hat{C}}{\exp\left[\frac{Z_\alpha \sqrt{Var\left(\hat{C}\right)}}{\hat{C}}\right]} \tag{3.24}$$

By similar reasoning and assuming a normal distribution for the exponent of the inverse power law model, the respective upper and lower bound can be shown to be equal to

$$m_U = \hat{m} + Z_\alpha \sqrt{Var\left(\hat{m}\right)} \tag{3.25}$$

$$m_L = \hat{m} - Z_\alpha \sqrt{Var\left(\hat{m}\right)} \tag{3.26}$$

The variance and co-variance of the parameters are estimated from the local Fisher Matrix, F, evaluated at the MLE estimators as shown in Equation 3.27. The local Fisher Matrix is evaluated from the partial differential of the total log likelihood function as shown in Equation 3.28.

$$F^{-1} = \begin{bmatrix} Var\left(\hat{\sigma}_{T'}\right) & Cov\left(\hat{C}, \hat{\sigma}_{T'}\right) & Cov\left(\hat{m}, \hat{\sigma}_{T'}\right) \\ Cov\left(\hat{\sigma}_{T'}, \hat{C}\right) & Var\left(\hat{C}\right) & Cov\left(\hat{m}, \hat{C}\right) \\ Cov\left(\hat{\sigma}_{T'}, \hat{m}\right) & Cov\left(\hat{C}, \hat{m}\right) & Var\left(\hat{m}\right) \end{bmatrix} \tag{3.27}$$

$$F = \begin{bmatrix} -\frac{\partial^2 \Lambda}{\partial \sigma_{T'}^2} & -\frac{\partial^2 \Lambda}{\partial C \, \partial \sigma_{T'}} & -\frac{\partial^2 \Lambda}{\partial m \, \partial \sigma_{T'}} \\ -\frac{\partial^2 \Lambda}{\partial \sigma_{T'} \, \partial C} & -\frac{\partial^2 \Lambda}{\partial C^2} & -\frac{\partial^2 \Lambda}{\partial m \, \partial C} \\ -\frac{\partial^2 \Lambda}{\partial \sigma_{T'} \, \partial m} & -\frac{\partial^2 \Lambda}{\partial C \, \partial m} & -\frac{\partial^2 \Lambda}{\partial m^2} \end{bmatrix} \tag{3.28}$$

The data used in the development of the deterministic model for wet gas, dry gas and aqueous conditions was extracted from Figure 3.3 and used to calculate the MLE estimators of the parameters as well as the confidence bounds. Plot of the inverse power model of the data as well as the lognormal distribution of the crack resistance is shown in Figure 3.4 to Figure 3.10.

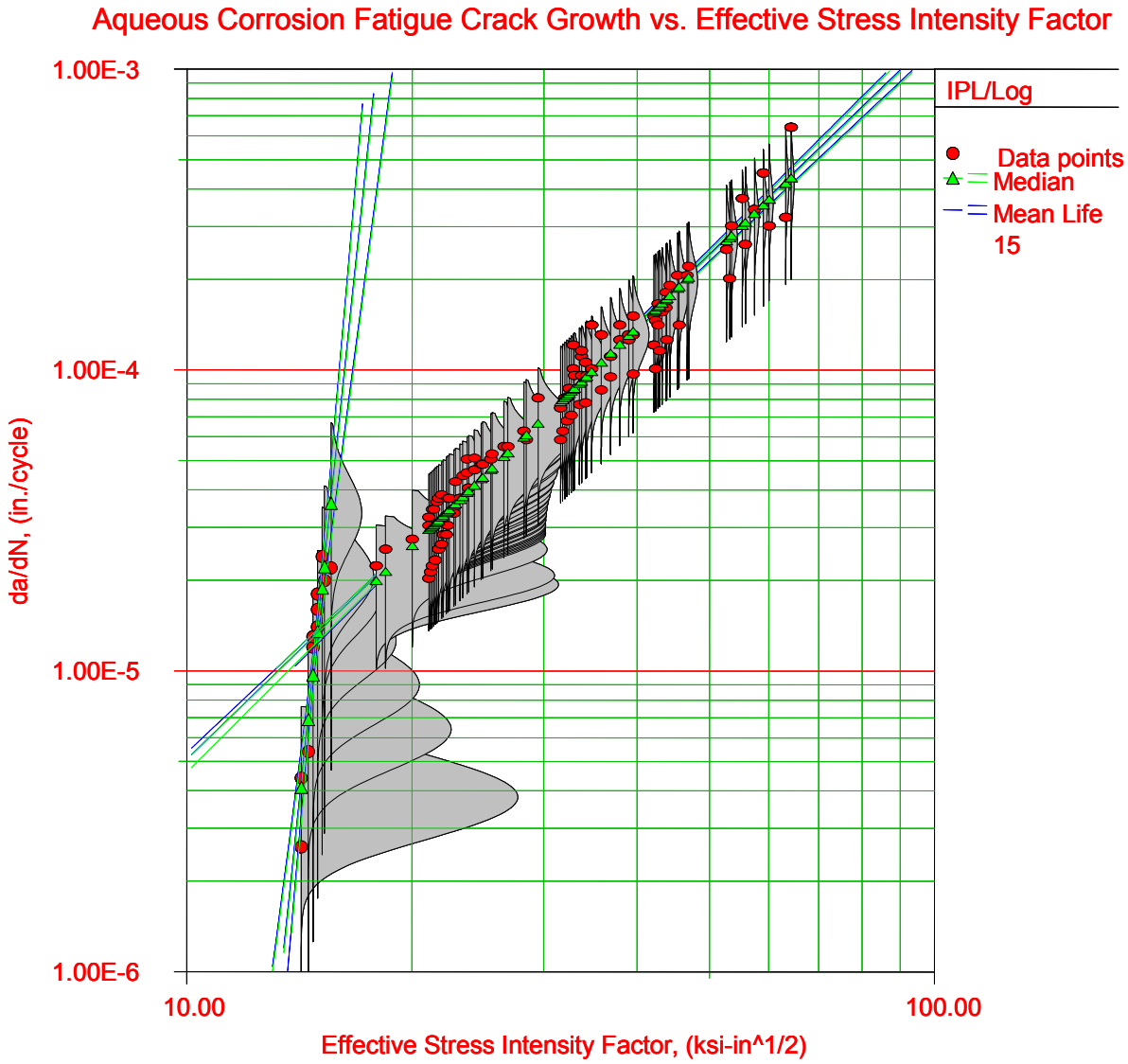

Figure 3.4 Fatigue Crack Growth Curve in Aqueous Environment vs. K'

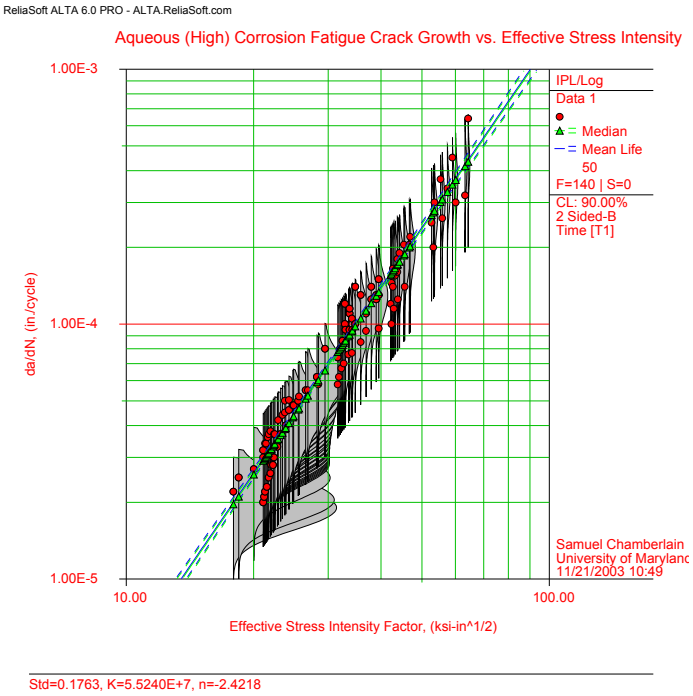

Figure 3.5 Fatigue Crack Growth Curve in Aqueous Environment At High *K'*

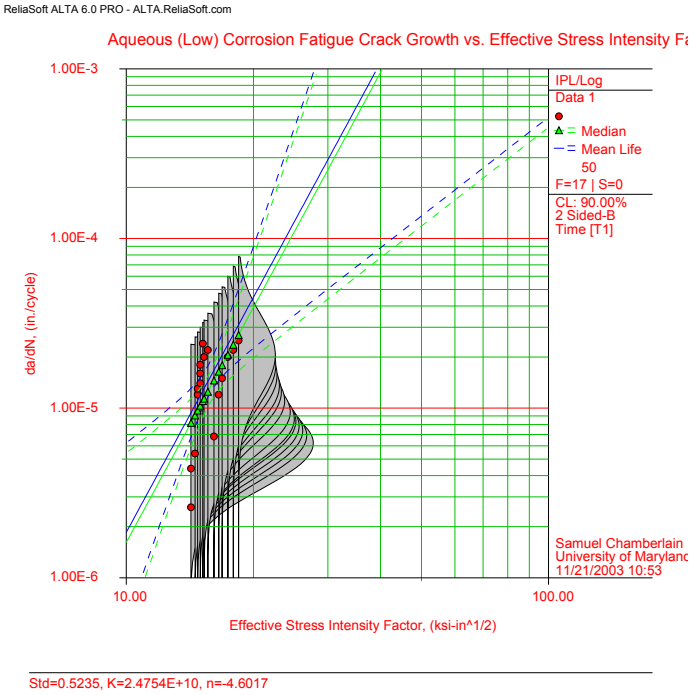

Figure 3.6 Fatigue Crack Growth Curve in Aqueous Environment at Low *K'*

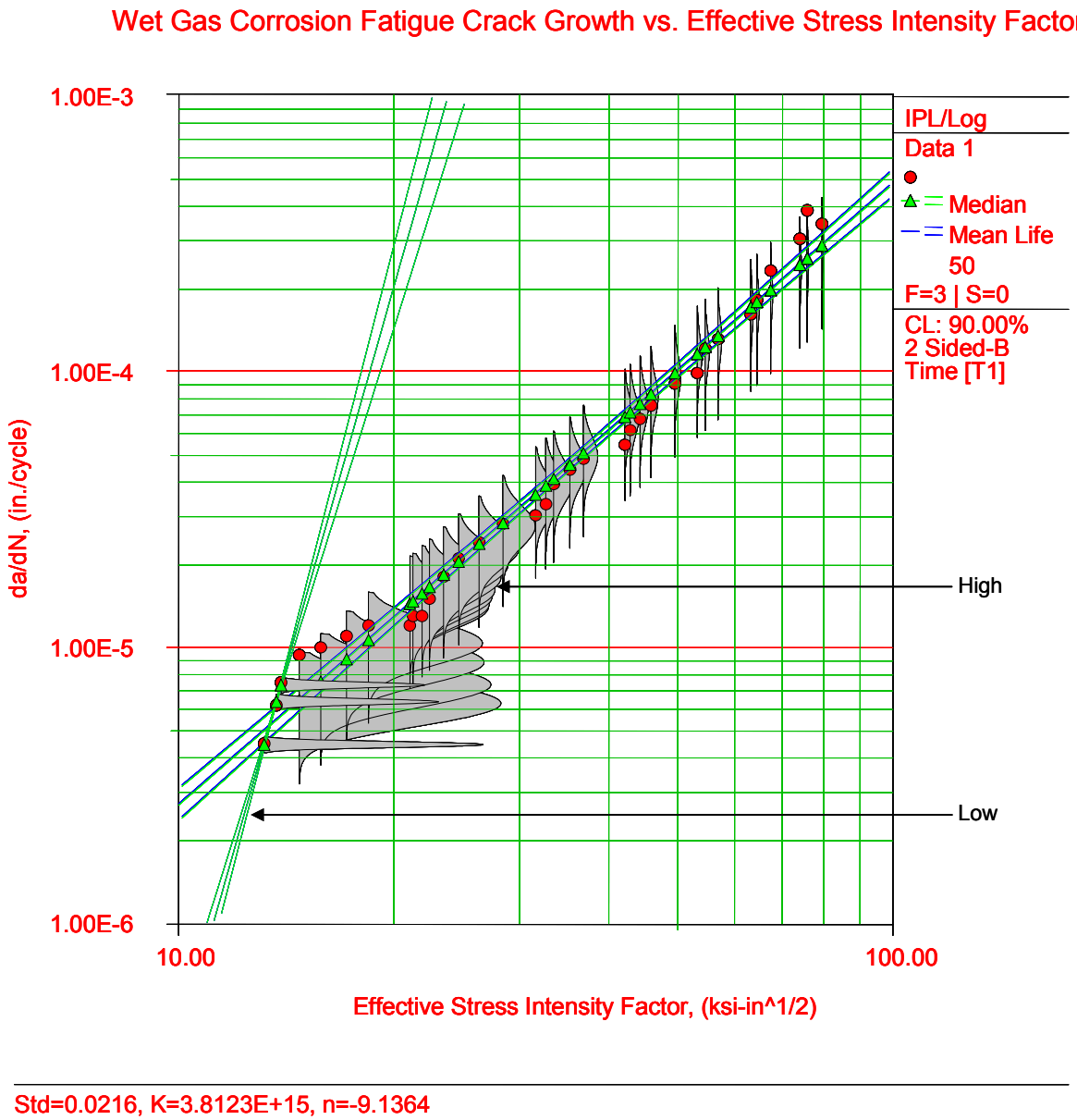

Figure 3.7 Fatigue Crack Growth Curve in Wet Gas Environment vs. *K'*

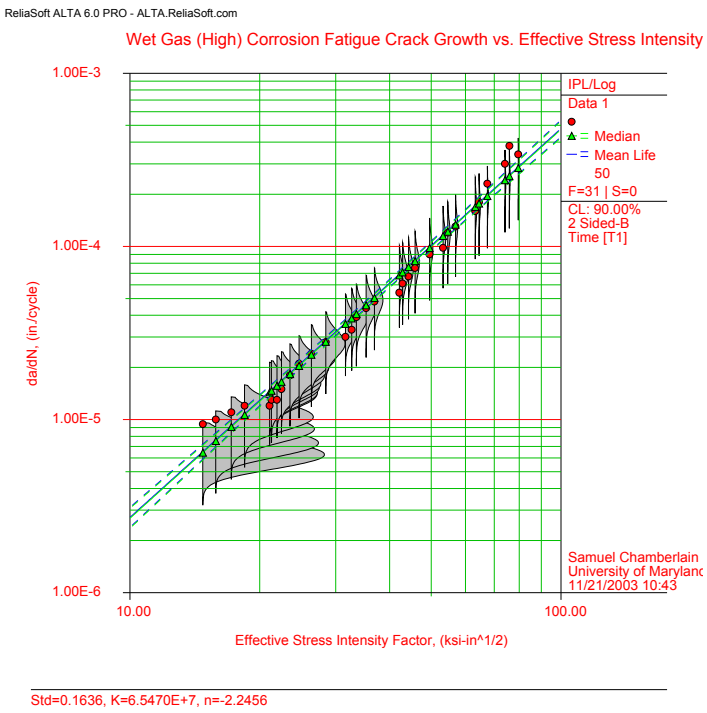

Figure 3.8 Fatigue Crack Growth Curve in Wet Gas Environment vs. High K'

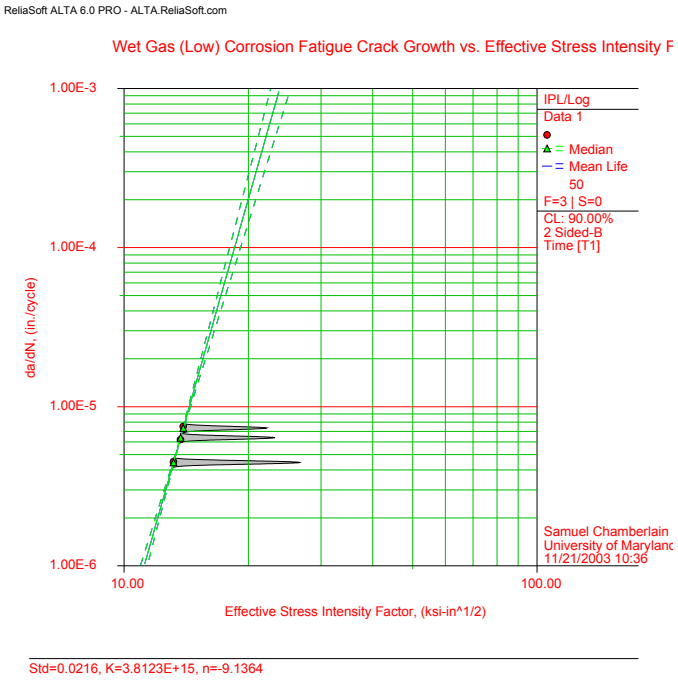

Figure 3.9 Fatigue Crack Growth Curve in Wet Gas Environment vs. Low *K'*

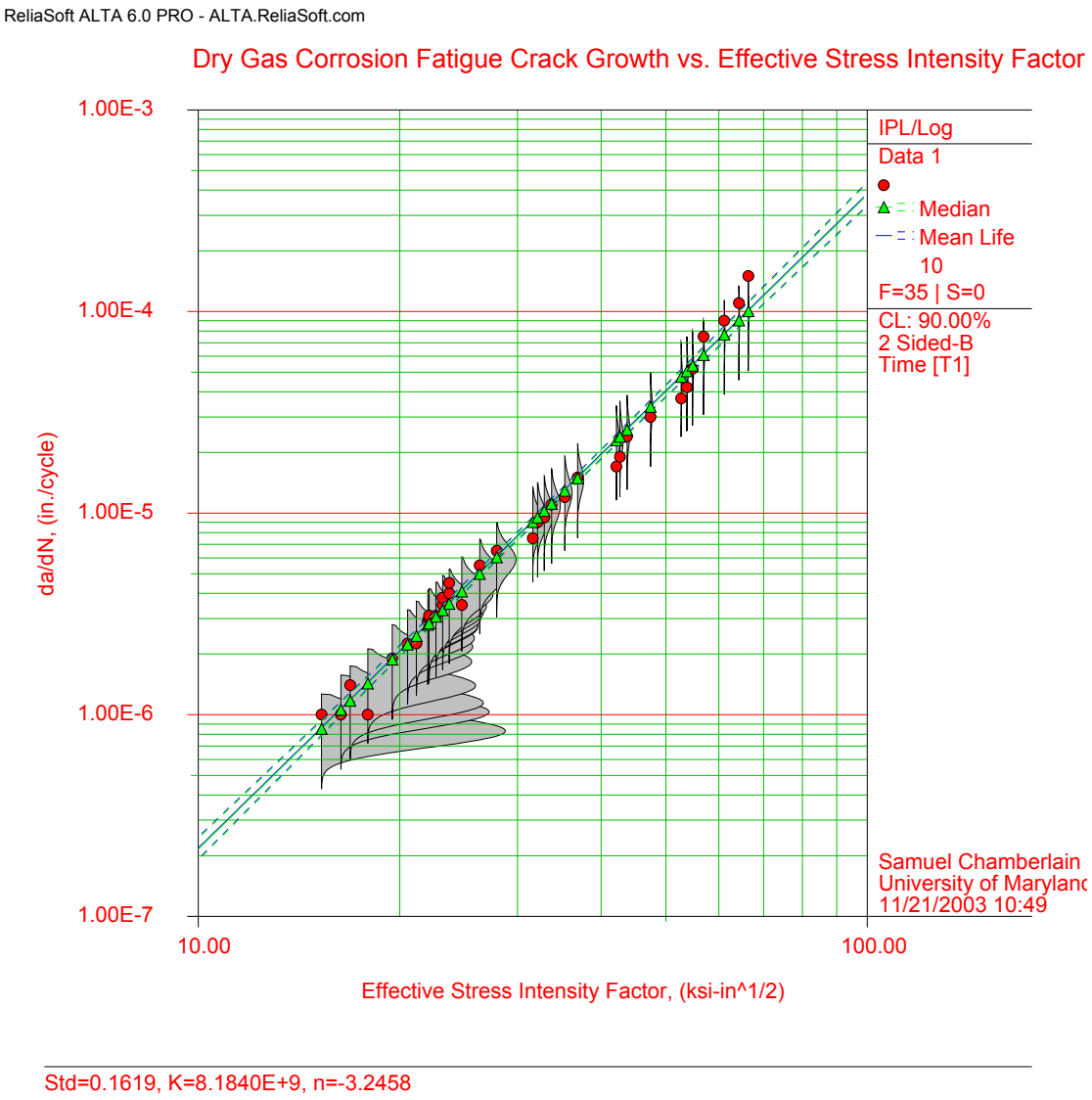

Figure 3.10 Fatigue Crack Growth Curve in Dry Gas Environment vs. *K'*

The MLE estimators of the parameters *C* and *m* are summarized below in Table 3.2 and Table 3.3. Table 3.4 summarizes the results for the standard deviation, for dry gas, wet gas and aqueous conditions.

Table 3.2 Results of Corrosion Fatigue Crack Growth Material Parameter

Environment	Model Parameters					
	Low Stress Intensity Factor			High Stress Intensity Factor		
	$\hat{C}_{1_{Upper}}$	$\hat{C}_1$	$\hat{C}_{1_{Low}}$	$\hat{C}_{2_{Upper}}$	$\hat{C}_2$	$\hat{C}_{2_{Low}}$
Aqueous	3.4721×10^{38}	4.5211×10^{32}	5.8870×10^{38}	7.2675×10^{7}	5.5240×10^{7}	4.1988×10^{7}
Wet Gas	3.9203×10^{16}	3.8123×10^{15}	3.7072×10^{14}	9.3175×10^{7}	6.5470×10^{7}	4.6003×10^{7}
Dry Gas				1.1784×10^{10}	8.1840×10^{9}	5.6836×10^{9}

Table 3.3 Results of Corrosion Fatigue Crack Growth Exponent

Environment	Model Parameters					
	Low Stress Intensity Factor			High Stress Intensity Factor		
	$\hat{m}_{1_{Upper}}$	$\hat{m}_1$	$\hat{m}_{1_{Low}}$	$\hat{m}_{2_{Upper}}$	$\hat{m}_2$	$\hat{m}_{2_{Low}}$
Aqueous	-18.6238	-23.6454	-28.6671	-2.3421	-2.4218	-2.2501
Wet Gas	-8.2434	-9.1364	-10.0294	-2.1477	-2.2456	-2.3435
Dry Gas				-3.1401	-3.2458	-3.3514

Table 3.4 Results of Corrosion Fatigue Crack Growth Standard Deviation

Environment	Model Parameters					
	Low Stress Intensity Factor			High Stress Intensity Factor		
	$\hat{\sigma}_{1_{Upper}}$	$\hat{\sigma}_1$	$\hat{\sigma}_{1_{Low}}$	$\hat{\sigma}_{2_{Upper}}$	$\hat{\sigma}_2$	$\hat{\sigma}_{2_{Low}}$
Aqueous	0.3893	0.2742	0.1930	0.1945	0.1763	0.1598
Wet Gas	0.0110	0.0216	0.0422	0.1327	0.1636	0.2016
Dry Gas				0.1330	0.1619	0.1971

The local Fisher Matrix evaluated at the MLE estimators of the parameters was used to calculate the variances and co-variances of the distributions. The variances along with the estimators in Table 3.2 to Table 3.4 define the distribution of the material parameter and the crack growth exponent. The co-variances are used in the data analysis section of Chapter 7, where the quality of the data is assessed. The local Fisher Matrices are summarized in Equations 3.29 to 3.33.

$$\left[F_{\text{Dry Gas}}\right]^{-1} = \begin{bmatrix} 3.75\times10^{-4} & -8.14\times10^{-6} & 2.90\times10^{-16} \\ -8.14\times10^{-6} & 3.28\times10^{-18} & -1.16\times10^{8} \\ 2.94\times10^{-16} & -1.16\times10^{8} & 4.13\times10^{-3} \end{bmatrix} \tag{3.29}$$

$$\left[F_{2_{\text{Wet Gas (low)}}}\right]^{-1} = \begin{bmatrix} 4.31\times10^{-4} & 1.13\times10^{-7} & -4.74\times10^{-16} \\ -1.13\times10^{-7} & 1.97\times10^{18} & -8.28\times10^{5} \\ -4.74\times10^{-16} & -8.28\times10^{5} & 3.54\times10^{-3} \end{bmatrix} \tag{3.30}$$

$$\left[F_{1_{\text{Wet Gas (high)}}}\right]^{-1} = \begin{bmatrix} 7.76\times10^{-5} & 9.31\times10^{2} & -9.36\times10^{-14} \\ 9.31\times10^{2} & 2.92\times10^{31} & -2.93\times10^{15} \\ -9.36\times10^{-14} & -9.36\times10^{15} & 2.93\times10^{-1} \end{bmatrix} \tag{3.31}$$

$$\left[F_{2_{\text{Aqueou (low)s}}}\right]^{-1} = \begin{bmatrix} 1.11\times10^{-4} & 6.40\times10^{-8} & -3.35\times10^{-16} \\ 6.40\times10^{-8} & 8.48\times10^{13} & -4.44\times10^{5} \\ -3.35\times10^{-16} & -4.44\times10^{5} & 2.36\times10^{-3} \end{bmatrix} \tag{3.32}$$

$$\left[F_{1_{Aqueou(high)}}\right]^{-1} = \begin{bmatrix} 3.42\times10^{-3} & -9.64\times10^{20} & 7.90\times10^{-13} \\ -9.64\times10^{20} & 1.39\times10^{67} & -1.14\times10^{34} \\ 7.90\times10^{-13} & -1.14\times10^{34} & 9.32 \end{bmatrix} \tag{3.33}$$

From Figure 3.4 and 3.9 the rate of crack growth for aqueous and wet gas increases rapidly from a minimum value and then reduces after a fairly well defined stress intensity factor is reached. This precipitous drop in the crack growth rates at the higher effective stress intensity factor can be explained by crack tip blunting and interaction with the asperities formed on the crack surface. The crack growth phenomenon is different at low and at high effective stress intensity factors and therefore will be modeled separately for each region. The parameter for crack growth in each region is denoted with a 1 and 2, respectively.

In addition to the transition stress intensity factor at which the growth phenomenon changes its mode of propagation, the presence of a minimum value for crack growth rate suggests that there is a threshold below which crack growth will not occur. This phenomenon is investigated in Section 3.4.2.3.

From the results in Tables 3.2 to 3.4 we can see that the AISI 4130X material is more susceptible to corrosion fatigue in an aqueous environment. This is with the same rise time for the loading and effective stress intensity factor. This is not totally unexpected because corrosion fatigue proceeds as shown in Chapter 2 by hydrogen embrittlement. The presence of oxygen in water causes oxidation of the recently cracked

surfaces. This process increases the partial pressure of hydrogen which acts as a catalyst for further hydrogen embrittlement and crack growth.

Even when the partial pressure of water vapor was controlled in the fatigue experiments conducted on the AISI 4130X material, condensed vapor was found on cracked surfaces. The presence of condensed vapor is sufficient to cause aqueous conditions to exist. Since it represents the worst case scenario, this is the condition that will be used for modeling the fatigue crack growth in the representative CNG cylinder.

3.4.2.2 Distribution of Parameters

The development of the distribution of *C* and *m* has been discussed in the previous section. As was stated earlier it will be assumed that *C* is lognormally distributed with upper and lower values as shown in Table 3.2. Since *C* is lognormally distributed it will have the following probability density function and complimentary cumulative distributions, [40] shown in Equations 3.34 and Equation 3.35. The median of this distribution is C_{50} and the standard deviation of the natural log of C is η.

$$f(C) = \frac{1}{\eta C\sqrt{2\pi}} \exp\left\{-\frac{1}{2}\left[\frac{\ln(C/C_{50})}{\eta}\right]^2\right\} \tag{3.34}$$

$$F(<C) = \frac{1}{2}\left\{1 + \text{erf}\left[\frac{1}{\eta\sqrt{2\pi}} \ln\left(\frac{C}{C_{50}}\right)\right]\right\} \tag{3.35}$$

$$\hat{C} = C_{50} \exp\left(\frac{\eta^2}{2}\right) \tag{3.36}$$

The median value of C, C_{50} is easily calculated from the results in Table 3.5 and Equation 3.36

Table 3.5 Results of Corrosion Fatigue Crack Growth Material Parameter Distribution

Environment	Model Parameters			
	Low Stress Intensity Factor		High Stress Intensity Factor	
	$\hat{C}_1$	η_1^2	$\hat{C}_2$	η_2^2
Aqueous	4.5211×10^{32}	1.3868×10^{67}	5.5240×10^{7}	8.4823×10^{13}
Wet Gas	3.8123×10^{15}	2.9163×10^{31}	6.5470×10^{7}	1.9720×10^{14}
Dry Gas			8.1840×10^{9}	3.2894×10^{18}

The crack growth exponent, m, was noted previously to be normally distributed. The corresponding normal density function and complimentary distribution functions are given by Equation 3.37, with σ being the standard deviation of m.

Table 3.6 Results of Corrosion Fatigue Crack Growth Exponent

Environment	Model Parameters			
	Low Stress Intensity Factor		High Stress Intensity Factor	
	$\hat{m}_1$	$\sigma_{1_m^2}$	$\hat{m}_2$	$\sigma_{2_m^2}$
Aqueous	-23.6454	9.3164	-2.4218	2.3464
Wet Gas	-9.1364	0.2946	-2.2456	3.5404
Dry Gas			-3.2458	4.1261

$$f(m) = \frac{1}{\sigma_m \sqrt{2\pi}} \exp\left[-\frac{1}{2}\left(\frac{m - \hat{m}}{\sigma_m} \right) \right]^2 \tag{3.37}$$

and

$$F(m) = \frac{1}{2}\left\{1 + \text{erf}\left[\frac{1}{\sigma_m\sqrt{2\pi}}\left(\frac{m - \hat{m}}{\sigma_m}\right)\right]\right\} \tag{3.38}$$

The distribution of the crack resistance property of the material is reflected in the scatter of the data shown in Figures 3.4 to 3.9. This is typical for fatigue crack resistance data. The scatter in the data will be assumed to be because aleatory or epistemic uncertainty in the resistance to crack growth and not the variability in how the experiments were carried out.

The standard deviation of the material resistance and therefore the crack growth rate averaged over all the different effective stress intensity factors is also shown in Table 3.4. This is an important parameter which is useful in fully characterizing the random nature of the crack growth rate. The level of complexity that this presents is unnecessary as the distribution of the material constant *C* and the exponent *m* is sufficient to describe the randomness in the crack growth rate. The standard deviation will therefore not be used in the ensuing analysis.

3.4.2.3 Crack Growth Transition and Threshold

The transition stress intensity factor under aqueous conditions, K'_T , was defined previously as the point when the crack growth rate is impacted significantly by corrosion products on the crack surface and the interaction of crack asperities. From Figure 3.8, this transition point is conservatively estimated to be approximately 15 ksi-in$^{1/2}$. This transition point is a source of uncertainty.

Another important aspect of the corrosion fatigue crack growth modeling is the threshold conditions below which crack growth will not occur. This threshold has been found to be independent of the environment but dependent on the R, the ratio of the minimum to the maximum loading. It has been shown to be also dependent on the tensile properties and microstructure of the material [41].

The effective stress intensity factor, defined in Equation 3.8b, is a reasonable parameter to account for the influence of R as environmental conditions do not seem to have much effect on the threshold conditions for crack growth. The work of Paris [42] and Ritchie [43] show that a threshold effective stress intensity factor for a given material, heat treatment and temperature is not as dependent on R, as the threshold cyclic stress intensity factor. This makes it a better measure of the threshold crack growth condition.

Research by Coke [44] found that a parameter resembling the effective stress intensity factor was independent of R. This suggests that this modified stress intensity factor could be used to characterize the threshold conditions, is applicable over all stress ratios and would be more representative of a true material constant. The expression of this threshold relationship is

$$K'_0 = \frac{\Delta K_0}{\sqrt{1-R}} \tag{3.39}$$

The threshold value of the effective stress intensity factor, in equation 3.39, is estimated from the data taken from Figure 3.3. A conservative value from the results in Figure 3.4 is 12 ksi-in$^{1/2}$.

Both the transition and threshold stress intensity factors are treated as constants in this analysis. More data would be required to fully evaluate the uncertainties and the sensitivity of the results. No consideration is taken of any underlying distribution that would be a better model of these quantities for the remainder of this analysis.

A model to adequately estimate corrosion fatigue crack growth has been developed. This model is superior to the deterministic model developed by SWRI and detailed before, since it characterizes the major epistemic uncertainties associated with corrosion fatigue crack growth. These uncertainties arise because of unknowns in the material response to stress field in the plastic zone surrounding the crack tip as well as the material properties itself. The model also takes into account transition and threshold stress intensity factors. These points on the crack growth curve identify the change in crack propagation phenomenon and the initiation of fatigue crack growth respectively.
In summary the corrosion fatigue crack growth rate will be given by the following expression:

$$\frac{1}{da/dN} = \begin{cases} \infty & K' < K'_0 \\ \dfrac{1}{C_1 K'^{m_1}} & K'_0 \geq K' \leq K'_T \\ \dfrac{1}{C_1 K'^{m_2}} & K'_T > K' \end{cases} \tag{3.40}$$

$$K'_0 = \frac{\Delta K_0}{\sqrt{1-R}} = 12$$

$$K'_T = 14$$

The parameters of the crack growth equation are distributed quantities. Parameter *C* is lognormally distributed with parameters given in Table 3.5. Parameter *m* is normally distributed with parameters given in Table 3.6. This result is assumed to be applicable to parent material, weld material and heat affected zone material for DOT 3AA specified material used to manufacture CNG cylinders. This relation will be used to model crack growth leading to failure whether by leakage or fracture. All that is required now to evaluate this expression is the stress intensity factor.

CHAPTER 4: STRESS INTENSITY FACTOR DETERMINATION

Stress intensity factors are determined within the framework of LEFM crack driving force solutions to finite element analysis of cracked surfaces. Two somewhat different approaches are required for cracks in the sidewalls of the cylinder and cracks in the transition regions and ends. Stress intensity factor solutions are obtained by relating the internal pressure, stresses, geometry, crack shape and geometry to crack driving force solutions obtained from finite element analysis. The stress intensity factor solutions are dependent on the region and the configuration of the cylinder being considered.

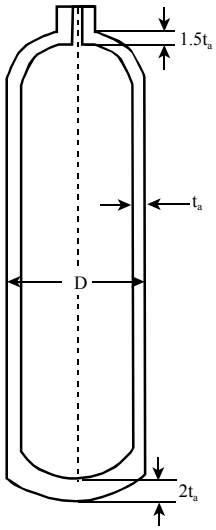

Figure 4.1 Cross-Section of Typical Hemispherical CNG Cylinder Design

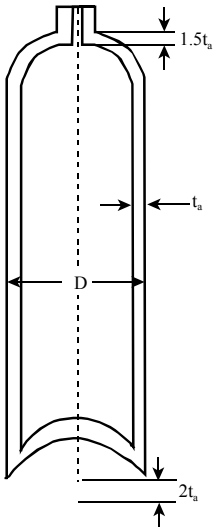

Figure 4.2 Cross-Section Typical Flat-bottom CNG Cylinder Design

Two configurations of cylinders are considered for this analysis. The first design in Figure 4.1 has a hemispherical dome at the bottom and is termed hemispherical cylinders. The second design shown in Figure 4.2 has an inverted hemi-spherical end which gives it a flat surface and is typically called a flat-bottom design. Laboratory and analytical research sponsored by Gas Research Institute (GRI) [4] has shown that both designs have different operating lives. Flat-bottom designs have been found to fail more by catastrophic rupture, by a crack growing until it becomes unstable rather than a crack growing through the sidewall causing leakage, as is typically found for the hemi-spherical design.

Stress analysis conducted on the two designs showed that the stress distribution and by extension the crack driving force for the hemi-spherical end cylinder is greatest in

the sidewalls. A crack is therefore most likely to originate in this area and under the influence of the crack driving force grow to failure. The nature of the failure, whether rupture or leaking is to be determined by the material properties, the initial crack size and the crack growth rate. Experiments have been done which shows resistance of CNG cylinder materials to rapid corrosion fatigue crack growth. Leakage is expected to occurring before rupture, for the hemispherical end design [3].

Flat-bottom cylinders have developed circumferential cracks in the transition region under fatigue testing. Small initial defect in the transition region tend to grow rapidly and usually results in rupture of the cylinders [4]. The sidewall region of the flat-bottom design showed similar fatigue performance as the hemi-spherical bottom design.

Determination of the stress intensity factor, in the transition region, and in the sidewalls of both designs is necessary in order to complete the probabilistic physical model of corrosion fatigue crack. The stress intensity factor will also help us determine whether the cylinder will fail by leakage as a crack grows through the sidewall and remains stable throughout the life of a cylinder or for unstable crack growth to occur resulting in rupture.

The stress intensity factor for the sidewall is the same for both configuration shown in Figure 4.1 and Figure 4.2. The stress profile in the transition region of the hemispherical and the flat bottom designs are quite different and as such the approach to

modeling is also quite different. In the case of cylinders with hemispherical ends it can be seen that hoop stress is the predominant in the transition region as is the case with the sidewall. The high residual bending stress arising from the spinning operation during manufacturing when combined with the hoop stress creates a complex stress distribution. The resultant stress is greater than the hoop stress and will cause a small initial defect to grow more rapidly resulting in a shorter fatigue life. The approach to determining the stress intensity factors is now detailed.

4.1 Sidewalls of Cylinder

For the cylindrical portion or sidewalls of the cylinder the stress intensity solution equations are based on fits to extensive three-dimensional finite element stress analyses of pressurized cylinders containing internal semi-elliptical surface cracks having a wide range of crack sizes and shapes by Newman and Raju [45]. Stress intensity factor solutions were obtained by solving the complimentary problem of applied stresses on the crack surface.

CNG cylinders are considered to be thin-walled pressure vessels. It is therefore assumed that the wall is thin enough such that the radial stress component in the wall is negligibly small compared to the tangential or hoop stress which is uniform across the thickness. Cracks in the sidewall of the cylindrical portion as shown in Figure 4.3, are therefore driven by stresses which are uniform through the thickness except at the crack surface. The assumption of the cylinder being thin-walled presents a significant

simplification as the longitudinal and the hoop stresses can be easily determined from closed form solutions. The tangential and longitudinal stresses are given by Equations 4.1 and 4.2

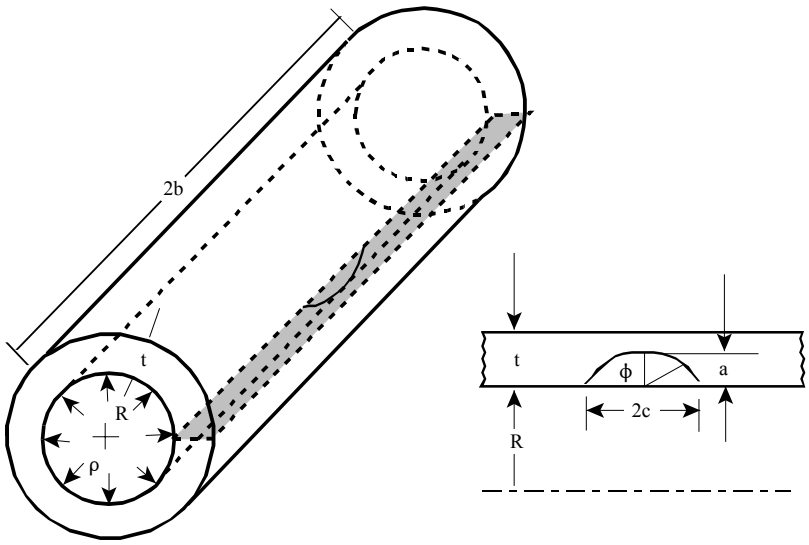

Figure 4.3 Typical Surface Crack in Cylinder Sidewall

$$\sigma_t = \frac{\rho D}{2t} \tag{4.1}$$

$$\sigma_l = \frac{\rho D}{4t} \tag{4.2}$$

Comparing the two equations it may be noted that the tangential or hoop stress, σ_t is twice the longitudinal stress σ_l. Because a biaxial state of stress exists we should consider both in the stress distribution. These stresses are also valid only for the sidewall

at a sufficient distance away from the transition region or the dome heads. For simplicity we will consider only the effect of the hoop stress on the crack surface and the crack driving force is assumed to apply to all of the sidewall.

The cylinder length, *2b*, has negligible effect on the stress intensity for the typical CNG cylinder being considered. This is determined to be so from the relationship [45]

$$\frac{b}{c} \geq 10 \tag{4.3}$$

The results for a typical cylinder are assumed to be applicable to all DOT-3AA cylinder sizes. The remainder of this analysis will be conducted with the dimensions for a typical cylinder used to represent performance of all cylinder sizes.

Stress intensity factor solution for a pressurized cylinder was obtained by Newman and Raju [45] by superposition of four stress distributions on a three dimensional finite element model of a cracked surface. The stress distributions applied to the cracked surface were constant, linear, quadratic and cubic. The in-plane symmetric stresses in the three dimensional finite element model in Figure 4.4, as a result of the four applied stress distribution to the crack surfaces, is shown in Figure 4.5. The stress distribution is given by

$$\sigma_j = \left(\frac{z}{a}\right)^j \tag{4.4}$$

for *j* from 0 to 3 identifying each stress distribution separately. *z* is measured from the crack mouth towards the crack front as shown in Figure 4.5 and *a* is the crack depth measured from the inside or outside surface of the cylinder.

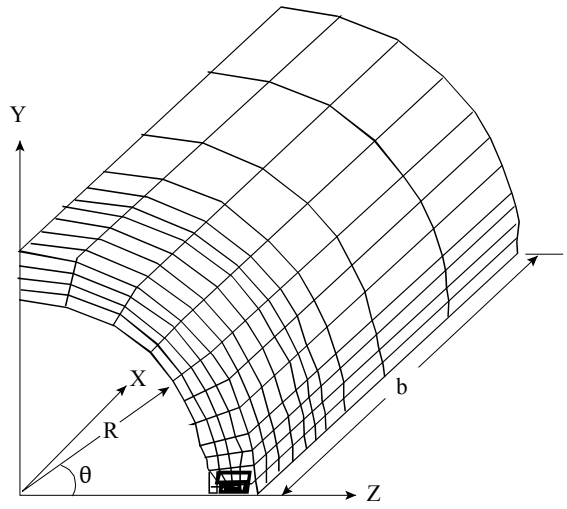

Figure 4.4a Three Dimensional Finite Element Model of Semi-Elliptical Surface Crack [45]

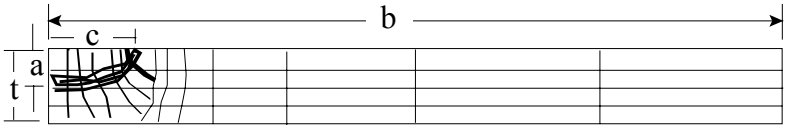

Figure 4.4b Element Pattern of Finite Element Model of Semi-Elliptical Surface Crack [45]

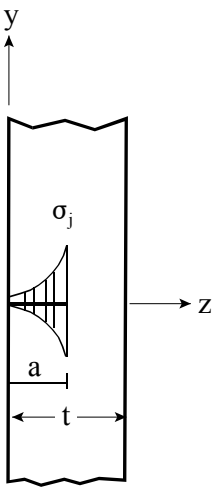

Figure 4.5 Distribution of Loading on Crack Surface [45]

Mode 1 stress-intensity factor, K_I, at any point along the crack surface can be written with respect to the crack parameters as [45]:

$$K_I = \sqrt{\pi \frac{a}{Q}}\, G_j\left(\frac{a}{c}, \frac{a}{t}, \frac{R}{t}, \phi\right) \tag{4.5}$$

where,

G_j = boundary correction factor corresponding to the jth stress distribution

Q = shape factor for an elliptical crack

a = crack depth

c = crack half angle

t = thickness of cylinder material

R = ratio of maximum to minimum stress

ϕ = angle around crack front measured from surface

For the four stress distributions $j = 0$ to 3. The shape factor for an elliptical crack, Q, is given by the square of the complete elliptical integral of the second kind and is approximated by Equation 4.6 [46].

$$Q = 1 + 1.464\left(\frac{a}{c}\right)^{1.65} \tag{4.6}$$

Superposition of the results for the different stress distributions and the general expression given in Equation 4.5 gives the stress-intensity factors solutions for two symmetrical surface cracks in an internally pressurized CNG cylinder. Incorporating the dimensions of the cylinder and the internal pressure for convenience the stress-intensity factor can be written as [45].

$$K_I = \frac{\rho R}{t}\sqrt{\pi\frac{a}{Q}}\ F\left(\frac{a}{c}, \frac{a}{t}, \frac{R}{t}, \phi\right) \tag{4.7}$$

where, $\rho R/t$ is the hoop stress and is equivalent to the average stress for the four loading conditions assumed in the finite element model. F is a function that accounts for boundary correction for a surface crack on the inside and outside of the cylindrical sidewall for an internally pressurized cylinder. F depends on the geometric parameters: *a/c, a/t, R/t* and ϕ which are defined in Figure 4.3.

The function *F* was determined from the first four terms of the power series expansion of Lame's stress intensity factor solutions [47] for the hoop stress in an internally pressurized cylinder, plus the internal pressure applied to the crack surface. An expression for *F*, obtained in terms of the boundary correction factor G_j, for the *jth* stress distribution is as follows:

$$F = \frac{t}{R}\left(\frac{R_0^2}{R_0^2 - R^2}\right)\left[2G_0 - 2\left(\frac{a}{R}\right)G_1 + 3\left(\frac{a}{R}\right)^2 G_2 - 4\left(\frac{a}{R}\right)^3 G_3\right] \tag{4.8}$$

where, G_j is obtained from the finite element solution for the stress distribution in each of the planes under consideration. The correction factor *F,* includes the influence of the internal pressure, ρ, acting on the crack surfaces. The finite element solutions for G_j under each loading conditions is shown in Table 4.1 to 4.4 for the particular values of *a/c, a/t, R/t* andϕ. These boundary correction factors will be used with the pressure fluctuation in the cylinder and the crack size distribution to determine the stress intensity factor distribution for the sidewalls of the cylinder. The stress intensity factor distributions will be used in the analysis of flat-bottom as well as hemi-spherical bottom cylinders.

Table 4.1 Influence Coefficients, G_j , Semi-Elliptical Crack on Inside of a Cylinder ($t / R = 0.1$) [45]

TYPE OF LOADING	a/c		0.2			0.4			1.0		
	2φ/π	a/t	0.2	0.5	0.8	0.2	0.5	0.8	0.2	0.5	0.8
UNIFORM (G_0)	0		0.607	0.791	1.179	0.777	0.936	1.219	1.140	1.219	1.348
	0.25		0.740	0.932	1.284	0.810	0.948	1.164	1.068	1.126	1.200
	0.5		0.945	1.188	1.568	0.940	1.076	1.243	1.033	1.074	1.091
	0.75		1.073	1.366	1.798	1.038	1.180	1.357	1.019	1.055	1.090
	1.0		1.115	1.427	1.872	1.072	1.217	1.393	1.015	1.050	1.090
LINEAR (G_1)	0		0.079	0.138	0.253	0.125	0.176	0.259	0.197	0.221	0.255
	0.25		0.206	0.268	0.374	0.246	0.291	0.356	0.359	0.377	0.397
	0.5		0.422	0.503	0.619	0.422	0.487	0.538	0.541	0.554	0.555
	0.75		0.603	0.705	0.859	0.608	0.657	0.727	0.669	0.683	0.703
	1.0		0.673	0.783	0.960	0.672	0.723	0.806	0.715	0.729	0.760
QUADRATIC (G_2)	0		0.023	0.052	0.104	0.043	0.069	0.106	0.074	0.085	0.099
	0.25		0.075	0.105	0.154	0.097	0.119	0.149	0.153	0.162	0.170
	0.5		0.237	0.277	0.331	0.256	0.279	0.302	0.333	0.339	0.337
	0.75		0.429	0.480	0.560	0.441	0.466	0.505	0.514	0.520	0.533
	1.0		0.514	0.571	0.671	0.523	0.549	0.601	0.588	0.596	0.618
CUBIC (G_3)	0		0.010	0.027	0.056	0.021	0.036	0.056	0.038	0.044	0.051
	0.25		0.032	0.049	0.077	0.044	0.058	0.074	0.075	0.080	0.085
	0.5		0.146	0.169	0.199	0.161	0.174	0.187	0.218	0.222	0.219
	0.75		0.332	0.363	0.412	0.346	0.360	0.385	0.417	0.420	0.429
	1.0		0.438	0.462	0.529	0.441	0.456	0.493	0.512	0.515	0.532

Table 4.2 Influence Coefficients, G_j , Semi-Elliptical Crack on Inside of a Cylinder ($t / R = 0.25$) [45]

TYPE OF LOADING	a/c		0.2			0.4			1.0		
	2φ/π	a/t	0.2	0.5	0.8	0.2	0.5	0.8	0.2	0.5	0.8
UNIFORM (G_0)	0		0.606	0.797	1.201	0.770	0.924	1.219	1.128	1.191	1.316
	0.25		0.736	0.925	1.270	0.801	0.932	1.154	1.058	1.105	1.180
	0.5		0.935	1.170	1.549	0.928	1.056	1.241	1.025	1.060	1.088
	0.75		1.057	1.343	1.838	1.024	1.157	1.385	1.013	1.045	1.099
	1.0		1.097	1.405	1.959	1.057	1.193	1.443	1.009	1.041	1.105
LINEAR (G_1)	0		0.079	0.141	0.262	0.123	0.174	0.263	0.194	0.214	0.248
	0.25		0.205	0.268	0.372	0.243	0.287	0.356	0.356	0.371	0.393
	0.5		0.419	0.498	0.615	0.438	0.481	0.540	0.538	0.550	0.556
	0.75		0.598	0.698	0.876	0.603	0.650	0.740	0.667	0.680	0.708
	1.0		0.666	0.776	0.996	0.666	0.715	0.828	0.713	0.726	0.768
QUADRATIC (G_2)	0		0.023	0.054	0.108	0.042	0.068	0.109	0.072	0.082	0.097
	0.25		0.075	0.106	0.154	0.096	0.118	0.150	0.152	0.159	0.169
	0.5		0.236	0.275	0.330	0.254	0.276	0.304	0.332	0.338	0.339
	0.75		0.426	0.477	0.571	0.439	0.462	0.513	0.512	0.519	0.537
	1.0		0.511	0.567	0.692	0.520	0.545	0.614	0.588	0.594	0.623
CUBIC (G_3)	0		0.010	0.028	0.059	0.021	0.036	0.059	0.037	0.043	0.050
	0.25		0.032	0.050	0.077	0.044	0.057	0.075	0.075	0.079	0.085
	0.5		0.145	0.168	0.199	0.160	0.173	0.188	0.217	0.221	0.220
	0.75		0.330	0.361	0.419	0.345	0.358	0.391	0.416	0.419	0.431
	1.0		0.426	0.460	0.542	0.439	0.454	0.509	0.511	0.515	0.536

Table 4.3 Influence Coefficients, G_j , Semi-Elliptical Crack on Outside of a Cylinder ($t / R = 0.1$) [Newman Raju]

TYPE OF LOADING	a/c		0.2			0.4			1.0		
	2φ/π	a/t	0.2	0.5	0.8	0.2	0.5	0.8	0.2	0.5	0.8
UNIFORM (G_0)	0		0.612	0.806	1.262	0.788	0.984	1.378	1.156	1.266	1.453
	0.25		0.750	0.968	1.432	0.823	1.002	1.325	1.082	1.165	1.278
	0.5		0.965	1.272	1.867	0.958	1.147	1.425	1.044	1.106	1.144
	0.75		1.102	1.502	2.208	1.061	1.267	1.541	1.029	1.083	1.125
	1.0		1.147	1.584	2.298	1.096	1.310	1.565	1.025	1.078	1.118
LINEAR (G_1)	0		0.080	0.142	0.277	0.128	0.192	0.309	0.202	0.236	0.286
	0.25		0.208	0.279	0.419	0.250	0.309	0.406	0.363	0.390	0.421
	0.5		0.428	0.530	0.715	0.448	0.511	0.595	0.544	0.565	0.570
	0.75		0.614	0.752	0.993	0.616	0.687	0.784	0.673	0.692	0.712
	1.0		0.685	0.839	1.099	0.680	0.755	0.858	0.718	0.738	0.765
QUADRATIC (G_2)	0		0.023	0.053	0.114	0.045	0.076	0.129	0.076	0.092	0.113
	0.25		0.076	0.110	0.175	0.099	0.128	0.173	0.155	0.168	0.181
	0.5		0.240	0.290	0.377	0.259	0.290	0.329	0.335	0.344	0.344
	0.75		0.434	0.504	0.626	0.445	0.481	0.531	0.515	0.524	0.536
	1.0		0.521	0.600	0.739	0.528	0.565	0.625	0.590	0.600	0.619
CUBIC (G_3)	0		0.010	0.028	0.062	0.022	0.040	0.070	0.039	0.048	0.059
	0.25		0.032	0.052	0.088	0.046	0.063	0.088	0.077	0.084	0.091
	0.5		0.147	0.177	0.226	0.163	0.181	0.202	0.219	0.224	0.222
	0.75		0.335	0.378	0.450	0.349	0.370	0.400	0.418	0.422	0.430
	1.0		0.432	0.480	0.568	0.444	0.466	0.505	0.513	0.518	0.533

Table 4.4 Influence Coefficients, G_j , Semi-Elliptical Crack on Outside of a Cylinder ($t / R = 0.25$) [45]

TYPE OF LOADING	a/c		0.2			0.4			1.0		
	2φ/π	a/t	0.2	0.5	0.8	0.2	0.5	0.8	0.2	0.5	0.8
UNIFORM (G_0)	0		0.612	0.786	1.160	0.793	0.994	1.400	1.163	1.286	1.498
	0.25		0.752	0.952	1.346	0.828	1.016	1.365	1.088	1.184	1.320
	0.5		0.972	1.278	1.860	0.967	1.175	1.513	1.049	1.123	1.183
	0.75		1.114	1.541	2.344	1.072	1.311	1.682	1.034	1.100	1.163
	1.0		1.162	1.640	2.510	1.109	1.360	1.727	1.030	1.094	1.156
LINEAR (G_1)	0		0.080	0.134	0.242	0.130	0.195	0.318	0.204	0.243	0.302
	0.25		0.209	0.272	0.372	0.252	0.315	0.421	0.365	0.396	0.435
	0.5		0.430	0.532	0.713	0.451	0.521	0.626	0.546	0.570	0.583
	0.75		0.618	0.767	1.044	0.620	0.702	0.833	0.674	0.698	0.724
	1.0		0.691	0.861	1.178	0.685	0.773	0.914	0.720	0.743	0.777
QUADRATIC (G_2)	0		0.023	0.049	0.097	0.045	0.078	0.134	0.077	0.096	0.122
	0.25		0.076	0.106	0.159	0.100	0.130	0.180	0.156	0.171	0.188
	0.5		0.241	0.291	0.376	0.261	0.295	0.345	0.336	0.347	0.350
	0.75		0.437	0.513	0.654	0.447	0.489	0.556	0.516	0.527	0.542
	1.0		0.524	0.613	0.782	0.530	0.575	0.653	0.591	0.603	0.625
CUBIC (G_3)	0		0.010	0.025	0.051	0.022	0.041	0.073	0.040	0.051	0.064
	0.25		0.032	0.050	0.079	0.046	0.064	0.093	0.077	0.086	0.095
	0.5		0.148	0.177	0.255	0.164	0.184	0.212	0.220	0.226	0.226
	0.75		0.337	0.383	0.468	0.350	0.375	0.416	0.418	0.424	0.433
	1.0		0.434	0.488	0.596	0.445	0.472	0.523	0.513	0.520	0.536

4.2 Transition Region and Ends of Cylinder

Cracks in the transition region and ends of the cylinder complicate the analysis of the CNG cylinder. At the transition region the stress distribution is much more complex because of the changing geometry and numerical analysis is required to obtain the stress distribution and the stress intensity factors for circumferential cracks in this section of the cylinder. Numerical analysis is required because unlike the case of the sidewalls the stress distribution in not uniform. The changing geometry of the cylinder causes the stress distribution on the crack surface to change with the cylinder profile. As a result the boundary correction factors and influence coefficients at any crack site cannot be determined by application of arbitrary stress fields and modeling the crack response. This complexity makes it difficult to determine both the crack driving force and the stress intensity factors in the vicinity of the crack tip.

Contrasting this with the case of the sidewalls where the stresses are uniform through the thickness of the cylinder so the stresses can be included into the stress intensity factor relationship without regards to variation across the cross section. These stresses are therefore directly calculable from closed form relationships and applicable to the stress intensity factor relationship.

The two geometries of the cylinder bottom and transition regions shown in Figure 4.1 and Figure 4.2 are considered separately. The end for fitting a threaded connection is the same in both cases. In order to simplify the analysis the highest stresses determined in the numerical analysis will be taken to represent the stresses to be expected in both the

transition regions and the ends where changing geometries are encountered. It should be noted that this assumption will not affect the accuracy of the results as the crack with the highest driving force will propagate to failure and we had assumed before that cracks are independently distributed and do not interact with each other as they grow to failure.

To obtain stress intensity factor solutions a detailed three-dimensional finite element analysis approach with representative cracks was attempted in a previous research project [4]. A finite element model of the transition region of the flat- bottom cylinder is shown in Figure 4.6.

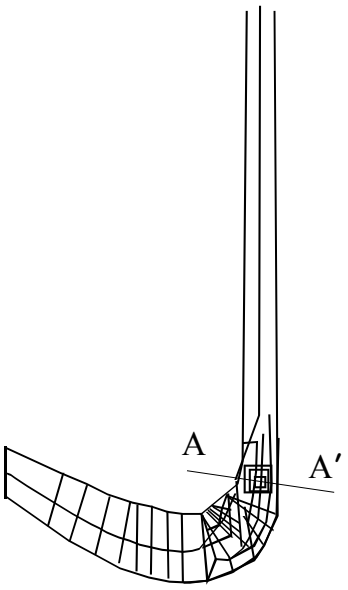

Two-dimensional global analysis

Figure 4.6a Two Dimensional Finite Element Model of Flat Bottomed CNG Cylinder [4]

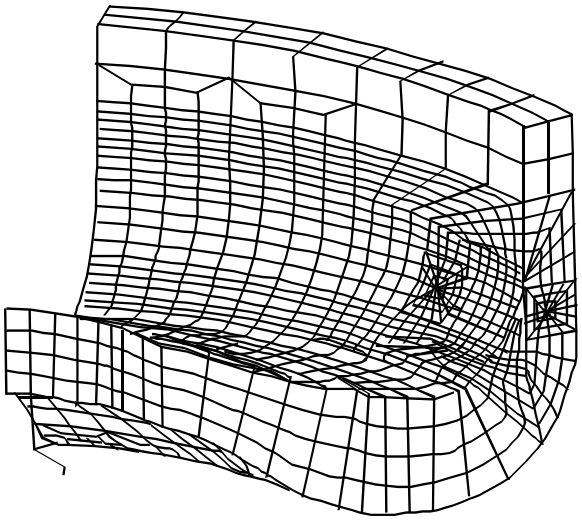

Three-dimensional local analysis

Figure 4.6b Finite Element Model of Flat Bottomed CNG Cylinder [4]

The three-dimensional analysis is complex and the results unable to be directly incorporated into probabilistic corrosion fatigue model that was developed in Chapter 3. It would not be possible to model the corrosion fatigue crack growth with the existing relationship developed. A simpler approximate approach was proposed to get the stress intensity factors [45] and will be used to determine the stress intensity factor solutions for cracks in the transition region and ends.

The essence of this approximate approach is to use existing stress intensity factor solutions developed for components with similar stress distributions and to calibrate the solutions based on results derived from three dimensional finite element analysis of actual CNG cylinder profile. In the case of CNG cylinders stress intensity factor solutions developed by Newman and Raju [46] for a surface crack in a flat plate in

bending and tension seems the most suitable. This is quite appropriate for CNG cylinders as we will recall from the manufacturing process of cylinders highlighted in Chapter 1, the residual stresses would be bending and tension, if the cylinder was manufactured from flat plate or billets. The spinning operations shown in Figure 1.7, used to form the bottom and neck of cylinder involving heating and bending the material in all three manufacturing processes. For these reasons it is assumed that the finite element solution for a flat plate under bending and tension is applicable to the transition regions of CNG cylinders.

The radius of curvature of a cylinder and the non-uniform profile in the transition region significantly affects the stress distribution and therefore the accuracy of the simplified approach being used. The three dimensional crack profile is a source of uncertainty in mapping the results of a flat plate under biaxial stress with a surface crack in a cylinder. A calibration factor is used to map the two results for a few crack sizes in the three dimensional model shown in Figure 4.6 to the predicted result using the simplified model.

To calibrate the results for a flat plate this approach involves multiplying the stress intensity factor solutions for a flat plate under bending and tension by a factor. This factor was determined from detailed three dimensional finite element analysis, done for a limited number of crack geometries in which the exact stress intensity factor at various angles around the crack front was calculated. A finite element model with the representative cracks was developed for the transition region of the cylinder where the

stresses were predicted from two dimensional analysis to be highest and where cracks were encountered in fatigue testing done in the laboratory. As was expected the highest stress intensity factors for the geometries was found along the deepest point at the front.

The results of the detailed three dimensional analysis were then compared with the stress intensity factors that are predicted by the Raju and Newman empirical stress intensity factor equations for a surface crack on a flat plate in bending and tension [46]. The exact crack geometries were used and the deepest point at the crack front was used to estimate the empirical result from the stress intensity factor solutions. Comparing the results shown in Table 4.5 we see that the highest ratio of under reporting of the stress intensity factor, for three different crack sizes and aspect ratio was 21 % [4].

Table 4.5 Comparison between Newman-Raju Empirical and Finite Element Stress Intensity Factor Solutions at the Deepest Point along Crack Front

Crack Geometry		**Stress Intensity Factor (ksi-in$^{1/2}$)**		**Factors**
a/t	**a/c**	**Empirical Results**	**Finite Element Results**	**% Difference**
0.15	0.50	17.9	22.7	21
0.30	0.50	21.8	25.7	16
0.50	0.50	22.2	26.3	16

Under prediction of the stress intensity factor by the empirical results is probably due to the use of a flat plate analysis to represent the cylinder which ignores the influence of the curvature. The stress intensity factor from this geometry is expected to be somewhat different for a radial crack in a cylinder. Additionally the use of the stresses determined by a two dimensional finite element analysis to represent the remote stresses at the crack surface is subject to errors in mapping the exact three dimensional conditions. We will therefore use a factor of 1.21 to map the impact of difference in

stress distribution and geometric profile making the results from the stress intensity factor solutions for a flat plate with a crack representative of a crack in the curvature of the transition region of a cylinder. This calibration factor was used for all crack sizes and will lead to conservative results for the stress intensity factors for other crack sizes.

Three dimensional finite element stress intensity factor solutions by Raju and Newman for flat plates under bending and tension [46], calibrated for the cylinder geometry can be used to approximate the stress intensity factors due to the complex stress distribution at the crack tips in the ends and transition regions of the CNG cylinder. The method of forming the head and the ends by the spinning process makes this a credible approximation for the complex stresses in the transition region.

The empirical stress intensity factor equation for a surface crack in a finite plate subjected to combined loading of tension and bending loads as a function of the crack parameters is given by Equation 4.9 [46].

$$K_I = (S_t + HS_b)\sqrt{\pi \frac{a}{Q}}\, F\left(\frac{a}{t}, \frac{a}{c}, \frac{c}{b}, \phi\right) \tag{4.9}$$

for $0 < a/c \leq 1.0$, $0 < a/t < 1.0$, $c/b < 0.5$, and $0 \leq \phi \leq \pi$. The crack parameters are defined in Figure 4.3.

S_t, is the remote uniform tensile stress and S_b, is the remote bending stress. The remote bending and tensile stresses in the transition region and ends can only be determined by numerical methods. An additional influence coefficient H, was added to

the stress intensity factor relationship to account for the difference in the stress distribution. Since the cylinder is thin enough for plain stress conditions to exist, two dimensional finite element analysis of the un-cracked cylinder will be used to determine the stresses. The nodal solution stresses of the inner surface will be used in Equation 4.9.

4.2.1 Finite Element Analysis

The finite element analysis was performed on the un-cracked cylinder to determine the bending and tension stresses which are then inputted into the stress intensity factor solution. This two dimensional analysis was carried out using ANSYS Mechanical and Structural Analysis finite element code. Eight-noded two dimensional elements were chosen, with two degrees of freedom at each node for translations in the x and y directions. This element was chosen as it has compatible displacement shapes and is well suited to model curved boundaries. Due to the symmetric nature of the cylinder geometry only one- quarter of the cylinder was modeled and automatic meshes used. The internal of the cylinder was subjected to a pressure loading of 2700 psi. The following material properties were used in the finite element analysis:

Young's Modulus 29 $x10^6$ psi

Poisson ratio of 0.3

Internal Radius 5.0 inches

Sidewall thickness 0.35

Analysis was performed for the hemi-spherical bottom as well as the flat bottom cylinders. The element solutions of the stress distribution for both types of cylinders are

shown in Figure 4.7 and Figure 4.8. Most notable result from this analysis is the presence of a region of high stress on the inner surface of the transition regions. This is the location where the crack driving force is expected to be the highest and accelerated crack growth is expected to occur. Further more, the stresses are much higher than the stresses in the cylindrical portion and therefore the areas where leakage is most likely to be expected. Notable from the analysis as well is the presence of a large bending moment where the stress go from tensile on the inner surface of the cylinder to compressive on the outside surface. The stresses in the flat-bottom design cylinder design are higher than the hemi-spherical bottom design as was expected. The results of the flat-bottom design will be used as input to the stress intensity factor solution. This will result in unnecessarily conservative result for cylinder fatigue life as this would be the lower bound expected for cylinder life as a result of cracks in the transition region.

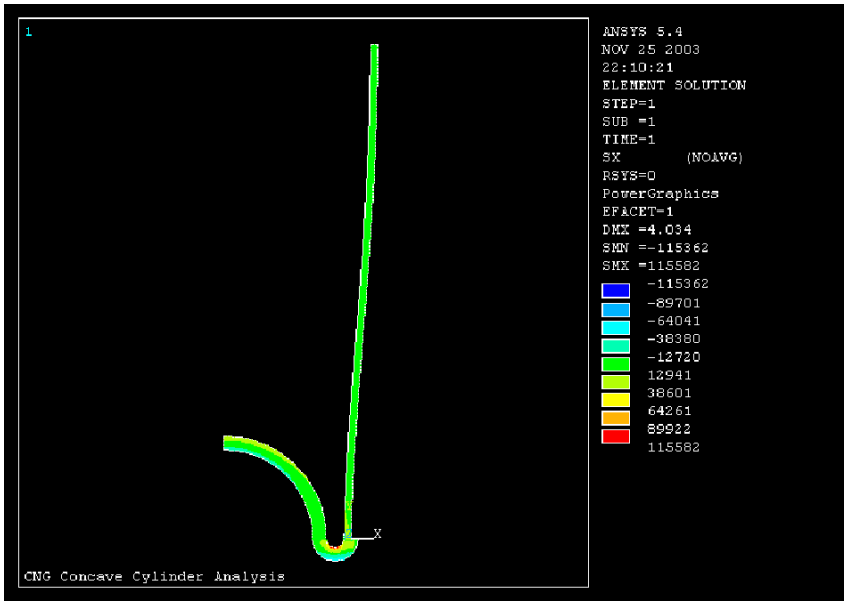

Figure 4.7 Elemental Stresses for Flat-Bottom Cylinder Design

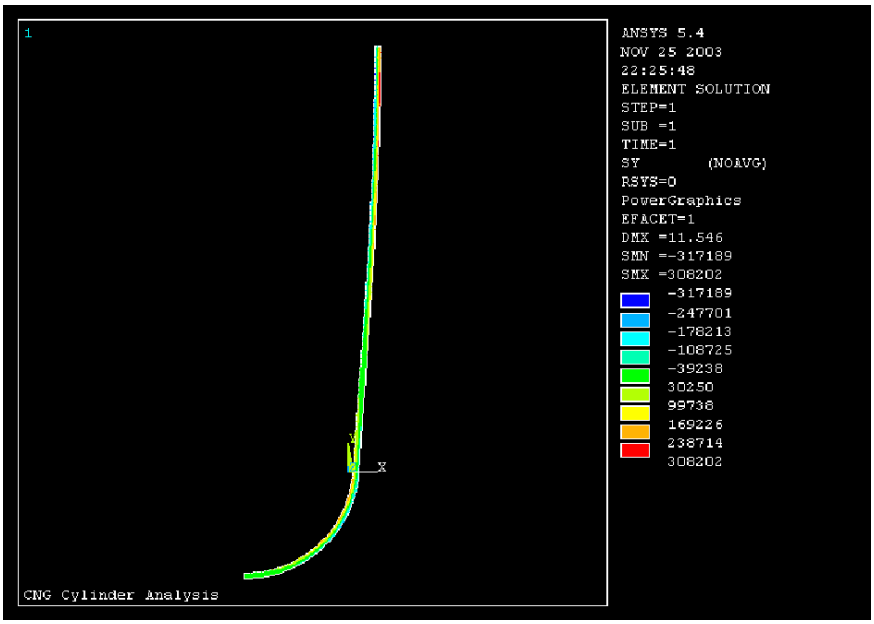

Figure 4.8 Elemental Stresses for Hemi-Spherical Bottom Cylinder Design

The linearized nodal stresses for a path defined across the transitional region for the flat bottom design is plotted in Figure 4.8. It can be seen that the linearized stresses are a straight line and would suggest that it is a combination of pure bending stress on which is superimposed a proportionately very small tension stress. The use of only bending stresses at nodal points along a path across the cross section of the transitional region in the stress intensity factor solution of Equation 4.9 is justified. This is how we will proceed for the rest of this analysis.

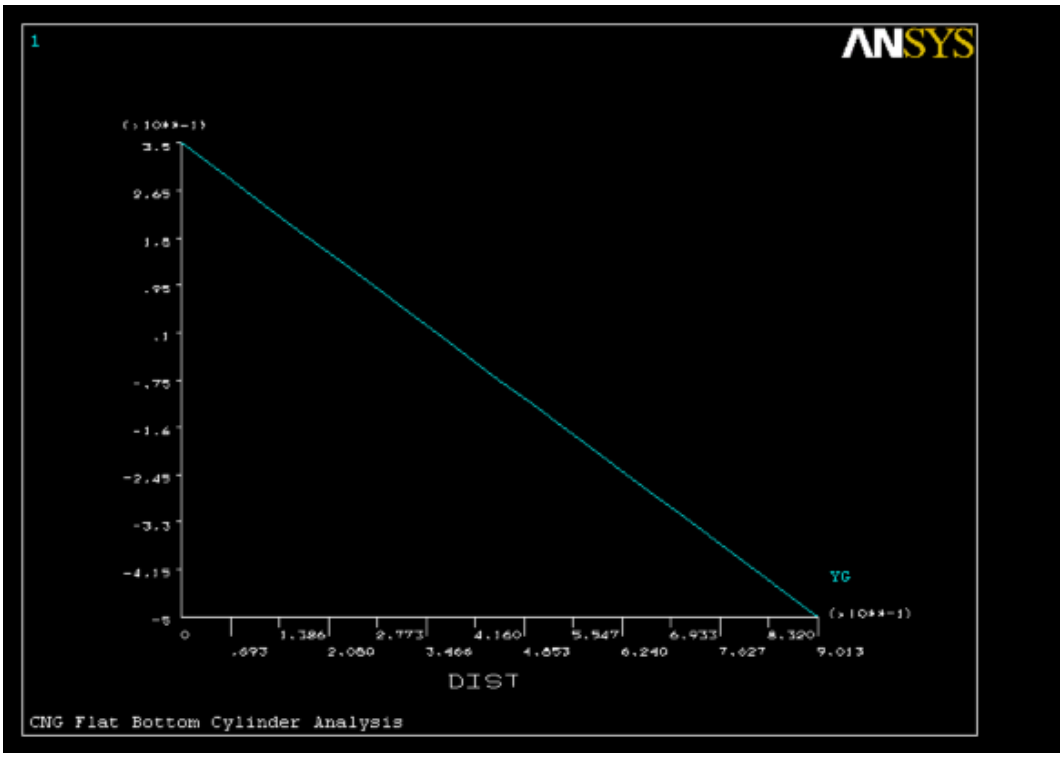

Figure 4.9 Linearized Stresses across Cross Section of Transition Region

Equation 4.10 was derived from the results for the linearized stresses across the thickness from the inside to the outside of the cylinder for a typical cylinder, similar to the one used in the previous finite element analysis. The results were obtained by meshing the digitized cross section of an actual CNG cylinder using ABACUS finite element code at SWRI. Since these results will more accurately represent the stress distribution in an actual cylinder they will be used instead of the generic shape that was used in this finite element analysis [4].

$$S = 66.139 - 219.19d \tag{4.10}$$

Where d, is the distance from the inner surface of the cylinder.

The linear relationship between the stress and the distance across the cross section shows that the stress is approximately pure bending with an insignificant tension stress superimposed on it. The tension stress will therefore be ignored in Equation 4.9 and the linearized result from Equation 4.10 will be used to calculate the stress intensity factor for the transition region in a CNG cylinder.

4.2.2 Transition Region Stress Intensity Factor

The stress intensity factor for the transition region is given by Equation 4.9. The stress component was determined by linearlizing the results of finite element analysis across the cross section. The approximation for Q is the same as in Equation 4.6 and shown below:

$$Q = 1 + 1.464\left(\frac{a}{c}\right)^{1.65} \quad \text{for } \frac{a}{c} \le 1$$

The function, F, was obtained by Newman and Raju from a systematic curve-fitting procedure by using double-series polynomials in terms of parameters a*/c, a/t*, and angular functions of φ. The stress intensity factor boundary correction factor relationship developed was [46].

$$F = \left[M_1 + M_2\left(\frac{a}{t}\right)^2 + M_3\left(\frac{a}{t}\right)^4 \right] g f_\phi f_c \tag{4.11}$$

where

$$M_1 = 1.13 - 0.09\left(\frac{a}{t}\right) \tag{4.12}$$

$$M_2 = -0.54 + \left[\frac{0.89}{0.2 + (a/c)}\right] \tag{4.13}$$

$$M_3 = 0.5 - \frac{1}{0.65 + (a/c)} + 14\left(1 - \frac{a}{c}\right)^{24} \tag{4.14}$$

$$g = 1 + \left[0.1 + 0.35\left(\frac{a}{t}\right)^2\right](1 - \sin\phi)^2 \tag{4.15}$$

The function f_φ, an angular function from the embedded elliptical crack solution [47], is

$$f_\phi = \sqrt[4]{\sin^2\phi + \left(\frac{a}{c}\right)^2 \cos^2\phi} \tag{4.16}$$

The function, f_w, a finite-width correction from [48], is

$$f_w = \sqrt{\sec\left(\frac{\pi c}{2b}\sqrt{\frac{a}{t}}\right)} \tag{4.17}$$

The function f_c is the ratio of boundary correction factor for cylinder to flat plate and corrects the flat plate boundary correction factor for the curvature in the cylinder.

$$f_c = \left(\frac{R_0^2 + R^2}{R_0^2 - R^2} + 1 - 0.5\sqrt{\frac{a}{t}}\right)\frac{t}{R} \tag{4.18}$$

The curvature correction factor f_c determined from boundary correction for a flat plate compared with a surface with a curvature [45] was determine to be true for $t/R \leq 0.25$ t/R, which applies to the typical CNG cylinders under consideration.

The function H, was also developed by curve fitting and engineering judgments and has the form [46].

$$H = H_1 + (H_2 - H_1) \sin^{\rho} \phi \tag{4.19}$$

where

$$\rho = 0.2 + \frac{a}{c} + 0.6\left(\frac{a}{t}\right) \tag{4.20}$$

$$H_1 = 1 - 0.34\frac{a}{t} - 0.11\frac{a}{c}\left(\frac{a}{t}\right) \tag{4.22}$$

$$H_2 = 1 + G_1\left(\frac{a}{t}\right) + G_2\left(\frac{a}{t}\right)^2 \tag{4.23}$$

and embedded parametric functions G_1 and G_2 are given by

$$G_1 = -1.22 - 0.12\left(\frac{a}{c}\right) \tag{4.24}$$

$$G_2 = 0.55 - 1.05\left(\frac{a}{c}\right)^{0.75} + 0.47\left(\frac{a}{c}\right)^{1.5} \tag{4.25}$$

The approximate expression for the stress intensity factor K_I for a wide range of configuration parameters was found to be within ± 5% of the results obtained by boundary layer integral method [49] and from finite-element methods [46].

The finite element solution results obtained for a single crack was found to be less than 4% [45 – 46], [50] of that obtained from the approximate equation for two symmetrically surface cracks given above. Thus the stress-intensity factor relationship can be used for a single surface crack without significant error.

Calibrating the stress intensity factor derived from this empirical relationship with the factor of 1.21 will effectively map the result for flat plate to a typical CNG cylinder. The resulting empirical stress intensity factor relationship, representing crack driving force at the crack front is given by

$$K_I = 1.21(HS_b)\sqrt{\pi \tfrac{a}{Q}}F\left(\tfrac{a}{t}, \tfrac{a}{c}, \tfrac{c}{b}, \phi\right) \tag{4.26}$$

where the bending stress, S_b, is given by Equation 4.10, shape factor for elliptical crack, Q, is given by Equation 4.6. F and H after simplification are given by Equations 4.27 and 4.28. [50].

$$F = \tfrac{t}{R}\left[\tfrac{R^2_o + R^2}{R^2_o - R^2} + 1 - 0.5\sqrt{\tfrac{a}{t}}\right]\left[M_1 + M_2\left(\tfrac{a}{t}\right)^2 + M_3\left(\tfrac{a}{t}\right)^4\right] \tag{4.27}$$

$$H = H_2 = 1 + G_1\left(\tfrac{a}{t}\right) + G_2\left(\tfrac{a}{t}\right)^2 \tag{4.28}$$

The stress intensity factor relationship for cracks in the transition region and sidewalls of the cylinder has now been developed. Only semi-elliptical crack shapes were considered and the crack is assumed to retain the shape as it grows through the sidewall. While undoubtedly cracks can change shape as they grow and may not have a semi-elliptical profile, such simplification should not affect the accuracy of the results [51 – 53]. What is left now is to categorize the cylinder fracture performance completing the development of the physics of failure model. Categorizing fracture involve modeling the behavior of the cylinder beyond sub-critical crack growth to when unstable final fracture or Stage III crack growth occurs. This will invariably lead to rupture of the cylinder.

CHAPTER 5: FRACTURE PERFORMANCE OF CYLINDER

5.1 EPFM Cylinder Fracture Performance

Unstable crack growth leading to final fracture for CNG cylinders is best characterized by EPFM. This is so because the typical thickness of a CNG cylinder is not enough for plain strain conditions determined by Equation 2.1, to exist. What this means is that the plastic region surrounding the crack tip will have an impact on the fracture performance. If this impact is such that nonlinear elastic conditions predominate then invoking LEFM criteria could lead to significant error in predicting the onset of failure. The results would be conservative as strain relaxation at the crack tip would reduce the effect of the crack driving force in propagating the crack with increased stress.

There are four EPFM criteria used to identify the onset of unstable crack growth which are applicable to CNG cylinder fracture analysis. The governing criterion to be used in this analysis is the one that predicts the smallest unstable crack size.

5.1.1 J-Integral Failure Criterion

This failure criterion is the exceeding of the critical J-integral value, J_{IC}. The parameter, J, is Rice's J-integral and is a measure of the crack driving force. J is the generalization of the strain energy release rate with respect to crack area and can be expressed as

$$J = \int_{\Gamma} w\, dy - T_i \frac{\partial u_i}{\partial x} dx \qquad (5.1)$$

The integral is performed around the arbitrarily chosen closed contour around the crack tip, Γ, shown in Figure 5.1, w is the strain energy density, T_i, is the outward traction vector on an increment of path, Γ, ds. The displacement of increment is ds along outward traction vector is u_i. Since J is an independent path, it will have the same values for all choices of Γ.

J-Integral fracture criterion has been extensively used to evaluate non-elastic crack growth and fracture [54 – 56]. Numerous experimental verification of its adequacy as a EPFM criterion has been completed [57 - 59] as long as applied loads increase monotonically.

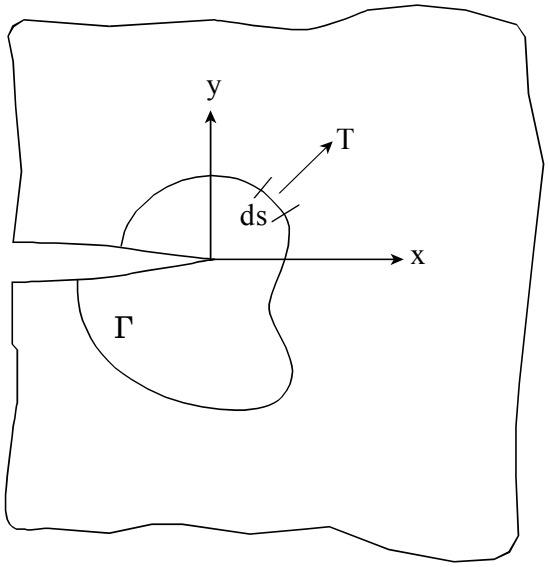

Figure 5.1 Crack Tip Parameters Used to Evaluate J-Integral

The elastic-plastic zone around the crack tip for which this model is valid is called the *J*-dominant region. The intensity of the crack-tip stress-strain fields in the *J*-dominant region are completely characterized by the single *J* parameter. Failure of the material by unstable crack growth will be associated with a critical value of *J*, namely, J_{IC} [60]. That is instability will exist and can propagate to failure when

$$J \geq J_{IC} \tag{5.2a}$$

or

$$J(\text{Driving Force}) \geq J(\text{Material Resistance}) \tag{5.2b}$$

If crack tip plasticity is negligible then J integral analysis will produce the same results as LEFM.

Use of J_{IC} as a sufficient criterion for unstable crack growth to occur leading to rupture is conservative. This is because it does not take into account the increased crack driving force required to grow a crack once J_{IC} is exceeded. In order to include the increased driving force required to grow a crack beyond J_{IC}, the tearing instability criterion by Paris [61] should be used.

5.1.2 Tearing Instability Criterion

The tearing instability criterion is derived from the J-resistance curve. From the schematic curve shown in Figure 5.2, it is obvious that if the crack driving force *J*, exceeds the critical value, J_{IC}, extending the crack further can cause the material resistance to be elevated to the applied *J* level. This rise in material crack resistance

follows significant growth in crack extension with applied *J* level which is explained by coalescing of micro voids in the material. Material resistance will subsequently increase as further crack extension can only occur with ductile tearing of the material at the crack front.

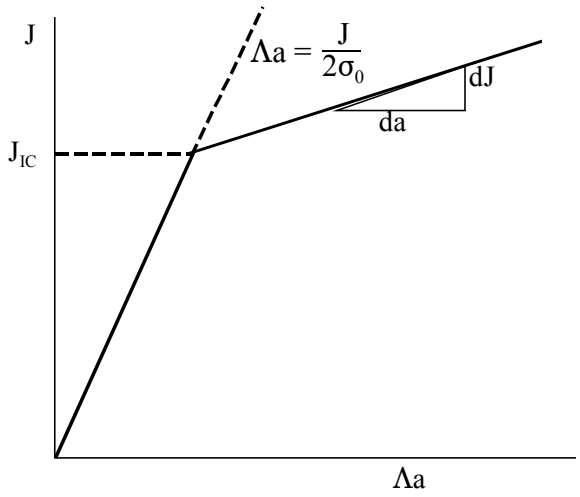

Figure 5.2 Schematic Representation of Material J-Integral Resistance Curve

From Figure 5.2 we can see that the applied crack driving force also increases with increasing crack extension. Unstable crack will occur when the rate of change of the material resistance to crack growth as the crack length increases is less than the rate of increase in crack driving force. This is the essence of the tearing instability criterion and can be expressed as shown in Equation 5.3.

$$\left(\frac{dJ}{da}\right)_{APPLIED} > \left(\frac{dJ}{da}\right)_{MATERIAL} \tag{5.3}$$

A dimensionless tearing modulus for the material is sometimes used. This is denoted by T_{MAT} and is given by the following expression [57].

$$T_{MAT} = \frac{E}{\sigma_0^2}\left(\frac{dJ}{da}\right)_{MAT} \tag{5.4}$$

where σ_0 is the flow stress of the material and is commonly defined as [62].

$$\sigma_0 = \frac{\sigma_{YS} + \sigma_{UTS}}{2} \tag{5.5}$$

and

E = is the Young's Modulus

σ_{ys} = yield stress

σ_{UTS} = ultimate tensile stress

Using the tearing modulus criteria, unstable crack growth leading to cylinder rupture will occur when the applied tearing modulus exceeds the material tearing modulus. Intuitively it can be seen that the applied tearing modulus is computed from Equation 5.4 by replacing the rate of increase in the crack resistance with crack growth with rate of increase of crack driving force with crack extension.

Values for J_{IC} and T_{MAT} have to be determined from data on AISI 4130X materials used to manufacture CNG cylinders. Such data sources could not be identified for this research so they will be derived from experimentation done to analyze the EPFM properties of CNG cylinder materials. In actuality J_{IC} and T_{MAT} are distributed quantities and should be treated as such. The data available for evaluating these quantities cannot be used to estimate the statistical distributions. This will produce results which are a best

fit and gives no insight into the uncertainty associated with the crack size at which instability and cylinder rupture is expected to occur.

From research conducted at SWRI [3] and at Powertech Laboratories [7] the graphs shown in Figures 5.3 and 5.4 were produced. In Figure 5.3, line *a* represents an estimate of the apparent crack extension associated with crack tip blunting, as the specimen is loaded. J_{IC} is defined as the J-value at which stable crack extension starts. It is represented by intersection of the crack blunting line (line *a*) and the stable crack growth line. This stable crack growth line is a linear regression fit of the data between two lines drawn, that are parallel to line *a,* and between which the data appears to satisfy a linear fit. The J_{IC} values are subsequently converted to K_{IC} using

$$K_{IC} = \left(\frac{EJ_{IC}}{1-\upsilon^2} \right)^{1/2} \tag{5.6}$$

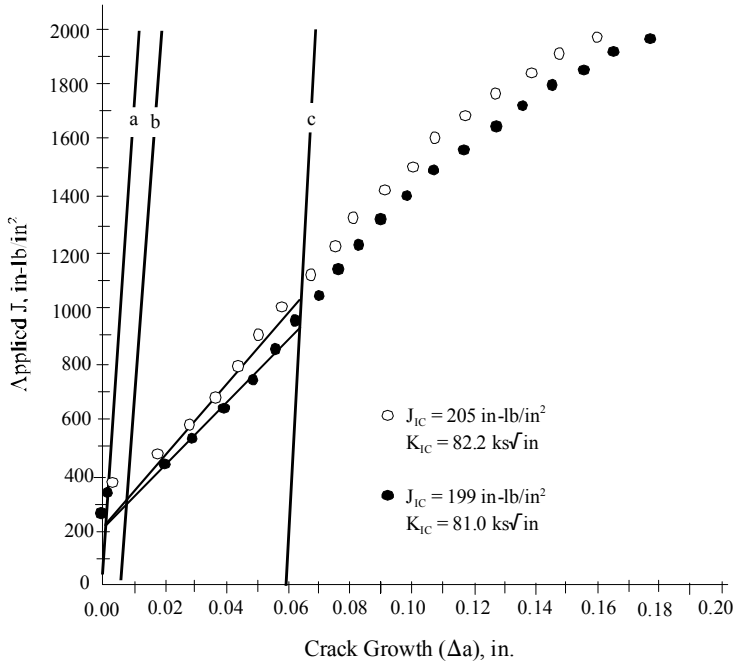

Figure 5.3 J-Resistance Curve Fracture Toughness of Martensitic 4130-M Steel [3]

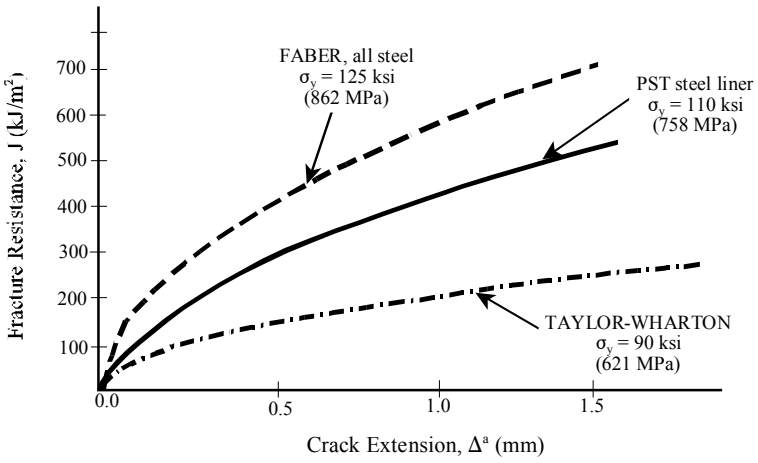

Figure 5.4 Fracture Resistances of the Steels of Type 1 Cylinders and Type 2 Liners [7]

Tensile and fracture properties of steel cylinders manufactured by different companies were measured using small scale test specimens at room temperature by Powertech Laboratories Inc [7]. Fracture properties of the materials were established using the ASTM E813-89 [63] fracture toughness test. This test method determines a critical value of J-integral which characterizes the toughness of a material near the onset of unstable crack extension from a pre-existing fatigue crack. The J-integral values are determined from the areas under the load vs. load-line displacement curve, obtained from tests. The tests also produce J-R curves which are plots of J-integral versus ductile crack extension, Δa. Plots for a range of CNG cylinder materials are shown in Figure 5.3 and Figure 5.4.

A critical value of J-integral for the onset of unstable crack growth, J_{IC}, is defined as the J-integral value corresponding to the intersection of the J-R of the material and an offset line drawn at a crack extension (a) value of 0.2 and having a slope of ($2\Delta a \sigma_y$), was

obtained from each of the materials. Table 5.1 summarizes the measured material properties.

Table 5.1 Material Properties of the Metal Cylinders

Cylinder/ Liner Type	**Outside Diameter mm (ins)**	**Wall Thickness mm (ins)**	**Average Yield Stress ksi (MPa)**	**UTS ksi (MPa)**	**J-Fracture Toughness (J_{IC}) in-psi (kJ/m^2)**
Faber	316 (12.44)	8.2 (0.322)	125 (860)	139 (957)	1428 (250)
Taylor-Wharton	238 (9.35)	7.11 (0.28)	90 (618)	110 (760)	491 (86)
Presses Steel Tank	340 (13.4)	5.8 (0.228)	111 (762)	123 (850)	57 (10)

The materials fracture resistance (J-R curves) for the all steel cylinders and steel liners are shown in Figure 5.4. The curve for the Faber all steel cylinder material is steeper than that of the Taylor Wharton cylinder material, reflecting a higher fracture toughness steel. The values for J_{IC} , T_{MAT} as well as $(dJ/da)_{MAT}$ and $(dJ/da)_{APPLIED}$ can be estimated from Figures 5.3 - 5.4 and Table 5.1 for determining whether tearing instability of the material will occur. The values for the Presses Steel Tank manufactured cylinders will be used for the remainder of this analysis even though these results will be conservative in the case of cylinders manufactured by Taylor-Wharton but underestimated for cylinders manufactured by Faber.

5.1.3 Critical Crack Length Excedence Criterion

An empirical relationship was developed by Cyltek, Inc [7] that could be used to predict the critical crack size for cylinder leaks without performing detailed EPFM analysis. The basis for development of this equation is the Failure Assessment Diagram

method [64 - 65], of identifying initiation of unstable crack growth due to plastic collapse at the crack front. The equation that was developed cannot be used for the transition regions or the domed ends.

Development of the equation was achieved by performing regression analysis on cylinder data generated in EPFM experimental analysis to obtain the functional relationship between the critical crack length and the cylinder properties. The basic functional relationship established was that:

L_D = f(Cylinder dimensions, Material Properties, Operating Conditions)

More specific to the cylinder and material properties, the critical crack size could be represented as follows:

$$L_D = f(r, t, \sigma_H, \sigma_y, J_0, J_I) \tag{5.7}$$

where L_D is the calculated crack length for cylinder to leak instead of fracture. Cracks with lengths less than L_D will leak when they penetrate the sidewall. Conversely, cracks greater than L_D are expected to cause cylinder to rupture. This equation covers all cylinders, so the critical crack dimensions could be easily determined by inputting the cylinder properties into the equation. The other parameters in the equation are:

r is the cylinder outer radius,

t is the wall thickness,

σ_H is the hoop stress,

σ_y is the yield stress,

J_0 is the critical J-integral parameter, and

J_1 is the slope of the crack growth resistance curve.

The values of the coefficients that define the regression equation were determined by statistical analysis and goodness of fit testing. The final form is shown in Equation 5.8.

$$L_D = 3.8E-4\, r\, t^{4.73E-1}\, \sigma_y^{2.087}\, J_I^{0.446}\, \sigma_H^{0.0313 J_1} \exp\left(-0.024\,\sigma_H - 0.008\,\sigma_y + 0.1 J_0 - 0.064 J_1\right) \quad (5.8)$$

The above equation provides a very accurate fit to the critical crack length and could therefore be determined without performing detailed fracture analysis. The variables in the parametric equation vary between ranges as shown in Table 5.2 [7].

Table 5.2 Typical Values for Variables in Parametric Equation

Variable	Description	Range	Typical Cylinder
rt	Product of Cylinder radius and thickness	$0.5 < rt > 5$	1.67
σ_y	Yield Strength	$90 < \sigma_y > 200$	125
σ_H	Hoop Stress	$50 < \sigma_H > 100$	94
J_0	Resistance Curve Intercept	$0.2 < J_0 > 1.0$	0.8
J_1	Resistance Curve Slope	$0 < J_1 > 60$	38

The critical crack length calculated from Equation 5.8 for the typical CNG cylinder being considered for this analysis is:

$$L_D = 2.89 \text{ inches} \quad (5.9)$$

This compares well with the results of testing done on all steel cylinders where a flaw was machined into the wall of the cylinder and pressurized to failure [66].

5.1.4 Net Section Applied Stress Excedence Criterion

This criterion mostly applies to circumferential cracks in a cylinder, which have been determined from experimentation [4] to occur mostly in the transition region. It is also applicable to cracks in the sidewalls except in this case the stress acting on the crack surface is hoop stress versus longitudinal stress which occurs with circumferential cracks.

It is possible that the fracture criteria established in the previous three sections can predict that crack growth can never go unstable. In fact such a conclusion has been drawn from studies done by [3], [67]. Complete and sudden failures could still occur if the remaining cylinder ligament cross-section was not sufficient to support the applied loads. This forms the basis of the net section criterion first suggested by Kanninen [68], [57].

Longitudinal applied stress, σ_L, in the cylinder has to be supported by the remaining ligament of the cylinder if there is a circumferential crack in the transition region and the hoop stress, σ_H, in the case of longitudinal cracks in the sidewall. The critical value of the net section stress has been observed to be equal to the flow stress [70]. Flow stress has been shown in Equation 5.10 to be equal to:

$$\sigma_0 = \frac{\sigma_{YS} + \sigma_{UTS}}{2} \tag{5.10}$$

Failure is determined to occur if the condition expressed in Equation 5.11 exists.

$$\sigma_F A_{LIG} = \sigma_0 (A_{LIG} - A_{CRACK}) \tag{5.11}$$

where σ_F is the stress acting on the remaining un-cracked ligament of the cylinder, A_{LIG} the cross sectional area of the untracked ligament and A_{CRACK} is the cross sectional area of the cracked section.

The flow stress σ_o has to be determined from the yield and tensile strength of the AISI 4130X material. These tensile properties are not constants, and in fact are variables with an under-laying distribution. Test data on the tensile properties of CNG cylinder materials were not available for this research, so deterministic values will be assigned based on what is published in the literature. The flow stress based on the available data is calculated to be:

$$\sigma_0 = 117 \text{ ksi} \tag{5.12}$$

based on the following published data:

$$\sigma_{YS} = 111 \text{ ksi} \tag{5.13}$$

$$\sigma_0 = 123 \text{ ksi} \tag{5.14}$$

The use of the hoop and longitudinal stresses as the load stress acting on the remaining ligament can be questioned. It should be noted however that these stresses are not affected by relaxation in the plastic region of the crack front or deformation of the cylinder. The stresses have to be supported by the uncracked cross section of the cylinder. The maximum cylinder pressure is used when calculating the load stress which gives us conservative results as the contents of the cylinder will be leaking thereby reducing the pressure. Ideally, the pressure in the cylinder should be estimated by calculating by crack mouth opening displacement and accounting for the pressure drop over time with gas flow through the crack mouth opening. Such complexity is not necessary for this analysis as the conservative results provides an adequate criterion.

5.2 LEFM Cylinder Fracture Performance

LEFM can been used to estimate when unstable crack growth and catastrophic rupture is likely to occur. This approach as has been discussed before is subject to errors [7] due to uncertainties arising from the influence of crack tip plasticity. Crack tip plasticity is the condition where a large plastic zone exists ahead of the crack tip (see Figure 2.2). Crack progression occurs because of small scale yielding in the small plastic zone surrounding the crack tip and the stress distribution is influenced primarily by the free crack surfaces. At lower frequencies, a precipitous drop in the crack growth rates has been noted in [4] as a result of crack flanks being wedged open. This wedging action occurs due to the build up of corrosion products within the crack and the increasing crack face asperities as a result of the rough surfaces produced by crack growth in the corrosive environment. The wedging action effectively relieves the high stresses at the crack tip

and produces an increase in crack closure with a concomitant drop in crack growth rates. This drop in crack growth rates effectively defines a threshold below which cracks will not grow in this environment.

The plastic zone is confined within an elastic field which determines the fracture behavior. The intensity of the local stress field in the region around the plastic zone is affected only by the remote boundaries and applied force. LEFM assumes that the stress-strain field near a crack tip in a linearly elastic solid is controlled by the stress intensity factor, K, and failure will occur when this exceeds a critical value, K_{IC}.

LEFM is a suitable criterion for mechanically thick sections of steel or where plasticity is contained in a small region near the crack tip. Plain strain conditions dominate in this situation. Test conditions with extensive plasticity shows an increasing resistance to crack growth as the crack extends upon loading, before it goes unstable, with the resultant uncertainty in crack growth behavior if LEFM techniques are applied.

Cracks in the cylinders can be either sub-surface or surface. For a given crack and stress level, surface cracks will be more severe because it will have a larger stress intensity factor. Interior and exterior surface cracks will have different stress distribution at the crack tips so the crack driving force solutions will be different. The same applies to cracks in the transition regions and ends of the cylinders. Cracks located totally within the cylinder wall are omitted from consideration in this analysis as only surface cracks can grow by fatigue. The consideration of the effects of embedded cracks is a refinement

which should be included in future studies on CNG cylinder risk analysis, its omission will not significant alter the calculated failure probabilities, especially if cracks in the three distinct regions of the cylinder are considered separately and their effect combined to get an overall distribution of failure frequency.

Using LEFM as a failure criterion states that a cylinder will fail catastrophically or rupture if the maximum stress intensity factor exceeds the fracture toughness of the material. More specifically if the stress strain field near a crack tip in a linear elastic solid is controlled by a single parameter, K, the stress intensity factor then the crack will go unstable when the applied value of K exceeds a critical value, K_C, the fracture toughness. Under plain strain a condition which applies to CNG cylinders, this property is called K_{IC}. The failure criterion can therefore be written as:

$$K_{applied} > K_{IC} \tag{5.15}$$

The fracture toughness can be considered a material property much like ultimate tensile stress which depends on temperature, alloying materials, loading rate and strength.

Fracture toughness is a distributed quantity dependent on the carbides present, temperature and other factor which results in uncertainties which are aleatory in nature [71]. Fracture toughness data typically exhibit noticeable scatter even when testing is performed according to the specifications in ASTM Standard E399-90 [72]. Low alloy steels in particular exhibit considerable scatter in the toughness especially in the ductile

to brittle transition region at low temperatures. This behavior is under current research and continues to be a phenomenon that can impact fatigue life of steel components especially at low temperatures [73].

Compressed natural gas buses are required to be used in various climactic conditions. The NGV-2 standard does not specify a minimum operating temperature for such vehicles. The cylinders can therefore be exposed to temperatures below the ductile transition temperatures. However the fatigue life at low temperatures have not been documented and consistent with the ductile to brittle transition expected at certain temperatures, the fatigue life is expected to be less. No data was available to compute the effect of temperature on the fracture toughness. This remains an area of considerable uncertainty based on the use profile of a typical bus. In the absence of relevant data to analyze this important effect, no attempt will be made to model the effect of temperature and carbide distribution on fracture toughness.

The distribution of K_{IC} will be estimated from Charpy-V-Notch data generated in the ISO WG-14 cylinder fracture performance testing [74]. K_{IC} was derived from the Charpy Impact data by the common elastic fracture toughness correlation relationship shown in Equation 5.16 [75 - 76]. The data used was for fracture test results for cylinder steels matching the typical cylinder in the transverse orientation at 20°C degrees C, and was fitted to a Weibull distribution. The results are shown in Figure 5.5 and Figure 5.6. The parameters of this distribution are also shown. J_{IC} values can be derived from the fracture toughness by assuming plain stress conditions and using Equation 5.17.

$$\frac{K_{IC}}{\sigma_y} = \frac{5}{\sigma_y}\left(CVN - \frac{\sigma_y}{20}\right) \tag{5.16}$$

$$J = \frac{K_{IC}^2\left(1-\nu^2\right)}{E} \tag{5.17}$$

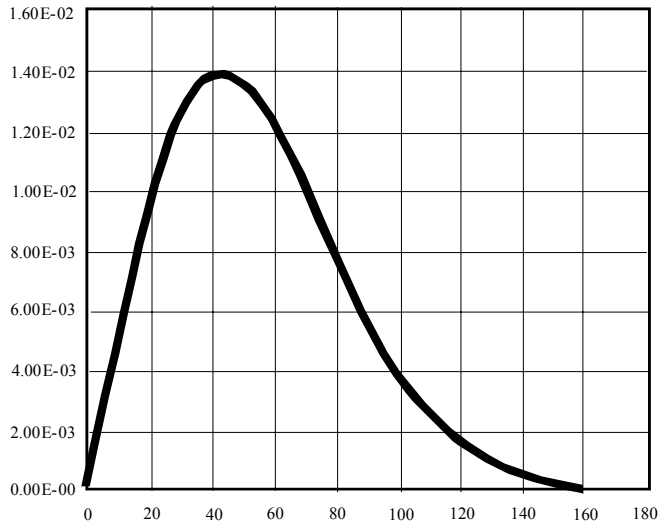

Figure 5.5 Distribution of Elastic Fracture Toughness

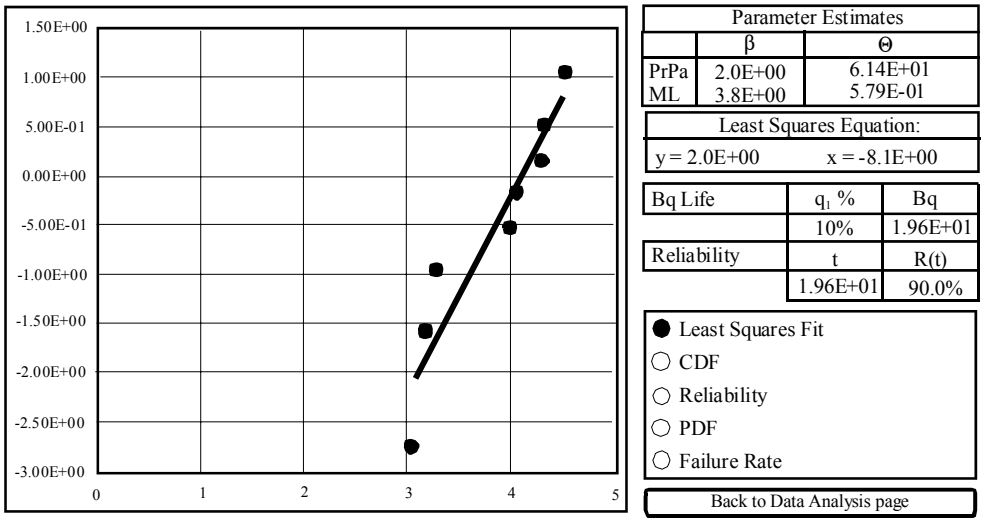

Figure 5.6 Least Square Fitting of Elastic Fracture Toughness Data

5.2 Fracture Criteria for CNG Cylinders

The fracture criterions that will most likely result in CNG cylinder failure due to corrosion fatigue crack growth will now be determined. The selection of the criterion will be based on which criterion results in the smallest critical crack size for a given crack driving force or applied stress.

Figure 5.4 and 5.5 can be used to estimate the crack size that would result in unstable crack growth due to tearing instability. This data is not considered to be sufficiently accurate to predict the crack extension that could result in instability so this criterion will not be considered any further used in this analysis.

Cracks in the circumferential direction are more likely to become unstable due to the remaining ligament criterion. From equation 5.10 we could estimate the crack length that would become unstable. The cross-sectional area of the crack after the geometry refinement of through wall cracks is given by [77].

$$A_{crack} = ac\left(2 + \frac{a}{R}\right) \tag{5.18}$$

where,

a = crack depth

c = crack half length

R = radius of cylinder

Using the longitudinal stress in the cylinder and the flow stress from Equation 5.11, the crack depth at which instability would occur can be calculated based on the crack aspect ratio of the crack being considered. This is how the criteria will be applied.

The LEFM (K_{IC}) and EPFM (J_{IC}) fracture toughness is derived from the critical J-integral value in Table 5.1 and not determined independently. As such only one will be used as a failure criterion. For this analysis the K_{IC} will be used as the failure criterion in the crack growth relationship to determine the critical crack depth. K_{IC} can be calculated from Equation 5.16. This relationship applies when LEFM conditions are valid. Never the less, this criterion has been used successfully to characterize crack-tip fracture conditions for elastic-plastic material behavior even when zones of crack-tip plasticity are

relatively large. The mean value of the distribution of fracture toughness from Table 5.1 and Equation 5.17 is

$$K_{IC} = 81 \text{ ksi} \tag{5.19}$$

Any crack not deep or long enough to cause unstable crack growth and rupture of a typical CNG cylinder will be considered to grow only as a fatigue crack until it grows through the sidewall. No further crack growth will be modeled once the crack grows through the sidewall, however the crack aspect ratio may change and the crack length at all possible aspect ratios will be checked to determine if the length will be such that unstable crack growth will occur. If none of these conditions are met then the cylinder will be deemed to have failed by leakage only. The application of the failure criterion is detailed in the numerical computations and shown in a flow diagram in Chapter 7.

CHAPTER 6: INITIAL SIZE CRACK DISTRIBUTION

The initial crack size is an important consideration in fracture mechanics modeling of cylinder reliability. In deterministic fatigue crack growth and fracture mechanics analysis the crack size is considered to be a specific quantity. In the analysis adopted for this physics of failure modeling, the crack size and the number of cracks are considered to be probabilistic in nature, requiring distributions to completely describe the crack geometry, and to account for the uncertainties in the available crack size data.

Initial crack size is the input to the physics of failure model that the least information is available in order to calculate the frequency of cylinder failure. Numerous attempts were made to ascertain the initial crack size distribution from the known manufacturers of cylinders for natural gas vehicles in service in the United States. This effort did not produce results, and as such a generic distribution was adopted based on the existing practice of rejecting pressurized industrial cylinders with defect depth greater than 5 % of the wall thickness [78]. Elsewhere, it has been reported that initial defect size of 0.02 inches can be expected in CNG cylinders [3]. The exact distribution of crack sizes would have been ideal for this analysis. However in most realistic situations, the crack depth, length and location through the thickness of the cylinder are important considerations, but are subject to such considerable variation that instead what has been developed is a methodology to update the generic distribution used for the typical cylinder used in this analysis with in service inspection and other data using Bayesian

methods. This way the distribution used in fatigue life model can be revised to make it more applicable to any cylinder being analyzed, whether from initial deployment, after inspection when data become available or after repairs. It should be noted that while the discussion so far has only mentioned crack size distribution, that the crack existence frequency which is a random variable is equally important and will be considered as part of the initial crack distribution. The initial crack distribution will therefore consist of two components:

1) The conditional crack size distribution which is the size distribution given that a crack is present.

2) The likelihood function of crack existence which is the underlying distribution accounting for the frequency of occurrence of cracks. This likelihood of existence is dependent on the region of the cylinder, whether inside or outside, sidewalls or transition region and also on the cylinder design being considered.

When cylinders are manufactured, cracks or other flaws that could contribute to corrosion crack growth can either be on the surface or at the sub-surface. For the purpose of this analysis, folds and other such defects which can contribute to crack growth will be included as cracks in the initial crack distribution. In the stress intensity factor discussions in Chapter 4, we have established that for a given crack size and stress level, the crack driving force on an interior surface crack will be more severe since it has a

larger stress intensity factor. For this analysis, we will concentrate on interior surface cracks. Cracks originating on the outside as well as cracks embedded in the walls will be omitted from consideration in the present analysis. The consideration of only interior surface cracks will not significantly affect the accuracy of the results because, based on the manufacturing processes, when cracks are expected to be introduced, they are more than likely to occur on the inside surface and these are the cracks that will propagate to failure [3 – 4], [7].

We note from the finite element analysis in Chapter 4, and from experimental work done on CNG cylinders [4], that circumferential cracks in the transition region occur more frequently and have a more damaging effect on cylinder life based on the crack driving force in this region. Consequently, as a further refinement, attention will be focused on circumferential cracks in the transition region. Some analysis will be done for cracks in the sidewall to demonstrate the accuracy of this approach. The typical crack geometry considered in this analysis is therefore a circumferential interior surface crack as shown in Figure 6.1.

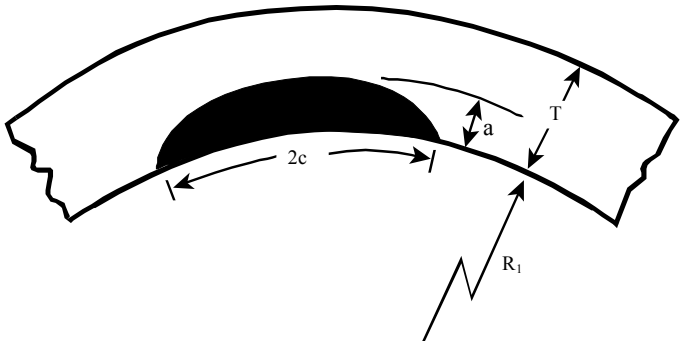

Figure 6.1 Initial Crack Geometry Considered In CNG Cylinder

Cracks introduced in the cylinder are assumed to have a fixed shape. The use of semi-elliptical cracks with random length to depth ratio would be more general in the treatment of initial crack size and shapes. However, the use of a more general crack geometry complicates the crack growth calculations and defining the distribution of the initial crack size. To make both the crack depth and length random variables we would need a bi-variate crack size distribution to fully describe the initial crack size. The absence of data to estimate the parameters of this distribution makes it necessary to consider only the crack depth to be randomly distributed. This will be further discussed in the Sensitivity Analysis section of Chapter 9.

The uni-variate distribution where a density function will only be developed for the crack depth is marginal distribution. The density function for this marginal distribution can be written as a function of the bi-variate distribution as shown in Equation 6.1. Equation 6.2 describes the bi-variate distribution.

$$p_0(a) = \int_0^{\infty} p_0(a, c)\, dc \tag{6.1}$$

$$\int_0^{t} \int_0^{\infty} p_0(a, c)\, dc\, da = 1 \tag{6.2}$$

This assumption greatly simplifies the initial crack size distribution. The effort is therefore reduced to determining the marginal distribution of the initial crack size based on the crack depth. The crack parameters are as follows:

a is the average of the distribution of crack depth across the material wall thickness

t is the material wall thickness

c is the crack half length

R is the cylinder inside diameter

R_0 is the cylinder outside diameter

Initial crack size, a, is considered to be a random variable that can be fitted to a parametric probability distribution density function which adequately accounts for the uncertainties in the observed crack size data. This distribution then describes the probability density on crack depth. The crack frequency of occurrence or density is subsequently determined from the observed number of cracks and the fraction of total cracks as predicted from the crack depth distribution in the expected depth range.

To account for a crack occurring in the CNG cylinder and propagating to failure, two important characteristics are therefore established. These are the crack depth distribution and the rate of occurrence of cracks in a typical cylinder (crack existence frequency). The former is the probability distribution of crack size, given that a crack exists and the latter is the crack frequency of occurrence. The two combined give the total cylinder

initial crack distribution, $f_o(a)$, used in the crack growth model. This is summarized in Figure 6.2.

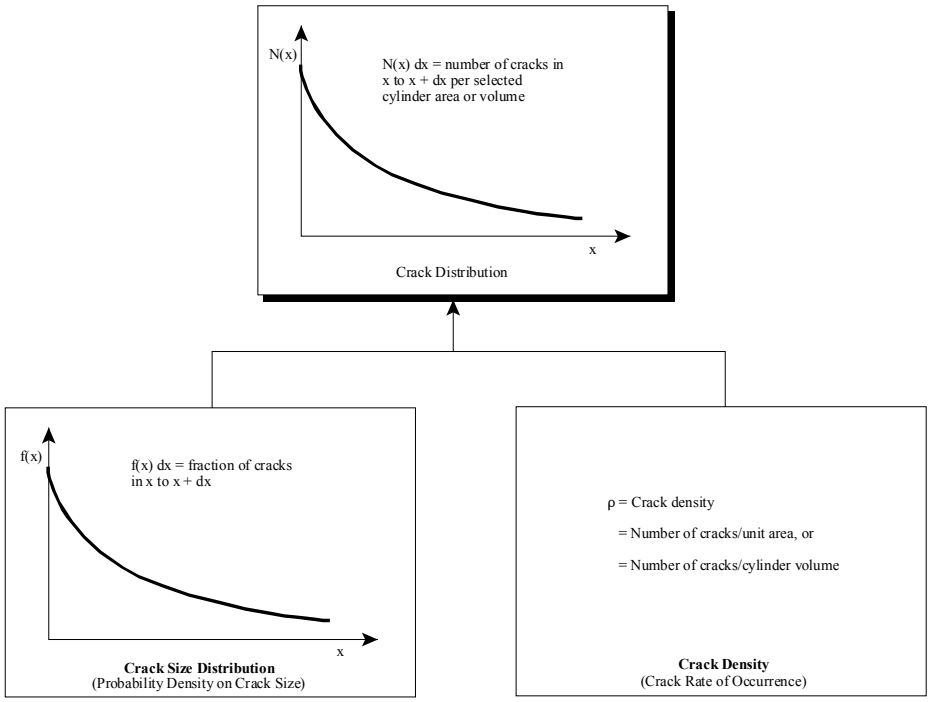

Figure 6.2 Components of the Crack Depth Distribution

The procedures that follow derive the initial crack distribution parameter in terms of its separate components. A methodology to update this distribution is also now developed.

6.1 Development of a Generic Crack Depth Distribution

The crack depth is the most important parameter when considering the corrosion-fatigue life of any component when only elastic strain loading conditions exist. Surface

length is not as significant. The initial crack depth distribution is generally estimated from non-destructive examination of cylinders coming off the production line as detailed in Chapter 1. This data is therefore subjected to a depth characteristic and a detection probability.

Information was requested from all the major manufacturers in order to determine the type of distribution that would be applicable to cracks in CNG cylinders as well as the parameters of this distribution of best fit. The information was not forth coming for this analysis from Faber or Pressed Steel Tank the major manufacturers of steel CNG cylinders. This was due to legal and propriety constraints being cited for divulging such information for this academic research. In fact, a meeting of the CSA/ANSI Technical Working Group on NGV was attended [79] with the objective of soliciting the opinion of the main participants in cylinder technology as part of an expert opinion solicitation process. This is an acceptable procedure in the absence of data in model and parameter uncertainty analysis. Invitations for such a process were declined by the experts in NGV cylinder technology. Other methods therefore, had to be resorted to in order to determine the particular distribution that best models the uncertainties associated with the existence of cracks in CNG cylinders and to estimate the parameters of this distribution.

The only published data on crack depth in manufactured components is provided in the work by Hudak of SWRI [80]. This data gives the results of observations on initial crack sizes in Inconel weldment. A lognormal distribution was found to be the best fit as

shown in Equation 6.3, with median crack depth , a_{50} , being 0.0150 inches and the shape parameter, *s*, having a value of 0.807.

$$p_0(a) = \frac{1}{sa\sqrt{2\pi}} \exp\left[-\frac{1}{2s^2}\left(\ln\frac{a}{a_{50}} \right)^2 \right] \tag{6.3}$$

Since the method of manufacturing compressed natural gas cylinders, detailed in Chapter 1, is a very different process from that which this model was derived it was not considered to be relevant. It is more relevant in repairing defective cylinders either after manufacturing or during in-service inspection. This model is used for the likelihood function in the subsequent Bayesian updating procedure for in-service inspection and repairs of existing cylinders. The application of data on crack depth distribution from one type of welding, material properties and thickness of weld-section is questionable. Some attempts will be made using the work of Chapman [81] to map the repair procedure of CNG cylinders with that of Inconel weldment.

A large number of models have been proposed in the literature to analyze pressurized vessels found in the nuclear industry. Some of them will now be reviewed for their relevance in analyzing compressed natural gas cylinders. The first such statistical model by Marshall [82] employs the exponential distribution for the marginal distribution of initial crack sizes. A model proposed by Wilson [83] based on expert judgment, also used the exponential distribution for crack depth and surface length.

Becher and Hansen [84] concluded based on inspection of weldments of reactor pressure vessels that the depth distribution was lognormal. Neilssen [85] showed that a gamma distribution fitted this same data very well. The exponential distribution which is derived from the Neilssen analysis also fits the data very well.

An analysis of various distributions used to analyze reactor data is shown in Figure 6.2 [57]. It clearly shows that the Marshall exponential distribution provides the most realistic estimate of the crack depth. It is also less conservative for small sized cracks (below 1 inch) and will be used in the succeeding analysis to represent the initial crack depth distribution.

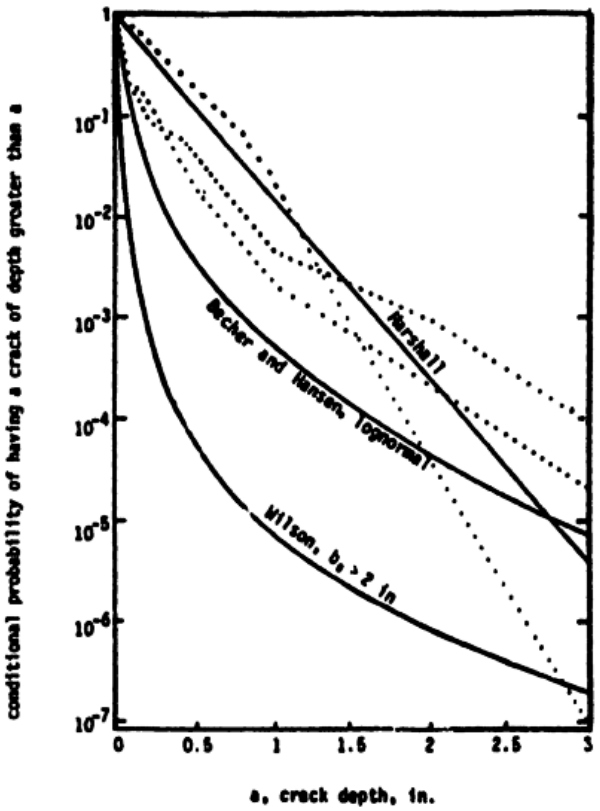

Figure 6.4 Various Complimentary Cumulative Marginal Crack Depth Distributions [57]

The exponential distribution representing the marginal distribution of the initial crack depth, has the density and cumulative distribution functions shown in Equations 6.4 and 6.5. This type of distribution has only one parameter, λ. The average crack depth μ, is given by Equation 6.6.

$$p_0(a) = \frac{1}{\mu} \exp\left(-\frac{a}{\mu}\right) \tag{6.4}$$

$$P_0(>a) = \int_a^{\infty} p_0(x)dx = \exp\left(-\frac{a}{\mu}\right) \tag{6.5}$$

$$\mu = \frac{1}{\lambda} \tag{6.6}$$

Equation 6.5 implies that cracks can be of any size from a minimum value. This technically is not possible as cracks cannot have a depth exceeding the cylinder wall thickness. To rectify this, the density function is normalized such that the probability of a crack exceeding the pipe thickness is equal to zero. That is:

$$P_0(a > t) = 1 - P_0(a \le t) \tag{6.7}$$

For this to happen, the probability of all cracks being equal to or less than t, $P_0(a \leq t)$ must be equal to 1. This is achieved by the normalization of the density function shown in Equation 6.8.

$$p_0(a) = \frac{\exp(-a/\mu)}{\mu[1-\exp(-t/\mu)]}, \quad \text{for } 0 \leq a \leq t \tag{6.8}$$

It has been discussed earlier in Chapter 6 that average crack depth in CNG cylinders resulting from the manufacturing process is not expected to exceed 5% of wall thickness. A value of 0.02 was suggested to be a realistic crack size [4]. This is what will be assigned to the expected crack depth in the typical cylinder being considered for this analysis. The distribution of initial crack depth for a typical cylinder is therefore now defined. What is left now to completely define the crack size distribution originating from the processes used to manufacture CNG cylinders is the frequency of occurrence of cracks or the crack existence frequency.

The uncertainty in the model as well as actual data to derive the parameter of the crack size distribution is a major source of uncertainty in the results of this analysis. These results have to be updated using the Bayesian methods described in Section 6.3 as soon as data becomes available.

6.2 Crack Existence Frequency

The distribution of crack depth discussed in the previous section integrates to unity. This distribution however is a conditional distribution on a crack being present. Just to reiterate, the definition of a crack here includes all defects such as voids, folds and other defects which could cause a crack to propagate under the influence of stress intensity factor as a crack driving force. Also, some defects below a certain size are not of concern because corrosion-fatigue will proceed at an infinitely slow pace. Otherwise, they are not treatable by the corrosion-fatigue crack growth model because the cyclic stress intensity factor falls below the threshold limit discussed in Chapter 3.

The crack existence frequency as shown in Figure 6.2 has two components. Firstly there is the probability of existence of cracks of a certain depth in the material coming out of the manufacturing process, and then there is the probability of detecting these cracks and characterizing their dimensions. Both are distributed quantities which will be combined in a Bayesian framework to develop the crack existence frequency.

6.2.1 Probability of Crack Existing

This section will investigate the probability associated with a crack initially existing in a cylinder coming out of the manufacturing process. Typically, the number of cracks in a component is assumed to be Poisson distributed with a mean existence of cracks specified per unit volume, area or length. Which of these are used as the reference unit is not important because large variations in the thickness of the cylinder are not

expected. Since only surface cracks are being considered, we will use unit of measure of crack existence to be per unit area of cylinder. We will also treat cracks in the sidewall and the ends including the transition region separately.

The surface area of the inside of the cylindrical portion or sidewall is given by:

$$A_C = 2\pi Rh \tag{6.9}$$

where *h* is the length of the cylindrical sidewall portion of the cylinder. Similarly for the ends and transition region the surface area is given by:

$$A_T = 4\pi R^2 \tag{6.10}$$

Since both ends of the cylinder are included the surface area of a sphere is used here and the surface areas of the hemi-spherical and flat-bottom designs are assumed to have the same surface area.

The probability of having *N* cracks assuming that the crack existence is a Poisson distribution is given by:

$$P(N) = (A\nu)^N \frac{\exp(-A\nu)}{N!} \tag{6.11}$$

where the intensity function of the Poisson distribution, rate of occurrence of cracks per unit area is given by ν ,and the area under consideration denoted by, A. The use of the Poisson distribution is justified based on the fact that if the inter-arrival crack sizes are exponentially distributed, as has been deduced to be the case for compressed natural gas cylinders, then the number of arrivals in a unit space interval are Poisson distributed [40], [71], [87]. The Poisson distribution has been recommended to model the number of defects in a batch of material or similar process [88 - 89]. This again is a source of uncertainty which has to be reduced when data becomes available.

The probability of having a crack is the compliment of not having a crack. This probability is given by Equation 6.12.

$$P_a = 1 - \exp(-A\nu) \tag{6.12}$$

By substituting into Equation 5.11 we can write the probability of having exactly one crack to be

$$P(1) = A\nu \exp(-A\nu) \tag{6.13}$$

Both expressions can be shown to be equal for very small value of the product of the area and the rate of crack occurrence, which is the expected number of cracks in A.

$$P_a = P(1) \approx A\nu, \quad \text{for} \quad A\nu << 1 \tag{6.14}$$

This shows that the probability of having a crack is approximately equal to the probability of having exactly 1 crack. Also the expected number of cracks varies linearly with the crack existence rate per unit area. We therefore need to estimate ν only, in order to describe the crack existence frequency.

As is the case with other data pertaining to cracks in compressed natural gas cylinders, no data was available in order to estimate this parameter. Other methods were therefore resorted to in order to estimate the crack existence frequency for a typical cylinder. Cracks in the base metal of steel sections used to make thin walled pressure vessels was available [90]. The bounds for high strength steel were found to be between 4×10^{-5} in^{-2} and 7.1×10^{-5} in^{-2}. It has been shown in Chapter 1 that the process used to manufacture CNG cylinders introduces defects and as such the use of results for base material not involved in any forging or other forming operations is very conservative. The upper bound value of 7.1×10^{-5} in^{-2} will be used for the crack density, in this analysis. This value of crack density is expected to be very conservative and will be treated as a deterministic value representing both the sidewalls and transition regions. The probability of a crack being present will be combined with the frequency of cylinder failure assuming a crack is present to get the unconditional frequency of cylinder failure, in Chapter 9 of Part III.

The probability distribution of a crack being initially present in the cylinder after manufacturing is now fully developed. The distribution of the crack as originating from

the manufacturing process will now have to be combined with the probability of detection of such a crack using the available ultrasonic inspection technology in order to completely define the existence frequency of cracks in a typical cylinder. This will be further combined with the crack distribution to develop the initial crack distribution. This is what will be fed into the crack growth model previously developed.

6.2.2 Probability of Crack Detection

Extensive research by Pacific Northwest National Laboratory (PNNL) [91], under funding from U.S. Nuclear Regulatory Commission (NRC) has established the distribution and parameters for crack detection in base metal of austenitic piping used in nuclear power plants. Data on the probability of detection of crack like flaws using ultrasonic inspection has also been reviewed by Harris [92 - 94] on ferritic piping. Research work by the Plate Inspection Steering Committee [95] has also provided data on the probability of non-detection of a crack like defect as a function of the defect depth.

The material of construction of CNG cylinders is banitic or martensitic, these results will still be helpful in estimating the probability of detection of representative crack sizes in CNG cylinders. The micro-structure of the steel should have no effect on the reliability of the ultrasonic inspection process.

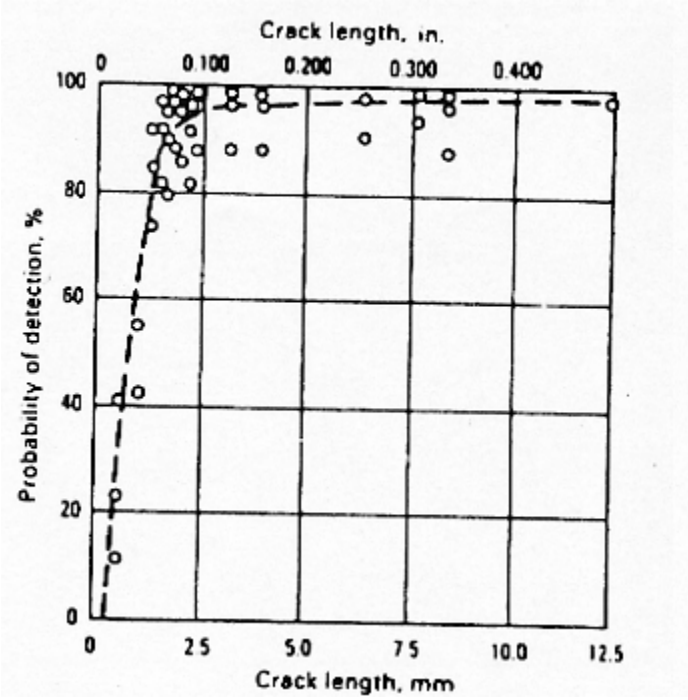

Figure 6.5 Probability of Crack Detection Using Ultrasonic Inspection Technique [96]

Figure 6.5 shows the probability of detection of cracks using ultrasonic inspection under controlled testing conducted by Rummell et al. [96]. From this and other data referenced above a lognormal distribution was found to be the best fit for the probability of non-detection of a crack of a given size, P_{ND}. Based on these data, a lognormal relation as shown in Equation 6.15 was found to be adequate to mathematically model P_{ND}.

$$P_{ND}(a) = \frac{1}{2}\operatorname{erfc}\left[s \ln\left(\frac{a}{a_{ND}}\right)\right] = \frac{1}{\sqrt{\pi}} \int_{s \ln\left(\frac{a}{a_{ND}}\right)}^{\infty} \exp\left(-\xi^2\right) d\xi \qquad (6.15)$$

where a_{ND} is the crack depth that has a 50 % chance of being detected and *s* is the shape parameter of the lognormal density function. The most reasonable values of the parameters based on best fit of all the available data [57] was:

$$a_{ND} = 0.35 \tag{6.16}$$

$$s = 1.46 \tag{6.17}$$

6.3 Generic Initial Crack Distribution

The "as-fabricated" crack depth distribution will now be combined with the probability of detection to determine the post-inspection crack distribution. Bayesian procedures will be used to update the "as-fabricated" crack distribution. By using Bayes theorem the posterior distribution or the detected crack size distribution is:

$$p_D(a/\lambda) = \frac{P_D(a)p_0(a/\lambda)}{\int_0^\infty P_D(a)p_0(a/\lambda)da} \tag{6.18}$$

where,

$p_D(a/\lambda)$ = the distribution of detected crack depth after ultrasonic inspection.

$p_0(a/\lambda)$ = the prior or the as fabricated crack depth distribution.

$P_D(a)$ = the probability of detecting a crack as a function of its depth.

$\int_0^\infty P_D(a)p_0(a/\lambda)da$ is a normalizing constant such that the posterior distribution remains a density function. That is so that

$$\int_0^\infty p_D(a/\lambda)da = 1 \tag{6.19}$$

The crack depth distribution parameter λ, is itself considered to be a random variable that has a gamma distribution. The probability density function would then be:

$$p(\lambda)' = \frac{b(\lambda b)^{k-1}}{\Gamma(k)}\exp(-\lambda b) \tag{6.20}$$

The parameters of the gamma distribution can be evaluated using methods of moments by equating the postulated mean and variance with the mean and the variance of the gamma distribution. The mean crack depth was previously determined to be 0.02 inches. The variance of λ is assumed on the basis of the degree of certainty on the value of λ. Using engineering judgment of the variation expected in a typical CNG cylinder crack, a standard deviation of 20 % of the mean was felt to be a good description of the degree of uncertainty on the crack depth. This is an acceptable degree of uncertainty based on the variation in the average crack depth that is possible [33]. The parameters can be evaluated from the following:

$$\frac{k}{b} = \frac{1}{0.02} = 50 \tag{6.21}$$

$$\frac{k}{b^2} = \left(\frac{0.2}{0.02}\right)^2 \tag{6.22}$$

Solving the simultaneous equations we get

$$k = 25 \tag{6.23}$$

$$b = 0.5 \tag{6.24}$$

This defines the prior distribution of the parameter of the crack depth distribution, p'(λ).

Testing done on used CNG cylinders have suggested that crack sizes of 5% [4], 7% [7] of thickness are acceptable for service. It has also been recommended that crack depth of 15% is acceptable if Acoustic Emission (AE) testing is done every five years [97]. Crack of these sizes have been found in cylinders tested [97]. The likelihood of detecting three cracks with the depths shown above is:

$$L(a_{0.05}, a_{0.07}, a_{0.15} / \lambda) = L(a_m / \lambda)$$

$$L(a_m / \lambda) = \prod_{a_m} p_D\left(a_m / \lambda\right)$$

The posterior distribution of the crack depth distribution parameter, *p″(λ)*, using the Bayes updating procedure again is:

$$p''(\lambda) = \frac{L(a_m/\lambda)p'(\lambda)}{\int_0^{\infty} L(a_m/\lambda)p'(\lambda)} \tag{6.25}$$

The updated mean value of the crack depth distribution function parameter is given by:

$$\overline{\lambda''} = \int_0^{\infty} p_0(a/\lambda)p''(\lambda)d\lambda \tag{6.26}$$

Similarly the non-conditional posterior crack distribution can be computed from:

$$p_0(a) = \int_0^{\infty} p_0(a/\lambda)p''(\lambda)d\lambda \tag{6.27}$$

The non-conditional crack depth distribution can be used as the initial crack depth distribution. We could also use the updated mean value of the crack depth distribution parameter and assume that the exponential distribution still applies. This would then be the used as the initial crack size distribution.

The posterior distribution of detected crack depth and detected crack depth parameter distribution can only be determined by numerical integration as the lognormal distribution for the likelihood of detecting a crack, as a function of its size is not conjugate with the exponential prior distribution. This is the procedure that will be used.

This updated average crack size will be used in the statistical distribution of initial crack sizes as detected from inspection.

6.4 Development of Crack Distribution from Inspection and Repairs

6.4.1 Crack Depth Distribution Function

The initial crack distribution can be developed from in-service inspection and repair data. This is in contrast to using a postulated prior distribution when inspection data was not available as was described in sections 6.1 to 6.3. The procedure developed is shown schematically in Figure 6.6.

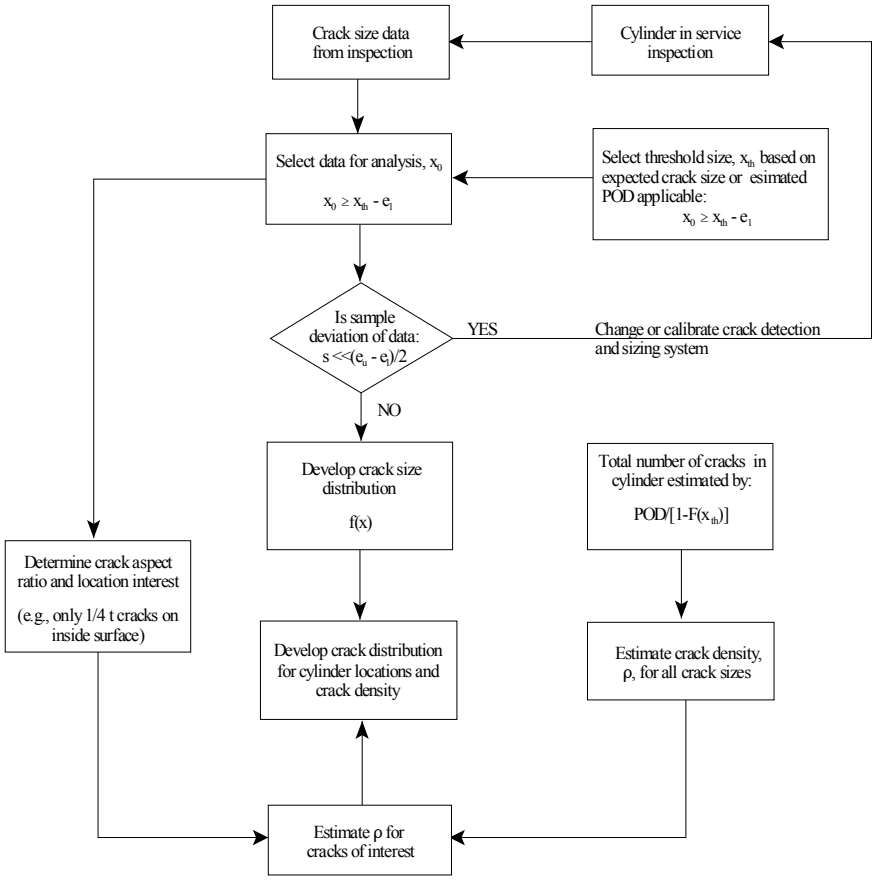

Figure 6.6 Procedure for Initial Crack Size Determination From Inspection

The crack depth, *x*, is considered to be a random variable that can be fitted to a parametric probability distribution density function which adequately accounts for the uncertainties in the observed crack size data. This distribution then describes the probability density on crack sizes. The crack density is subsequently determined from the observed number of cracks and the fraction of total cracks as predicted from the crack size distribution in the observed size range.

The following are the important items that will be determined from the inspection data:

1. The probability density function of crack size in terms of depths measured, f*(x)*.

2. The crack density, ρ, which essentially determines the expected number of cracks found in the two separate sections of the cylinder being considered, namely the transition region and the sidewall, per unit area. This can be considered to be deterministic in nature if the manufacturing process is well established and not too much variation exists from one batch to another.

Weibull distribution is chosen to describe the initial crack sizes found from ultrasonic inspection of CNG cylinders. The parameters of this distribution are α and β, usually called the scale and shape factors respectively.

A number of assumptions are made about the true population of cracks in evaluating the parameters of the distribution. These assumptions should not have significant effect on the accuracy of the results because of the physics of the crack initiation, propagation and growth. The main assumptions are:

- The cracks in each section of the cylinder are from a homogenous population with a single true crack distribution. This approach recognizes the non-homogenous nature of the different cylinder sections described earlier if all cracks were considered together.

- The crack size, X, in each section is follow a Weibull distribution, the parameters of which can be derived from the individual crack data available for each section.

- Ultrasonic inspection used to detect the cracks has a low limit crack size that cannot be detected with the available technology. Above this crack size all other cracks has a constant probability of detection (POD) which is independent of the crack size.

- Observed crack sizes from ultrasonic inspection includes an additive error, *E*, due to the instrument calibration. This error is uniformly distributed between the calibration ranges, e_l and e_u, which represents the lower and upper limits of the calibration for each crack dimension. This calibration is constant for each crack size with no bias towards under-sizing or over-sizing.

The Weibull distribution of the crack size, X, is given by the probability density function,

$$f(x) = \frac{\beta}{\alpha^{\beta}} x^{\beta-1} e^{\left(-\frac{x}{a}\right)^{\beta}}, \quad \text{for } x \geq 0 \tag{6.28}$$

The corresponding cumulative distribution function is given by:

$$F(x) = 1 - e^{\left(-\frac{x}{a}\right)^{\beta}}, \quad \text{for } x \geq 0 \tag{6.29}$$

This distribution is for the true crack size that exists in the cylinder either after manufacturing or during the course of its usage on the NGV. This has to be modified to account for the observation of the cracks by ultrasonic detection during routine NDE inspection.

The minimum flaw size assumed to be detectable for this to be a true density function is 0. There is a limit to the capability of the UT equipment in detecting cracks. This minimum detectable size is called x_{th}. The density function above is therefore normalized with respect to the actual cumulative probability distribution function. This normalizing constant, *K*, is given by

$$K = \frac{1}{1 - F(x_{th})} \tag{6.30}$$

This gives

$$K = e^{\left(\frac{x_{th}}{a}\right)^{\beta}} \tag{6.31}$$

The function for the detectable crack size truncated at the lower limit and normalized to be a density function is given by

$$f(x) = \begin{cases} K \dfrac{\beta}{\alpha^{\beta}} x^{\beta-1} e^{\left(-\frac{x}{a}\right)^{\beta}}, & \text{for } x \geq x_{th} \\ 0, & \text{elsewhere} \end{cases} \tag{6.32}$$

The density function, $f(x)$, represents the detectable crack size distribution.

All that is left now is to account for the probability of detecting a crack using the available technology. This is the reliability of the crack detection process referred to as the probability of detection, *POD* with its complimentary function, P_{ND} and P_{ND}. The P_{ND} is affected by the sensitivity of the inspection instrumentation, the inspection process and the skill of the operator. The P_{ND} consideration has two components.

Firstly, the crack size distribution is the actual size of the crack observed, given the inherent instrument measurement error, called the calibration error. The bias for UT instruments is additive in nature and the true reading is uniformly distributed between some lower value, e_l and the upper value, e_u, in the vicinity of the true readings respectively. This range is dependent on the instrument calibration error. This uniform distribution can be represented as $f_E(e)$**.** Two important considerations about the calibration error are as follows:

- This uniform distribution, $f_E(e)$ is not a function of the crack size and each crack size is assumed to be equally affected by the calibration error.
- The shape and form of the actual crack size distribution itself is not affected by the calibration error

The second component is the probability of detecting a crack in the range that the instrument is capable and calibrated to detect cracks, P_D. It is dependent on the sensitivity of the instrument setup to detect crack sizes that are considered fracture

mechanics important and the skill of the operator. This probability is assumed constant for each crack size but is a function of the cracks sizes. The total crack count and the density or rate of occurrence per unit area is proportionately affected by P_D.

Both cases are now discussed in the following section.

6.4.2 Crack Size Error Correction

The crack size that is observed consists of the actual crack size and an additive error, *E*. This additive error will result in an observed crack size that is uniformly distributed between the actual size and an upper and lower value. The joint probability density function of observed crack size, *X*, given the instrument error, *E*, is shown in Equation 6.33.

$$g(x/E) = g[f_x(x) f_E(e)] \tag{6.33}$$

where

$f_E(e)$ is the error distribution of the instrument

$f_X(x)$ is the distribution of actual crack sizes

The likelihood of observing a randomly distributed crack of size, *x*, is known to be approximately uniformly distributed [98] in the calibration range given by, e_l and e_u, representing the lower and upper calibration limits respectively. The probability density function considering the error is given by:

$$f_E(e) = \begin{cases} \dfrac{1}{e_u - e_l}, & \text{for } e_l \le e \le e_u \\ 0, & \text{for all other values of } e \end{cases} \tag{6.34}$$

We have determined before that the crack size distribution is the truncated Weibull distribution given by Equation 6.35.

$$f_X(x_0) = \begin{cases} K\dfrac{\beta}{\alpha^\beta} x^{\beta-1} e^{-\left(\frac{x}{a}\right)^\beta}, & \text{for } x \ge x_{th} \\ 0, & \text{otherwise} \end{cases} \tag{6.35}$$

For an observed crack X_o, to make the transform to the actual crack size we introduce a random variable, *W*, then

$$X_0 = W + E \tag{6.36}$$

where

E = calibration error

W = *X*, the actual crack size

Assuming that the error distribution function and the crack size function are independent, then the joint probability density function of observed crack size given the actual crack size,

$$g(x_o/w) = f_E(e) f(w) \tag{6.37}$$

Substituting for $f_E(e)$ and $f(w)$ into Equation 6.37, the joint probability density function is evaluated to get,

$$g(x_0/w) = \frac{K}{e_u - e_l}\frac{\beta}{\alpha}\left(\frac{w}{a}\right)^{\beta-1} e^{-\left(\frac{w}{a}\right)^{\beta}} dx_0\, dw, \quad \text{for } x \geq x_{th},\ e_l \leq e \geq e_u \tag{6.39}$$

$$g(x_0/w) = \frac{K}{e_u - e_l}\int_{x_{th}}^{\infty} \frac{\beta}{\alpha^{\beta}} x_0^{\beta-1} e^{-\left(\frac{x_o}{a}\right)^{\beta}} dx \tag{6.40}$$

The marginal distribution in X_o alone is obtained by integrating the joint distribution with respect the other variable, W, for all possible values. The marginal density function is given by

$$h(x_0/w) = \int_V g(x_0/w)dw \tag{6.41}$$

$$h(x_0/w) = \int_0^{\infty} \frac{K}{e_u - e_l}\frac{\beta}{\alpha}\left(\frac{w}{a}\right)^{\beta-1} e^{-\left(\frac{w}{a}\right)^{\beta}} dw \tag{6.42}$$

$$h(x_0/w) = \frac{K}{e_u - e_l}\int_0^{\infty} \frac{\beta}{\alpha}\left(\frac{w}{a}\right)^{\beta-1} e^{-\left(\frac{w}{a}\right)^{\beta}} dw \tag{6.43}$$

Remembering that, w, is the actual crack size and that detectable crack size using ultrasonic inspection is, x_{th}, in evaluating the interval we would therefore have to take that into account. The actual crack size distribution has been truncated at x_{th}, as shown previously in Equation 6.35. To account for the calibration error, readings observed at the threshold can be anywhere in the interval:

$$x_{th} - e_l \leq x_0 \geq x_{th} + e_u \tag{6.44}$$

The integral has to be evaluated with the respective interval as shown:

$$h(x_0/w) = \frac{K}{e_u - e_l} \int_{x_{th}-e_l}^{x_{th}+e_u} \frac{\beta}{\alpha}\left(\frac{w}{a}\right)^{\beta-1} e^{-\left(\frac{w}{a}\right)^{\beta}} dw, \quad \text{for } x_{th} - e_l \leq x_0 \geq x_{th} + e_u \tag{6.45}$$

and

$$h(x_0/w) = \frac{K}{e_u - e_l} \int_{x_{th}-e_l}^{x_{th}+e_u} \frac{\beta}{\alpha}\left(\frac{w}{a}\right)^{\beta-1} e^{-\left(\frac{w}{a}\right)^{\beta}} dw, \quad \text{for } x_{th} + e_u \leq x_0 \geq \infty \tag{6.46}$$

A review of UT inspection data derived in controlled tests have shown that crack size error (e_u-e_l) and error distribution $f_E(e)$ is largely invariant with crack size for the same UT system [98 - 99]. Once we have accounted for the probability of detecting a crack, in the observed crack size function, $h(x_o / w)$, then the problem then reduces to determining

the values of the parameters α and β that will maximizes this function. Evaluating the intervals and substituting for the actual crack sizes limits and *K* we get:

$$h(x_0/\alpha,\beta)=\frac{\exp(x_{th}/\alpha)^{\beta}}{e_u-e_l}\, e^{-\left(\frac{x_{th}-e_l}{\alpha}\right)^{\beta}}-e^{-\left(\frac{x_{th}+e_u}{\alpha}\right)^{\beta}} \quad \text{for } x_{th}-e_l \le x_0 \ge x_{th}+e_u \quad (6.47)$$

and

$$h(x_0/\alpha,\beta)=\frac{\exp(x_{th}/\alpha)^{\beta}}{e_u-e_l}\, e^{-\left(\frac{x_0-e_l}{\alpha}\right)^{\beta}}-e^{-\left(\frac{x_0+e_u}{\alpha}\right)^{\beta}} \quad \text{for } x_0 \ge x_{th}+e_u \quad (6.48)$$

Equations 6.47 and 6.48 define the depth distribution of cracks given that a crack is present in the cylinder. The conditional distribution of crack size is therefore now defined. What remains in completely defining the initial crack size distribution is the probability that a crack is initially present and detected. Combining both will give the distribution of initial crack size in the cylinder either originating from the manufacturing process or shortly after being put into service.

6.4.3 Crack Frequency of Occurrence

The number of cracks detected as a result of UT inspection of the cylinder per unit volume is given by *n*. The actual number of flaws in the detectable range in the cylinder based on the reliability of the instrument, n_a, is given by

$$n_a = \frac{n}{P_D} \tag{6.49}$$

Some of the cracks will be missed by the instrument if they fall below the threshold range, x_{th}. The total number of cracks including those that are outside the calibration range of the instrument and therefore cannot be detected is, n_t, is given by

$$n_t = \frac{n_a}{\int_{x_{th}}^{\infty} f(x)dx} \tag{6.50}$$

$$n_t = \frac{n_a}{\int_{x_{th}}^{\infty} \frac{\beta}{\alpha^{\beta}} x^{\beta-1} \exp\left[-\left(\frac{x}{\alpha}\right)^{\beta}\right] dx} \tag{6.51}$$

Evaluating this integral with the maximum likelihood values of the parameters of the distribution, and β will give us the total number of cracks in the cylinder. Dividing this result by the respective surface area of the cylinder segment under consideration, will give us the crack existence frequency, ρ.

$$\rho = \frac{n_t}{A} \tag{6.52}$$

The probability of a crack being present is assumed to be controlled by the surface area of the section of the cylinder being considered and is different for the three sections considered, namely; inside sidewall, outside sidewall and transition regions of top and bottom. The thickness of the cylinder does not impact on the crack existence probability.

The probability of having N cracks in a section area of A is a Poisson distribution and is given by [100] the following expression.

$$P(N) = (\rho A)^N \frac{\exp(-\rho A)}{N!} \tag{6.53}$$

The crack existence probability is equal to one minus the probability that no crack exist. This is given by the expression:

$$p = 1 - \exp(-\rho A) \tag{6.54}$$

This is approximately equal to:

$$p \approx \rho A \tag{6.55}$$

By similar reasoning, the probability of having exactly one crack is equal to:

$$P(1) = (\rho A)\frac{\exp(-\rho A)}{N!} \tag{6.56}$$

If *pA* is very small then this reduces to the expression

$$P(1) \approx \rho A \tag{6.57}$$

This shows that the crack existence probability is equal to the probability of having one crack, which can be evaluated from the crack density expression in Equation 6.52, if the number of cracks and the surface area under consideration is known.

For the Weibull distribution the mean and variance are given by Equations 6.58

$$\mu_{X_N} = \alpha\,\Gamma\left(1+\frac{1}{\beta}\right)$$
$$\sigma^2_{X_N} = \alpha^2\left[\Gamma\left(1+\frac{2}{\beta}\right)-\Gamma^2\left(1+\frac{1}{\beta}\right)\right] \qquad (6.58), (6.59)$$

The method of maximum likelihood estimation (MLE) [40] can be used to estimate the parameters of the Weibull distribution. The assumed Weibull function is evaluated to obtain the values of the parameters which would maximize this function for the data collected on crack sizes present in the cylinder. Based on the data the Likelihood of the data found is given by

$$L(\alpha,\beta; x_{01}, x_{02}, x_{03}, \ldots, x_{0n}) = L(x_{01})L(x_{02})L(x_{03})\cdots L(x_{0n}) \qquad (6.60)$$

assuming that the process of generating each data-set is independent. This value of the total likelihood is maximized with respect to the parameters α and β.

6.4.4 Crack Distribution with Repairs

The crack depth distribution after welding repairs is similar to the procedure used to develop the initial crack distribution in Section 6.3. The main difference is that a lognormal distribution will be used for the prior crack distribution as given by Equation 6.3. The parameters for this distribution can be evaluated if data exist on the number of cracks in cylinders after being weld repaired. In the absence of data the weld defects and

variables considered in the Chapman Model [81] can be used to map the welding procedure, base material and type of defect to derive the model parameters. A summary of the variables are shown in Figure 6.7.

The detailed mapping procedure will not be attempted here. This procedure is similar to that done in the Nuclear Industry when data is not available in quantitative modeling exercises [101]. Essentially a probabilistic judgment is made on the applicability of each variable when welding Inconel tubes to CNG cylinders. The probabilities are aggregated for all the variables and the factor derived can be used to update the prior distribution of weld defects by using Bayes theorem. The likelihood function would be the cumulative distribution that best represents the mapping results.

A methodology has been developed for the estimation of the generic initial crack distribution and procedures described for developing this distribution from inspection results after manufacturing, in-service or after repairs. The generic initial crack size distribution will be used in the crack growth life model.

Process	Manual Metal Arc Submerged Arc Autogenous Manual TIG Manual TIG with Filler Autogenous Automatic TIG Automatic TIG with filler Autogenous EB/Laser Short Circuiting Dip MIG		
Joint Geometry	E.B Insert Single Pass Open Root		
Restraint	High Medium Low		
Material	Carbon or CMn Steel Low Alloy Steel Austenitic Ferrite Uncontrolled Stainless Ferrite Uncontrolled Martensitic and Ferritic Stainless Monel Cupronickel Nickel Alloys		
Location	Work Shop Subassembly Site Subassembly Site Weld		
Position*	1G (Down Hand) 2G (Horizontal/Vertical) 3G (Vertical Up) 3G (Vertical Down) 4G (Overhead) 5G (Horizontal Fixed Pipe) 6G (45° Fixed Pipe)		
Access	Good Average Restricted		
TYPE OF DEFECT			
Centre Cracks	HAZ Cracks	Lack of Fusion	Pores with Tails

Figure 6.7 Summary of Weld Variables and Defects Considered In Chapman Model

CHAPTER 7: CYLINDER FREQUENCY OF FAILURE NUMERICAL PROCEDURES

Numerical methods are required to evaluate the probability of failure due to the distributed nature of the crack size and the complicated nature of the stress history. The need to use numerical procedures is even more evident because the input parameters to the crack growth relationship are random in nature and as such have to be sampled at intervals. A random crack is sampled from the initial crack distribution. This crack is then grown using numerical integration until leakage occurs by the crack growing through the sidewalls or due to unstable crack which growth causes rupture. The parameters of the fatigue crack growth relationship are distributions and are sampled, employing the same kind of sampling scheme, as with the initial crack size distribution. At each stage of crack growth the crack length and depth are checked using the fracture criterion to determine if rupture is likely to occur. If none of the criterion suggest that the crack will become unstable crack growth will continue until it grows through the sidewall and leakage occurs. The number of filling cycles to cause rupture or leakage is noted within the useful life of a cylinder and is expressed as the number of cycles to failure.

The probability of a leak or complete rupture of a CNG cylinder is equal to the probability of cracks with depth larger than the wall thickness, or cracks larger than the critical size for one of the unstable crack growth criterion selected. In the case being considered for corrosion fatigue crack growth, the factors that define the physical model

are described by parameters which are random variables. Some form of numerical scheme is required.

Monte Carlo simulation is the numerical technique that is used in light of its simplicity and its computation appeal. Other techniques using variance reduction techniques such as Latin Hypercube sampling could have been used to improve the efficiency of the calculations and the accuracy of the results for the number of iterations used. The procedure for using Monte Carlo simulation to estimate the frequency of occurrence of failure within the specified lifetime of a typical cylinder can be done by randomly selecting a crack, based on the crack size distribution. The probability of selecting a given crack is controlled by the generic initial crack size distribution and the probability of detecting this size crack. This crack is then grown through a stress history or several cycles of filling and emptying the cylinder using the corrosion-fatigue crack growth relationship. Values of the parameters of the crack growth relationship are randomly selected from the uncertain distributions of these parameters, and used in the crack growth calculations. The crack growth occurs in increments and the crack size at the end of each interval is compared with the critical crack size. Failure is deemed to occur if unstable crack growth is predicted by any of the failure criterion or the crack grows through the wall of the cylinder. The number of cycles to rupture or leakage is noted for the development of a distribution of the number of cycles to failure.

Sampling is performed a large number of times using a code written in the symbolic computational software MATHCAD. Statistics are gathered on the number of cycles to failure. A cumulative distribution as well as a density function is developed. The frequency of postulated failure, whether leakage or rupture, can be determined from the cumulative distribution, for any number of cycles considered to be in the useful life range of for a typical cylinder. The probability that failure occurs at or before the number of cycles, N_l, can be expressed as follows:

$$P(N_f \le N_l) = \frac{N_f^*}{N} \tag{7.1}$$

where N_f is the number of cycles (or time) to failure, N_f* is the number of simulations that predict that a failure will occur and N is the total number of iterations.

To improve computational efficiency the assumption is made that if multiple cracks are present in the cylinder, they do not coalesce but grow independently to cause failure. With this assumption the result obtained above for a single crack is approximately equal to the result if several cracks are present. We can therefore ignore the probability of failure conditioned on the number of cracks present in the section of the cylinder under consideration, and compute this probability on the basis of a single crack resulting in a failure. This completes the procedure for the determination of the frequency of failure of a typical compressed natural gas cylinder. A summary of the other assumptions follow that were necessary follows in Section 7.1.

The generic initial crack distribution will be developed using the Bayesian procedure detailed in Chapter 6. This initial crack distribution will be one of the inputs to the sampling scheme and as such will be calculated first before the frequency of failure is determined. The structure of the Monte Carlo scheme will be described and the results calculated will be presented. A summary of all the assumptions used in the numerical procedure are detailed below.

7.1 Summary of Numerical Procedures Assumptions

In order to understand the results of this analysis and to define the quality of the prediction as well as identify areas for future research, the major assumptions are summarized below as follows:

a) Micro-cracks are present in the cylinder as a result of the manufacturing process and these will propagate by corrosion fatigue to failure.

b) The cylinders will operate in an environment where contaminants are present in such quantities that the partial pressures present will cause corrosion fatigue to be an important failure mechanism.

c) Cylinder life is controlled by corrosion fatigue only.

d) Fatigue crack growth data previously obtained is relevant and applied to the assumed filling rates of CNG vehicles of 0.05 Hz.

e) Refueling is done at 2 cycles/day for 365 days for the life of vehicle.

f) Pressurization is between 300 at empty and 3000 psi when cylinder is full.

g) Variation in the stress amplitude associated with the filling and utilization of CNG between cycles is not taken into consideration.

h) Fatigue life is controlled by crack growth through the sidewalls or ends including the transition region and crack can grow from outside in or vice versa.

i) The growth rate of each crack is not affected by the presence of other cracks and the cracks do not coalesce to form a single larger crack.

j) The crack growth law will be assumed to apply to cracks partially and even completely through the wall of the cylinder

The two failure modes considered in this analysis are cylinder leakage and cylinder rupture. These will be evaluated separately. Crack growth can occur from the inside surface or from the outside. We have determined that inside surface cracks will most likely cause a failure due to the presence of a higher crack driving force. The result for both inside and outside surface cracks will be computed in order to confirm this hypothesis.

7.2 Generic Initial Crack Size Distribution

The prior initial crack distribution described in Chapter 6, consist of the initial crack depth distribution updated by the inspection probability of detection using Bayesian methods. This is further updated to get the generic posterior distribution of the initial crack depth. The average value of this distribution is used in the assumed exponential

distribution of the initial crack depth, to give the initial crack distribution. The procedure to numerically integrate the product of the likelihood function and the prior distribution was discussed in Chapter 6. This routine is written in MATHCAD.

The limits of the numerical integration were adjusted to improve the convergence of the results. Upper limit of infinity caused some convergence problems so an "if statement" was inserted to adjust the upper limit of the integration to a large enough value to ensure that the integration covered as much area under the curve as is possible while avoiding the computational difficulties. The prior and posterior distributions of the initial crack size parameter are shown in Figure 6.1. The crack depth parameter distribution was updated by the probability of detection distribution given by Equation 6.15 and crack size results that was reported in the literature [3 - 4], [7], [74]. The crack size distribution is exponentially distributed, and the average parameter from the Bayesian updating will be used. The result is given by Equation 7.2 and will be used in the crack growth relationship.

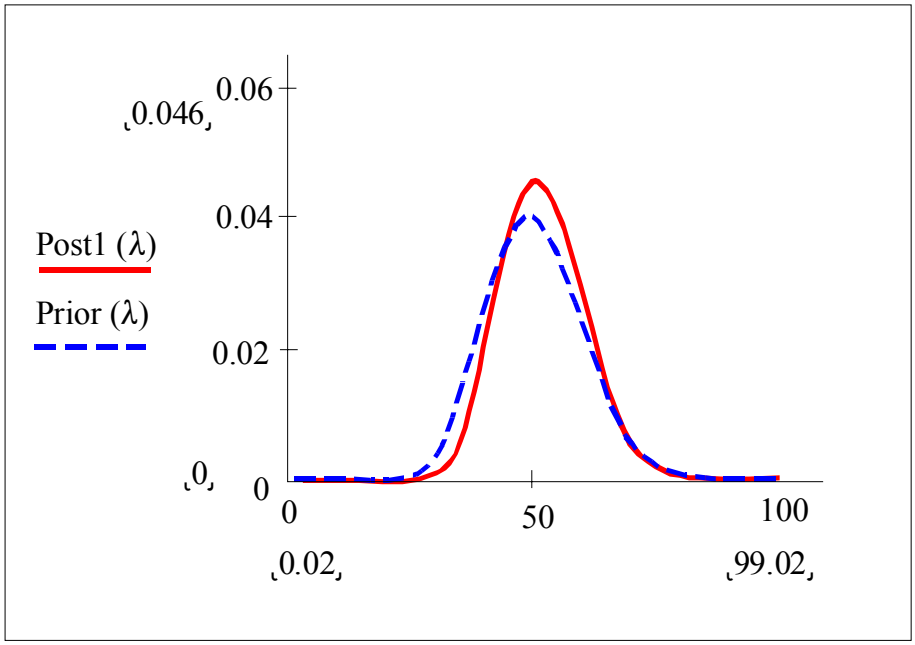

Figure 7.1 Updated Crack Depth Parameter Distribution

$$f(a_0) = 54.67 \exp(-54.67*a) \tag{7.2}$$

7.3 Monte Carlo Simulation Procedure

The procedure to compute the frequency of occurrence of cylinder failure was coded in MATHCAD. A simplified flow chart of the procedure is shown in Figure 7.2. Steps involved in the procedure include setting up the numerical scheme in terms of the number of trials and using Simpson Rule [102] to perform the crack growth. The basic steps in the process are summarized as follows:

1. Select the number of trials (iterations) and the number of crack growth increments. The larger the number of iterations and crack growth increments, the

more accurate the results.

2. Select the initial crack size from the crack size distribution using a random number generator to select the probability to be sampled.
3. Perform the crack growth through the assigned crack growth increments using Simpson Rule.
4. Check the crack at each growth step for failure whether through leakage or rupture.
5. Aggregate the iterations that result in each failure type and develop distributions of each. This is then used to determine the frequency of cylinder failure from the postulated useful life.

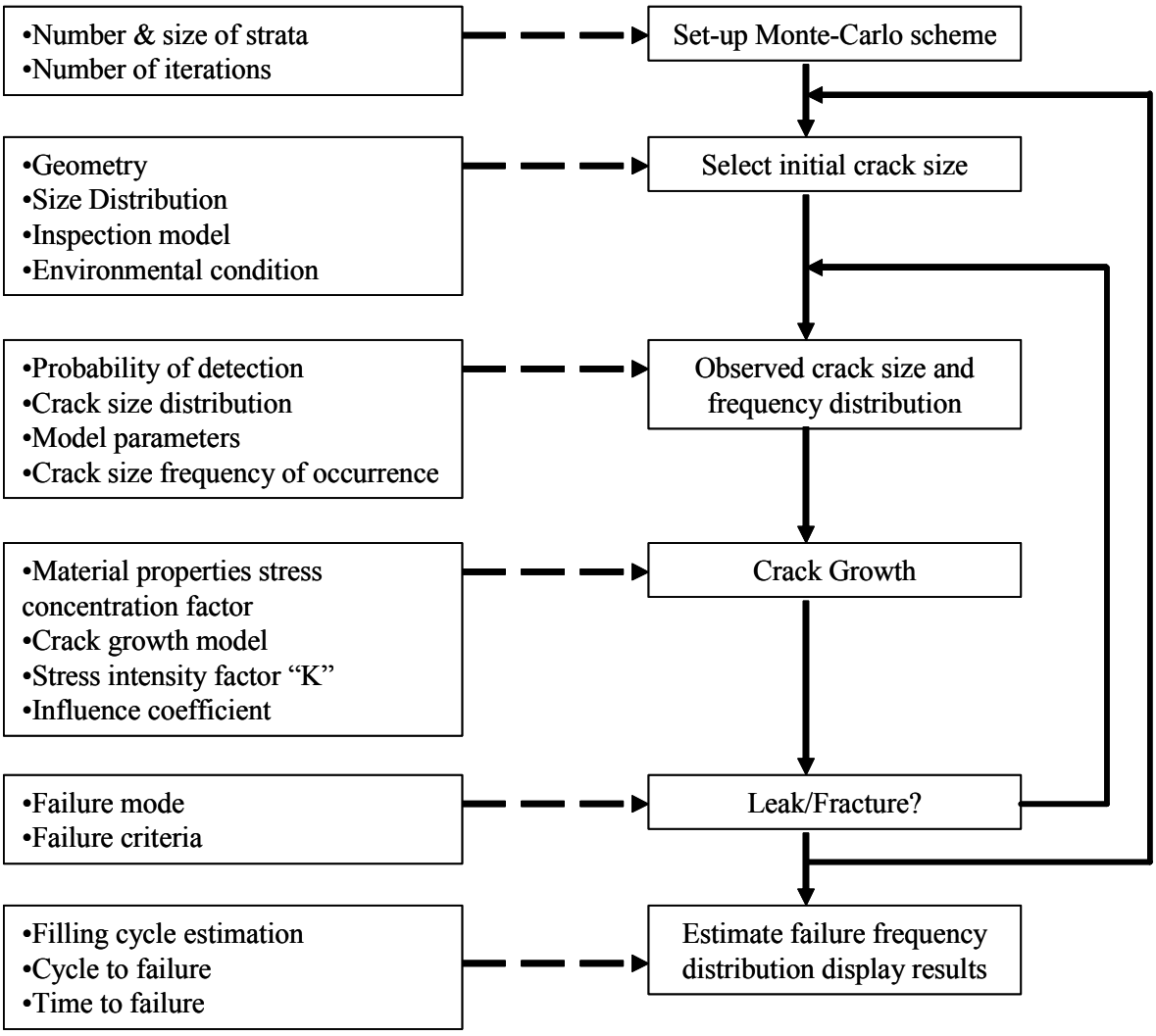

Figure 7.2 Flow Chart of Numerical Procedure

The numerical procedure is subject to the limitations and assumptions accepted for the crack growth model and the fracture criterion chosen. The process is limited to single cracks in a CNG cylinder that grows to become unstable causing rupture or through the wall causing leakage. The calculation steps are now described in some detail with some of the key results.

7.4 Sampling Scheme Definition

The crack size distribution is represented by the crack depth *a*, with the aspect ratio, assumed to be a deterministic quantity to include a wide range of crack shapes as is computationally possible. The crack depth can take values between 0 and the wall thickness of the cylinder *t*. The aspect ratio can take values of 1 representing a semi-circular crack the half length equal to the wall thickness at leakage, 0.2 and 0.4 representing a much sharper crack profile. The stress intensity factors for all three aspect ratios will be computed and the profile predicting the highest value will be used in the corrosion-fatigue crack growth calculations. Crack shape is expected to remain semi-elliptical even when leakage has taken place.

The generic initial crack size is chosen based on the probability of occurrence based on the crack size distribution and the Monte Carlo sampling scheme. Since most of the cracks that exist in the cylinders will not result in leakage of a cylinder within some reasonable lifetime, stratification schemes would be useful to improve the efficiency of sampling procedure. Once such method is the variance reduction technique used is the stratified sampling method. This method will be used in the future to improve the accuracy of the results and to improve the computational efficiency.

For the Monte Carlo simulation procedure, the number of trials selected was $5x10^5$. This large number of trials while it was time consuming to calculate gives a reasonable probability of the likely occurrence leakage or rupture. Each selected crack

size was broken down into 50 increments and the numerical integration performed to determine the number of cycles required for this crack growth increment. The total number of cycles to failure is the summation of the incremental crack growth cycles.

7.5 Corrosion-Fatigue Crack Growth Computation Procedures

Crack growth calculations were performed for typical cylinder geometry for cracks occurring on the inside as well as the outside of the transition regions and sidewalls of both the flat-bottom and the hemi-spherical designs. The results for both designs and location of the crack are compared in analyzing which cylinder type is more susceptible to failure. Crack growth calculations will be performed using the deterministic model and compared with the results from the probabilistic model to show the superiority of this model in calculating the frequency of failure of CNG cylinders.

The routine coded in MathCAD consist of the six basic steps shown below:

1. Select a crack size from the initial crack distribution
2. Calculate the corresponding value of the cyclic stress intensity factor for the three possible crack shapes.
3. Identify the crack shape which gives the highest stress intensity factor.
4. Evaluate the number of cycles through each increment of crack growth assuming constant cyclic stress intensity factor.
5. Determine whether crack growth will lead to rupture or leakage and the number of cycles leading to failure.
6. Plot a histogram of the number of cycles leading to rupture and leakage.

A flow chart of the algorithm used in the crack growth calculations and subsequent determination of failure is shown in Figure 7.3.

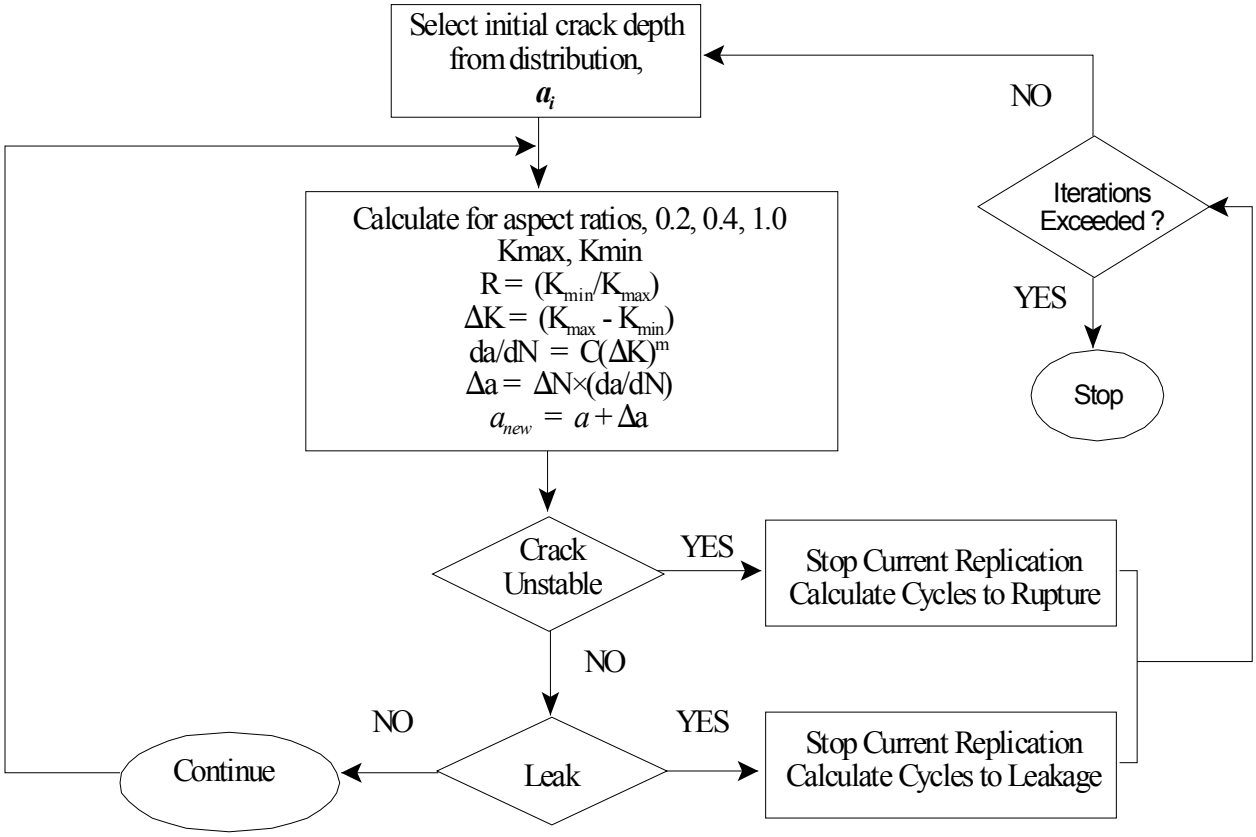

Figure 7.3 Crack Growth Algorithm

The sub-critical crack growth has been assumed to occur as a result of fatigue crack growth that has been environmentally accelerated by corrosion products in the CNG cylinder resulting in the failure mechanism of corrosion fatigue. Fatigue crack growth is assumed to occur under linear elastic conditions until the crack grows through the sidewall of the cylinder. For simplicity in calculations the cyclic stress intensity

factor is assumed to remain constant throughout each increment of crack growth. What this means is that the effect of the extension of the crack during each increment of crack growth interval has no effect on the stress intensity factor used for subsequent crack growth in each interval. This is a reasonable assumption as the crack growth intervals are incrementally small, thereby negating the effect of any variation in the stress intensity factor between intervals. EPFM failure criterion as well as LEFM is used in the analysis of the onset of unstable crack growth and rupture of a typical CNG cylinder.

The deterministic and probabilistic growth models of crack are discussed in Chapter 3. Equations for the employed in the crack growth relationship are shown below.

$$\frac{1}{da/dN} = \frac{A_1}{\Delta K^{n_1}} + \frac{A_2}{\Delta K^{n_2}} - \frac{A_1}{\left[(1-R)K_c\right]^{n_2}} \qquad \text{(Deterministic Model)}$$

$$da/dN = C(\Delta K)^m \qquad \text{(Probabilistic Model)}$$

where $\Delta K = K_{max} - K_{min}$

and $R = \frac{K_{min}}{K_{max}}$

For the deterministic crack growth relationship the parameters $A_1, n_1, A_2, n_2,$ and K_c are constants and are inputted as such in the MathCAD routine. R is the ratio of the minimum to maximum loads in each fatigue cycle. The parameters C and m in the

probabilistic model are random variables which changes from replication to replication. The distributions for each variable were developed in Chapter 3.

In calculating the cyclic stress intensity factor the load for the sidewall is considered differently than the transition region for the two designs a follows:

(a) Uniform stresses across the sidewall cross-section, and

(b) Combined bending and tension stresses linearized across the cross section as shown in Chapter 4.

In both cases the stress intensity factor is calculated by combining the load with the influence coefficients and the boundary correction factors.

The first failure mode that has to be evaluated is fracture leading to catastrophic rupture of the cylinder. This will only occur when unstable crack growth is predicted by one of the fracture criterion chosen. If this is not predicted to occur then leakage will be the resulting failure mode. Leakage is likely to occur when the crack grows through the wall of the cylinder. Under LEFM considerations this would be confined to Stage II crack growth alone where fast fracture does not occur, but result in leakage of CNG to the atmosphere notwithstanding. If the crack size is such that the critical stress intensity factor is exceeded then Stage III unstable crack growth will occur leading to fast fracture and subsequent rupture of the cylinder.

The crack growth life, in terms of cycles to failure, may be calculated using the crack growth relationships shown in Equation 3.40. The procedure may be generally described by the following:

If

$$\frac{da}{dN} = f(K) \tag{7.3}$$

Then, cycles to failure, N_f, may be calculated as

$$N_f = \int_{a_i}^{a_f} \frac{da}{f(K)} \tag{7.4}$$

where a_i is the initial crack depth and a_f is the final (critical or thickness of cylinder) crack depth. Using the probabilistic crack growth relationship,

$$N_f = \int_{a_i}^{a_f} \frac{da}{C(\Delta K)^m} \tag{7.5}$$

Because ΔK is a function of the crack depth and the boundary correction factors are dependent on crack length, cylinder geometry, etc, no closed form solution of the integral Equation 7.5 is possible. Numerical integration is therefore required.

The procedure for performing the more complex numerical computation in determining the fatigue life of CNG cylinders takes into consideration the dependency of the stress intensity factor and correction factors on crack geometry as well as the distributed nature of the crack growth and failure criterion parameters. For this procedure Monte Carlo simulation techniques and numerical integration using Simpson's Rule is utilized. The Monte Carlo sampling scheme has already been discussed in Section 7.4. The numerical integration procedure is now discussed in some detailed.

Crack growth is broken up into ranges based on the crack depth at which the influence coefficients shown in Table 4.1 - 4.4 are applicable and the crack shape defined by the a/c ratio. Only influenced coefficients for t/R ratio of 0.1 is used in the calculations as this is more consistent with thickness to radius ratios found in a typical CNG cylinder.

For a generic loading profile G_j the ranges are assigned as follows:

$G1j$ for $a/c = 0.2$

$G2j$ for $a/c = 0.4$

$G3j$ for $a/c = 1.0$

Each influence coefficient is further broken down according to the following crack depth ranges:

Gnj_1 for $0 < a/t \geq 0.2$

Gnj_2 for $0.2 < a/t \geq 0.5$

Gnj_3 for $0.5 < a/t \geq 1.0$

The values assigned to the influence coefficients from Table 4.1 – 4.4 were for the deepest points at the crack front. That is where

$$2\phi/\pi = 1.0 \tag{7.6}$$

In order to perform the numerical integration, the ranges of crack depth is divided up into increments, Δa. The increments in each range are assigned equal sizes because of the simplicity of the crack growth curve shown in Figure 3.3. Alternatively the increments could be chosen such that each succeeding crack growth increment is a fixed ratio of each other. This would ensure that the increments are sufficiently small to capture the steepest sections of the curve while improving efficiency of sampling for relatively flat sections. The number of crack growth increments assigned to each range is fifty (50).

Another important assumption made in order to simplify the crack growth procedure is that the crack growth rate remains constant during the interval. If conditions are such that the crack size is initially below threshold conditions, the life is infinite. Checks are performed at each replication and subsequent iterations as follows:

- Ratio of the crack depth to thickness for assignment of the applicable influence coefficient.

- Initial crack size at each replication and an infinite life is assigned for N_f if ΔK for that crack size is less than ΔK_{th}.
- If the crack size exceeds any criterion which would predict unstable crack growth.

The critical crack size is determined from the various failure criteria. A random value of the fracture toughness distribution is sampled in much the same way that the other distributions are sampled. Constant values are also assigned where the failure criterion is deterministic in nature. This critical crack size is compared with the crack size, after each iteration, and the number of cycles to failure noted if conditions for rupture is predicted. If this does not suggest that cylinder cracking instability and rupture will occur, then the crack growth algorithm will continue until leakage occurs. The replication is stopped at this point.

The crack growth rate for each increment is evaluated at the ΔK for the crack size at the midpoint of the increment and incremental cycle increase ΔN for that increment is

$$\Delta N = \Delta a \times \frac{da}{dN} \tag{7.7}$$

The number of cycles to failure whether this be leakage or rupture is then the summation of the incremental ΔNs and the growth relationship between a and N is obtained by summing Δas and ΔNs. The number of cycles to failure is therefore the sum of the

number of cycles to grow a crack from the initial crack size through each range of crack growth until conditions for rupture is detected or the crack grows through the wall of the cylinder.

The cumulative distribution and density function for the number of cycles to failure is determined by computing the probability of having a failure before a certain number of cycles using the summation process above. Since a Monte Carlo technique is used to estimate the failure probabilities, these estimates will have some sampling errors. In Section 7.6.4 the variance of these probabilities will be evaluated. The variances will be used to construct the confidence intervals for the estimated frequency of failure.

If leakage is the failure mode that is estimated to have occurred, then the crack size at leakage is noted for analyzing before the consequence of such a leakage can be determined. A method was developed using crack tip opening displacement (CTOD) methods to determine the size of the opening and as a result the leak rate of CNG to the atmosphere. The procedure developed for leak rate determination and evaluation of the consequence of a cylinder leak rupture is described in Chapter 8.

Calculations for the frequency of cylinder failure were completed for:

1. Cracks on the inside of the cylinder sidewall
2. Cracks on the outside of the cylinder sidewall
3. Cracks on the inside of the transition region and ends.
4. The initial crack size distribution.

7.6 Frequency of Cylinder Failure Results

Three numerical schemes were written in MATHCAD to perform the calculations, as described in the computational procedures, for each segment of the crack growth process. The routine calculates the frequency of failure for cracks on the inside and outside of the sidewall cylindrical portion, and the inside of the transition region. Since cracks in these regions are assumed to originate independently and will grow to cause failure they are considered separately in the risk analysis and the results combined in the determination of the overall risk.

7.6.1 Stress Intensity Factor Results

The ratio of crack depth to cylinder thickness in the sidewall of the cylindrical portion is plotted with the stress intensity factor, for the three aspect ratios of 0.2, 0.4 and 1.0, shown in Figure 7.4, Figure 7.5 and 7.6 for cracks originating on the inside, outside and the transition region respectively. In the graphical output from the stress intensity factor determination routine, the stress intensity factor converges for the three aspect ratios for crack depth below 25% of the cylinder thickness for the cylindrical portion. Above relative crack depth of 0.25, the stress intensity factor diverges relative to the initial crack aspect ratio, the sharpest crack showing the greatest relative increase. This is expected as the stress intensity factor is governed by the stress distribution at the crack tip and the crack depth.

For the transition region the relationship between the stress intensity factor and the relative crack depth is similar to the cylindrical sidewall. The major difference being total convergence below 25% relative crack depth and significantly more divergence as the crack grows through the wall of the cylinder. The stress intensity factor for the transition region is considerably more at smaller relative crack depth. This is due to the combined stresses present. As the crack grows through the wall, the stresses at the crack tip will change from compressive to tensile. This is evident in the results for the transition region. Catastrophic failure is therefore much more likely to occur early in the crack growth process for the transition region than for the cylindrical portion. The reverse holds as the crack grows through the sidewall.

Overall the sharpest crack with the 0.2 aspect ratio gives the highest stress intensity factor for crack growth across the thickness of the cylinder. The results for this shape crack will be used for calculating the life of a cylinder.

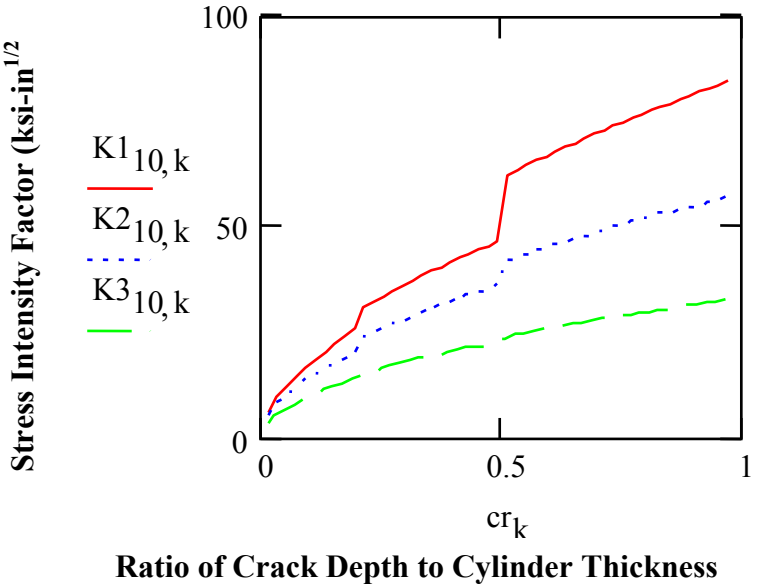

Figure 7.4 Cylindrical Inside Crack Stress Intensity Factor vs. Crack Depth

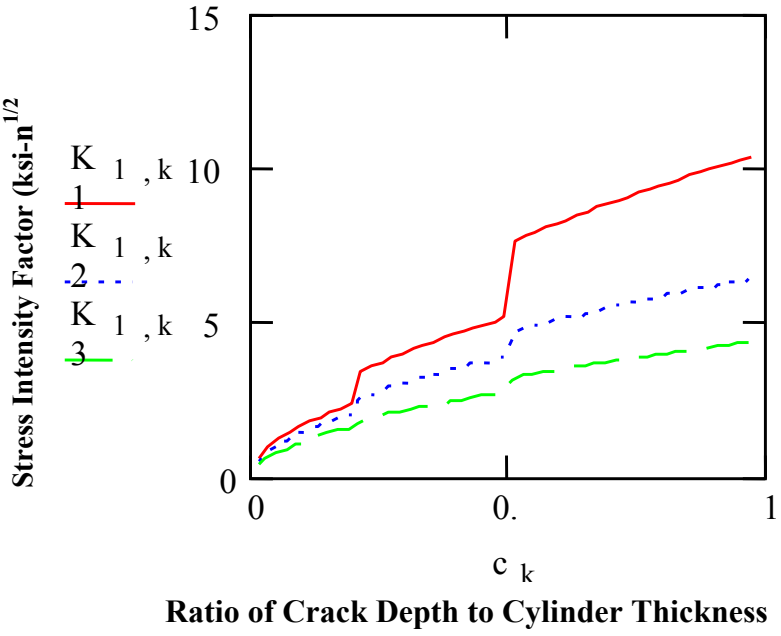

Figure 7.5 Cylindrical Outside Crack Stress Intensity Factor vs. Crack Depth

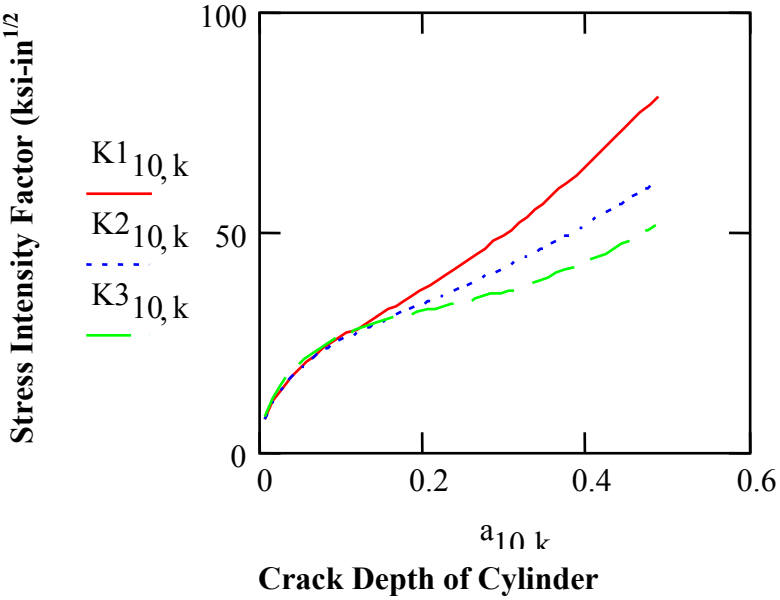

Figure 7.6 Transition Inside Crack Stress Intensity Factor vs. Crack Depth

7.6.2 Frequency of Cylinder Leakage Results

Cylinder leakage will occur when the crack grows through the wall without any of the criteria for rupture being achieved. Figures 7.7 and 7.8 shows the corrosion-fatigue life of a typical cylinder follows an exponential distribution with initial crack size for both the deterministic (See Appendix 1 and 2) and probabilistic crack growth relationship, in the cylindrical portion. The probabilistic model predicts shorter fatigue life for the same initial crack size. In fact the fatigue life is significantly under predicted for smaller initial crack sizes when the results of the two models are compared.

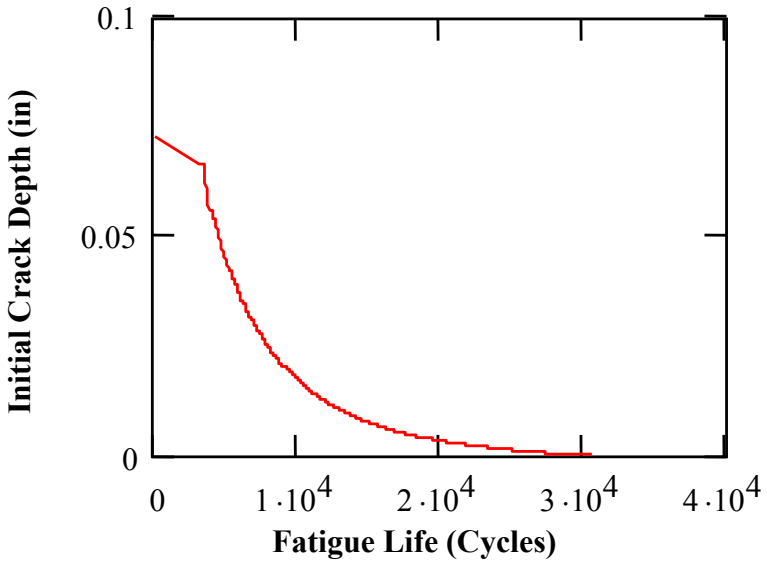

Figure 7.7 Probabilistic Model Simulated Fatigue Life vs. Initial Crack Size For Cracks on Inside Sidewall of Cylinder

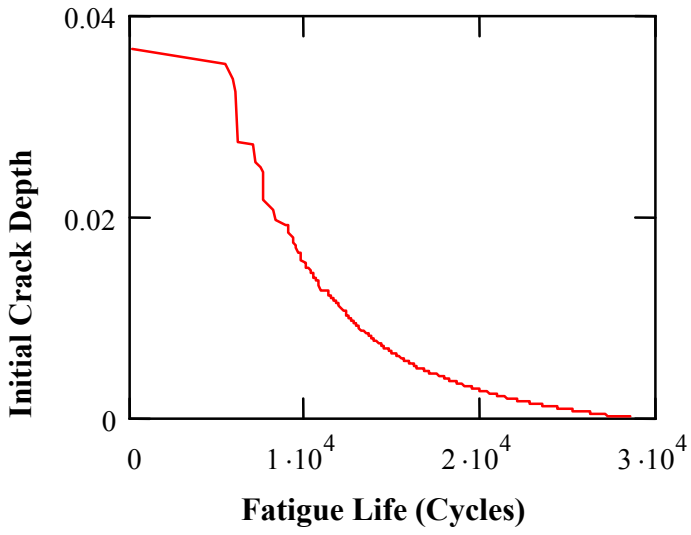

Figure 7.8 Probabilistic Model Simulated Fatigue Life vs. Initial Crack Size For Cracks on Outside Sidewall of Cylinder

The corrosion-fatigue life of cracks originating on the inside of the cylinder was in general less than for cracks originating on the outside. This is expected because the crack driving force on the inside is expected to be greater and as such will propagate faster for each increment of crack growth.

In the transition region a similar relationship between the initial crack size and the fatigue life is shown in Figure 7.9. The deterministic model predicts much shorter life than the probabilistic model. Cracks have been shown to occur most often in the transition region so the results are therefore even more significant.

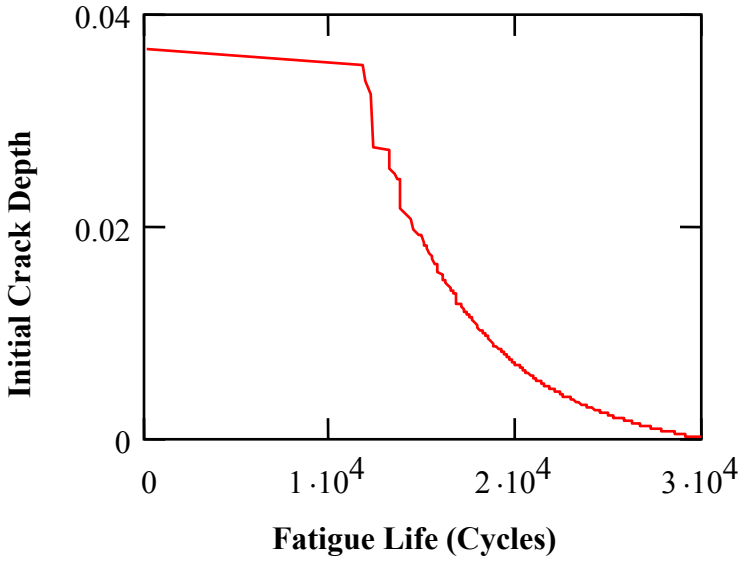

Figure 7.9 Probabilistic Model Simulated Fatigue Life vs. Initial Crack Size For Cracks on Inside of Transition Region of Cylinder

The cumulative distribution of cylinder leakage at different filling cycles for all the initial crack sizes considered is shown in Figures 7.10 – 7.12 for cracks on the inside, and outside of the cylindrical sidewall and the inside of the transition region respectively. The histogram of the binned number of times a simulation predicted leakage would occur for a particular crack size is shown in Figures 7.13 – 7.15. Fitting a curve to the histogram results gives us the probability density function of the number of cycles to cylinder leakage.

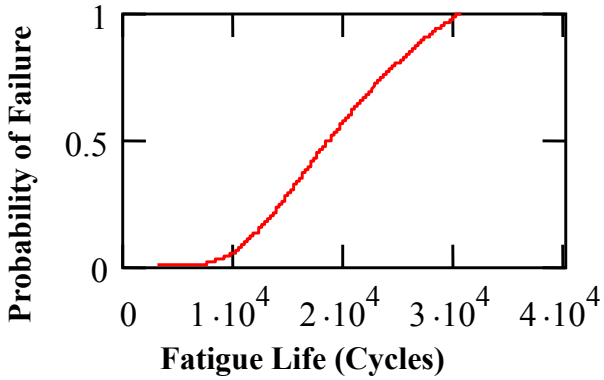

Figure 7.10 Cumulative Distribution of Simulated Probability of Cylinder Leakage For Sidewall Inside Cracks

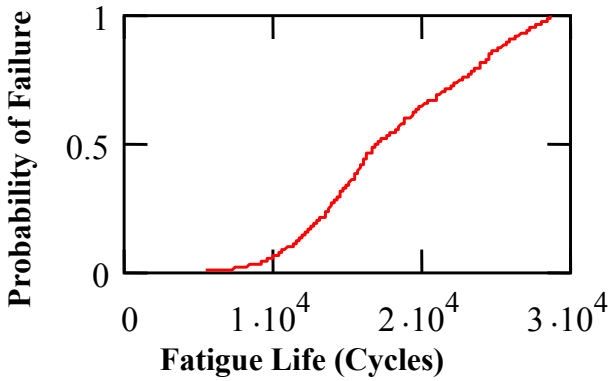

Figure 7.11 Cumulative Distribution of Simulated Probability of Cylinder Leakage For Sidewall Outside Cracks

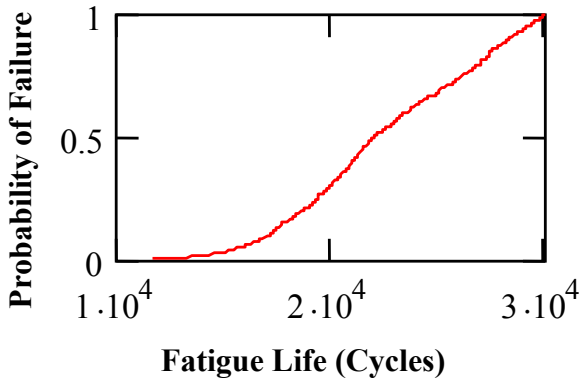

Figure 7.12 Cumulative Distribution of Simulated Probability of Cylinder Leakage For Transition Region Inside Cracks

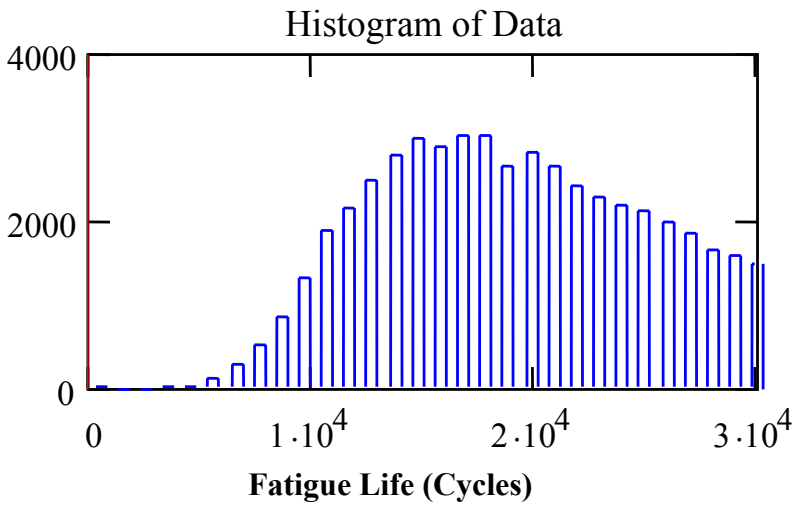

Figure 7.13 Probability Density Function of Simulated Probability of Cylinder Leakage for Sidewall Inside Cracks

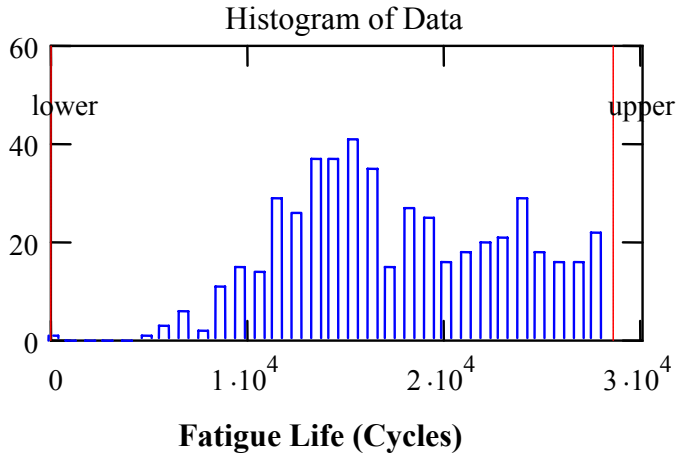

Figure 7.14 Probability Density Function of Simulated Probability of Cylinder Leakage For Sidewall Outside Cracks

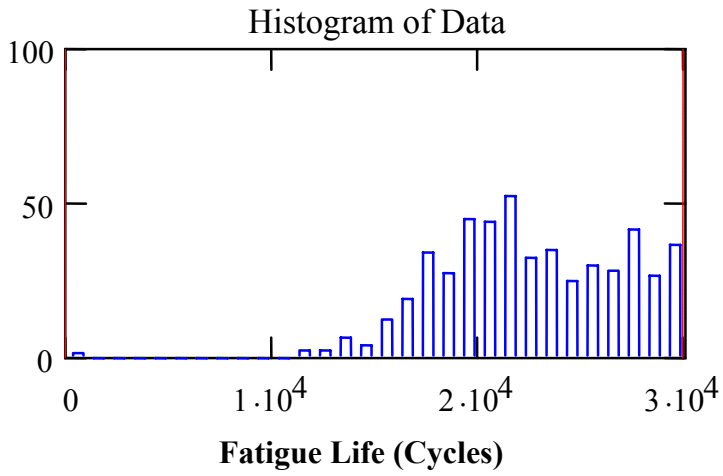

Figure 7.15 Probability Density of Simulated Probability of Cylinder Leakage For Transition Region Inside Cracks

The probability of cylinder leakage is predicted to be higher for the probabilistic model for all the crack sizes considered. The histogram data suggests that the cylinders display a bimodal failure mechanism. This is explained by the fact that the crack growth has two characteristic regions where the rate of crack growth is different due to crack blunting and plastic relaxation of the stresses at the crack tip. Cracks which are above a certain size will propagate to failure very quickly due to the high stress intensity factor. Smaller size cracks will grow rapidly at first and then slow down considerably, requiring much longer cycling before failure will occur. This validates the probabilistic model which also allows the uncertainty of the results to be evaluated.

From Figure 7.10 - 7.12, the probability of leakage of a cylinder increases with the number of filling cycles that a typical bus has undergone. This is consistent with the

corrosion-fatigue mechanism which is a gradual degradation process governed by the crack growth relationship. The age of a bus selected from that population is random and as such the mean time to leakage and frequency of occurrence, for a typical bus in an entire fleet can be derived from the number of cycles that is predicted by the cracks growth relationship and the number of filling cycles per year. This is expected to be constant for a typical bus in a fleet.

The desired life for a typical CNG fueled bus is 15 years [2]. This amounts to 10, 958 cycles at two filling cycles per day. For a cylinder to leak in this number of cycles and less, initial crack size has to be greater than 0.02 for cracks on the inside, 0.015 for cracks on the outside and 0.035 for cracks on the inside of the transition region, as shown in Figures 7.7 -7.9. The frequency of leakage failure on a annualized basis assuming a constant rate model, for the cumulative distribution shown in Figures 7.10 – 7.12 and a designed filling cycle life of 10,958 is summarized in Table 7.1.

Table 7.1 Frequency of Release of CNG from Through Wall Crack

Gas Leakage Initiating Event	**Probability of Leakage For Lifetime**	**Frequency /Bus/Year**
Crack on Sidewall Inside Surface	0.08	5.56×10^{-3}
Crack on Sidewall Outside Surface	0.07	4.84×10^{-3}
Crack on Inside Surface of Transition Region	0.05	3.42×10^{-3}

Higher number of filling cycles would impact adversely on the frequency of failure. Similarly fewer filling cycles would produce a smaller number of failures per year. Two fillings per day are considered conservative and therefore the frequency of leakage used in the calculations of the risk would give results that are conservative for a typical bus.

7.6.3 Frequency of Cylinder Rupture Results

Three criteria were chosen for determining when cracks in the cylinder would become unstable resulting in catastrophic rupture of a typical cylinder. The deterministic model predicted that rupture could occur within a reasonable lifetime of a cylinder only from the EPFM criterion of critical crack length. The probabilistic model predicted that rupture could occur with both the LEFM and EPFM criteria. This applied to cracks on the inside and outside of the cylindrical sidewall as well as cracks on the inside of the transition region as shown in Figures 7.16 – 7.21.

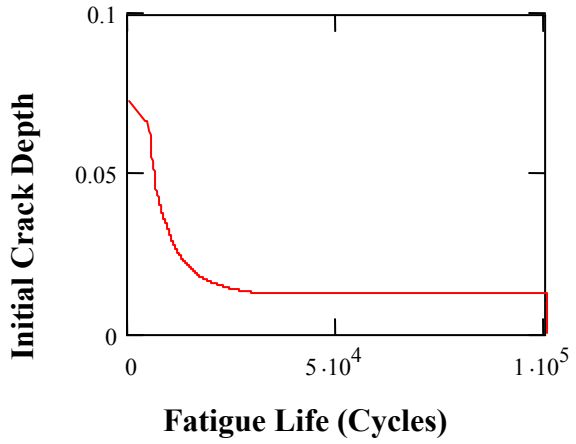

Figure 7.16 LEFM Predicted Cycles to Rupture vs. Initial Crack Size For Cracks on Inside Sidewall of Cylinder

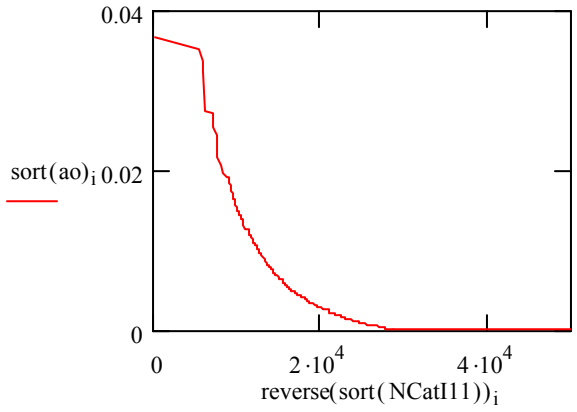

Figure 7.17 LEFM Predicted Cycles to Rupture vs.

Initial Crack Size For Cracks on Outside Sidewall of Cylinder

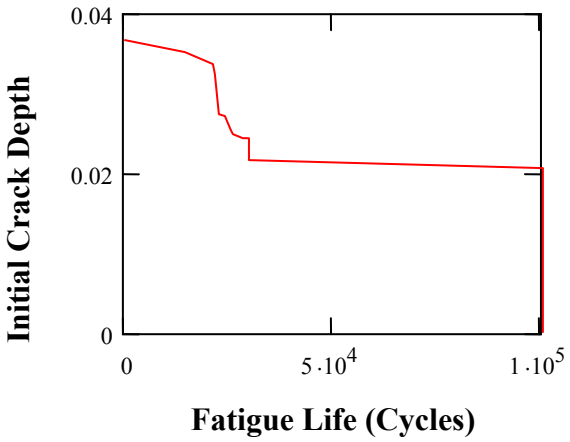

Figure 7.18 Figure LEFM Predicted Cycles to Rupture vs.

Initial Crack Size For Cracks on Inside of Transition Region of Cylinder

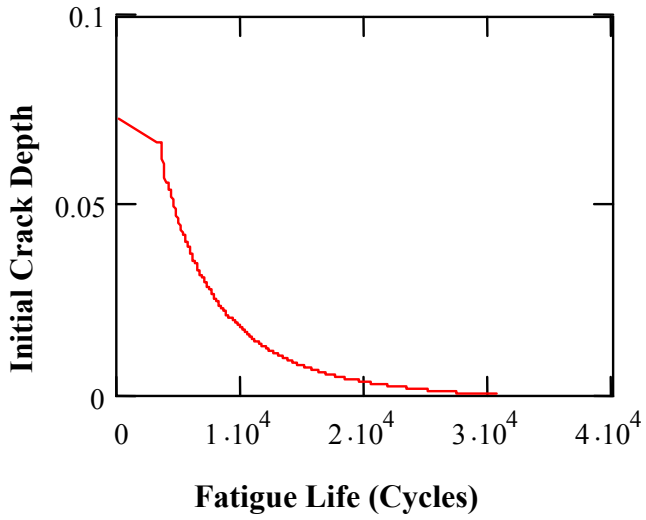

Figure 7.19 EPFM Predicted Cycles to Rupture vs.

Initial Crack Size For Cracks on Inside Sidewall of Cylinder

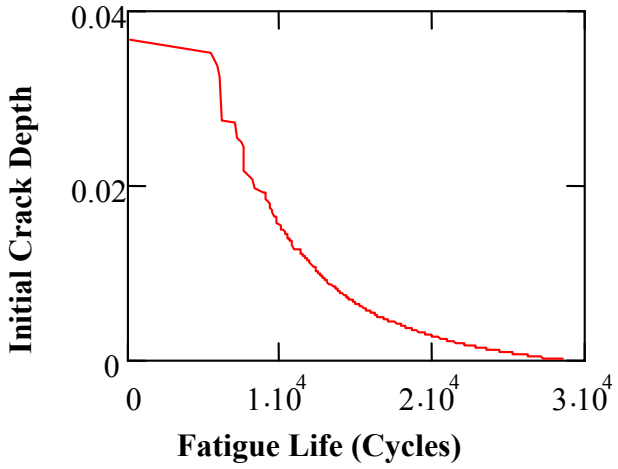

Figure 7.20 EPFM Predicted Cycles to Rupture vs.

Initial Crack Size For Cracks on Outside Sidewall of Cylinder

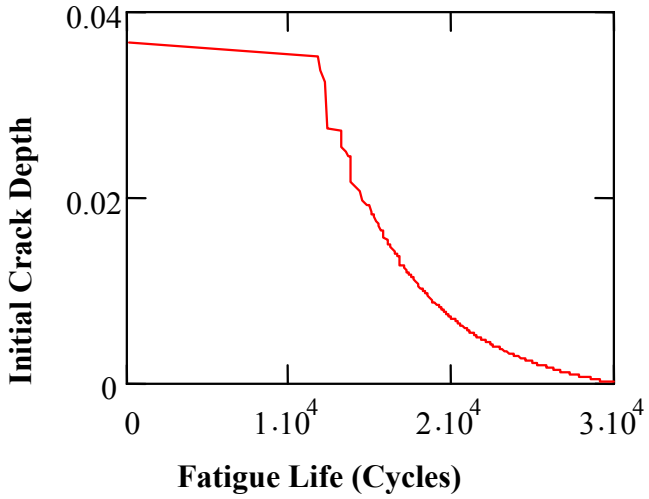

Figure 7.21 EPFM Predicted Cycles to Rupture vs.

Initial Crack Size For Cracks on Inside of Transition Region of Cylinder

On closer examination it can be seen that the critical crack length criterion predicts that cylinder rupture would occur because of unstable crack growth, for all cracks growing through the cylinder with an aspect ratio of 0.2. In fact all cracks with aspect ratios of 0.22 and less will cause rupture of the cylinder. In developing the initial crack size distribution, ideally the crack size is a joint distribution of the crack depth and aspect ratio. Since no data were available to estimate the aspect ratio distribution, only the initial crack depth distribution was developed.

In the absence of data for this analysis it will be assumed that crack aspect ratios are uniformly distributed between a thumbnail crack with aspect ratio of 0.167 and a

semi-circular crack of aspect ratio 1.0. It has been found that cracks [103] with aspect ratios less than 0.167 is highly unlikely (probability being $1x10^{-6}$), so this will be the sharpest crack presumed to exist in the cylinder at any one time. The cumulative distribution of cracks in the range 0.167 to 0.22 is given by Equation 7.8.

$$F_X(x) = \begin{cases} 0 & x \le a \\ \frac{x-a}{b-a} & a \le x \ge b \\ 1 & x \ge b \end{cases} \tag{7.8}$$

The probability of cracks in the range 0.167 – 0.22 is therefore equal to

$$\begin{aligned} F(0.22) &= \frac{0.22 - 0.167}{1-0.167} \\ &= 0.064 \end{aligned} \tag{7.9}$$

The probability of rupture given that a crack with aspect ratio less than 0.22 is in the cylinder must be multiplied by the likelihood of the existence of such a crack to get the unconditional probability of failure. The EPFM criterion along with the probability of existence of crack of this shape gives the highest probability of cylinder rupture and will be used to derive the frequency of cylinder rupture.

Aspect ratio distribution has been found elsewhere to be lognormally distributed [62], [104]. Assuming a uniform distribution will give a higher probability of existence of cracks with aspect ratios below 0.22. The frequency of rupture predicted will be less

conservative than would be obtained in reality. This will have to be addresses in the future research when an aspect ratio distribution is developed.

The conditional cumulative failure distribution is shown in Figures 7.22 – 7.24.

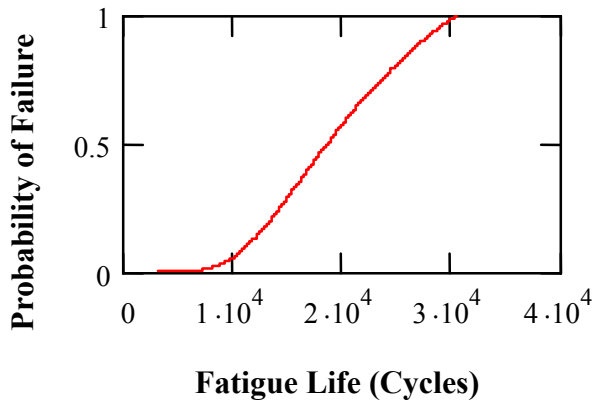

Figure 7.22 Cumulative Distribution of Simulated Probability of Cylinder Rupture For Sidewall Inside Cracks

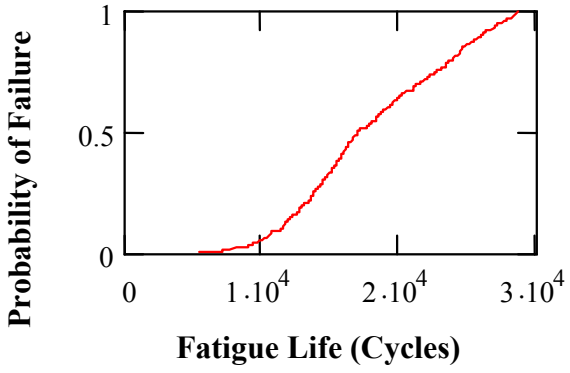

Figure 7.23 Cumulative Distribution of Simulated Probability of Cylinder Rupture For Sidewall Outside Cracks

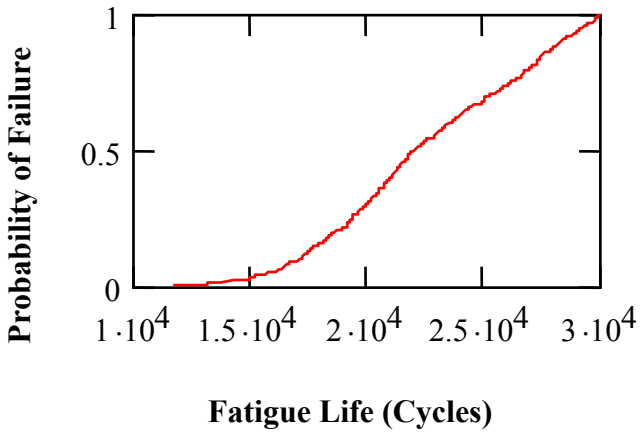

Figure 7.24 Cumulative Distribution of Simulated Probability of Cylinder Leakage For Transition Region Inside Cracks

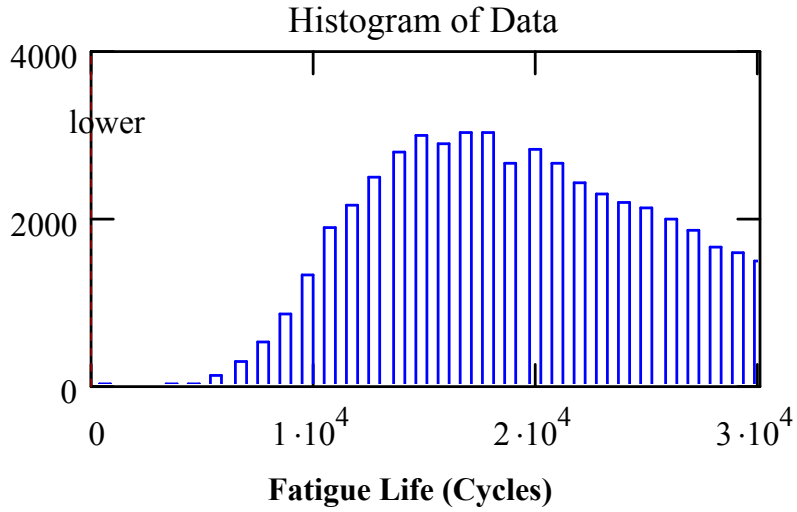

Figure 7.25 Probability Density Function of Simulated Probability of Cylinder Rupture For Sidewall Inside Cracks

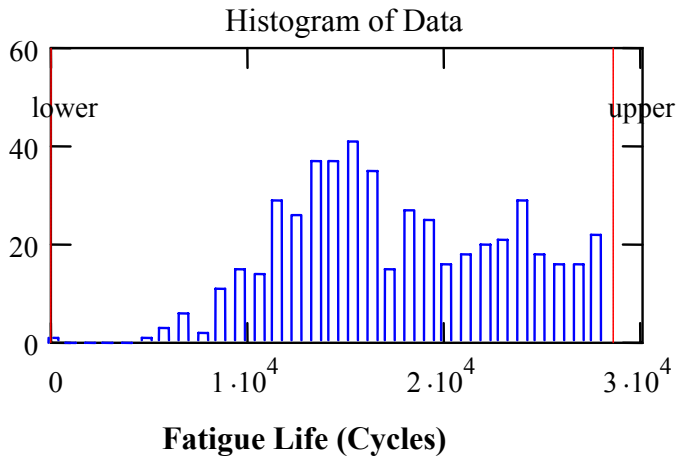

Figure 7.26 Probability Density Function of Simulated Probability of Cylinder Rupture For Sidewall Outside Cracks

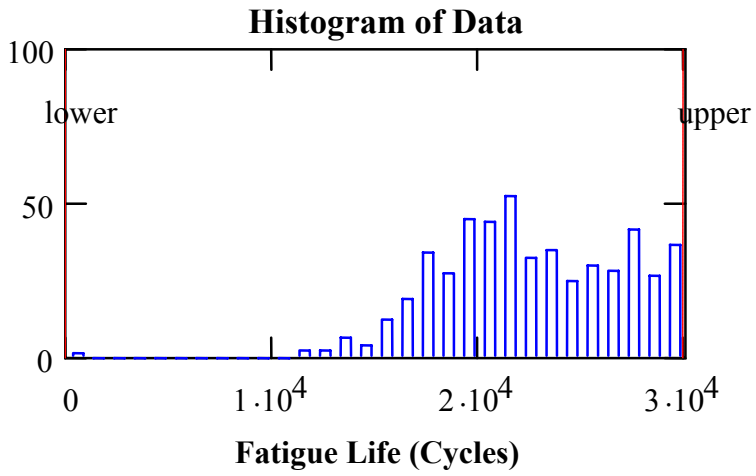

Figure 7.27 Probability Density of Simulated Probability of Cylinder Rupture For Transition Region Inside Cracks

By similar reasoning the frequency of cylinder rupture can be derived from the unconditional probability of cylinder rupture using a constant failure rate model to get the annualized frequency of failure. The results are shown in Table 7.2.

Table 7.2 Frequency of Release of CNG from Cylinder Rupture

Gas Release Initiating Event	Probability of Rupture Over Lifetime	Frequency /Bus/Year
Crack on Sidewall Inside Surface	5.09×10^{-3}	3.40×10^{-4}
Crack on Sidewall Outside Surface	4.45×10^{-3}	2.98×10^{-4}
Crack on Inside Surface of Transition Region	3.18×10^{-3}	2.12×10^{-4}

As in the case with leakage of CNG from the cylinder, higher number of filling cycles would impact adversely on the frequency of rupture. Similarly fewer filling cycles would produce a smaller number of failures per year. Two fillings per day are considered conservative and therefore the frequency of cylinder rupture used in the calculations of the risk would give results that are conservative than for a typical bus.

7.6.4 Frequency Uncertainty Analysis

The probability of failure was estimated using a Monte Carlo technique. This procedure is subject to sampling errors. An unbiased estimator of the variance of the mean frequency will now be developed. This variance can be used to construct confidence intervals of the estimated probability of leakage and rupture along with corresponding annualized frequency of occurrence of failure.

The estimator of the probability of failure before the assumed lifetime of filling cycles is given by Equation 7.1 which is repeated here.

$$F(t) = \frac{N_F(t)}{N} \approx P(t_F \leq t) \tag{7.10}$$

where

N is the total number of trial or replications.

$N_F(t)$ is the total number of iterations that predict that leakage or rupture will occur at or before the specified lifetime of 10, 985 filling cycles.

$P(t_F \leq)$ is the true, but unknown probability that cylinder leakage or rupture will occur at or before the design lifetime.

At the end of each iteration the cylinder is either in a failed state, that is it has leaked or ruptured, or not. These are two mutually exclusive states and so we could use the Bernoulli distribution to map from the sample space of failed or not failed to the integer values, 0 or 1. A random variable can therefore be defined such that;

$$I_i(t) = \begin{cases} 1 \text{ if the cylinder has failed in time t,} \\ 0 \text{ if the cylinder has not failed after time t.} \end{cases} \tag{7.11}$$

The subscript *i,* denotes the particular iteration being considered.

In terms of $I_i(t)$, the number of times leakage or rupture is predicted to occur over the entire simulation space is given by;

$$N_F(t) = \sum_{i=1}^{N} I_i(t) \tag{7.12}$$

Similarly the cumulative distribution of failures is estimated by

$$F(t) = \frac{\sum_{i=1}^{N} I_i(t)}{N} \tag{7.13}$$

It can be shown [40], [88] that an unbiased estimator of for the variance of F(t) is

$$\begin{aligned} s^2(t) &= \tfrac{1}{(N-1)} F(t)\left[1 - F(t)\right] \\ &= \tfrac{1}{(N-1)}\left[F(t) - F^2(t)\right] \end{aligned} \tag{7.14}$$

$$s^2(t) = \tfrac{1}{N(N-1)}\left[\left(\sum_{i=1}^{N} I_i(t)\right) - \tfrac{1}{N}\left(\sum_{N=1}^{N} I_i(t)\right)^2\right] \tag{7.15}$$

Using Taylor series expansion [105], about the mean frequency of failure, the approximate variances for frequency of leakage and rupture are tabulated in Tables 7.3.

Table 7.3 Variances of Frequency of Release of CNG from Cylinder re

Gas Leakage Initiating Event	Variance for Frequency of Leakage	Variance for Frequency of Rupture
Crack on Sidewall Inside Surface	7.92×10^{-4}	5.04×10^{-5}
Crack on Sidewall Outside Surface	2.05×10^{-4}	1.30×10^{-5}
Crack on Inside Surface of Transition Region	7.0×10^{-5}	4.45×10^{-6}

The physics of failure model that was developed gave more conservative results for the frequency of cylinder failure by leaking and catastrophic rupture than the previous results that was derived from generic data [1]. The results from this model while they are conservative is expected to be more accurate since it captures the random nature of the crack growth process by the parameters being distributions, while it accounts for the threshold conditions from which crack growth will start, which the deterministic model did not.

These results will be combined with the likelihood of subsequent events to the gas being released and a fire starting, or explosive event occurring to get the frequency of fires occurring. The consequence of various fire scenarios will be combined with the frequency of occurrence to give the fire fatality risk. The consequence of each release and the likelihood of subsequent events are evaluated in Part II of this dissertation.

PART II

CONSEQUENCE OF FIRES AND FIRE RISK ASSESSMENT

CHAPTER 8: CONSEQUENCE ANALYSIS

The use of compressed natural gas (CNG) has been growing in transit and other fleet vehicles in response to increasingly stringent emissions standards. While CNG has some benefits related to reduced emissions compared with other fuels, its use also introduces new and different fire safety risks relative to these other fuels. The purpose of this analysis is to determine the consequences of different fire incidents occurring for a typical bus that uses CNG as fuel.

Previous studies promoting the use of CNG as a viable vehicular fuel [106 - 108], have suggested that CNG represents a reduced fire risk relative to traditional liquid fuels because the fuel system construction is more rugged and because CNG is lighter than air and consequently would be expected to dissipate in the atmosphere if released accidentally. While this may be true for many external releases of CNG, it is not true for CNG released within or beneath a vehicle or a structure. Under these circumstances, CNG can accumulate within the enclosure until it reaches a flammable concentration, at which point the CNG-air mixture can ignite and propagate, in some cases with explosive forces resulting in multiple fatalities.

For the typical bus considered in this analysis CNG is stored in steel cylinders and is delivered through a fuel delivery system to the vehicle engine. There are a number of scenarios where CNG represents a potentially significant fire hazard as a vehicular fuel.

Most of these scenarios involve the loss of containment of CNG from the fuel system and subsequent ignition of the discharged CNG. In Chapters 2 – 7 of this analysis a probabilistic model was developed of the predominant failure mechanism found in CNG cylinders, corrosion-fatigue, and a methods demonstrated for analytically determining the frequency of release of CNG due to the degradation of the containment. Two types of releases were determined to be possible. These are instantaneous, as from a ruptured cylinder, when a crack grew to become unstable, or gradual, when a crack grew through the wall of the cylinder but not satisfying the criteria for fracture to occur. The latter failure mode is describes as leak before break scenario.

The CNG may be ignited immediately upon release or the ignition may be delayed. The matrix in Table 8.1 is used to generally identify the different loss of containment scenarios and ignition modes.

Table 8.1 CNG Release and Subsequent Scenario

CNG release mode	**Ignition mode**		
Instantaneous	Immediate	Delayed	No Ignition
Gradual	Immediate	Delayed	No Ignition

If ignition occurs in each of these scenarios, different types of fires are expected to develop. Table 8.2 shows the types of fires resulting from the release of CNG from a typical cylinder and subsequent ignition.

Table 8.2 CNG Fire Scenarios

CNG release mode	Ignition Mode	Expected Consequence
Instantaneous	Immediate	Fireball
	Delayed	Vapor cloud explosion or flash fire
Gradual	Immediate	Jet flame
	Delayed	Vapor cloud explosion or flash fire

The potential for fire fatality or other severe effects are dependent on the volume occupied by the fire and the heat flux generated. The actual relative volume of atmosphere rendered flammable by an accidental release of CNG into the atmosphere will depend on the nature of the release (i.e., instantaneous or gradual), the nature of the ignition (i.e., immediate or delayed) and the nature of the mixing of the CNG with the air in the atmosphere (i.e., buoyant plume, momentum jet or uniform dispersion). Enclosure effects will influence the mixing and accumulation of CNG in the atmosphere, such as for CNG releases within buildings (e.g., parking or service facilities) or within vehicle spaces (e.g., engine, cargo or passenger compartments).

CNG released from a cylinder through an orifice, such as a long through-wall crack in the cylinder with a wide mouth opening, is likely to issue as a momentum-dominated jet propelled by the pressure difference between the cylinder and the atmosphere. In free surroundings, the only external forces influencing the jet are gravitational, or buoyancy, forces. For natural gas, with a specific gravity relative to air

of about 0.56, these buoyancy forces will cause the jet to rise. Thus, a natural gas leak under pressure will have the characteristics of a pure jet in the vicinity of discharge and the characteristics of a buoyant plume at distances further away from the point of discharge. For a small leak such as a pin-hole crack, the leaking CNG will have little initial momentum and will act as a purely buoyant plume.

With the multitude of potential release, ignition and enclosure scenarios, it is difficult to generalize about the potential for ignition in a particular scenario. This would require a detailed analysis of the fluid dynamics of a release along with a probability distribution for the positions and intensities of potential ignition sources. The heat flux generated at points in and adjacent to the fire are determined and checked for its lethality effects.

The objective of the consequence analysis can be summarized as follows:

1. Determine the expected types of CNG release from a failed cylinder.
2. Simulate each type of gas release to determine how it disperses and the potential for formation of a flammable mixture.
3. Assess the likelihood of a fire or explosion from this mixture.
4. Determine the heat flux generated from the fire event at specific distances.
5. Identify lethal exposures to heat flux.
6. Compute the fire and explosion fatality for passengers and others, potentially exposed to the lethal heat flux.

Some of the most important fire scenarios resulting from CNG being released and the subsequent events that follow are now discussed. The detailed simulation of a release and the fire modeling calculations of the consequence of each fire event will follow.

8.1 Consequence Severity Factors

How natural gas is dispersed in the atmosphere from a failed cylinder depends on many factors. The most important factors are:

- Physical and chemical properties of the gas.
- Meteorological characteristics in the vicinity of the CNG release.
- Location of the gas release.
- Relative location of obstructions to gas and air motions.
- Ventilation characteristics.

The consequence of a fire resulting from the accidental release of natural gas is determined by the following factors:

- Volume of gas contained before release.
- Pressure at which gas is contained.
- Rate of gaseous release.
- Duration of release.
- Ignition source and the type of fire produced.
- Thermal energy released.
- The number of people occupying the exposure zones

To determine the lethality of each fire scenario, location is of paramount importance. This is so because the number of persons occupying the exposure zones is dependent on the bus location. The accident scenes chosen cover existing situations that a CNG bus is likely to be found in based on normal use. There is a likelihood of a bus being present in any one of these location. This likelihood is computed from the frequency at which a bus is expected to be in each location. The accident scenarios chosen for the consequence analysis are:

- Vehicle fire in parked or storage facility.
- Vehicle fire in a station affecting CNG equipment.
- Vehicle fire due to collision or otherwise on suburban roadway.
- Vehicle fire due to collision or otherwise on urban roadway.
- Vehicle fire in tunnel or under bridges.

Fires occurring at the described locations will determine the number of persons exposed to thermal radiant fluxes that would result in fatalities.

8.2 Types of Fire Scenarios

The types of fires contemplated from any release will now be detailed to provide understanding of the comparative thermal radiation effects and the potential for other fatalities. Figure 8.1 gives a logical basis of describing each fire scenario. The consequences of fires in terms of its effects and the potential for fire fatality are shown at the end of the propagated fire event.

Each incident and its outcome have a different likelihood of occurrence. A qualitative analysis of the consequences of each fire scenario will be done. The objective of this qualitative analysis is to identify all the possible sources of fatality associated with each fire scenario. Based on engineering judgments and the dynamics of fire initiation and propagation, if the likelihood of occurrence of an outcome is low, then this effect will be ignored in the quantitative analysis. Severity of each outcome of a fire scenario, in terms of the numbers of fatalities expected, will be computed in the quantitative analysis. The results will incorporate factors such as type of release, location of bus and the number of persons occupying the immediate area adjacent to the incident.

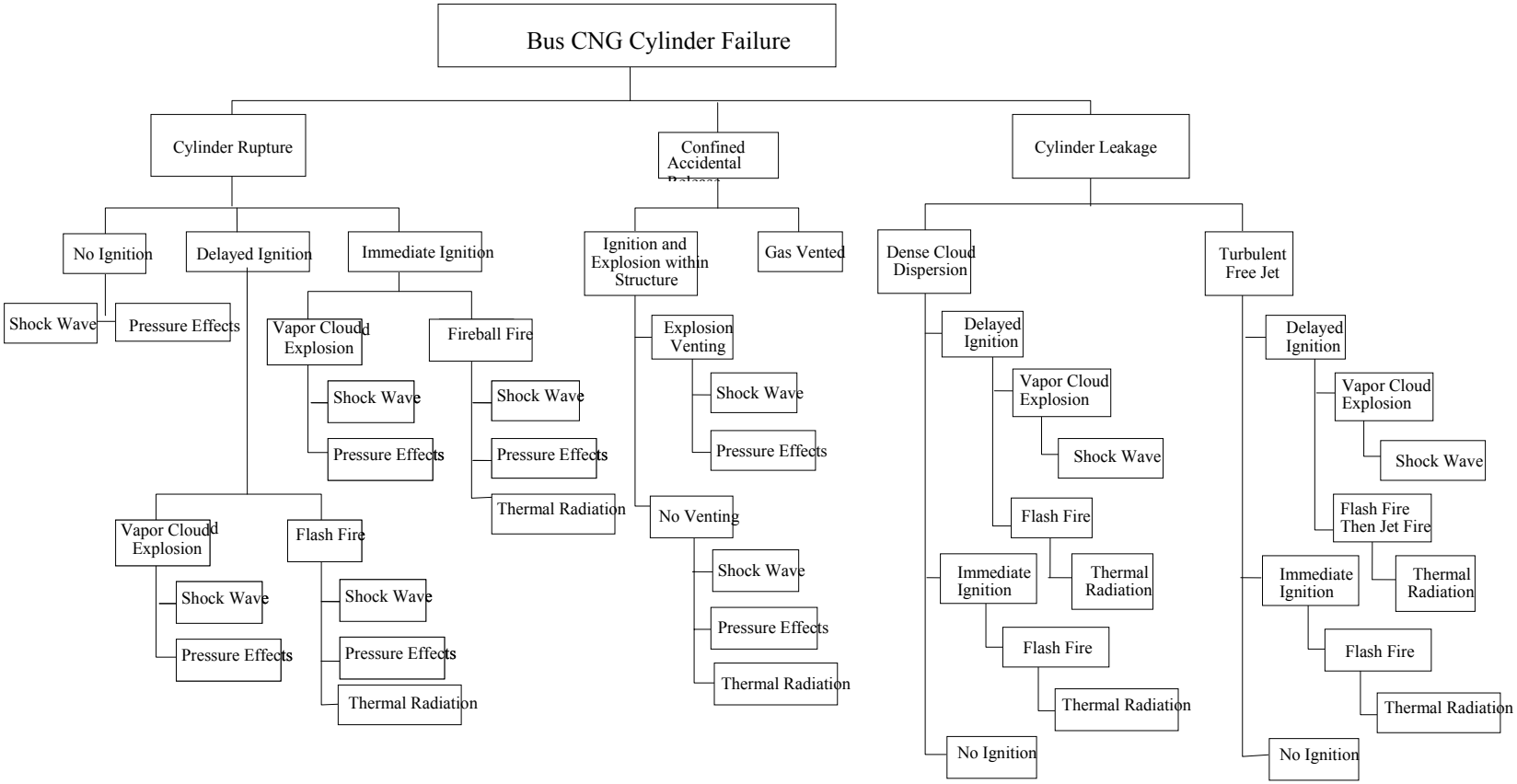

Figure 8.1 **Logical** Representation of Fire Scenario

Some of the fire scenarios identified in Figure 8.1 are accompanied by explosions. The energy contained in the high pressure gas of an explosion is dissipated as a shock wave as the gas is rapidly equilibrated. Explosions associated with CNG cylinder failures occur either as a result of the catastrophic ruptures of the pressurized cylinder or from the combustion of a flammable natural gas/air mixture. The effect of an explosion depends as in the case of fires on the location, whether in a confined or un-confined state. The consequence of concern in CNG related explosions are shock wave overpressure effects and the generation of projectiles. In some instances explosions are accompanied by fires. In such instances the thermal radiation effects and pressure effects are considered. In cases where dispersion of the fuel is not achieved an explosion is less likely. For this reason shock wave effects will be ignored, unless it is the only outcome expected in the consequence analysis in such circumstances. This will give a conservative estimate of CNG fire fatalities as in all instances when explosions are possible fatalities could arise because of the effects of the explosion or its combined effect with thermal radiation.

Each of the fire scenarios will now be analyzed qualitatively to determine the likelihood of producing lethal thermal radiation effects, projectiles and shock waves. The fires and explosions that will be analyzed based on the outcomes shown in Figure 8.1 are:

1. Fireball
2. Unconfined Vapor Cloud Explosion and Flash Fire
3. Confined Explosion
4. Jet Fire
5. Cylinder Physical Explosion

8.2.1 Vapor Cloud Explosion and Flash-Fire

When a large amount of CNG is rapidly dispersed to the atmosphere, a vapor cloud forms and disperses. The pathways to the formation of a vapor cloud are shown in Figure 8.1. If this cloud is ignited before the mixture disperses below the lower flammable limit, an unconfined vapor cloud explosion and or a flash fire will occur. Ignition of the vapor cloud results in sufficiently rapid propagation of the flame to cause overpressure and shock waves. In general the qualitative requirements for a vapor cloud explosion are as follows:

- A relatively large quantity of natural gas.
- A highly energetic ignition source or
- An obstructed environment supportive of turbulence-induced flame accelerations.

Except for the presence of the ignition source, all the other factors are expected to be present in the event that a cylinder failure by rupturing. Vapor cloud explosion is therefore very likely to occur with the catastrophic rupturing of a CNG cylinder and there is delayed ignition of the gas released.

If a CNG cylinder fails by leaking, the rate of release and formation of a vapor cloud is much less than in the case of cylinder rupture. If dispersion and accumulation followed by delayed ignition occurs then vapor cloud explosion is a possible outcome to follow leaking of a cylinder. The most likely scenario however if there is delayed

ignition of natural gas released from a crack is that a flash fire will be produced without significant overpressure effects. A flash fire is the non-explosive combustion of a natural gas-air cloud resulting from a release of flammable CNG into the open air. Flash fire results from ignition of a natural gas cloud when there is essentially no increase in the combustion rate and consequently no significant build-up of pressure.

In most instances a vapor cloud explosion accompanies a flash fire inside an enclosure such a bus, maintenance building or bus depot. Strong blast pressures are associated with high flame speeds. In turn, high flame speeds are associated with turbulence-enhanced burning rates or with constrictions caused by obstructions in the flow field. Confinement of a vapor cloud within an enclosure will increase the potential for a vapor cloud explosion, although overpressures may be related simply to restrictions on the free expansion of the combustion gases by the enclosure boundaries. The thermal radiation produced if vapor cloud explosion occurs with a flash fire is of a lower intensity than a fireball but covering a wider area.

Vapor cloud explosions are relatively unusual however if leakage occurs outdoors, because several features need to be present for a vapor cloud explosion with damaging overpressure, to occur. These include:

- The released natural gas must achieve a flammable mixture in the atmosphere and at suitable conditions of temperature and pressure.
- A cloud of sufficient size must form prior to ignition;

- A sufficient amount of the cloud must be within the flammable range to cause extensive overpressure;
- The blast effects can vary greatly and are determined by the speed and structure of flame propagation. In most cases the mode of flame propagation is deflagration; under extraordinary conditions, a detonation might occur.

A flammable natural gas cloud may be ignited by a number of occasional sources once it is formed. These ignition sources include lighted cigarettes, bus and other vehicle exhaust, electrical wiring and the engine compartment temperature. The effect of ignition is to terminate the spread of the natural gas cloud in that direction. Flash fires will expand in all directions once combustion has started. Initially it will expand upwards because of buoyancy effects. The likelihood of ignition of a natural gas cloud depends on the probability of the existence of an ignition source. This is dependent on the number of such ignition sources and the location of the bus. The possibility of ignition early in the cloud formation or later, to give full effect of a vapor cloud explosion or flash fire is also dependent on the location of the bus. Traffic too will be considered as part of this analysis of the likelihood of ignition.

The consequence of interest with a vapor cloud explosion is the effects of the shock wave produced. In a flash fire scenario the main consequence of interest is the thermal radiation produced and direct flame contact. The size of the vapor cloud before ignition to a large extent determines the area of possible direct flame contact. Radiation

effects on a target depend on its distance from flames, flame geometry and emissive power, local atmospheric transmissivity and cloud size.

Where shock wave effects are significant in the consequence analysis, equivalent TNT models will be used to assess the effects on humans and the potential to produce fatalities. Assumptions will be made of ideal blast wave correlations based on shock wave energy to TNT equivalent energy. The limitation to the theoretical validity due to the differences between TNT detonations and vapor cloud deflagrations are ignored in this assumption. Leakage from a crack will be simulated with the computational fluid dynamics code and several ignition cases applied to this release of natural gas. The fire fatality predicted by the case that is most likely to occur, will be used in the consequence estimation for flash fires.

8.2.2 Fireball

Catastrophic rupture of a pressure vessel containing CNG will result in a rapid increase in the volume of the gas. This rapid mixing with air in the presence of an ignition source will form a fireball as soon as a flammable mixture is achieved. A sudden increase in volume of over 200 is usually required for a fireball [109] to occur. The estimation of the likelihood of ignition and consequence of fireballs is similar to the case of flash fire. Only the differences in analyzing the effects of a fireball will be discussed in this section.

The effects of interest in a fireball are:

- Thermal radiation
- Shock wave effects as the escaping gas expands in the atmosphere
- Highly energetic particles generated during the explosion and fire

Pressure effects from a fireball itself is limited in magnitude as ignition is instantaneous and burning is accompanied by further mixing and more burning which sustains the fireball. The pressure effect from the initial rupture of the CNG cylinder is considered separately. It should be noted that if the rupture was due to heating of the CNG cylinder as in a non-CNG fire or adjacent cylinders, then effects of fragmentation and shock wave would be relevant. Only rupture from degradation of a CNG cylinder is being considered in this analysis as the pressure relief devices are assumed to work and will release the contents of the cylinder before rupture will occur. This however will add to the volume of fuel available to the fire ball and significantly increase the dimensions of it.

Thermal radiation effect is the outcome that is of most significance in estimating the consequence of a fireball. More specifically the intensity as a function of time is the radiative characteristic that is of importance. This is so because the response of human skin to thermal radiation from a fire is dependent on the intensity and duration of exposure [110]. The burning time of large fireballs is less than ten seconds [111] which makes the duration of the radiation heat pulse comparable to that of a nuclear explosion [112].

The unconfined volume of the natural gas released when the cylinder ruptures, will burn as an unsteady turbulent diffusion flame in which buoyancy is induced by the burning process. The volume of the cloud and combustion process could be increased by the entrainment of ambient air at the edge of the burning cloud. Buoyancy-induced forces could lift the cloud to a semi-steady height. Thermal flux models [113], derived from empirical correlations from experiments with pure methane will be used to estimate the effects of a natural gas fireball. The thermal effects will be calculated by considering atmospheric transmissivity and surface emitted heat flux that for what would be a rapidly changing thermal flux. Assumptions will be made in determining exposure zones.

8.2.3 Jet Flame

A Jet Flame is formed from the pressurized release of CNG from a crack in the presence of an ignition source. This fire scenario tend to be localized in effect unlike the two types of fires mentioned above and the main concerns is to establish the potential for affecting other components rather than for affecting large numbers of people in the vicinity of a bus. Issues of flame height, trajectory and gas release velocity are important to determine the potential for lethal results.

In analyzing the outcome of jet flames, the effects of impingement on adjacent cylinders will no be investigated. Thermal radiation is the only consequence considered to be important and the following will be looked at in estimating the thermal effects:

- Discharge rate of natural gas.
- Fire duration and total heat released before flame burn-out.

- Estimated radiant fraction.
- Transmissivity of the atmosphere.
- Incident thermal radiation in the exposure zone.
- Thermal effects and potential for fatality.

The technique used in analyzing jet flames is similar to that used to analyze flares [114]. The assumption is that the radiant fraction of total combustion energy is derived from a point source along the jet flame path. Flame length and diameter will be estimated from theoretical models developed [115 - 116] with appropriate assumptions to determine actual length. No consideration will be given to the effects of cross wind on flame length even though this will give conservative results.

8.2.4 Confined Explosion

Ignition of a flammable mixture of natural gas inside a bus or depot can result in a deflagration or detonation. The confined explosion inside of a bus or building that is not vented for explosions usually will result in a deflagration. In a deflagration the combustion wave propagates away from the source at subsonic speeds, while supersonic speeds are achieved in detonations. Estimation of the peak pressure associated with the flame speed is required in order to determine the effects of the shock wave. Only pressure effects are considered as failure of structures and the implications for other related fatalities are not considered.

Some simplifying assumptions are made in determining the pressure rise from a confined explosion. These include:

- Heat loss is neglected as the explosion occurs sufficiently quickly.
- The pressure in the bus is uniform at any given time during the explosion for a deflagration.
- Maximum pressure rise is proportional to the mass fraction of the bus that is occupied by the gas/air flammable mixture.

8.2.5 Physical Explosion

The catastrophic rupture of a CNG cylinder will result in a release of the stored energy in the form of a shock wave. Fragments produced in the explosion will also be accelerated forming projectiles. In analyzing the consequence of physical explosions only the effects of the shock wave will however be considered. This is so because unstable crack growth leading to rupture as a result of corrosion fatigue is not expected to produce many fragments.

Failure of the cylinder will be assumed to occur at the maximum fill pressure of 3000 psig. All of the energy released in bursting of the cylinder will be assumed to be absorbed in producing the shock wave. This will give the maximum blast pressure from the shock wave. Implicit in this assumption is that no kinetic energy will be lost to fragments, no heating of the ambient air takes place by the released air and that at the point of failure brittle fracture occurs. These assumptions should not affect the validity of the results for a physical explosion of a CNG cylinder. This is so because the gas is

assumed to be at ambient temperature at failure and no energy is required to propagate the crack once unstable crack growth is predicted by the applicable failure criterion in Chapters 5 and 7.

8.3 Consequence Analysis Computational Procedures

Deterministic modeling will be used to quantify fire and explosion intensities that could lead to fatalities from the outcomes of the various fire scenarios discussed. The models estimates discharge rate of fuel released, dispersion hazards, fire and explosion risks including overpressure rupture and fragmentation hazards. Analyzing the consequence in terms of loss estimates, is primarily done by estimating the heat release rate, flame height, exposure temperature from fire plume modeling and estimating the time to achieving critical damage thresholds.

Quantifying the thermal radiation intensities of a fireball will be done using analytical models developed in laboratory scale experiments by Fay J.A et al [117]. Heat flux of a flash fire will be estimated from theoretical models developed by Raj P.K. et al [118] for burning of a large unconfined vapor cloud. Equivalent TNT models [119] will be used to determine the outcomes of physical explosion of the cylinder, confined and unconfined vapor cloud explosion. Fire inside the bus will be simulated using a computational fluid dynamics code, FDS, developed by the Energy Research Laboratory of the United States National Institute of Standards and Technology (NIST).

On the basis of the results of the calculated outcomes further calculations are done in order to arrive at the fire fatality associated with each fire scenario. Those calculations include:

- Calculates worst-case fire and explosive intensities, associated with each gaseous release that is ignited.
- Estimates fatalities from the heat flux and duration combination along with the explosive energy outcomes from each scenario.
- Plots the effect distances in determining the number of persons that would be affected based on the estimated occupation of the affected zone.

In general the calculated worst-case conditions are assumed for each of the fire scenarios. Both for the outcome of the fire scenario and the amounts of people affected. No mitigation will be considered as the time scale of events are expected to occur within one minute which would not give enough time for emergency response including evacuation. Each type of cylinder failure will be considered separately and the type of fire resulting will be analyzed based on the type of release, gas dispersion and subsequent ignition.

8.3.1 Modeling of a Jet Flame Outcome

A jet flame is will develop when the natural gas from a crack that has grown through the wall of a cylinder is ignited immediately. The dynamics of the flame is determined by rate of release as other factors such as obstruction and wind are ignored. The steps in determining the outcome in term of thermal radiation produced is shown schematically in

Figure 8.2. Since the release of natural gas from a crack invariably occurs at high velocities, only models of turbulent flames will be used in determining the outcome of jet flames.

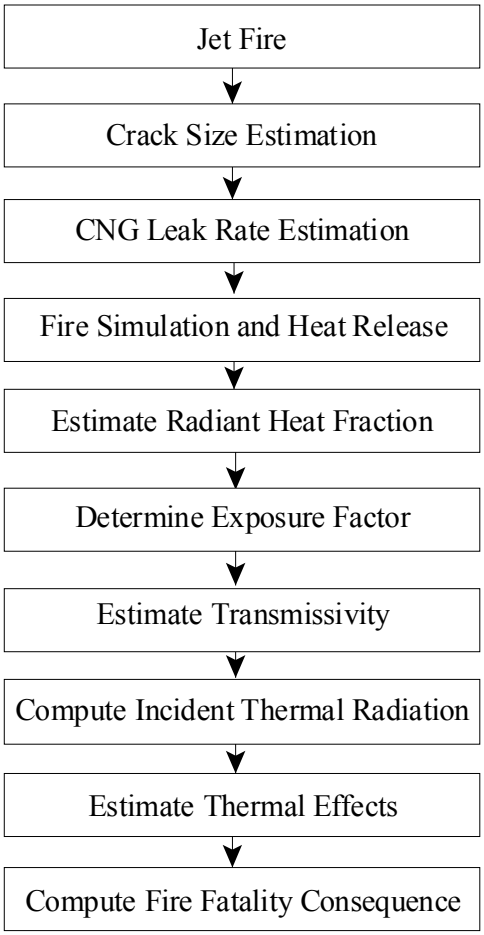

Figure 8.2 Flow Diagram of Jet Fire Consequence Calculations

In order to simulate the fire, the gas release rate had to be determined first. A method using crack tip opening displacement methodology was developed to quantify the release rate of natural gas. CNG released from a crack with a displaced opening in the

cylinder wall, is likely to issue as a momentum-dominated jet propelled by the pressure difference between the cylinder and the atmosphere. In free surroundings, the only external forces influencing the jet are gravitational, or buoyancy, forces. For natural gas, with a specific gravity relative to air of about 0.56, these buoyancy forces will cause the jet to rise. Thus, a natural gas leak under pressure will have the characteristics of a pure jet in the vicinity of discharge and the characteristics of a buoyant plume at distances further away from the point of discharge. For a small leak, e.g., through a hairline crack (no displacement at the mouth) in the cylinder wall, the leaking CNG will have little initial momentum and will act as a purely buoyant plume. A methodology developed for quantifying the leak rate from the former crack is now discussed.

8.3.1.1 Methodology for Determining Leakage Rate of CNG from Crack through Cylinder Wall

A defect that grows to become a through wall crack will result in leakage if the cylinder strength is not exceeded at the time of failure. This is described as leak-before break (LBB) failure. To estimate the leakage and thereby the potential for mixing and the formation of a flammable mixture, the flow rate through the crack has to be estimated which therefore requires the estimation of the crack opening. The probability of detecting the leak depends on its size and flow rate of gas. This probability along with the likelihood of detection will evaluated when analyzing events subsequent to initial the release of natural gas.

The method of crack tip opening displacement (CTOD) can be used to estimate the size of the opening when a LBB failure occurs. Crack opening is assumed to have the following properties:

(a) Crack opening is rectangular with a constant opening, δ.

(b) Crack has constant length of $2c$, where c is the crack half length.

(c) RMS surface roughness is assumed to be 10 %.

Tortuosity of typical naturally occurring cracks is uncertain as is surface roughness. Fatigue cracks have been known to be relatively straight in the depth direction with relatively little meander. Roughness of the crack of 10 % is believed to be reasonable [57].

Initial conditions for the leakage flow of CNG are taken at typical cylinder operating conditions of pressure of 3000 psig and temperature between 30 and 120 °F. The effects of reduction in flow across a section of the cylinder was not considered nor was the effect of obstructed flow resulting in discharge resistance caused by the presence of objects in the flow path outside of the cylinder.

Critical flow of gas for simple geometries will be used to estimate the actual flow. We will only consider isentropic gas flow from the crack. Using the Euler's equation of motion for an inviscid fluid in compressible critical flow [120], the upper bound gas flow rate can be estimated.

$$\left(\frac{dp}{dV}\right)_S = -\rho V \tag{8.1}$$

From the equation of continuity, the mass flow rate per unit area (mass velocity)

$$G = \frac{w}{A} = \rho V \tag{8.2}$$

This implies that from the Euler equation

$$G = \left(-\frac{dp}{dV}\right)_S \tag{8.3}$$

The variation of the states of the gas along the lines of constant entropy between the inside surface of the crack and the outside can be defined in a control volume as shown in Figure 8.3. The inside surface when the gas velocity is zero is one isentropic state. The isentropic stagnation pressure (p_0) is the normal cylinder pressure. This pressure is assumed to be 3000 psig.

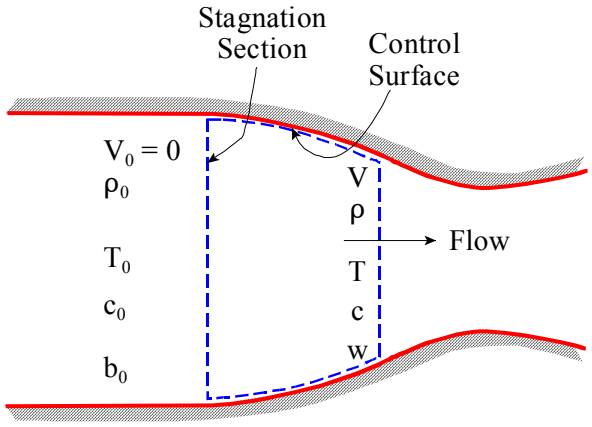

Figure 8.3 Flows between Stagnation and Other Sections [115], [120]

Since the leak from the crack is an isentropic process, the entropy at any point is equal. The enthalpy per unit mass at any state and the density may be expressed as functions of the entropy and pressure at that point as follows:

$$h = h(s, p)$$
$$\rho = \rho(s, p) \qquad (8.4)$$

Charts have been created for CNG representing the equations of state [121]. The value of the stagnation enthalpy, h_0, is independent of whether or not entropy change occurs since it has the same value for all states which are reachable from it under adiabatic conditions.

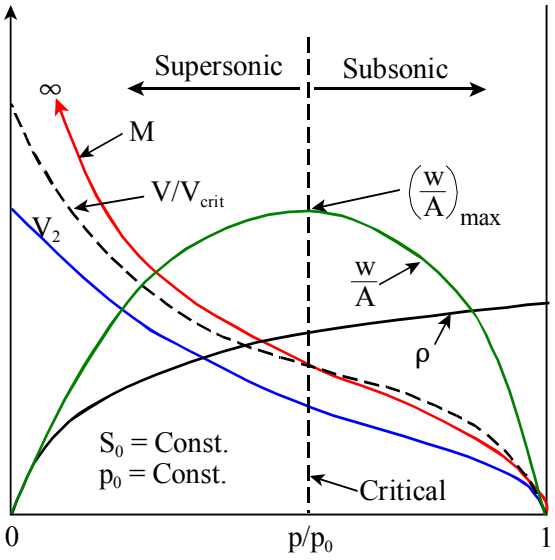

Figure 8.4 Typical Variations of Flow Properties in Isentropic Flow [120]

For a given stagnation condition performance curves can be constructed for the gas under any pressure change scenario. Typical curves for gases and vapors are shown in Figure 8.4. A most interesting feature of typical isentropic flow properties is that there is a maximum in the flow per unit area. The pressure ratio, (p/p_0) where the flow is maximized is called the critical pressure ratio. For CNG this pressure ratio is found to be approximately 0.542 [120]. This means that gas flow from the crack to the outside at atmospheric pressure will be experiencing choked flow. Under these conditions the velocity becomes constant at its maximum value.

The maximum velocity may be derived as follows:

$$\left(\frac{w}{A}\right)_{max} = \frac{p_0}{\sqrt{T_0}}\sqrt{\frac{k}{R}\left(\frac{2}{k+1}\right)^{\frac{k+1}{k-1}}} \qquad (8.5)$$

where *k*, is the ratio of the specific heats at constant pressure and constant volume [120]. Substituting for the mass velocity, *G*, which is equal to *w/A* from Equation 8.5 and simplifying the expression we get

$$V_{max} = \sqrt{\frac{p}{\rho}}\sqrt{k\left(\frac{2}{k+1}\right)^{\frac{k+1}{k-1}}} \qquad (8.6)$$

The maximum flow from the crack is therefore only dependent on the initial pressure to density ratio. Assuming that natural gas is a perfect gas, the pressure to density ratio is a constant with a value of 1.4×10^5 m^2/s^2
(1.51×10^6 ft^2/s^2). Using the value for methane which, has properties almost identical to natural gas, *k*, has a value of 1.32. Substituting these into Equation 8.6, the maximum velocity for the natural gas flow velocity through the crack is:

$$V_{max} = 250 \text{ m/s or } 820 \text{ ft/s} \qquad (8.7)$$

The crack opening displacement, δ, is then combined with the maximum velocity to estimate the maximum flow rate through the crack.

Crack opening displacement is influenced by plastic deformations at the crack tip and the cylindrical nature of the CNG vessel. Bulging of the cylinder at the crack site due to shell effects can significantly increase the crack opening displacement above say a flat plate in tension. Ideally these should be considered in calculating the crack opening displacement. The opening displacement of a typical crack is shown schematically in Figure 8.5.

Estimate of crack opening displacement is best determined by use of elastic-plastic relations between J-integral values and opening displacement. For purposes of this analysis crack opening displacement is separated into elastic and plastic components.

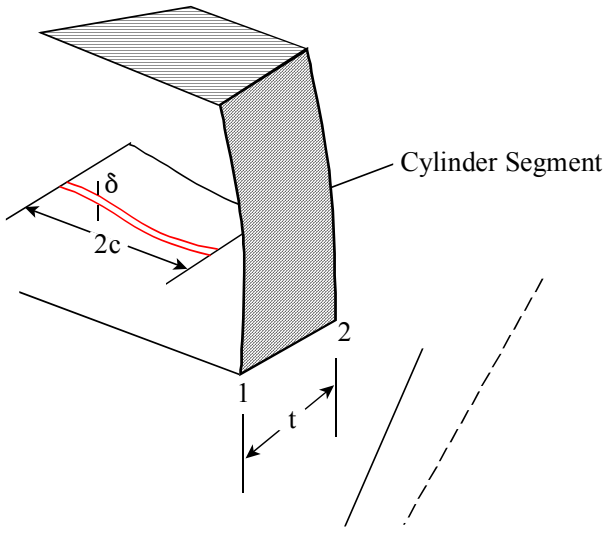

Figure 8.5 Schematic of Opening Displacement of Through Wall Crack in Cylinder

Elastic crack tip opening displacement is given by Equation 8.8, where the stress intensity factor, *K*, is related to the internal pressure applied [123].

$$\delta_{elastic} = \frac{K^2\left(1-\nu^2\right)}{\sigma_{YS}E} \qquad (8.8)$$

The plastic component is derived from an assumption that under plastic conditions the sections of the cylinder adjacent to the crack rotates about a hinge. The plastic displacement at the crack mouth, V_p, is related to the crack opening displacement by the relationship shown in Equation 8.9.

$$\delta_{elastic} = \frac{r_p\left(t-a\right)V_p}{r_p\left(t-a\right)+a} \qquad (8.9)$$

where, r_p , is the plastic rotational factor, a constant between 0 and 1 that defines the relative position of the apparent hinge point.

Because of the complexity involved and the absence of relevant data to accurately determine the crack opening displacement due to plasticity, only the elastic relationship will be used. This will give a conservative size for the crack opening, δ, and would represent a lower bound value of the opening displacement of a through wall crack

The lower bound opening displacement for a through wall crack of length 2*c*, in a cylinder subjected to a constant pressure, can therefore be determined from Equation 8.8

once the stress intensity factor is known. The minimum value of *c* is the thickness of the cylinder in accordance with the assumption of cracks having length of least twice the depth. The stress intensity factor at the crack tip will be used to determine the crack opening displacement. The flow rate, *Q*, from the rectangular crack opening is determined by multiplying the cross-sectional area of the crack opening by the velocity of gas through the opening.

$$Q = AV = 2c\,\delta\,V_{max} \tag{8.10}$$

8.3.1.2 Numerical Calculations of Leak Rate through Cylinder Wall

The maximum velocity of gas release from the crack in the cylinder wall is given by Equation 8.7. Equation 8.8 gives the crack opening displacement. The stress intensity factor that will be used to calculate δ, is the maximum for the different crack aspect ratios. Using crack with an aspect ratio of 0.2, the stress intensity factor, just prior to the crack growing through the cylinder wall, K_t can be determined from the stress intensity factor relationship in Chapter 4 for cracks in the sidewall and the transition region. The respective equations are Equation 4.7 and 4.9 which are repeated here.

$$K_I = \frac{pR}{t}\sqrt{\pi\frac{a}{Q}}\;F\left(\frac{a}{c},\frac{a}{t},\frac{R}{c},\phi\right) \tag{8.11}$$

$$K_I = \left(S_t + HS_b\right)\sqrt{\pi\frac{a}{Q}}\;F\left(\frac{a}{t},\frac{a}{c},\frac{c}{b},\phi\right) \tag{8.12}$$

From the stress concentration factor calculations, the maximum value is equal to 85.8 ksi-√in. Substituting into Equation 8.11 and 8.12, for the stress intensity factor and the other material properties, δ can be computed. The calculated crack opening displacement and flow rate results are:

$$\delta = 2.486 \times 10^{-3} \text{ in} \qquad (8.13)$$

$$Q = 77.06 \text{ in}^3/\text{s} \qquad (8.14)$$

8.3.1.3 Thermal Radiation from a Jet Flame and Effects

Immediate ignition of the plume of gas exiting the crack in the cylinder wall will result in a jet flame. The primary output of modeling a jet flame is the thermal radiation that it produces and is received at adjacent cylinders and on people in the vicinity of the fire. Fire duration is also estimated as it affects the potential for fire fatalities.

Combustion in a jet fire is believed to occur in the form of a strong turbulent momentum jet flame in a cross-wind [115], [113]. In order to compute the thermal effects we need estimate the flame length, heat released and the radiant fraction incident on a certain location. In the ensuing analysis the effects of cross-wind on flame shape and size will be ignored.

The length of a turbulent jet flame is has been shown by Hawthorne and Hottel [124], based on experimental data, to be approximately constant for natural gas being

discharged from a given nozzle diameter. A larger nozzle diameter will sustain a longer flame for the same velocity. In this analysis we will conservatively assume that the flame diameter is approximately half the length of the crack from which the gas is being released. This flame length remains constant even with increased fuel flow rate [115]. The relationship between flame length and diameter is shown in Equation 8.15.

$$\frac{L}{d_j} = \frac{5.3}{C_T}\sqrt{\left\{\frac{T_F}{\alpha_T T_j}\left[C_T + \left(1 - C_T\right)\frac{M_a}{M_f}\right]\right\}} \qquad (8.15)$$

where

L = length of turbulent flame

α_T = moles of reactant per mole of product
for stoichimetric natural gas - air mixture

C_T = fuel concentration in stoichimetric mixture

M_a, M_f = molecular weight of air and natural gas

T_F, T_j = adiabatic flame temperature and jet absolute temperature

Using the properties for methane which is the major constituent of natural gas, the constants in the expression are:

$$\alpha_T = 1.0$$

$$C_T = 0.091$$

$$M_a = 28.84 \qquad (8.16)$$

$$M_f = 16$$

$$\frac{T_F}{T_j} = 7.4$$

Substituting into Equation 8.15 we get the constant for the flame length to diameter ratio to be

$$\frac{L}{d_j} = 208.4 \qquad (8.17)$$

Using the assumed diameter of flame of half of the crack length, we get the flame length, L, to be

$$L = 328.2 \text{ inches} = 27 \text{ feet} \qquad (8.18)$$

All the models available references a circular nozzle velocity so the equivalent circular opening for the velocity and flow rate computed in Equations 8.7 and 8.14 will be used. This equivalent jet velocity is used to determine if flame blow-out stability is exceeded and therefore the inability to sustain a jet flame. Flame instability is established to be the point when the burning velocity is just less than the flow velocity anywhere in the jet downstream of the base of the jet flame. The critical value of the release velocity

of natural gas from the crack for blow-out to occur will depend on the burning velocity, density ratio and Reynolds number based on flame height along the axis of the jet.

Two established thermodynamic principles will be relied on to establish whether or not flame blow-out will occur. The first is based on the distance along the axis of the jet where the mean fuel concentration falls to the stoichiometric level. In a flame dominated by a momentum jet, the base of a stable flame will be lifted from the surface of the cylinder. It is unlikely that the base of this lifted flame will be downstream of the point along the jet where the fuel concentration is predicted to fall to the stoichiometric level. This distance along the axis of the jet is independent of the gas discharge velocity and is given by [125]

$$H = \left[4 \frac{\bar{\theta}_e}{\bar{\theta}_s} \sqrt{\left(\frac{\rho_e}{\rho_\infty} \right)} - 5.8 \right] d_e \qquad (8.19)$$

H = is the distance along the jet axis where the mean fuel concentration falls to the stoichiometric level.

d_e = effective nozzle diameter

$\bar{\theta}_e$ = fuel mass fraction at the crack exit

$\bar{\theta}_s$ = fuel mass fraction in the stoichiometric mixture of fuel and ambient air

ρ_e = is the density of natural gas

ρ_∞ = is the ambient air density

The effective nozzle diameter accounts for density differences between the jet and the ambient air. A relationship between the nozzle diameter and the effective diameter was given by Thring and Newby [126].

$$d_e = d\sqrt{\left(\frac{\rho_e}{\rho_\infty}\right)} \tag{8.20}$$

Using a diameter at two orders of magnitude greater than the crack opening displacement computed in Equation 8.13, we can effectively account for any possibility that plasticity would result in a much wider crack opening.

$$d = 0.2486 \tag{8.21}$$

Substituting into Equation 8.20, the effective diameter was calculated.

$$d_e = 0.1844 \text{ inches} \tag{8.22}$$

Methane as the predominant fuel in natural gas, the properties to be used to compute *H*, is as follows:

$$\begin{aligned} \bar{\theta}_e &= 0.95 \\ \bar{\theta}_s &= 0.055 \\ \rho_e &= 0.66 \text{ kg/m}^3 \\ \rho_\infty &= 1.20 \text{ kg/m}^3 \end{aligned} \tag{8.23}$$

Substituting the chemical properties of methane and the equivalent diameter into Equation 8.19, the result for the distance along the jet for formation of a stoichiometric concentration is

$$H = 8.39 \text{ inches} \tag{8.24}$$

The second principle is the critical exit velocity at blow-out of natural gas from the crack, forming a jet flame. This velocity is dependent on the stoichiometric distance, the maximum laminar burning velocity, the kinematic viscosity of natural gas and the ratio of the density of natural gas and ambient air. The laminar burning velocity is used because the maximum turbulent burning velocity will depend on the laminar velocity along with the local turbulence parameters and the fuel concentration at exit from the crack in the cylinder. This relationship has been expressed using dimensional analysis [127] as shown in Equation 8.25.

$$\frac{U_e}{S_u} = f\left(R_H, \frac{\rho_e}{\rho\infty}\right) \tag{8.25}$$

where

$$R_H = HS_u \frac{\rho_e}{\mu_e} \tag{8.26}$$

is the Reynolds number based on the length along the axis of the turbulent jet that the mean concentration equals the stoichiometric level, *H*, shown in Equation 8.26.

The universal stability limit of hydrocarbon jet flame based on research by Kalghatki [115], [128] is given by Equation 8.27.

$$\overline{U}_e = 0.017 R_H \left(1 - 3.5x10^{-6} R_H\right) \qquad (8.27)$$

The critical velocity at jet exit for natural gas is derived from Equation 8.27 and shown in Equation 8.28.

$$\overline{U}_e = \frac{U_e}{S_u}\left(\frac{\rho_e}{\rho_a}\right)^{1.5} \qquad (8.28)$$

where

$\overline{U}_e$ = non-dimensional critical velocity at exit from crack for a stable flame

ρ_e = the natural gas density at exit from the cylinder

ρ_a = the ambient air density

U_e = critical velocity at exit from crack for a stable flame

S_u = maximum burning velocity

R_H = Reynolds number

μ_e = dynamic viscosity of natural gas

Using the properties of natural gas and using the previously computed value of *H*, we can determine the critical at exit from the crack for blow out to occur. The properties natural gas used are taken from published values [115], [129] for methane as follows:

$$H = 0.21 \text{ m}$$

$$\rho_e = 0.716 \text{ kg/m}^3$$

$$\rho_a = 1.20 \text{ kg/m}^3 \qquad (8.29)$$

$$S_u = 0.52 \text{ m/s}$$

$$\mu_e = 0.0000116 \text{ Pascal second}$$

Substituting the values into Equations 8.26-8.38, we get the critical velocity of the gas discharge from the crack to be equal to

$$U_e = 131.7 \text{ m/s} \qquad (8.30)$$

The critical velocity computed is less than the flow velocity of natural gas from the crack, so blow-out is expected to occur. This result is consistent with the stability curves for various hydrocarbon fuels shown in Figure 8.6. From this figure the minimum jet discharge diameter for methane under conditions of choked flow, to sustain a stable diffusion flame is 41.4 mm. This dimension is larger than the maximum postulated opening in the cylinder wall.

We can therefore conclude that a flame cannot be sustained from the leakage of natural gas from a crack in a typical cylinder even if an ignition source is present. The result above was derived even without consideration for a cross wind and would be the

limiting conditions for a turbulent jet flame from a leak in a CNG cylinder in still air. The only fire scenario of interest for leakage of natural gas from a crack in a typical CNG cylinder is therefore the accumulation of gas and the delayed ignition, causing a flash fire. This will now be examined.

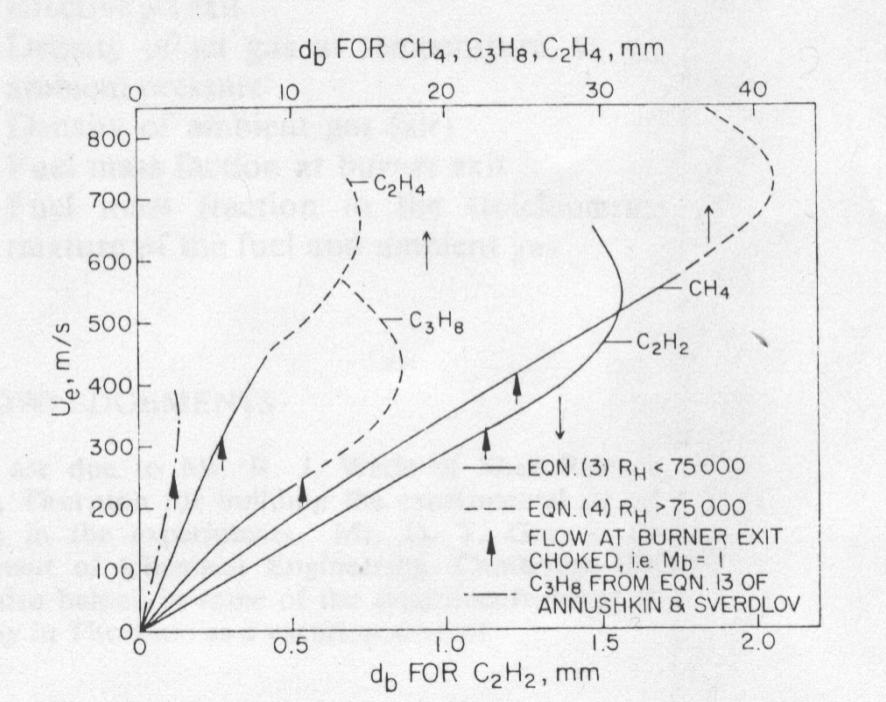

Figure 8.6 Stability Curves for Various Hydrocarbons Where Nozzle Exit Velocity Is Choked At Blow-Out [130]

8.3.2 Modeling Fireball Outcomes

A fireball is produced when there is a catastrophic rupture of a CNG cylinder and immediate ignition of the released gas. This requires the ignition source to be present and in sufficient strength to cause ignition of the fuel rich discharge in the flammable regions. The subsequent impingement of the flame produced in a flash fire or fireball caused by

leakage and rupture of one cylinder will cause the pressure relief device on the other cylinders to discharge gas, thus causing a fire ball of much larger proportions.

The step wise procedure to estimate the outcomes of a fireball is shown in Figure 8.7. Considerations of overpressure and fragmentation of a cylinder is covered in the other sections. Primarily the outcome that will have the greatest effect in terms of fire fatality is thermal radiation. Even though fuel rich natural gas vapor clouds are expected to burn rapidly, no significant over-pressure results from this fire scenario which could result in fatalities. On the other hand thermal radiation from the burning gases, are expected to be sufficiently intense to be considered hazardous.

The models for determining the emitted thermal flux are derived from empirical correlations from laboratory experiments using methane [131]. The radiation incident on a source in the affected area is computed by considering the atmospheric transmissivity, emitted flux and the view factor which is the degree to which a target would be exposed to the incident radiation. Once the radiation received is calculated then the effects can be determined in terms of fire fatalities.

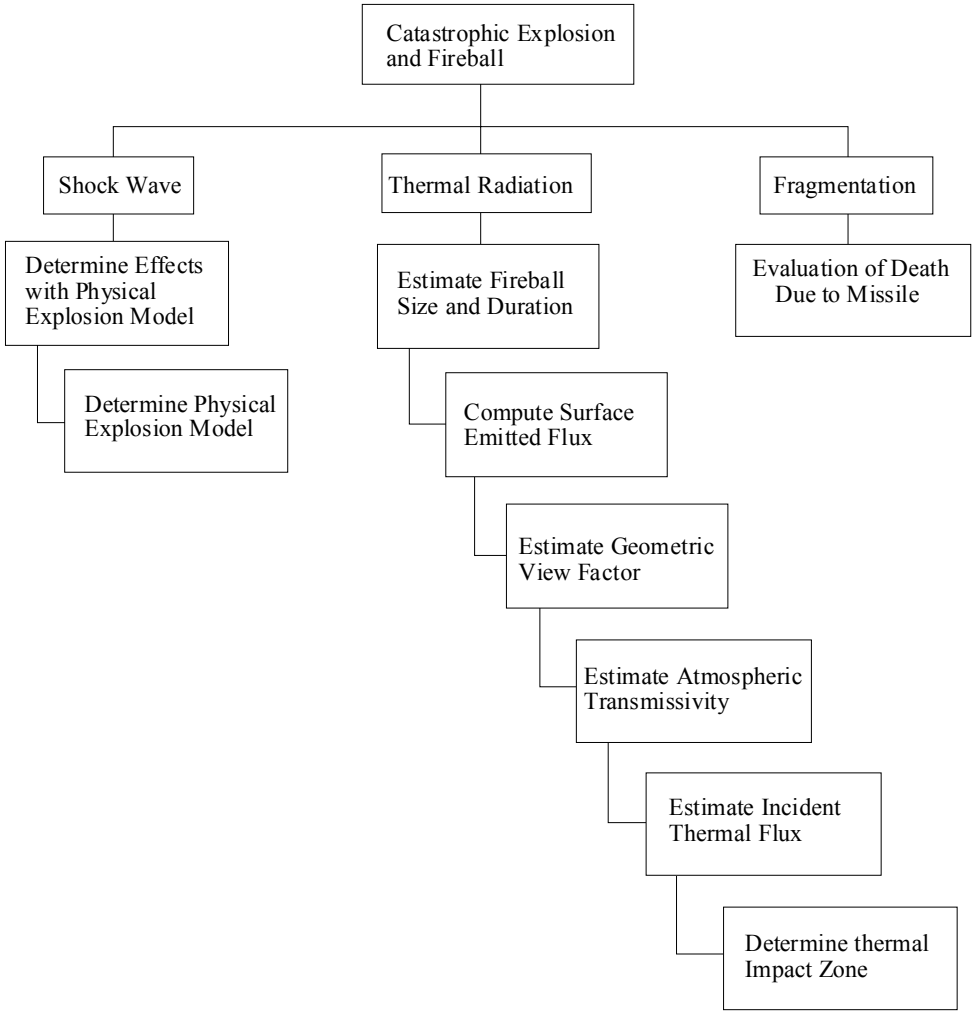

Figure 8.7 Logic Diagram for Explosion and Thermal Radiation Effects of Fireballs

8.3.2.1 Modeling Fireball Thermal Radiation

The initial volume of the fireball, V_0 will be estimated from the initial ground level hemispheric flaming volume before buoyant forces lifts it up. Maximum size, height and duration of burning of a natural gas fireball, can be estimated from relationships developed empirically for methane in small scale experiments [132], which have been validated in actual large scale accidents.

$$V = 111.22 V_f \tag{8.31}$$

$$d = 5.97 V_f^{1/3} \tag{8.32}$$

$$z_p = 9.47 V_f^{1/3} \tag{8.33}$$

$$t_p = 0.20 V_f^{1/6} \tag{8.34}$$

where

d = maximum diameter of fireball (m)

z_p = maximum height of the visible flame (m)

t_p = duration of the fireball (s)

V_f = initial volume of the CNG contained in the cylinder (m^3)

V = maximum volume of fireball

The transient geometry of the fireball may be expressed in terms of the dimensionless time after ignition, η, until burn-out as shown in Equations 8.35 and 8.36 [133].

$$d_t = 1.15 \eta^{0.84} \tag{8.35}$$

$$z = 2.80 \eta^{0.66} V_f^{1/3} \tag{8.36}$$

$$\eta = \frac{tg^{1/2}}{V_f^{1/6}} \tag{8.37}$$

The initial volume of the fuel-rich natural gas vapor cloud released from the cylinder, at

ambient conditions, could be estimated by assuming ideal gas behavior at constant temperature. If the entire water volume of a typical cylinder is released are then

$$p_{cyl} V_{cyl} = p_{atm} V_f \tag{8.38}$$

where

p_{cyl} = pressure in cylinder after filling

V_{cyl} = water volume of typical cylinder considered

p_{atm} = ambient atmospheric pressure

V_f = volume occupied by vapor cloud before mixing

For a typical cylinder being considered the physical properties are as follows:

$$\begin{aligned} p_{cyl} &= 3000 \text{ psi} \\ V_{cyl} &= 3051 \text{ in}^3 \\ p_{atm} &= 14.7 \text{ psi} \end{aligned} \tag{8.39}$$

Substituting into Equation 8.38 the initial volume occupied by the vapor rich cloud before mixing is calculated to be

$$\begin{aligned} V_f &= 6.23 \text{x} 10^5 \text{ in}^3 \\ &= 10.21 \text{ m}^3 \end{aligned} \tag{8.40}$$

Similarly substituting into Equations 8.31 to 8.34, the estimated maximum volume, diameter, height and time to burn out of the fireball is as follows:

$$V = 1135.46 \text{ m}^3$$

$$d = 12.95 \text{ m} \qquad (8.41)$$

$$z_p = 20.54 \text{ m}$$

$$t_p = 5.6 \text{ s}$$

The averaged normalized dimensionless heat transfer rate $\bar{v}$ for ethane, methane and propane, can be plotted as a function of dimensionless time as shown in Figure 8.8. The dimensionless heat transfer rate was normalized with respect to the initial volume of fuel.

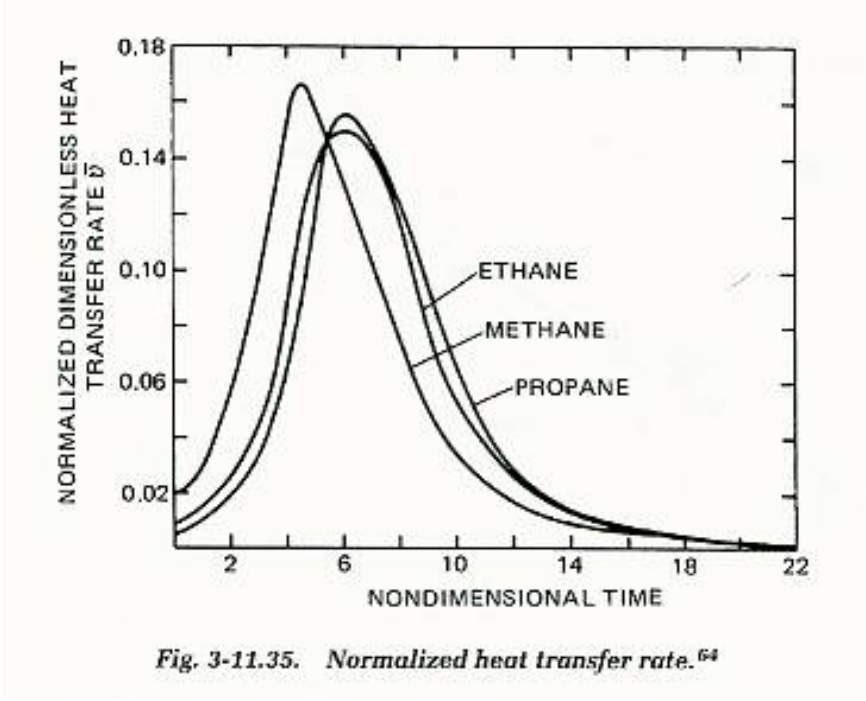

Fig. 3-11.35. Normalized heat transfer rate.[64]

Figure 8.8 Normalized Heat Transfer Rate as a Function of Dimensionless Time for Methane, Ethane and Propane [13].

It was deduced from the curves in Figure 8.8 that a dimensional scaling relationship exist and that the normalized dimensionless heat transfer rate is fuel dependent [134]. This could therefore be used to estimate the actual heat transfer rate, as a function of time, at any location in the vicinity of the fireball. The relationship is:

$$\dot{q}''(\eta) = \frac{\bar{\nu} f g^{1/2} \rho_f \Delta h_f V_f^{5/6}}{4\pi\left[x^2 + (z-h)^2\right]} \tag{8.42}$$

where

f = fraction of combustion energy which is radiated to the environment

τ = atmospheric transmissivity

ρ_f = density of vapor at ambient conditions (kg/m^3)

Δh_f = heat of combustion of vapor (kJ/kg)

x = horizontal distance to location of interest (m)

h = height above ground level of location of interest from fireball

Equation 8.42 will be used in an iterative process to plot a heat flux map around the bus in order to determine the effect of a fireball. The values of the parameters of interest to be used to in developing this profile map are as follows:

$$\begin{aligned} f &= 0.24 \\ \tau &= 0.85 \\ \rho_f &= 0.72\ (kg/m^3) \\ \Delta h_f &= 50020\ (kJ/kg) \end{aligned} \tag{8.43}$$

The fraction of combustion energy radiated to the environment by the fireball is conservatively estimated to be 0.24. Radiated fraction of heat has been found to vary between 0.20 and 0.24 [135] depending on the fireball size. It should be noted that for extremely large fireballs an estimate of 0.20 would over predict the surface heat flux of the fireball at the beginning of the burn cycle. Atmospheric transmissivity accounts for attenuation by scattering and absorption of the emitted radiation from a fire by water vapor in the air and carbon monoxide, at any arbitrary temperature and composition. The curve in Figure 8.9 [136] is used to estimate the constant value of 0.85, to be used in this analysis. This is a reasonable value based on the assumed relative humidity of the atmosphere and the expected path length.

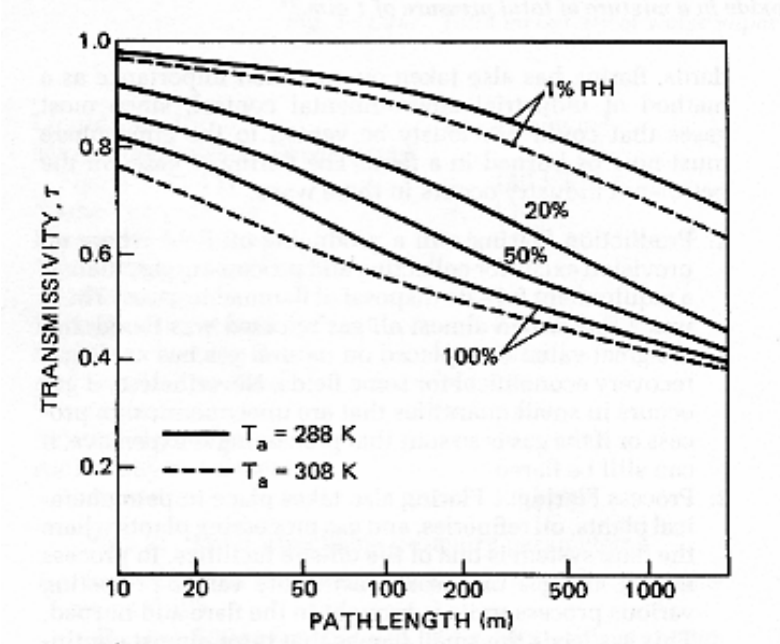

Figure 8.9 Transmissivity as a Function of Path Length [136]

8.3.2.2 Numerical Computation of Fireball Thermal Radiation

A numerical program written in MatLab was written to determine the time-dependent thermal flux. The program was based on solving the Equations described in the previous section at incremental time steps from the ignition to the estimated burn out time of the fireball. The real time is used to calculate the non-dimensional time, which is then used to estimate the geometry, location and heat flux from the fireball incident on receptors designated distances from the fireball. The chosen time step was every second. The natural log of the heat flux results are shown in contour maps for each time step in Figures 8.10 – 8.16.

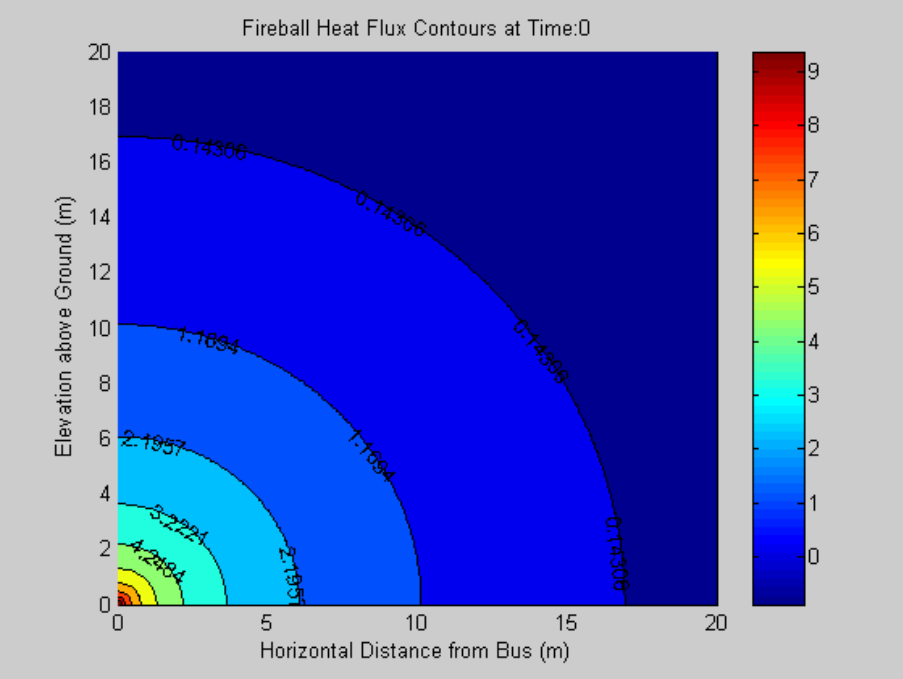

Figure 8.10 Heat Flux Contour Map at Ignition, t = 0.

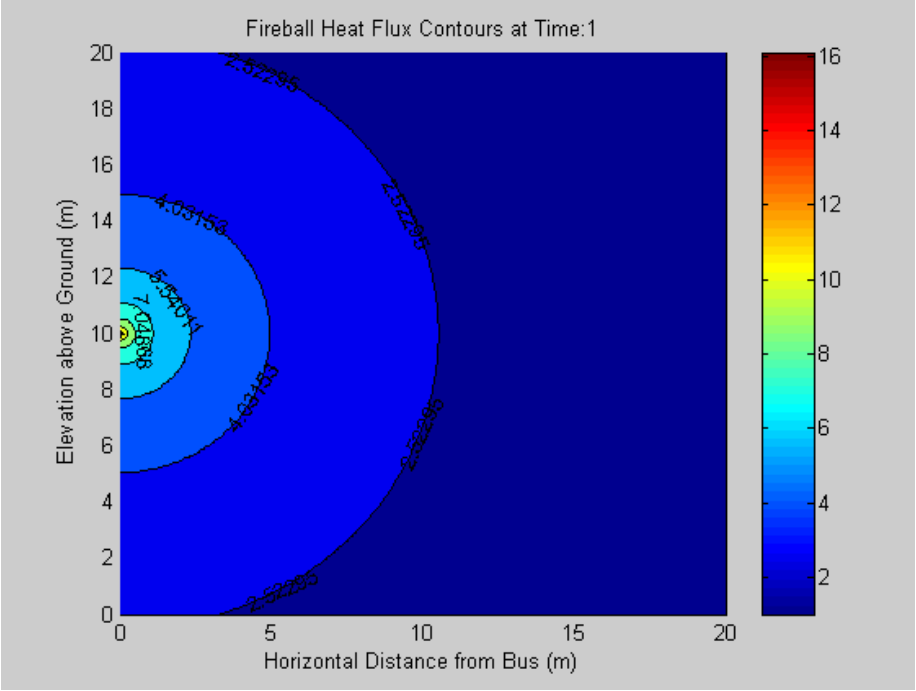

Figure 8.11 Heat Flux Contour Map after t = 1 second.

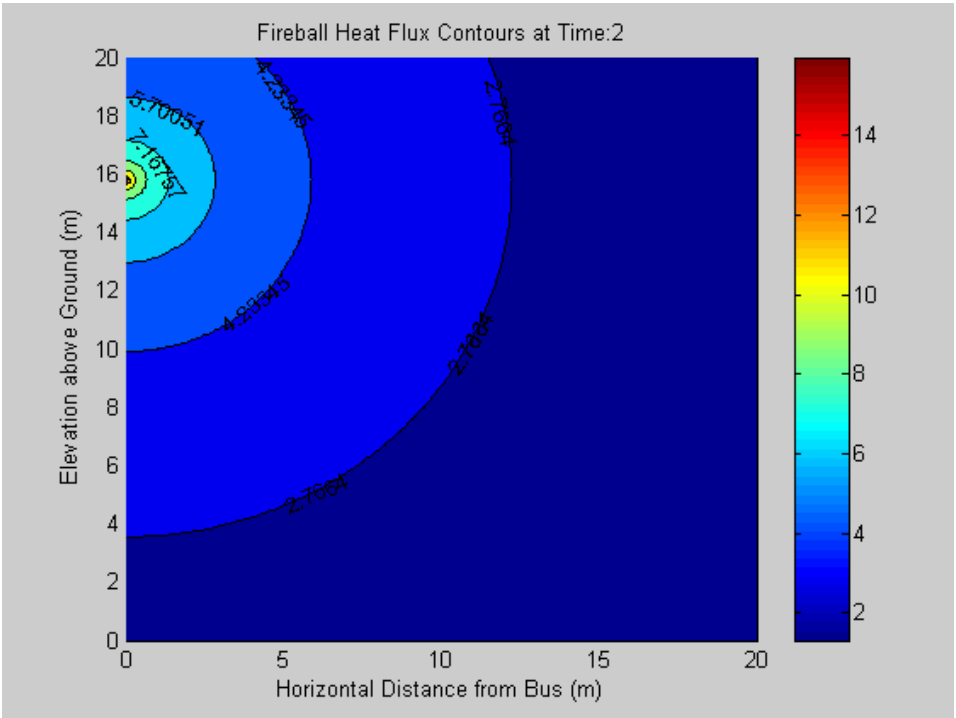

Figure 8.12 Heat Flux Contour Map after t = 2 second.

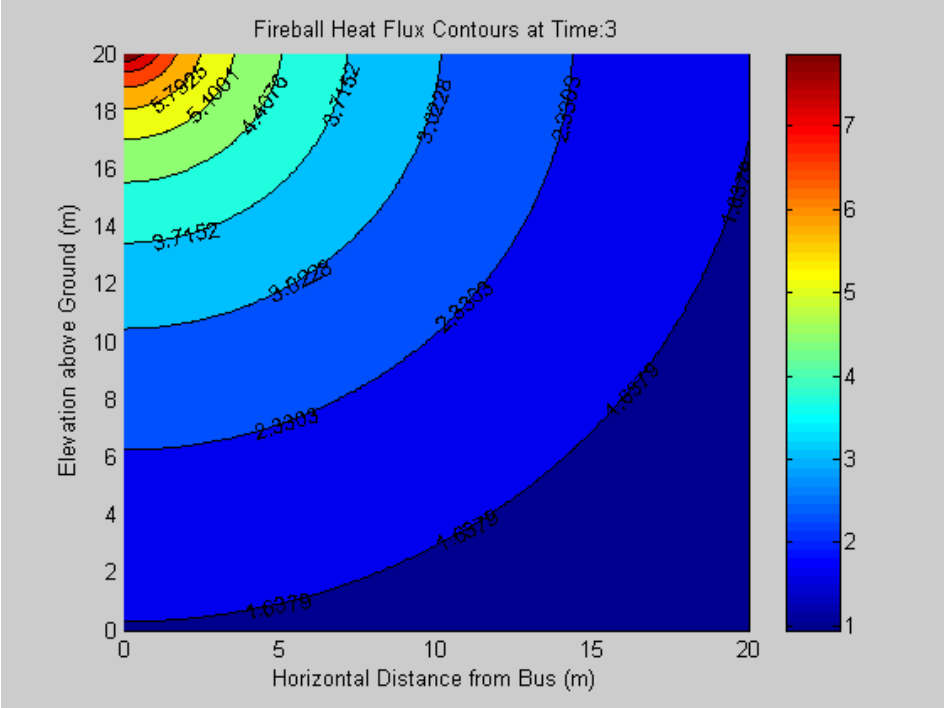

Figure 8.13 Heat Flux Contour Map after t = 3 second.

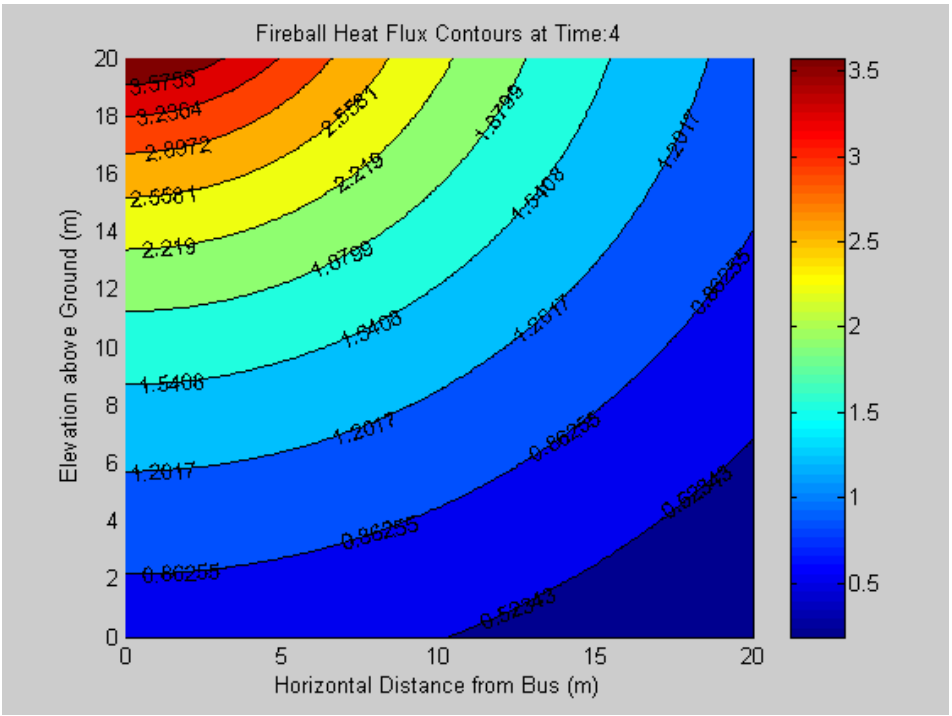

Figure 8.14 Heat Flux Contour Map after t = 4 second.

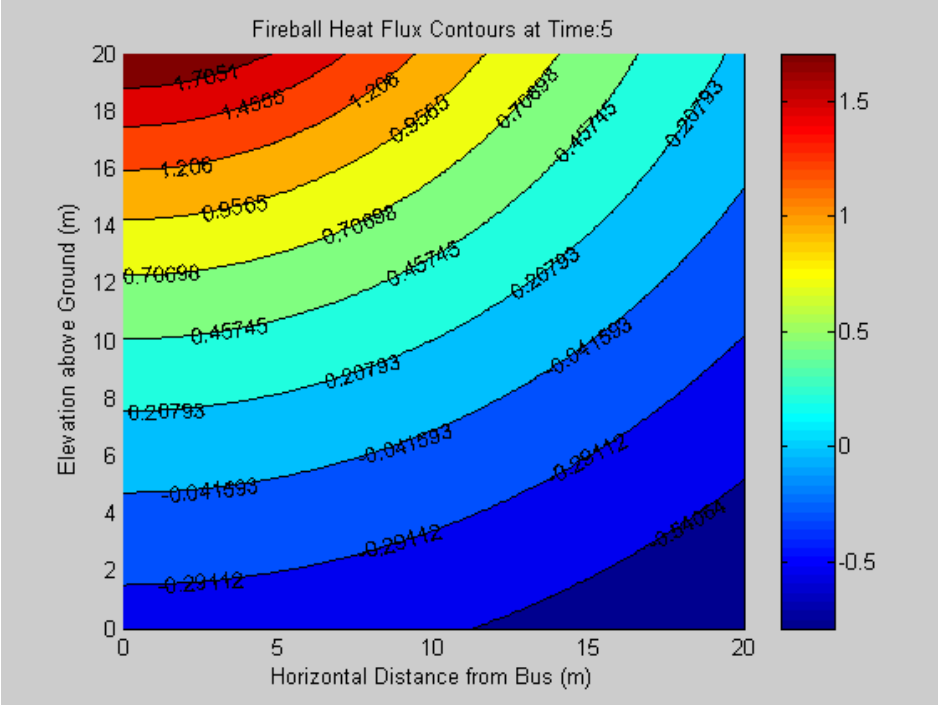

Figure 8.15 Heat Flux Contour Map after t = 5 second.

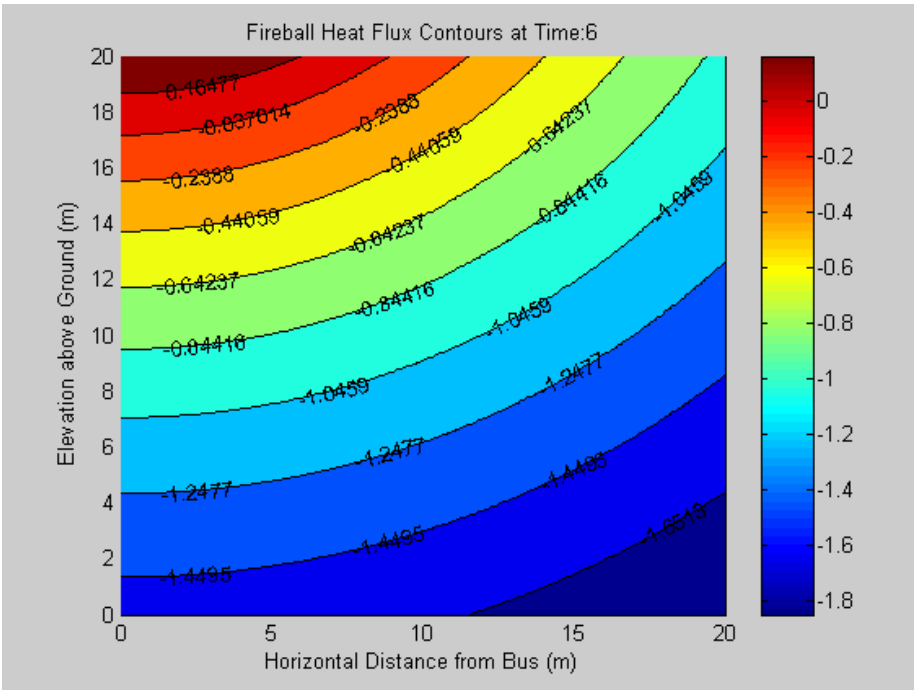

Figure 8.16 Heat Flux Contour Map after t = 6 second.

From Figures 8.10 to 8.16 the trajectory of the fireball from ignition until flame out after approximately 6 seconds is clearly shown. Figure 8.17 to 8.23 shows similar results for the natural log of the heat flux incident on receptors at specific horizontal distances from the bus, for constant height of 1.5 meters (5 feet). These results can be used to estimate the effects and potential for fatality for passengers and persons that may be within the vicinity of a typical bus who may be impacted by a fireball.

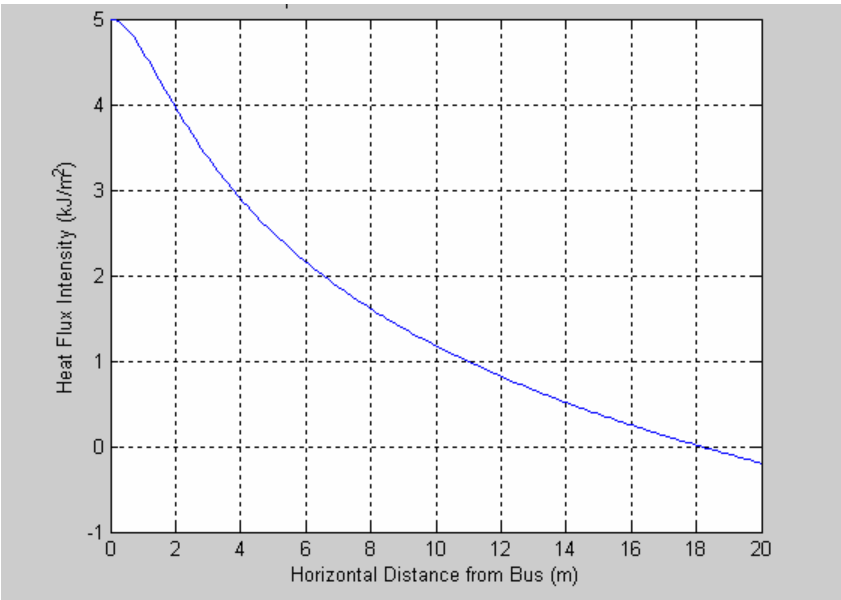

Figure 8.17 Heat Flux Intensity following Ignition, t = 0 second.

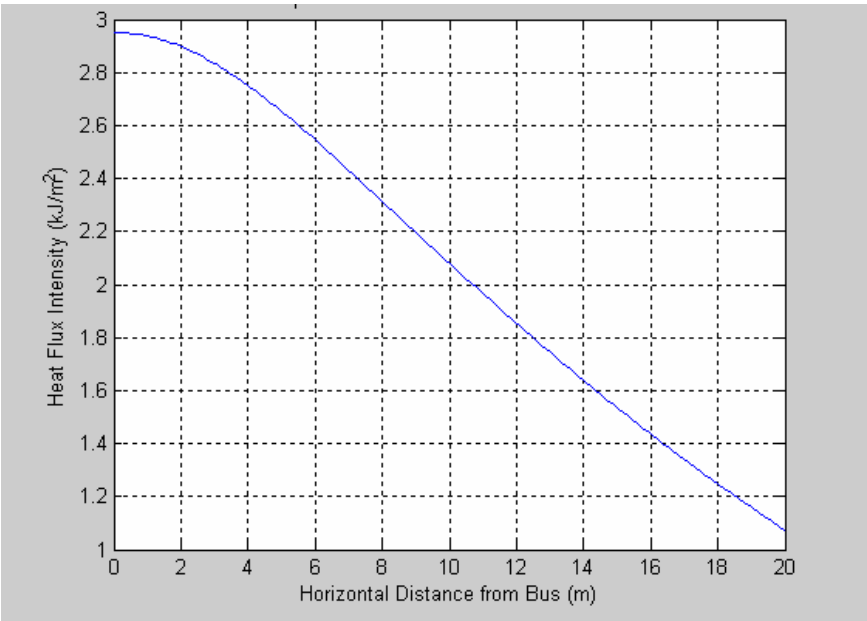

Figure 8.18 Heat Flux Intensity after t = 1 second.

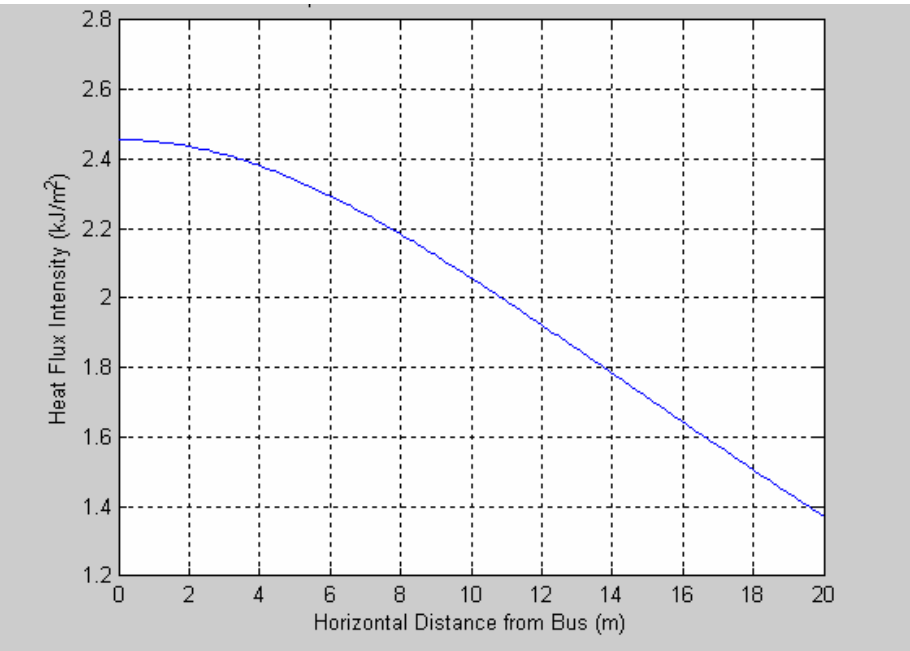

Figure 8.19 Heat Flux Intensity after t = 2 second.

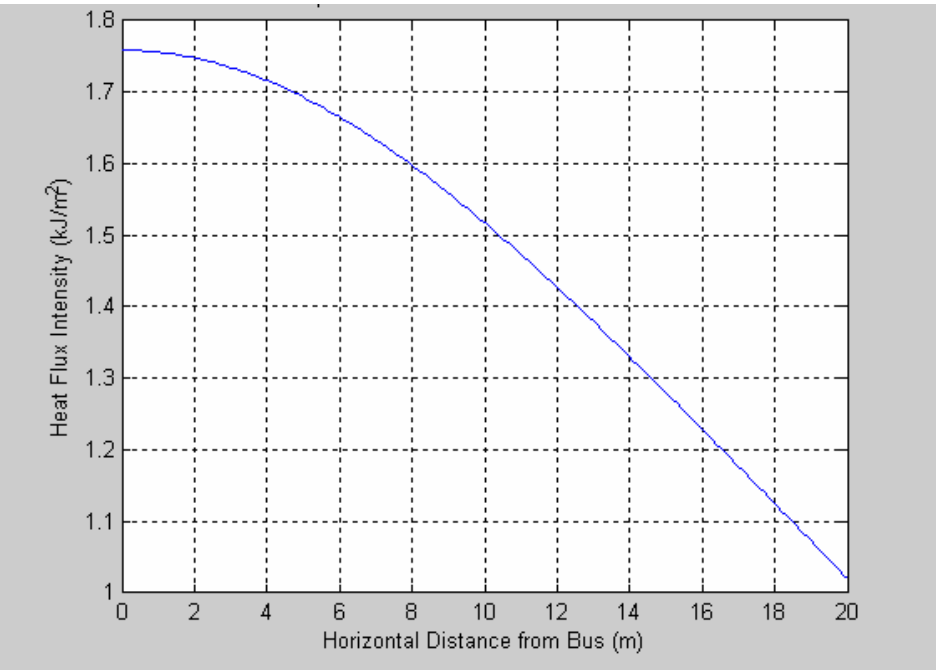

Figure 8.20 Heat Flux Intensity after t = 3 second.

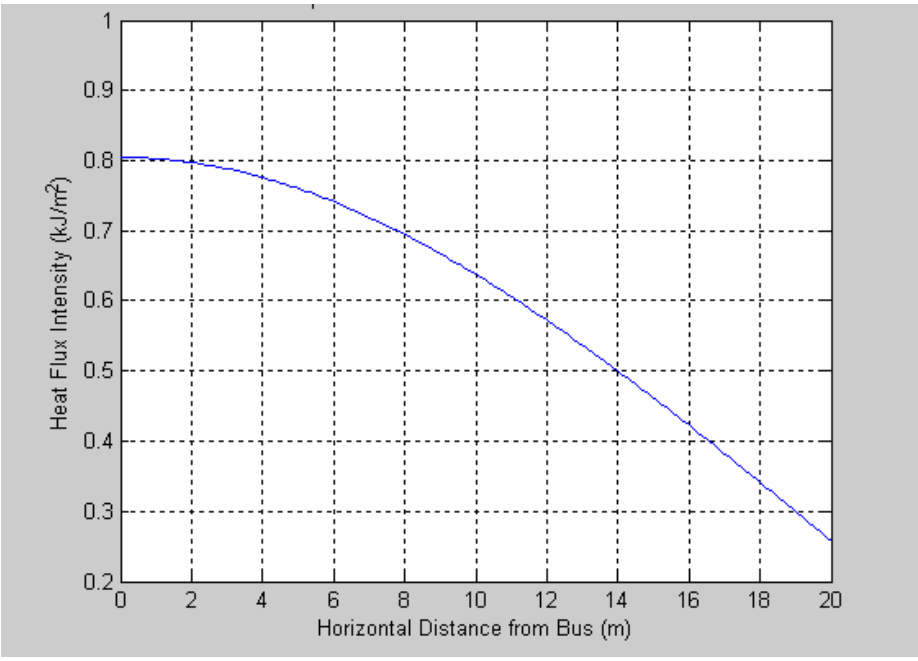

Figure 8.21 Heat Flux Intensity after t = 4 second.

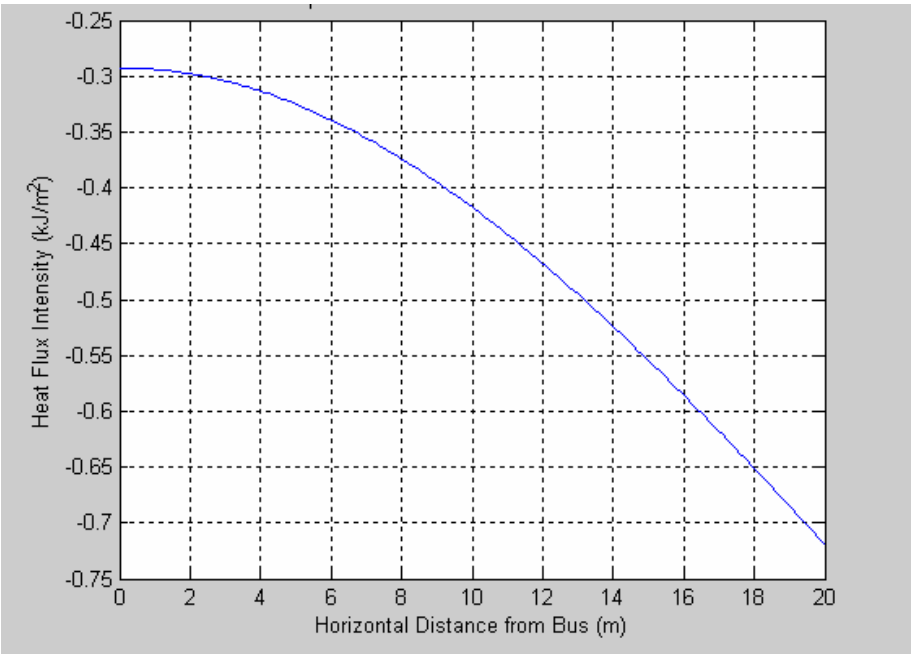

Figure 8.22 Heat Flux Intensity after t = 5 second.

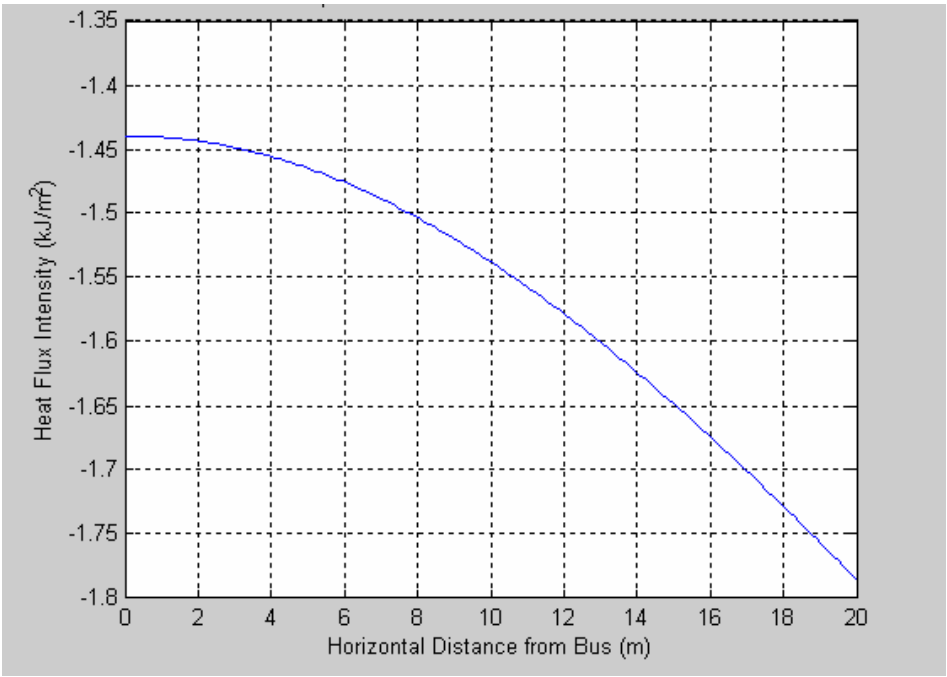

Figure 8.23 Heat Flux Intensity after t = 6 second.

8.3.2.3 Computation of Secondary Fireball Thermal Radiation

A secondary fireball will be formed from the fireball caused from catastrophic rupture of the CNG cylinder. The intense heat produced causes the pressure relief device on the cylinders to rupture, releasing the entire contents of the other five cylinders. For simplicity the secondary fireball is assumed to burn independently and not interacts with the first one. Also it is assumed that ignition of the secondary fireball will occur when the entire contents of the five cylinders are released. The volume of fuel available to this fireball is five times the volume of the initial fireball as shown in Equation 8.44.

$$\begin{aligned} V_{f_{sec}} &= 5V_f \\ &= 51.1\ m^3 \end{aligned} \tag{8.44}$$

Duration of the secondary fireball can be calculated from Equation 8.34 and is

$$t_{p_{sec}} = 7.7\ s \tag{8.45}$$

The procedure for computing the outcome of the secondary fireball is identical to the initial fireball. The results for the natural log of the heat flux at a height of 1.5 m, and at specified horizontal distances from the bus, at two second intervals is shown in Figures 8.24 to 8.28. It should be noted that a flash fire will produce a secondary fireball as well. The results here will be used to estimate the effect and potential for fatality for secondary fireballs in both cases.

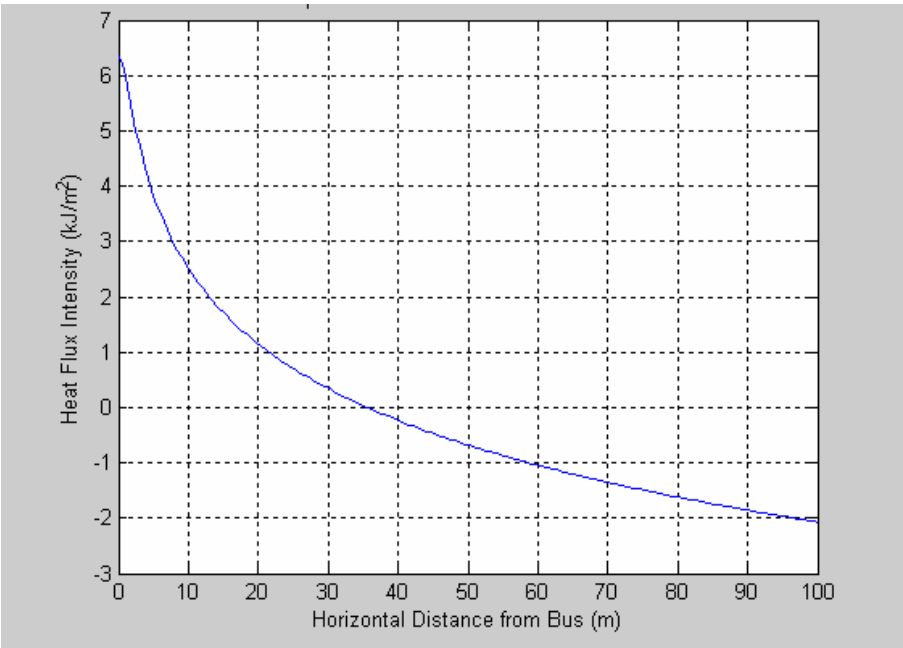

Figure 8.24 Heat Flux Intensity after Ignition, t = 0 second.

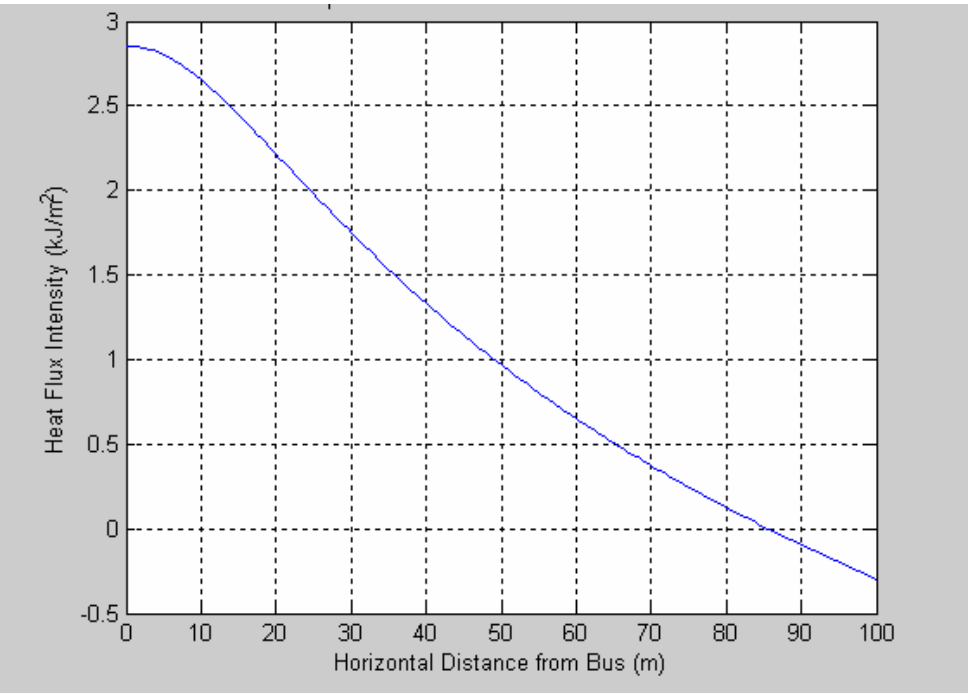

Figure 8.25 Heat Flux Intensity after t = 2 second.

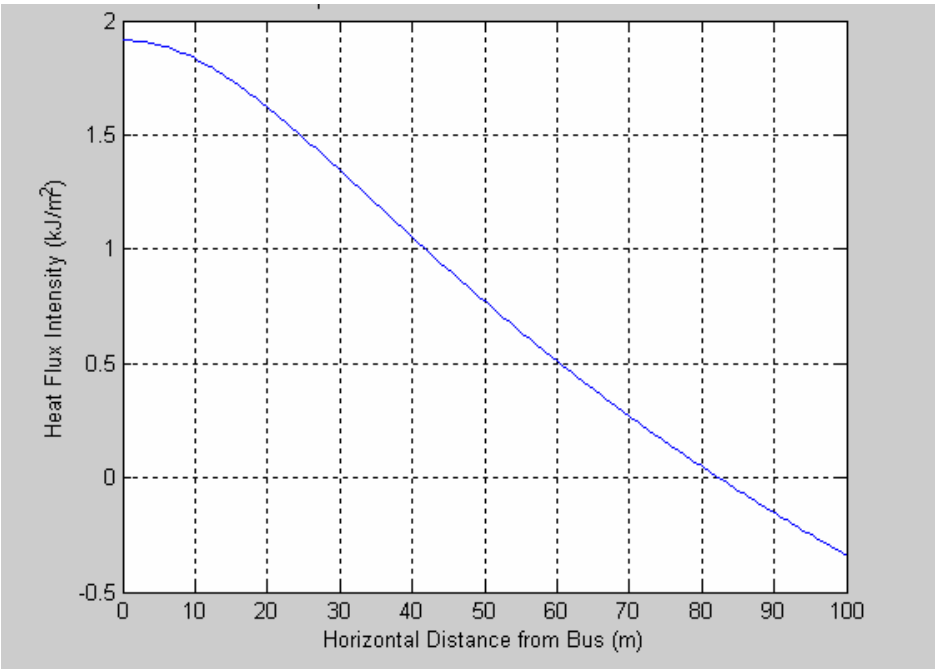

Figure 8.26 Heat Flux Intensity after t = 4 second.

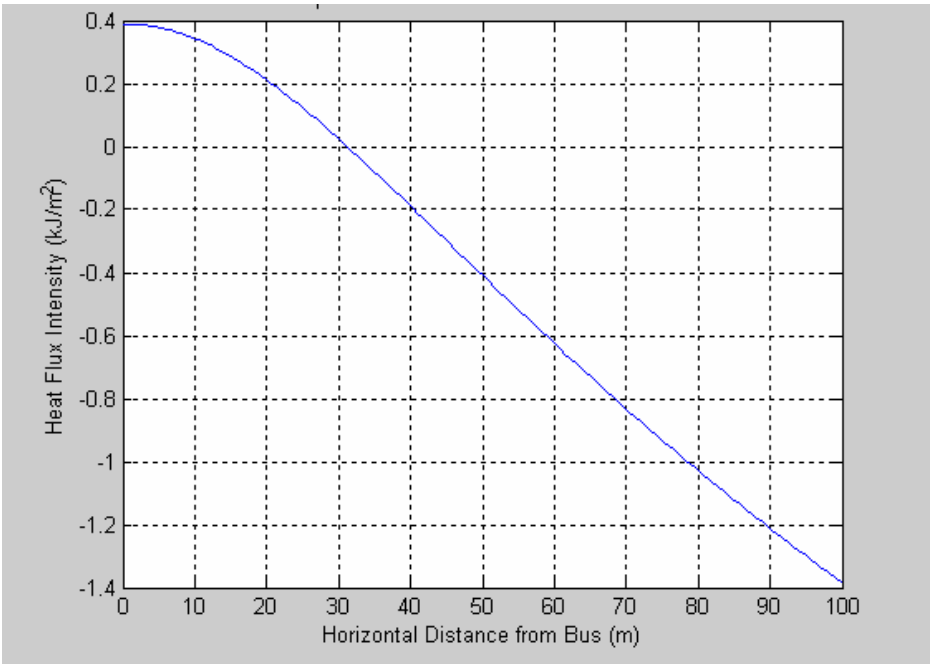

Figure 8.27 Heat Flux Intensity after t = 6 second.

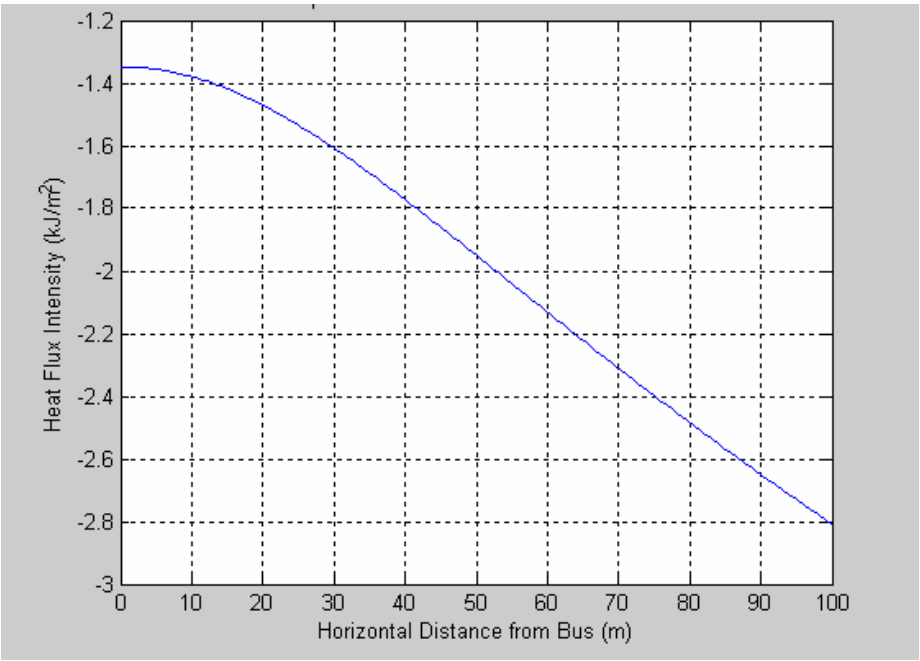

Figure 8.28 Heat Flux Intensity after t = 8 second.

8.3.3 Modeling of Vapor Cloud Explosion and Flash Fire Outcome

The two outcomes of interest associated with the delayed ignition of a CNG release that have accumulated over time are unconfined vapor cloud explosion and flash fire. Release of a small amount of CNG has been shown historically to result in a flash fire without significant overpressure. Experimental work [137] shows that some form of confinement and vapor cloud turbulence is required for damaging overpressure to occur. There is also indication that initial vapor cloud must be above a critical size for flash fire to be accompanied by damaging overpressure. Notwithstanding that the combustion process of large vapor clouds are not completely understood and no analytical models exist to full describe the chemical reactions and the corresponding physical phenomenon. Figure 8.29 is a logic diagram of the steps in calculating the effects of a vapor Cloud Explosion and Flash Fire.

Correlations for flammable mass versus vapor cloud explosion probability based on historical data [138] suggest that there is a probabilistic relationship between the mass of fuel released and the likelihood of a vapor cloud explosion accompanying a flash fire. This relationship is evaluated in the Likelihood of Ignition section of Part III. The result of this likelihood is used in computing the risk due to individual fire events.

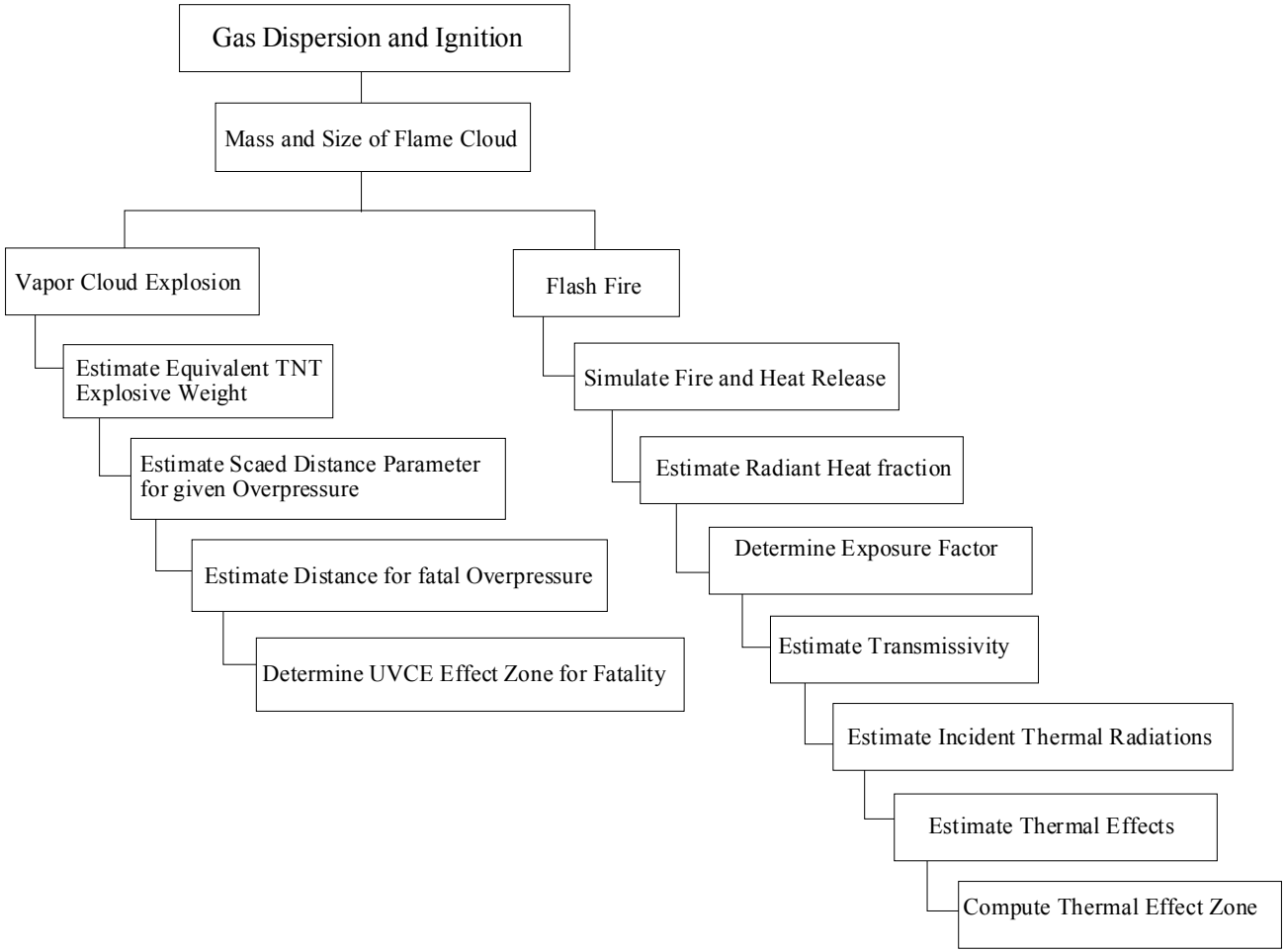

Figure 8.29 Logic Diagram of Vapor Cloud Explosion and Flash Fire Outcomes

We can see from the logic diagram that thermal as well as over pressure effects are important in modeling the effects of flash fires. Overpressure effects are significant depending on flame acceleration to produce detonation instead of deflagration effects. The two most important mechanisms that affect flame acceleration are thermal expansion and turbulence. The presence of the bus structure around the cylinders and the cylinder compartment itself, contribute to partial confinement and turbulence. In the event of a flash fire the effects of an unconfined vapor cloud explosion will be present.

Modeling of the outcome of a flash fire is similar to the procedures for a fireball. The main distinction being that the vapor cloud is widely dispersed before ignition takes place. The ignition source is usually away from the natural gas release unlike a fire ball where the source is present to cause immediate ignition. The likelihood of ignition of a flash fire is developed in Chapter 10 along with the likelihood of other events subsequent to the natural gas release. In this part of the analysis a flammable mixture and delayed ignition is presumed to occur. Important parameters in analyzing combustion incidents are as follows:

- Flammable limits of natural gas
- Auto-ignition temperature
- Heat of combustion
- Molecular weigh and
- Combustion stoichiometry

A flash fire is in the form of a propagating plume, producing an unsteady diffusion flame. Models for the effects of radiation are not well developed, however a combination of simulation using CFD and analytical modeling will be used to determine the transient incident radiation within specific zones. In the case of vapor cloud explosion a TNT model will be used. This model is based on the assumption of equivalence between the flammable material and TNT, factored by an explosion yield term.

8.3.3.1 Estimation of Natural Gas Flash Fire Radiation

Determining the geometry of the vapor cloud over time is fundamental in estimating the thermal radiation field surrounding the diffusion flame. Estimating the emissive power and finally the radiant intensity at a given location, as shown in Figure 8.29, is important in determining the thermal effects of a flash fire. As was said earlier the two conditions for a burning cloud; presence of an ignition source away from the gas release; and a flammable mixture of natural gas is presumed to exist. The dispersion of the natural gas before ignition, flame propagating velocity, geometry and thermal radiation will now be estimated.

8.3.3.2 Modeling of Natural Gas Dispersion

Theoretical predictions have shown that natural gas released from high pressure storage could be heavier than air at exit [139 - 140]. High pressure release of natural gas has been found to disperse as a dense cloud [141] close to the floor and does not rise immediately. Analytical results show that the large pressure difference between a CNG fuel cylinder and the atmosphere expands the released gas adiabatically. During

expansion the gas exiting from a crack becomes cold (calculated to be -260^0 F or 112 K), increasing the density to approximately 1.5 times greater than that of surrounding air.

The fuel rich discharge jet of gas, initially above the upper flammability limit, undergoes turbulent mixing with ambient air, resulting in a flammable mixture at the edges of the vapor cloud [142]. This occurs because the high velocity release from a crack produces a momentum dominated jet which moves the gas in the direction of the gas jet and causes rapid mixing with air. Analyses have shown that the diluted gas continues to move along the jet axis or in the direction it is deflected by a solid object. This continues until the magnitude of the inertial forces due to the initial momentum diminishes and the cloud then becomes a buoyant plume, remaining close to the ground for a significant amount of time. Crosswind will affect the dispersion and shape of the final vapor cloud. Some simplifying assumptions will be made for the purposes of this analysis as follows:

- The release of natural gas, mixing and formation of a buoyant cloud occurs in less than five minutes.
- This cloud will be formed adjacent to the typical bus configuration shown in [1].
- The shape of the cloud is rectangular and follows the profile of the bus undercarriage.
- Effect of cross wind and bus motion on the shape of the vapor cloud is ignored.

The extent of the vapor cloud could be estimated by assuming ideal gas behavior at constant temperature and using the same procedure as shown in Section 8.3.2.1. Equation 8.46 was used to estimate the initial volume of natural gas at ambient conditions that was released

$$p_{cyl} V_{cyl} = p_{atm} V_f \tag{8.46}$$

where

p_{cyl} = pressure in cylinder after filling

V_{cyl} = water volume of typical cylinder considered

p_{atm} = ambient atmospheric pressure

V_{atm} = volume occupied by vapor cloud before mixing

Using the same typical cylinder physical properties as follows:

$$\begin{aligned} p_{cyl} &= 3000 \text{ psi} \\ V_{cyl} &= 3051 \text{ in}^3 \\ p_{atm} &= 14.7 \text{ psi} \end{aligned} \tag{8.47}$$

The volume occupied by the vapor rich cloud before mixing is calculated to be

$$V_f = 6.23 \text{x} 10^5 \text{ in}^3 \tag{8.48}$$

From this we can estimate the volume of air-natural gas mixture that would be rendered flammable by leaking the entire contents of the cylinder from a crack. The

flammable mixture would be bounded by the upper and lower flammability limits of natural gas, which is approximately 15 and 5 percentage by volume respectively [115]. Substituting these values we get the maximum and minimum flammable air-natural gas mixture.

$$V_{MaxFL} = 12.5x10^{6} \text{ in}^3 \tag{8.49}$$

$$V_{MinFL} = 4.2x10^{6} \text{ in}^3 \tag{8.50}$$

Using the dimensions of a typical large school bus [143], which are 40 ft long and 8 ft wide, we can estimate the thickness of the vapor cloud. The cloud is assumed to follow the rectangular profile of the bus undercarriage, extending by 4 ft outside the bus profile. Accounting for the obstructed volume of the bus, the minimum and maximum vapor thickness (height of the vapor cloud) is calculated to be:

$$\delta_{max} = 13.6 \text{ ft} \tag{8.51}$$

$$\delta_{min} = 7.33 \text{ ft} \tag{8.52}$$

From the above we can conclude that the vapor cloud when fully dispersed would surround and completely enclose the bus. Seepage of natural gas into the bus compartment, will therefore likely result in a vapor cloud explosion inside the bus. The profile of the vapor cloud fire is shown in Figure 8.30.

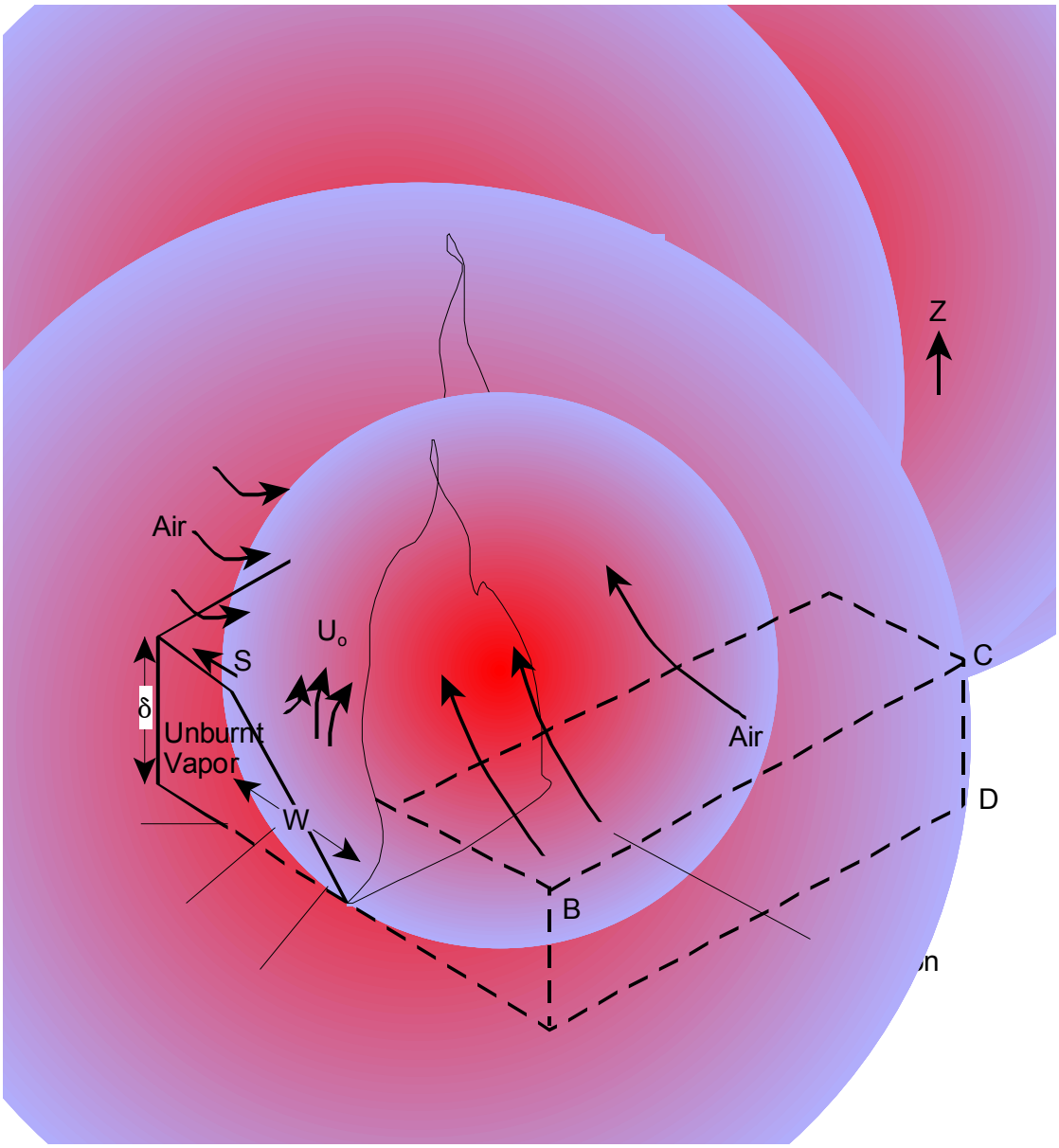

Figure 8.30 Profile of the Unconfined Natural Gas Vapor Cloud [147]

In modeling the flame velocity and thermal radiation we are concerned with unsteady diffusive burning of the unconfined vapor cloud. The dimensions of the cloud were determined by assuming uniform mixing of the gas released from the turbulent jet. Even

if that is not the case the results for thermal radiation would not be affected. This is deduced from the fact that the cloud would be diluted with air at the edges. Ignition of the flammable regions will cause a flame to propagate through these regions. Combustion then proceeds as an unsteady diffusive burning in which gravitational buoyancy forces mix air into the vapor cloud, further propagating the flame and ultimately consuming the entire released natural gas vapor.

8.3.3.3 Modeling Unconfined Vapor Cloud Flaming Characteristics

Immediately following ignition, flames begin to spread in all directions away from the ignition source. Frame travel will be uniform in all directions if the entire mixture is flammable and the vapor cloud is over the ignition source. Initially the flames produced are contained within the cloud propagating through regions where the mixture is most flammable. Subsequently the flames become extended in the form of buoyancy driven turbulent fire plume above the vapor cloud.

In the transient period of flame growth an average flame propagation velocity with respect to ground can be established. This is given by adding the wind speed to the burning velocity. The maximum laminar burning velocity of methane flame is found to be approximately equal to 0.5 m/s [113], [115]. Laminar flame speed for an unconfined methane cloud fire was found to be approximately 3.5 m/s [113]. Turbulent flame propagation velocity of natural gas, S, is expected to be similar. For this analysis we will approximate the value of, S, for a burning vapor cloud to be

$$S = 4.0 \text{ m/s} \qquad (8.53)$$

This will be used to estimate the transient behavior of the flame over time as well as the thermal radiation produced.

Another important transient characteristic of the flash fire that determines the amount of thermal radiation that it produces is the ground level width. A theoretical model is given by Raj and Emmons [145]. This model is based on the principle that the plume is characterized by the heating source. That is the rate of burning controls the plume characteristics which is itself a function of the gas velocity within the plume. The essential features of the model as it relates to the natural gas vapor cloud bus fire are shown in Figure 8.31. The difference between a flash fire and a fireball can be seen by comparing with the equivalent fireball fire in Figure 8.32.

The flame width as a function of time for experimentally derived values flame height-to-width ratio and flame propagating velocity, is shown in Equation 8.54. [145].

$$\tau = \left(\frac{F_f}{F}\right)^{\frac{1}{3}} \left\{ \frac{\pi}{3\sqrt{3}} + \frac{2}{3} \ln\left[\frac{\sqrt{\chi^2+\chi+1}}{(1-\chi)} \right] - \frac{2}{\sqrt{3}} \tan^{-1}\left[\frac{2}{\sqrt{3}}\left(\chi + \frac{1}{2}\right) \right] \right\} \qquad (8.54)$$

and

$$\chi = \sqrt{\left[\left(\frac{F}{F_f}\right)^{1/3} \xi \right]} \qquad (8.55)$$

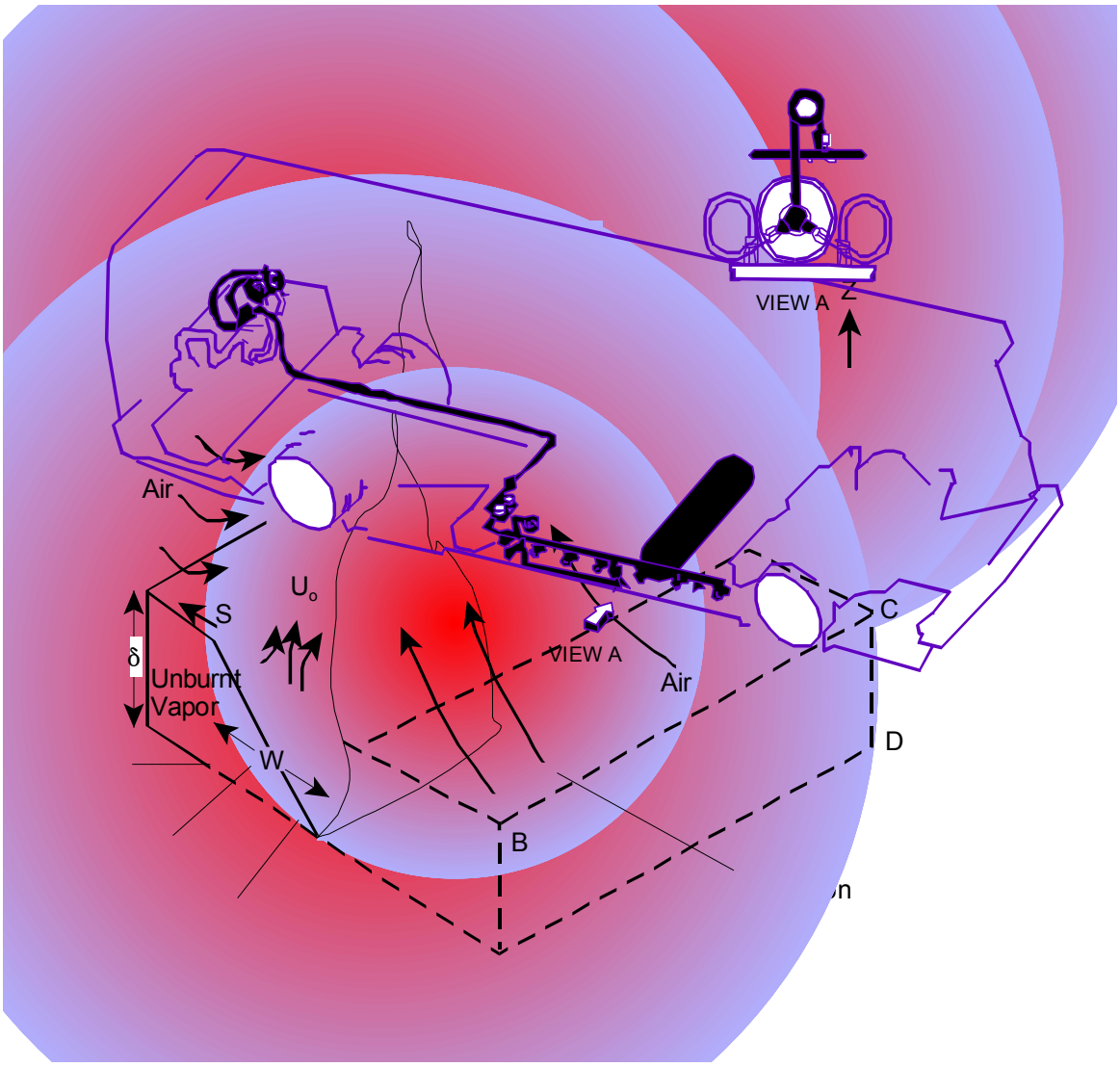

Figure 8.31. Schematic Diagram of the Unconfined Burning of a Flammable Natural Gas Vapor Cloud

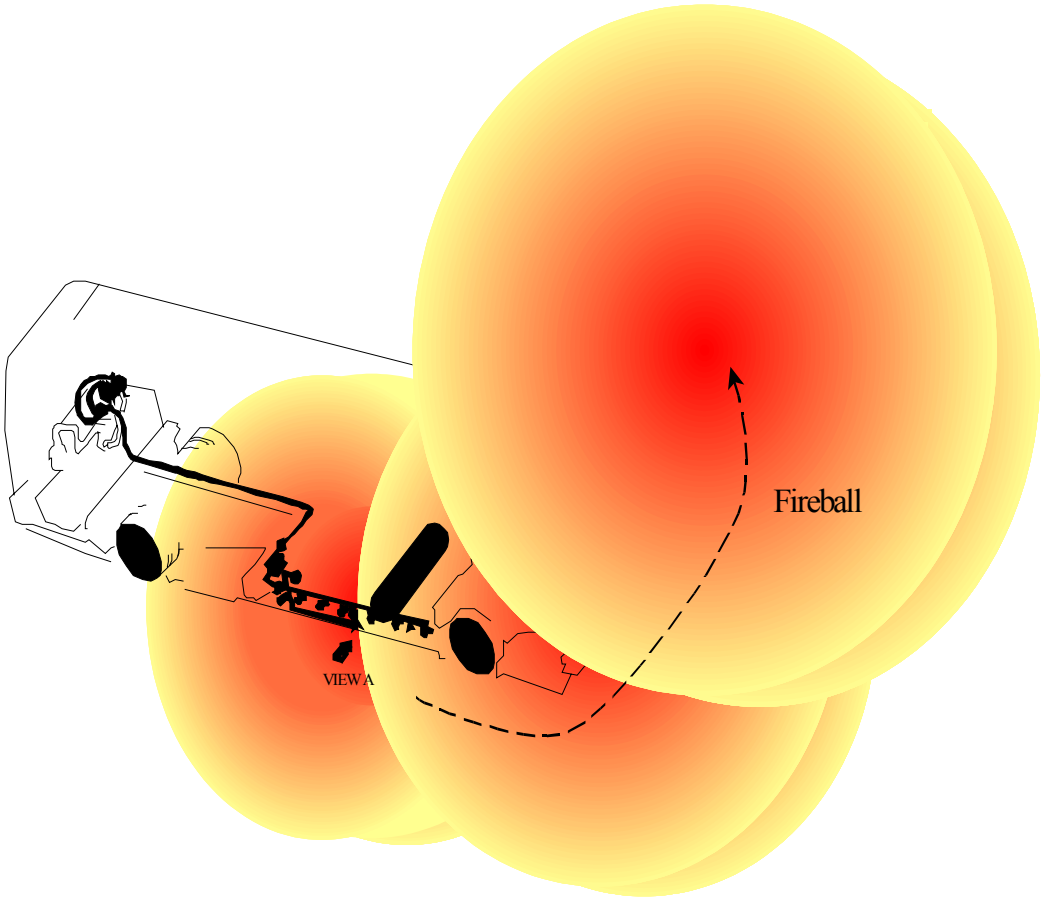

Figure 8.32 Schematic Diagram of a Fireball and Trajectory

The maximum width of the vapor fire is given by the following equation:

$$\xi_{\infty} = \frac{W_{\infty}}{\delta} = \left(\frac{F}{F_f}\right)^{-1/3} \tag{8.56}$$

where

$\xi = \frac{W}{\delta}$

$\tau = \frac{2St}{\delta}$

$F_f = \frac{S^2}{g\delta}$, is the Flame Froude number

$F = \frac{U_0^2}{gW}$, is the Froude Number

S = flame propagating velocity

g = acceleration due to gravity

δ = unburnt vapor cloud thickness

U_0 = upward velocity at flame base

W = flame width

Typically the flame width increases as a function of time until the entire flammable vapor is consumed. Experimental data on methane which is applicable for natural gas, shows that the rate of increase in the flame width is slightly less than the flame propagation velocity, relative to the ground. Equation 8.54 can be used to calculate

the time-dependent flame width, enabling us to be able to calculate the thermal radiation. This is the outcome of interest in quantifying the consequence of a flash fire.

8.3.3.4 Modeling Thermal Radiation from Flash Fire

The transient nature of the burning process, influenced mainly by the changing geometry of the flame, prevents a detailed modeling of the thermal radiation from a flash fire. Heat flux incident on subjects in the affected areas is a combination of several factors including:

- Emissive power of the fire
- Fire duration and steady state burning period
- Area of the visible flame
- Distance to the flame surface
- The geometry of the flame relative to the observer
- View factor

Using a simple rectangular flame geometry, the centerline horizontal and vertical view factors can be determined using Equations 8.57 and 8.58 [146].

$$F_h = \frac{1}{2\pi}\left(\tan^{-1}\gamma + \frac{X}{\sqrt{1+X^2}}\tan^{-1}\frac{Y}{\sqrt{1+X^2}}\right) \quad (8.57)$$

$$F_v = \frac{1}{2\pi}\left(\frac{X}{\sqrt{1+X^2}}\tan^{-1}\frac{Y}{\sqrt{1+X^2}} + \frac{Y}{\sqrt{1+Y^2}}\tan^{-1}\frac{X}{\sqrt{1+Y^2}}\right) \quad (8.58)$$

where

X = flame length divided by the observer distance

Y = flame width divided by observer distance

The incident thermal flux on a subject in the affected area based on the view factors of Equations 8.57 and 8.58 is given by Equation 8.59.

$$\dot{q}'' = EF_{v,h}\tau \tag{8.59}$$

where,

$$\tau = 0.85, \text{ atmospheric transmissivity}$$
$$\text{E} = 157 \text{ kW/m}^2, \text{ surface emissive power of the flame} \tag{8.60}$$

From the above modeling exercise it is evident that without simplifying assumptions, estimating the thermal flux from the complex phenomenon of a flash fire, as a result of the burning of an unconfined vapor cloud would be impossible. A numerical program would be required to estimate the thermal flux received within a specified distance from the flash fire.

8.3.3.5 Computation of Flash Fire Thermal Radiation

In order to explicitly determine the thermal flux the time-dependent flame width must be calculated. This is calculated from Equation 8.54 at incremental time steps from the ignition of the flame to the flame-out time. The elapsed time for the flame to reach

the maximum or asymptotic width, W_∞, is a constant for the particular fuel and is given by:

$$t_{rise} = \frac{W_\infty}{2S} \tag{8.61}$$

This assumes that the width increases at a constant rate during the flame spread from ignition. The time to flame-out will be assumed to be equal to the flame-out time for a fireball as the amount of fuel is the same in both cases. This is given by Equation 8.61.

The asymptotic width of the flame is the maximum possible width given by Equation 8.62. By substituting for the Froude Number for the natural gas vapor cloud and the flame in Equation 8.62, the maximum flame width can be reduced to

$$W_\infty = \delta\left(\frac{F}{F_r}\right)^{-1/3} \tag{8.62}$$

The Froude number is dependent on the upward velocity of the natural gas vapor at the base of the flame. If the vapor cloud is burning freely there is no means of estimating this explicitly. Experiments have shown that the visible flame height to flame width ratio is a constant [147]. It has been shown that this ratio can be written in terms of the Froude Number, *F*, the ratio of density of natural gas to that of ambient air, ρ_0', the inverse volumetric expansion ratio for the vapor, ω, and the stoichiometric fuel to air mass ratio, r, as follows:

$$\left(\frac{H}{W}\right)_{\substack{visible\\flame}} = 20\left[F\rho_0'^2\,\frac{\omega\left(r+\frac{\omega}{\rho_0}\right)^2}{(1-\omega)^3}\right]^{1/3} \tag{8.63}$$

Experimentally determined values for the height to width ratio have been found to be between 1.5 and 2.5 for methane gas [147]. A value of 2.5 will be used in this analysis to determine the Froude Number. Substituting values for the thermodynamic properties of methane and rearranging we get:

$$F = 0.56 \tag{8.64}$$

Similarly substituting the flame speed and chemical properties, the flame Froude number is

$$F_f = 0.40 \tag{8.65}$$

The average thickness of unburnt vapor at the start of the fire is equal to 4.1 m. From this and the Froude numbers, the maximum width of the flame on the dispersed vapor, from Equation 8.62 is equal to:

$$W_\infty = 4.6 \text{ m} \tag{8.66}$$

Similarly we could determine the time required to ramp up the flame width from zero to the asymptotic width. This could be achieved by substituting into Equation 8.61, giving the result:

$$t_{rise} = 0.60 \text{ s} \tag{8.67}$$

Once the flame width reaches the maximum width the duration is assumed to be identical to that of a fireball computed earlier, given that the same amount of fuel is involved and the mixing and entrainment of air into this burning cloud is expected to be the same.

The thermal radiation is proportional to the area of the visible flame. This as the flame is assumed to be optically thick. The incident flux also increases with the flame surface area are will drop off as burnout occurs. In addition to the width of the flame the height is required to estimate the thermal flux incident on receptors at specified distances from the fire. Flame height as a function of its width for a linear heat source [148] is given by:

$$\frac{H}{W} = 3.35 N_{CO}^{1/5} \tag{8.68}$$

Where, N_{CO} is a dimensionless number known as the combustion number and ω is the inverse volumetric expansion ratio due to combustion. They are defined by:

$$\omega = \frac{1}{\left(1+\frac{Q_c}{rC_pT_a}\right)} \tag{8.69}$$

$$N_{CO} = \frac{Q^2\left(r+\frac{\omega}{\rho_0}\right)^2}{\rho_a{}^2 Q_c{}^2 g W^5 (1-\omega)^5} \tag{8.70}$$

and

$$Q = \pi W^2 U_0 \rho_0 Q_c \tag{8.71}$$

where

$\rho_0{}'$ = density ratio of natural gas vapor and air

r = stoichiometric air/fuel mass ratio

ω = inverse volumetric expansion ratio

Q_c = heat of combustion

Q = heat release rate

C_p = specific heat

T_a = ambient temperature

The following values of these parameters were used in estimating the dimensions of the flame.

$$\begin{aligned} &\rho_0' = 0.60 \\ &r = 17.2 \\ &Q_c = 500.2 \text{x} 10^5 \text{ J/kg} \\ &C_p = 2.219 \text{x} 10^3 \text{ J/kg}^\circ\text{K} \\ &T_a = 298 \text{ K} \end{aligned} \qquad (8.72)$$

A numerical procedure was written in MatLab in order to compute the transient thermal flux. This is based on the flame width as a function of time, flame height with time, view factor and received thermal flux equations. The routine was used to estimate the thermal flux incident on receptors at specified distances from the fire. A simple rectangular geometry was assumed for the flame from which the horizontal and vertical centerline view factors are determined using Equations 8.57 and 8.58.

The results are shown in Figures 8.33 to 8.39. These results can be used to estimate the effects and potential for fatality for passengers and persons that may be within the vicinity of a typical bus who may be impacted by a flash fire. The effects will be added with the effects of an explosion to get the total fire fatality from such a fire scenario.

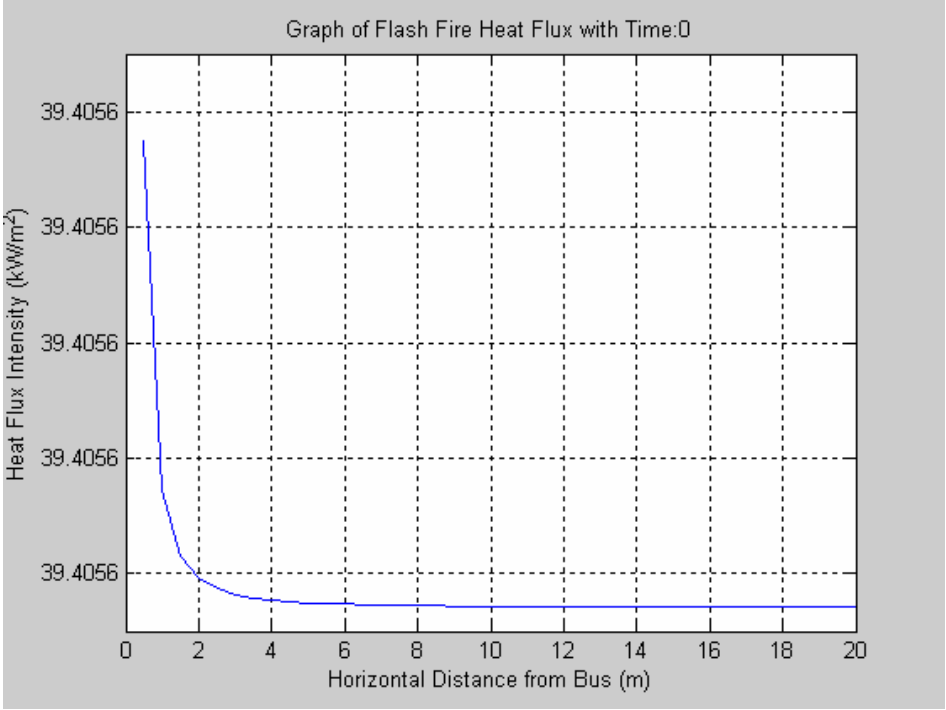

Figure 8.33 Heat Flux Intensity just after Ignition, t = 0 second.

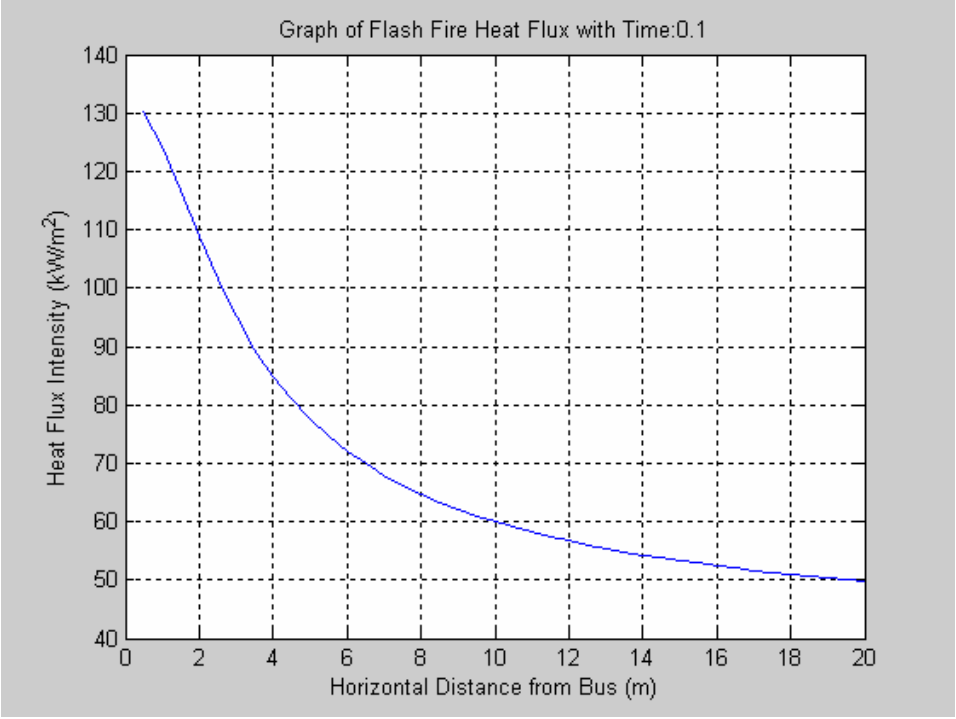

Figure 8.34 Heat Flux Intensity after, t = 0.1 second.

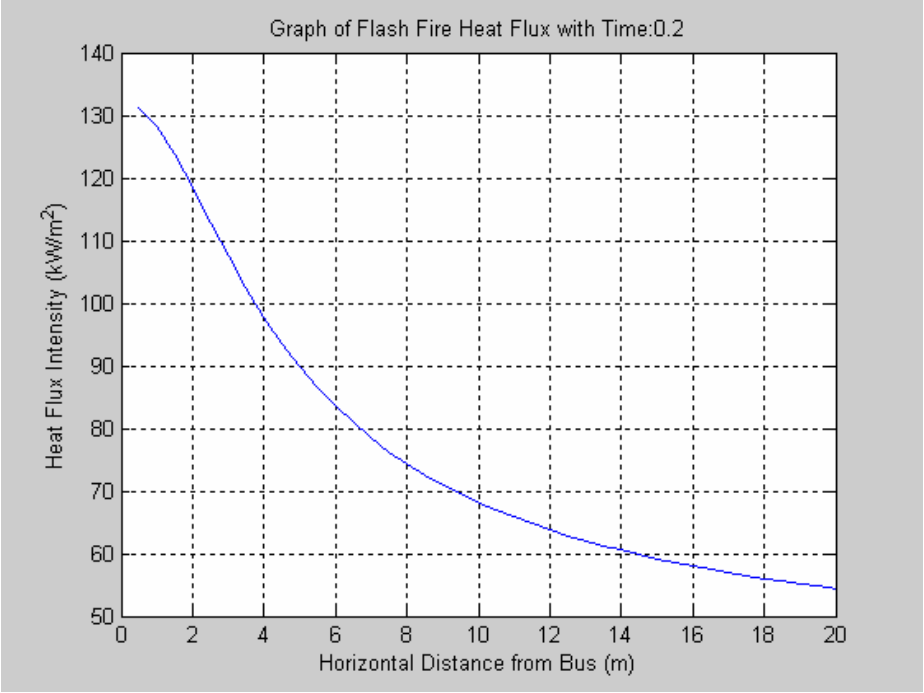

Figure 8.35 Heat Flux Intensity after, t = 0.2 second.

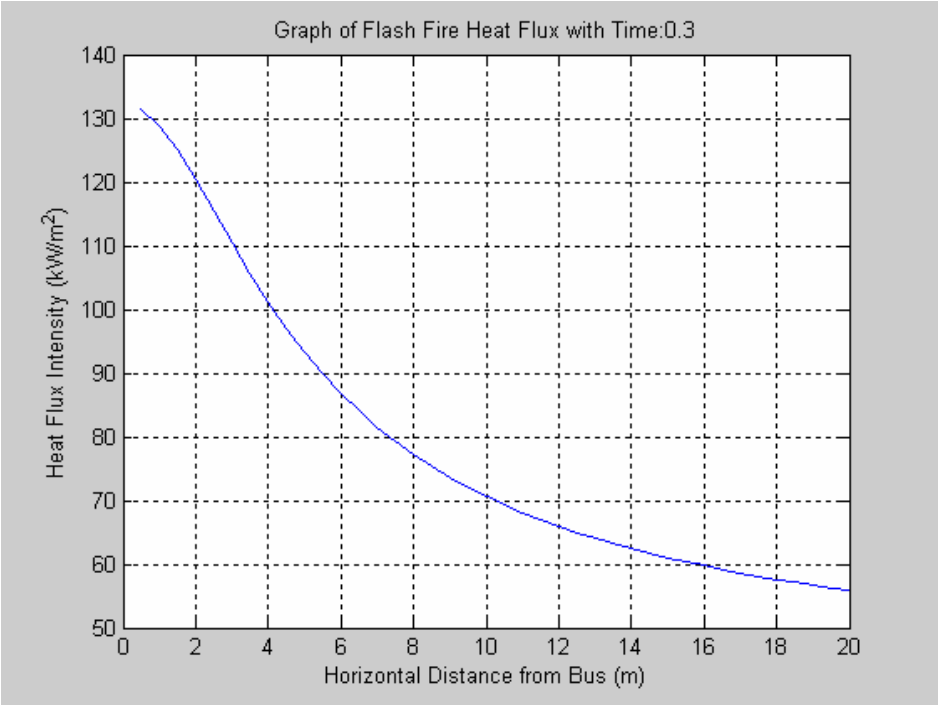

Figure 8.36 Heat Flux Intensity after, t = 0.3 second.

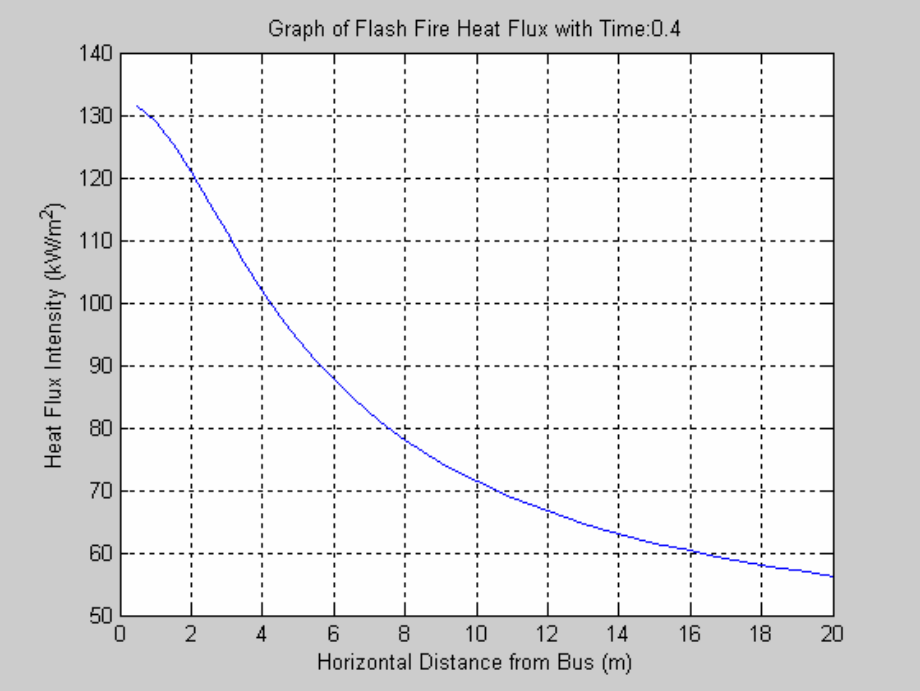

Figure 8.37 Heat Flux Intensity after, t = 0.4 second.

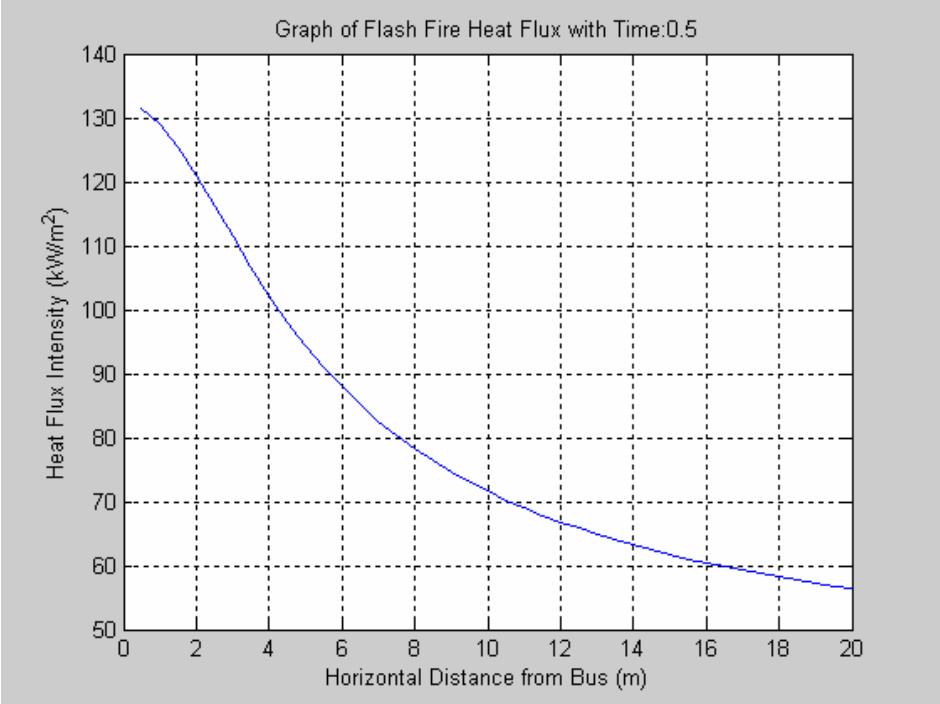

Figure 8.38 Heat Flux Intensity after, t = 0.5 second.

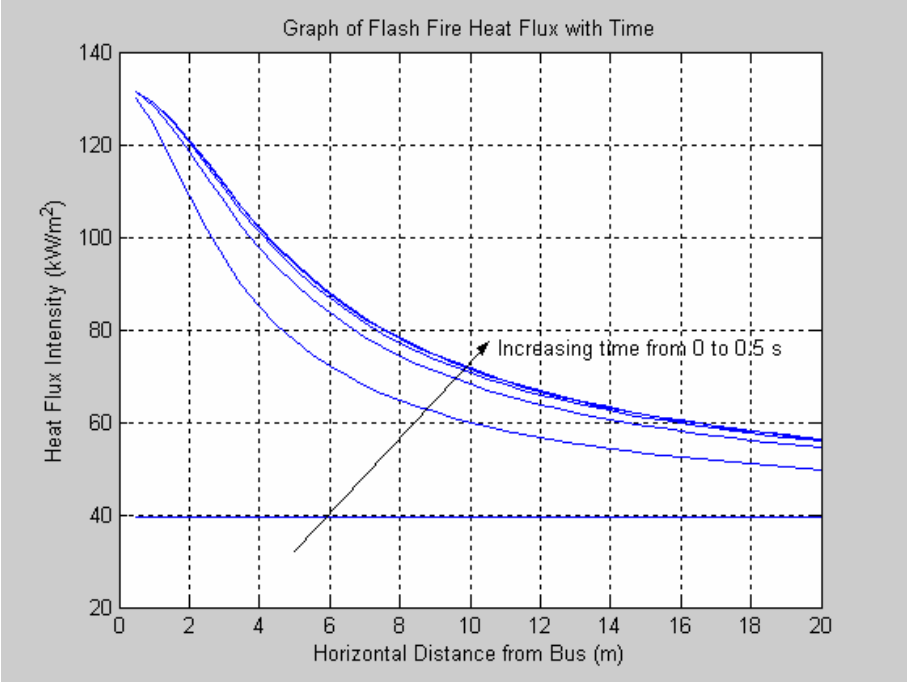

Figure 8.39 Variation of Heat Flux Intensity with Time.

8.3.3.6 CFD Simulation of Thermal Radiation from Natural Gas Vapor Cloud Fire inside a Typical Bus

Simulation of a fire inside of a bus was required in order to establish the thermal radiation that could be expected should a fireball engulf the bus or a flash fire is present inside the bus as opposed to outside as have been modeled in the previous exercises. The Fire Dynamics Simulator (FDS) code developed by NIST was used for this simulation. In addition to the large eddy simulation assumptions used in the code algorithm, some simplifying assumptions were made for the fire inside the bus. These assumptions were included in the data file shown in Appendix 7 and include:

- Fire and combustion products enter the bus through a single door or window at the back of the bus.

- Ventilation is provided by two open windows located close to the front of the bus.
- Fire and combustion products are injected into the computational domain at a wind speed of 4 m/s.
- The heat release rate per unit area of the fire is chosen to reflect the size of the fire that would be blazing inside the bus.

The radiative heat transfer is modeled by solving the radiation transport equation for a non-scattering gray gas [149]. This model adopts the idea of a set of discreet emitters to the large eddy simulation technique adopted for the FDS hydrodynamic model. The assumption is that a prescribed fraction of the heat released from each thermal element used to describe the fire is radiated away. This emitted flux is assumed to be the actual radiant energy emitted locally by the thermal element. Typically this amounts to about thirty-five percent of the energy released in a combustion process [150]. For the natural gas fire contemplated in this analysis, the radiant energy absorbed by smoke particulate matter can be neglected. The actual radiant energy can therefore be estimated explicitly.

The radiative flux, q_R at a given point on the surface of the target, $\vec{r}_s$ can be expressed as [150]:

$$q_r = \sum_{i=1}^{N_p} \chi_r \dot{q}_i \frac{(\vec{r}_s - \vec{r}_i).\vec{n}}{4\pi|\vec{r}_s - \vec{r}_i|^3} \exp\left\{-\lambda\left(\vec{r}_s, \vec{r}_i\right)\right\} \qquad (8.73)$$

where

$$\lambda = \int_0^{|\vec{r}_s - \vec{r}_i|} \kappa\left\{\vec{r}_i + s\frac{(\vec{r}_s - \vec{r}_i)}{|\vec{r}_s - \vec{r}_i|}\right\} ds \tag{8.74}$$

Here $\vec{n}$ is a unit normal vector to the surface at point $\vec{r}_s$, and N_p is the total number of radiating elements at the instant in question. The divergence of the radiant heat flux to some point of interest, $\vec{r}$, from the same set of point emitters is given by:

$$\nabla \cdot \vec{q}_R = -\kappa(\vec{r}) \sum_{i=1}^{N_p} \chi_r \dot{q}_i \frac{1}{4\pi|\vec{r}_s - \vec{r}_i|^2} \exp\left\{-\lambda(\vec{r}_s, \vec{r}_i)\right\} \tag{8.75}$$

Where, κ, the absorption coefficient is taken to be the Planck mean absorption coefficient for soot given by [151]:

$$\begin{aligned} \kappa &= 11.86 f_v T \\ &= 11.86 Y_s \frac{\rho T}{\rho_s} \text{ / cm} \end{aligned} \tag{8.76}$$

The soot volume fraction f_v or mass fraction Y_s is calculated by assuming that a fixed fraction of the fuel burned in each Lagrangian thermal element is converted to soot. For natural gas this is negligible, allowing the radiant heat transfer at each instant of time to be calculated with an exact solution found.

In the simulation exercise, the sum in Equation 8.73 is calculated as a running average over several time steps. At each time step, a random number of sample elements are

chosen and the sum is carried out and weighted to account for all of the emitted radiation. The mathematical model discussed, along with other solution improvement techniques, was implemented in the computational fluid dynamics simulation exercise. This was used to compute the heat flux inside and surrounding the bus during a flash fire.

For the simulation a numerical grid consisting of 64 by 64 by 32 cells was used to span a domain of 12x3x4 m^3. The cell sizes were chosen to achieve the greatest accuracy in the results. The bus structure defined the computational domain was included as an obstruction. Ambient atmospheric temperature was assumed to be uniformed at 25 $^\circ$C and the heat release rate of natural gas taken to be 1688 kW/m^2. The fraction of the chemical heat released rate converted to thermal radiation that is emitted from the thermal elements was assumed to be 35%.

8.3.3.7 Results of CFD Simulation of the Unconfined Natural Gas Cloud Fire

The snapshots of the Lagrangian elements that represent the fire plume at different time steps were animated and show the spread of the fire across the bus instances in time. The results indicate that the temperature of the combustion products as well as the heat flux inside the bus is likely to result is fatality of all the occupants.

8.3.3.8 Modeling of Natural Gas Vapor Cloud Explosion Outcome

The procedure for modeling the effects of a vapor cloud explosion is shown in Figure 8.29. Inputs required for calculating the intensity of the explosion include the mass of fuel released, dimensions of the flammable cloud and an estimate of the explosion yield. The effects are measured in the damage level with distance and the peak overpressure estimated.

Of the models available the TNT model with its simplicity will be applied. This model is based on the assumption [152 – 155] that the explosion as a result of the natural gas cloud is equivalent to that of a TNT charge, factored by an explosion yield term. That relationship may be expressed as:

$$m_{TNT} = \frac{\eta m_f \Delta h_{c_{gas}}}{\Delta h_{c_{TNT}}} \tag{8.77}$$

where

m_{TNT} = equivalent mass of TNT

m_f = mass of natural gas released

η = assumed or empirical explosion yield

$\Delta h_{c_{gas}}$ = heat of combustion of natural gas

$\Delta h_{c_{TNT}}$ = heat of combustion of TNT

The maximum expected for explosion yield based on historical data [156] for a symmetrical cloud is 0.2. The equivalent mass of TNT will be determined by substituting values from Equation 8.78 into Equation 8.77.

$$\begin{aligned} m_f &= 7.7 \text{ kg} \\ \eta &= 0.2 \\ \Delta h_{c_{gas}} &= 50000 \text{ kJ/kg} \\ \Delta h_{c_{TNT}} &= 4437 \text{ kJ/kg} \end{aligned} \tag{8.78}$$

$$m_{TNT} = 17.4 \text{ kg} \tag{8.79}$$

This result will be used in calculating the effect of the vapor cloud exploding from documented TNT explosion monographs such as shown in Figure 8.40. This chart was developed for a hemispherical TNT surface charge where explosive parameters are plotted as a function of the scaled range. The estimated peak overpressure with distance is used in the consequence modeling of Section 8.5, to determine the possibility of fatalities.

The fatality results derived are only approximations as the physical and chemical interactions in an unconfined vapor cloud deflagration are very different from that which occurs in a TNT detonation. Without a more detailed model these will be used as a first approximation.

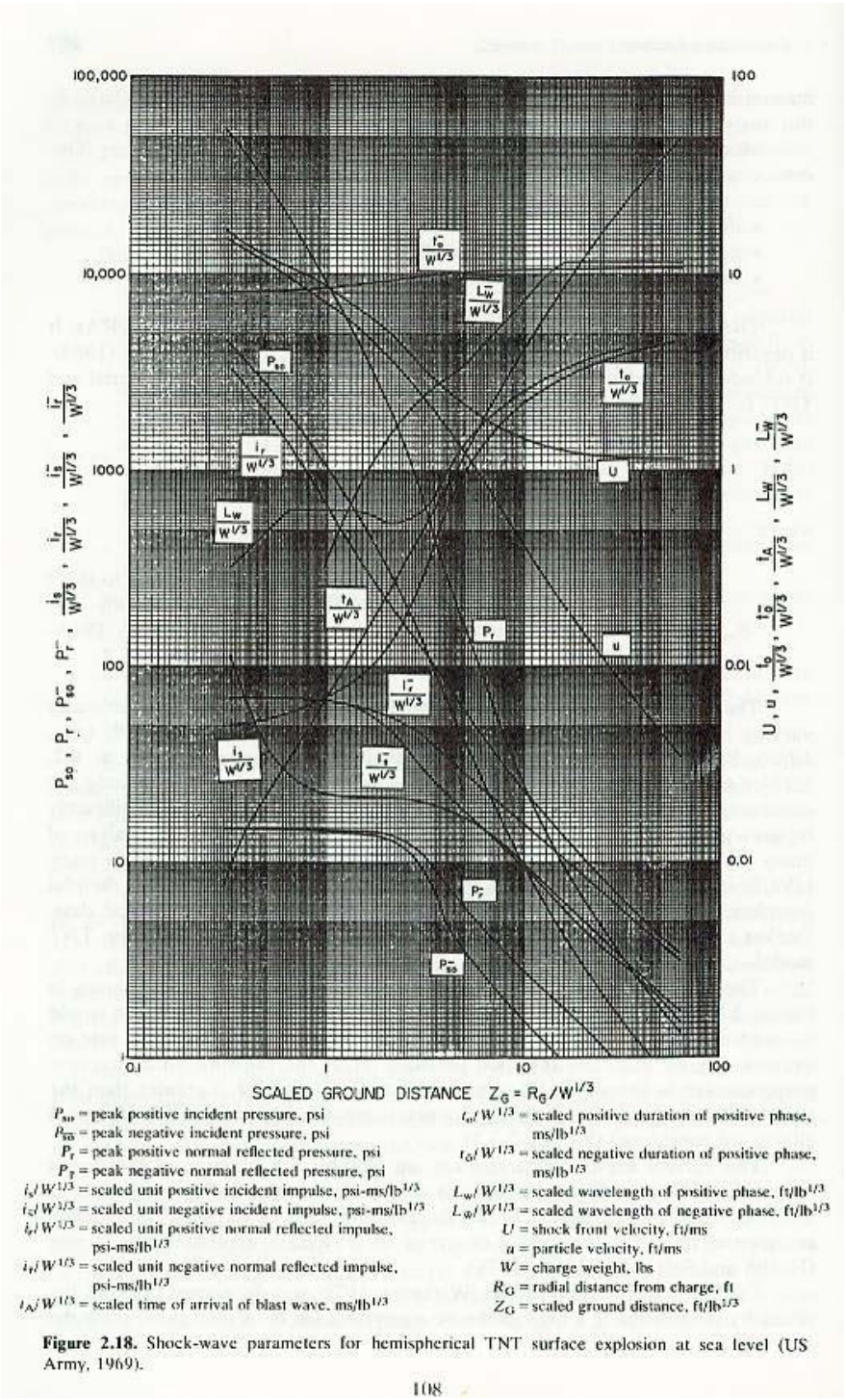

Figure 2.18. Shock-wave parameters for hemispherical TNT surface explosion at sea level (US Army, 1969).

108

Figure 8.40 Shock Wave Parameters for Hemispherical TNT Surface Explosion [157]

8.3.4 Cylinder Physical Explosion Outcome

The outcomes of a physical explosion from rupture of a CNG cylinder are the result of shock waves produced and energetic particles or missiles generated. Since we are evaluating the risk with the bus in normal use, the effects of missiles will be considered to be integral with all other outcomes of an explosive event.

Shock waves will be generated from sudden expansion of the gas in the pressurized cylinder. Catastrophic rupture of a cylinder will occur with brittle type failure. It is assumed that energy losses to generation of projectiles and heating the atmosphere are negligible and 100% of the available energy producing the shock wave. The procedure for calculating the outcome of a physical explosion is shown in Figure 8.41. This procedure estimates the equivalent energy in lbs of TNT that isothermal expansion of natural gas would produce in response to the decreasing of pressure to ambient conditions. A shock wave correlation curve will be used to estimate the overpressure produced and potential for damage. Ideal gas laws are assumed to apply.

The equivalent TNT energy for expanding natural gas from its initial and pressure to atmospheric conditions is given by Equation 8.80 [158].

$$W_{TNT} = 1.4x10^{-6} V\left(\frac{p_1 T_0}{p_0 T_1}\right) R T_1 \ln\left(\frac{p_1}{p_a}\right) \qquad (8.80)$$

where,

W_{TNT} = energy in lb TNT

V = volume of compressed gas, ft^3

$p_1 = 3000$ initial pressure of compressed natural gas, psia

p_a = ambient pressure

$p_0 = 14.7$ psia, standard pressure

$T_1 = 536\ ^\circ R$, temperature of compressed gas

$T_0 = 492\ ^\circ R$, standard temperature

$R = 1.987$ Btu/lb mol-$^\circ R$

Substituting into Equation 8.81, the equivalent energy is

$$W_{TNT} = 2.42 \text{ lb TNT} \tag{8.81}$$

The blast pressure at the surface of the exploding CNG cylinder can be estimated from [159]

$$P_b = P_s \left\{ 1 - \frac{[3.5](\gamma - 1)(P_s - 1)}{\left[(\gamma T / M)(1 + 5.9 P_s)\right]^{1/2}} \right\}^{-2\gamma/(\gamma - 1)} \tag{8.82}$$

where,

P_s = pressure at surface of cylinder

P_b = burst pressure of cylinder

γ = ratio of specific heats

T = absolute temperature, ˚K

M = molecular weight of natural gas, lb/lb mole

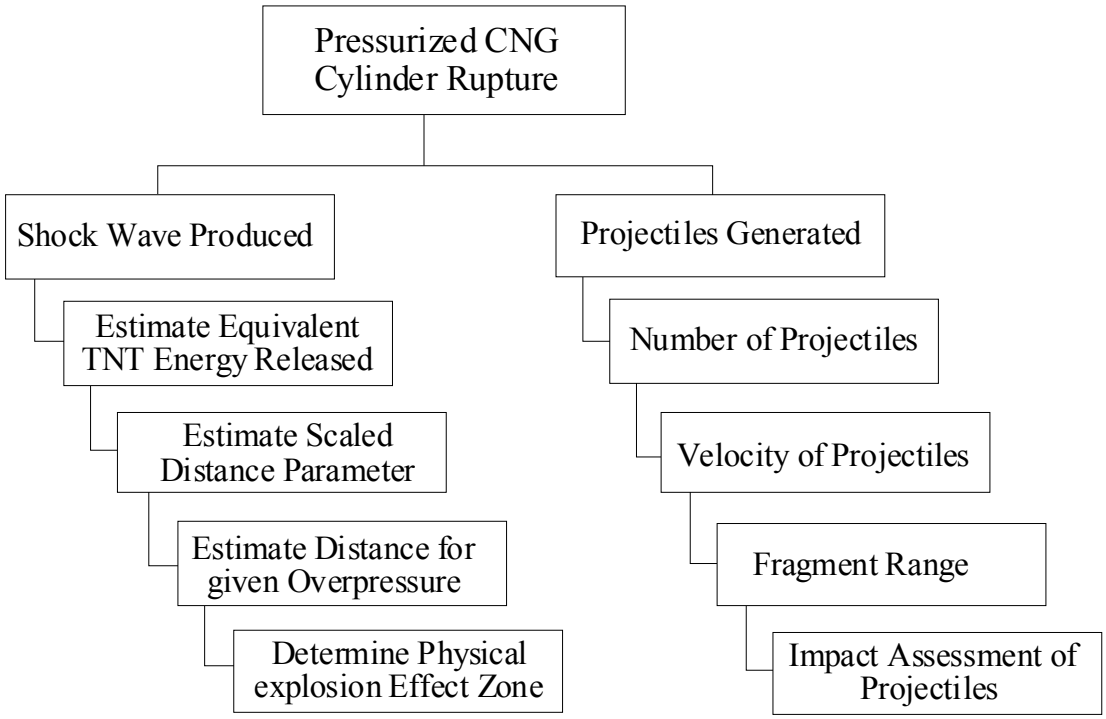

Figure 8.41 Logic Diagram of Outcome Calculation for Physical Explosion

An iterative solution will be implemented to determine the blast pressure. In solving the expression the assumption is made that expansion will occur in air at standard atmospheric pressure and temperature of 25°C. The other properties of the natural gas used are shown in Equation 8.83.

$$\begin{aligned} P_b &= 206.8 \text{ bars} \\ \gamma &= 1.31 \\ T &= 298, \ ^\circ\text{K} \\ M &= 16.97 \text{ lb/lb mole} \end{aligned} \tag{8.83}$$

The scaled distance based on the blast pressure at the surface could be determined from Figure 8.40 which is for pressure vessels at ground level. The scaled distance is given by [160]:

$$Z_G = \frac{R_G}{\sqrt[3]{E_{TNT}}} \tag{8.84}$$

where,

R_G = radial distance from center of explosion, ft

E_{TNT} = equivalent energy in mass of TNT charge

Using the secant method of iteration for a routine implemented in MatLab, the blast pressure at the surface is calculated to be:

$$P_s = 169 \text{ psia} \tag{8.85}$$

The corrected center of explosion can be determined from Equations 8.84 and 8.85 and the scaled distance from Figure 8.40. From Figure 8.40 for a blast pressure of 169 psia, the scaled distance is

$$\begin{aligned} Z_G &= 4.0 \\ &= \frac{R_G}{W^{1/3}} \end{aligned} \tag{8.86}$$

Substituting the equivalent mass of TNT the radial distance of the explosion surface from the center of explosion can be calculated. This radial distance has to be corrected with the diameter of the cylinder. This corrected radial distance, R'_G of the charge surface has to be added to any radial distance in evaluating the effects of a cylinder physical explosion.

$$R'_G = 4.87 \text{ feet} \tag{8.87}$$

The equivalent mass of TNT as well as the distance at which certain pressure effects will be felt will be used in evaluating the pressure effects of an explosion of a typical CNG cylinder considered in this analysis.

8.3.5 Outcome of Confined Vapor Explosion in the Bus of Building

The outcome of interest for a gas explosion in a confined space such as a bus of the depot is the shock wave produced by the overpressure. Thermal effects are accounted for in the fire scenarios considered while fatalities due to projectiles generated are ignored. A simplified approach will be used in estimating the outcome of overpressure

outcome. In this approach we will assume that the bus and depot is occupied by a stoichiometric mixture of air and natural gas. It is further assumed that all the combustion energy goes into producing a shock wave. The energy produced by this combustion can be estimated from the mass of fuel available and the specific heat of combustion of methane. The equivalent TNT energy is then calculated and the procedure for a physical explosion used to estimate the effects of a confined explosion.

The volume of air in a the typical bus is approximately [143]

$$V_{bus} = 3200 \text{ ft}^3 \tag{8.88}$$

The mass of fuel in this stoichiometric mixture of natural gas and air is

$$m_{busfuel} = 13.56 \text{ lb} \tag{8.89}$$

The energy produced in this combustion process can be determined from the mass of fuel and the heat of combustion of natural gas which is assumed to be the same as methane.

$$E_{comb} = 291600 \text{ Btu} \tag{8.90}$$

Assuming that 1 lb TNT is equivalent to 2000 Btu then the energy released in equivalent weight of TNT is

$$W_{busTNT} = 145.8 \text{ lb TNT} \tag{8.91}$$

The effect of a confined explosion inside of a bus or depot will be determined from the equivalent TNT, Figure 8.40 and Equation 8.86. The potential for fatality is determined from the shock wave which is conservatively assumed to be created by 20% of the

combustion energy available. Analysis for fatality is identical to the procedure for physical explosion once the equivalent TNT has been determined.

8.4 Fire Scenarios Effects Analysis

The effects of the outcomes from the different fire scenarios are used to estimate the likely injury or damage to people, including fatality, from thermal radiation and explosions. The potential for fatality will be determined from theoretical models based on the physiology of response of human skin to thermal radiation and the effect of direct and reflected blast overpressure. It is assumed that the skin is bare for the duration of the exposure. The effect of missiles created in explosions and human body translation is ignored even though both are very likely to cause fatalities.

8.4.1 Thermal Radiation Effects Modeling

Modeling of the effect of thermal radiation on human skin and underlying tissue is not possible due to the complexity of the thermal system with blood flow interacting with tissue. Thermal radiation incident on human skin causes denaturation of skin proteins in the epidermis and destroys the cell structure and collagen protein in the dermis [161]. The severity of damage depends on the extent of destruction of the tissues. Empirical models are available for estimating burns and time for pain threshold. Determination of the thermal flux levels at which fatality will occur is subjective. The most appropriate model for estimating the effect of thermal radiation is based on the

relation between thermal radiation intensity and burn injury for nuclear explosions at different yields [162]. This model is based on the probit method. The probit estimated from Equation 8.92 can be used to estimate the percentage fatality expected from Table 8.3. The results are summarized in [163] and shown in Figure 8.42.

$$\mathrm{Pr} = -14.9 + 2.56 \ln\left(\frac{tq^{4/3}}{10^4}\right) \tag{8.92}$$

where,

Pr = probit

t = duration of exposure

q = thermal flux

The probit method has more application for toxic effects. Its application for thermal injuries [164] has been shown to be relatively inaccurate. Thermal radiation fatalities will therefore be estimated from the monograph shown in Figure 8.42.

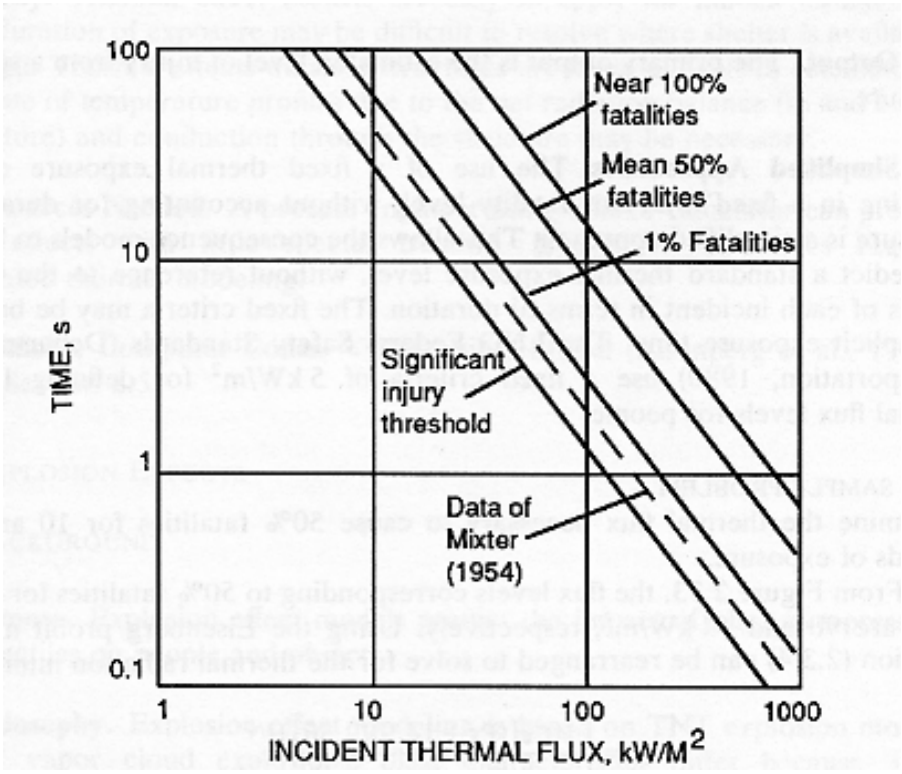

Figure 8.42 Fatality Levels for Thermal Radiation [163]

In this analysis the effects of secondary fires which are started because of the presence of a large primary natural gas fire is not considered. Taking into account the effect of secondary fires requires analysis of the radiation intensity and duration for excedence of threshold values for pyrolysis of bus structure and internal components. Mitigating factors are conservatively assumed to significantly reduce the effects of secondary fires in the time required for them to develop. No consideration is given to injuries that do not produce fatalities. This is a very conservative approach as third degree burns frequently results in fatality.

Using an average fixed thermal exposure criterion, resulting in a fixed number of fatalities, without accounting for duration of the exposure is a simplified approach. The probit method however allows us to evaluate the consequence of each fire scenario, without reference to the changes in thermal flux over time. This will give us the average consequence in terms of fire fatality for each scenario.

8.4.2 Explosion Effects Modeling

The effects of explosions are determined from the overpressure outcomes of the fire scenarios considered. Explosion models reviewed predict the impact of this overpressure on humans in determining potential for fatalities. Secondary effects due to projectiles formed when a structure explodes, are considered as well as fatalities due to whole body translation, which are expected to produce the most fatalities. The total fatalities from all outcomes are determined from research on total fatality from a nuclear explosion without the effects of ionizing radiation [162].

The best available model for quantitatively estimating fatalities due to explosions is the probit method by [162]. The primary inputs to this model are the equivalent TNT explosion yield and the yield that would cause 50% fatality for a certain blast pressure and shelter category. These values are extracted from empirical curves considering all mechanisms of fatality for low yield explosions shown in Figure 8.43 and summarized in Equations 8.94 and 8.95. The percentage of fatality expected within a certain distance from the blast center is given by

$$\mathrm{Pr} = 5 + 3.406 \ln\left(\frac{p_b}{p_{b50}}\right) \qquad (8.93)$$

and

$$p_{b_{50}}(\text{inside}) = 16.151 - 0.897 W_{TNT} + 0.0245 W_{TNT}{}^2 - 0.0002 W_{TNT}{}^3 \quad (8.94)$$

$$p_{b_{50}}(\text{outside}) = 37.945 - 7.750 W_{TNT} + 0.776 W_{TNT}{}^2 - 0.021 W_{TNT}{}^3 + 0.0002 W_{TNT}{}^4 \quad (8.95)$$

where

Pr = probability of fatality due to explosion

$p_{b_{50}}$ = blast pressure that would give 50% fatality

p_b = blast pressure produced by explosive event

The explosion yield in lb TNT outcome computed in Section 8.3 is used to estimate the overpressure produced from Figure 8.43, based on the scaled distance from the corrected blast surface, and to estimate the blast pressure that would produce 50% fatality from Equations 8.94 to 8.95. These estimates are used in computing the Probit of expected fatality from each explosion event whether inside the bus, inside the depot or outdoors. The percentage of fatality is determined from the probit of each event using Table 8.3

Explosion effect modeling as described in Section 8.3 is based on TNT explosion modeling. This requires qualification however as vapor cloud explosions are characterized as deflagrations and TNT explosions are detonations. The effects are similar however provided the distance is sufficient to predict an overpressure of greater than 14.7 psi [160].

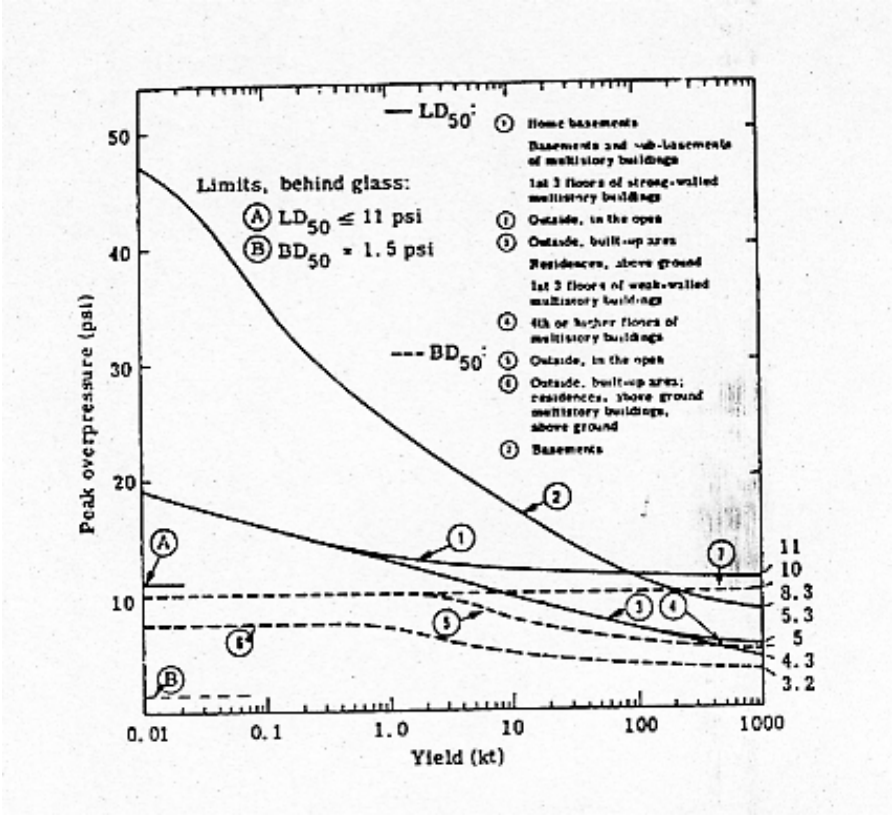

Figure 8.43 Mid-Lethal Free Field Overpressures for Various Shelter Categories [162]

%	0	2	4	6	8
0	—	2.95	3.25	3.45	3.59
10	3.72	3.82	3.92	4.01	4.08
20	4.16	4.23	4.29	4.36	4.42
30	4.48	4.53	4.59	4.64	4.69
40	4.75	4.80	4.85	4.90	4.95
50	5.00	5.05	5.10	5.15	5.20
60	5.25	5.31	5.36	5.41	5.47
70	5.52	5.58	5.64	5.71	5.77
80	5.84	5.92	5.99	6.08	6.18
90	6.28	6.41	6.55	6.75	7.05
99	7.33	7.41	7.46	7.65	7.88

Table 8.3 Transformation of Probits to Percentages [160]

8.5 Fire Consequence Assessment

The consequence of any fire scenario considered is determined by combining the outcome of each event, the effect of that outcome in terms of fatality, with the occupancy of the effect zone at the time of the incident. Location of the bus is incorporated in the occupancy figures reported. Determination of the occupancy will complete the variables required to estimate the consequence of the fire scenarios considered.

8.5.1 Zone Occupancy Modeling

Occupancy of the effect zones was detailed in [1] and is summarized in Table 8.4. The occupancy considered in this analysis only includes persons in direct contact with the fire incident and does not include persons in adjacent buildings who may be affected by secondary fires and explosion. This is a very conservative assumption and would produce the lower bound of fatalities all other things being considered. Persons in direct contact with the fire are summarized as follows:

- The driver and an average passenger load in a single bus estimated to be 28 persons total.
- Persons in private vehicles on the roadway with average passenger load of 2 persons, based on traffic density for that location, in a populous state where CNG vehicles would be expected to be used.
- Pedestrians based on population density of a populous state.

The effect zone is measured in distance from the bus which is involved in the fire and is assumed to be static without consideration for peak and off peak traffic. Tunnel traffic is assumed to be identical to urban traffic.

Table 8.4 Occupation of Exposure Zones

Location	**Zone Radius (m)**				
	5	**10**	**15**	**20**	**25**
Urban Roadway	36	39	43	49	53
Sub-Urban Roadway	32	33	35	38	42
Garage	5	6	8	11	15
Station	7	8	10	13	17
Tunnel	36	39	43	49	53

8.5.2 Consequence Numerical Results for Fire Scenarios

The consequence of each fire scenario is determined by combining the effect within a certain distance that would cause fatality with the occupancy of the zones with this effect. The effect of each fire scenario outcome is dependent on the distance from the source as well. In the case of thermal radiation, the thermal radiation incident on a receptor at a given distance from the source is noted. The lethality of this flux in terms of the percentage fatality expected is noted. This is multiplied by half of the expected occupancy of the zone of interest, to arrive at the fire fatality consequence due to thermal flux. Half of the expected occupancy is used to be conservative in the fatality estimation.

A similar procedure is done for explosions and both combined to give the total fire fatality for each fire scenario. The results are summarized in Table 8.5.

The consequence results along with the frequency of the initiating events identified in Part I are important new information developed through this research. In performing a risk analysis, the likelihood of subsequent events is necessary in evaluating the pathways from a gaseous release to formation of a type of fire with its attendant consequences. The likelihood of these subsequent events will now be evaluated along with development of a risk model to compute the fire fatality risk. Part III completes this aspect of the research.

Table 8.5 Consequence of Fire Scenarios

Location	Fire Scenario								
		Initial Fireball		Secondary Fireball		Flash Fire		Confined Explosion	Physical Explosion
		Thermal	Explosion	Thermal	Explosion	Thermal	Explosion	Explosion	Explosion
Urban Roadway	Passenger	28	0	28	0	28	0	28	6
	Non-Passenger	9	0	13	0	5	18	16	2
Sub-Urban Roadway	Passenger	28	0	28	0	28	0	28	2
	Non-Passenger	5	0	6	0	1	7	6	2
Garage	Passenger	0	0	0	0	0	0	0	0
	Non-Passenger	5	0	7	0	3	10	8	2
Station	Passenger	0	0	0	0	0	0	2	1
	Non-Passenger	8	0	10	0	3	13	6	2
Tunnel	Passenger	28	0	28	0	28	0	28	6
	Non-Passenger	9	0	13	0	5	18	16	2

PART III

QUANTITATIVE RISK ASSESSMENT and DISCUSSION OF RESULTS

CHAPTER 9: QUANTITATIVE RISK ASSESSMENT

The quantitative risk assessment develops fire scenarios and consequence resulting from the initial release of natural gas from one of the failure modes identified in Part 1, the subsequent scenarios and eventually leading to fatalities quantified in Part 2. Risk is then computed from the frequency of the initiating events, likelihood of the subsequence events leading to a fire and the consequence of each scenario. The approach for risk modeling is summarized in Figure 9.1.

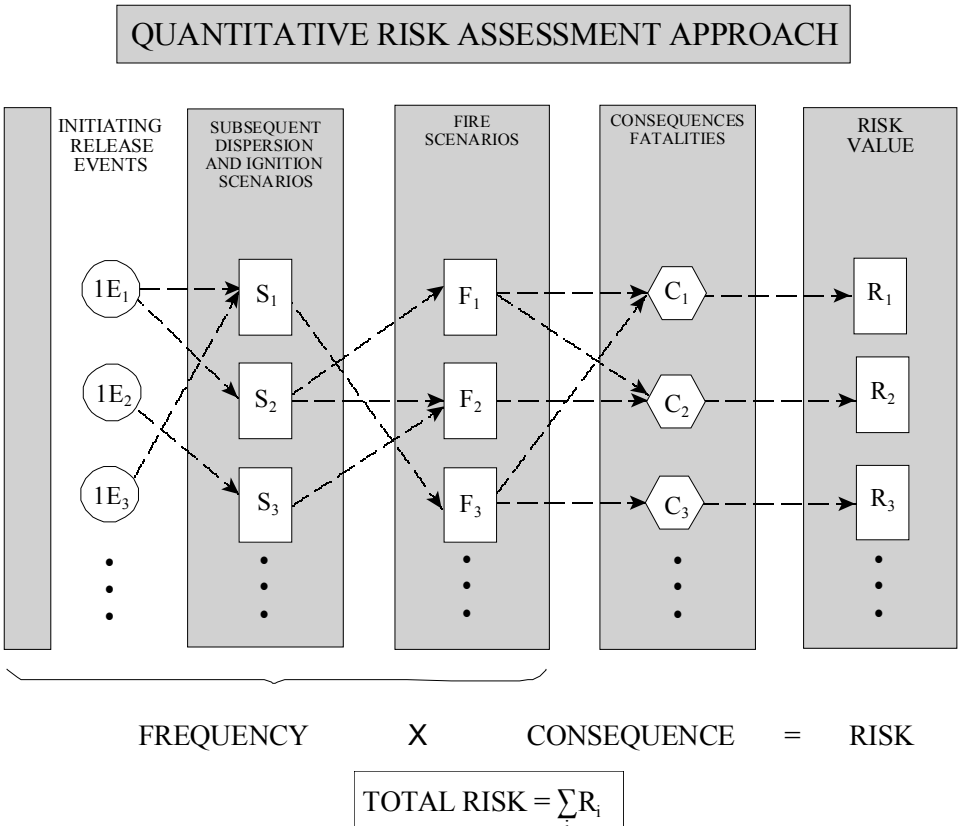

Figure 9.1 Risk Assessment Model

9.1 Model Description

The quantitative risk procedure determines the risk by combining the elements of the model as follows:

- Frequency of release of natural gas from leakage or catastrophic rupture from a crack originating on the inside, outside or transition region surface. The point estimate and the variance are shown in Tables 7.1 – 7.3.
- Dispersion and mixing probabilities which would produce a flammable vapor cloud.
- Likelihood of ignition of the flammable vapor cloud immediately with a catastrophic release or delayed after dispersion and mixing.
- Probability of fire and explosion occurring together or separately after ignition of the vapor cloud.
- Location of the bus when the incident is occurring.
- Consequence of each scenario derived from the fire scenario and the expectation for fatalities, shown in Table 8.5.

Each of the subsequent events will now be defined and the probability of occurrence investigated.

9.2 Probability of Vapor Cloud Being Flammable

Dispersion of a pressurized release of natural gas from a cylinder at 3000 psig has been found to occur as a dense cloud [142] in the vicinity of the release point. In a jet discharge as from a crack in the cylinder wall, the edges of this cloud would have

undergone sufficient mixing to be flammable. Similarly in a puff discharge from the catastrophic rupture of a cylinder the edge of the cloud was found to be flammable. Buoyant dispersion and further mixing will occur when the natural gas vapor is heated up by ambient air, rendering the entire discharge ignitable. Deterministic approaches were used in the fire modeling exercise of Chapter 8 assuming that ignition of a flammable cloud had occurred. The probability of the vapor cloud achieving and remaining flammable will now be evaluated.

Atmospheric boundary layer exhibits turbulent fluctuations. The concentration of flammable natural gas vapor released into the atmospheric boundary layer will fluctuate around a time averaged mean concentration within the dispersed cloud. At the edges this will fluctuate into and out of the flammable limits of natural gas or 5% at the lower limit (LFL) and 14% at the higher level (HFL). A plot of the cumulative probability of a potentially flammable concentration occurring at a given point based on laboratory and field experiments by Birch [165] is shown in Figure 9.2. This curve was plotted from the area of the probability density function (PDF) of the concentration variation between the static flammable limits, which was found to be directly related to the PDF of turbulent velocity fluctuations [166].

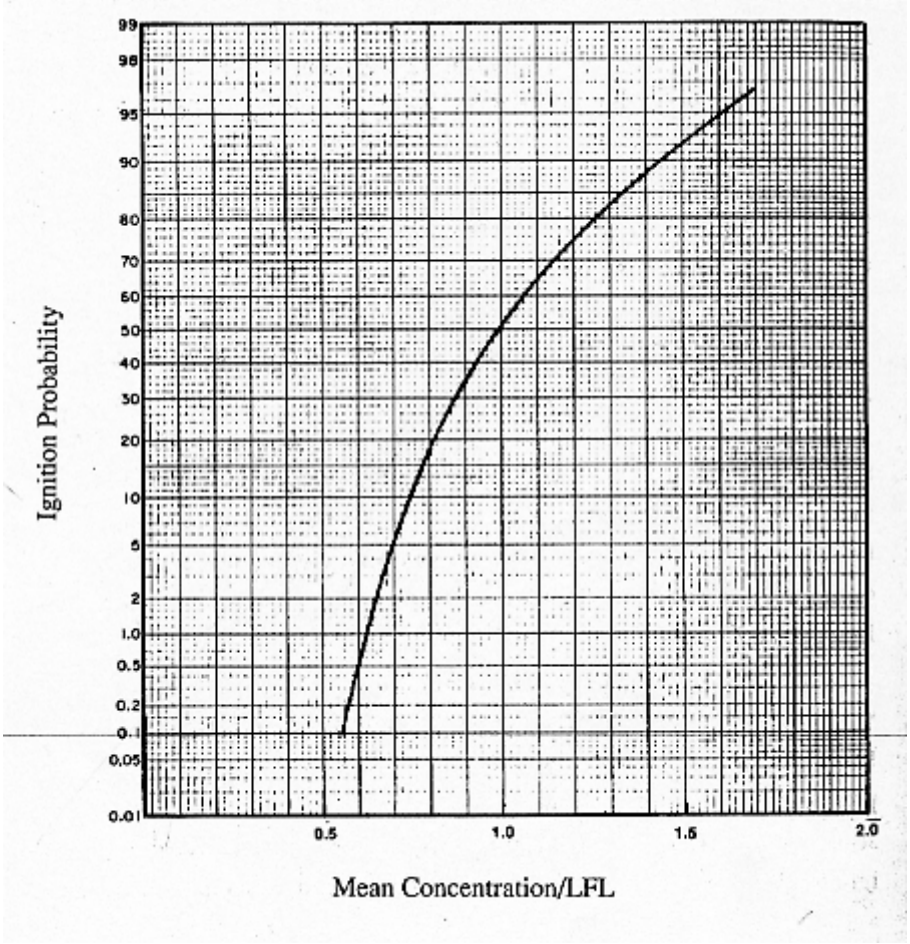

Figure 9.2 Probability of Formation of a Flammable Natural Gas Cloud [165]

The curve in Figure 9.2 plots the cumulative probability of a potentially flammable concentration as a function of concentration ratio. It can be seen that when the mean concentration equals the LFL, the probability of the cloud being flammable is 50%. The flammability probability increases with mean concentration and approaches a 99% at a mean concentration of about twice the LFL or 10% by volume. At lower concentrations the flammability potential decreases rapidly. The initial dense cloud dispersion ensures that high vapor cloud concentrations are achieved prior to ignition. For this analysis a uniform distribution will be used for the probability that the vapor

cloud will be flammable, with upper and lower limits for the ratio of mean concentration to LFL being 0.4 and 1.6 respectively. The density function and the cumulative function for the uniform distribution is given by

$$p_{fl} = \begin{cases} \dfrac{1}{b-a} & \text{for } a \le x \ge b \\ \\ 0 & \text{otherwise} \end{cases} \qquad (9.1)$$

$$P_{fl} = \begin{cases} 0 & x \le a \\ \dfrac{x-a}{b-a} & a \le x \ge b \\ 1 & x \ge b \end{cases} \qquad (9.2)$$

where

$x = \text{ratio of mean concentration and LFL}$
$a = 0.4, \text{ lower limit of ratio}$
$b = 1.6, \text{ upper limit of ratio}$

Equations 9.1 and 9.2 will be used to estimate the probability that a fully dispersed natural gas vapor cloud could be ignited in the presence of an ignition source.

9.3 Probability of Ignition

Ignition likelihood is an indicative assessment of the expected occurrence of ignition of the natural gas vapor. The ignition likelihood estimate is cumulative for each fire scenario considered. It is a function of time as well energy available for different

types of ignition. Ignition of the flammable natural gas air mixture in the presence of an ignition source depends on the following:

- Frequency of time the ignition source is present in the immediate area of the gas air flammable mixture, expressed in terms of a probability assuming a constant rate model, *Pi*.
- Probability that the source exceeds the ignition threshold, P_{se}.
- Probability that the configuration between the source and the mixture produces ignition, P_c.
- Probability that the source is not extinguished by the turbulence created by the gas air mixture, P_{ne}.

Natural gas vapor clouds may be ignited by different sources that may be continuous or intermittent. Such sources include engine temperature, traffic lights, a lighted cigarette, an activated lighter, electrical sparks or other vehicles. The ignition sources relevant to a natural gas cloud will be analyzed using data from a study of over one hundred and fifty potential ignition sources for a natural gas vapor cloud in urban areas [167]. The probability of ignition by each source can be expressed as the product of the probabilities of the various events or conditions required for ignition identified above.

Using rare event approximation and assuming independence of each event of condition, the likelihood of ignition by each source is given by

$$P_{ig} = P_e \times P_{se} \times P_c \times P_{ne} \qquad (9.1)$$

A Fault Tree model shown in Figure 9.2 is used to compute the ignition potential of each source as well as the likelihood of ignition of a dispersed natural gas cloud. Estimation of the Fault Tree probabilities will be done using data from [167] and estimates based on engineering judgments.

9.3.1 Identification and Analysis of Relevant Ignition Sources

Potential ignition sources for a gas release from the CNG tank of a typical bus are listed as follows:

- Smoking which includes the lighted cigarette, car lighter and flame lighter.
- Open fires from any source including other vehicle fire.
- Electrical system arching
- Other automobile systems producing high intensity spark.
- Traffic lights in daytime operations.

The probability in each category of importance for igniting a vapor cloud is shown in Table 9.1. In the case of frequency of occurrence for each source, the probability of activation of this source during the dispersion and existence of a vapor cloud is used. This probability of activation is determined from the density of each ignition source in the specific area under consideration. This density is very site specific but values for urban Boston area [167] is used in the computations. Probability of activation is different for delayed and immediate ignition. For immediate ignition, the sources have to be activated for a longer time and closer to the release point on the cylinder. This reduces

the probability of being activated and the accessibility of the source to the dispersing vapor cloud. The results are shown in Table 9.1

Ignition potential of each ignition source represents the likelihood of igniting a flammable vapor cloud when contact is made with the source. Two types of ignition are possible with natural gas, namely piloted ignition and auto- ignition. Piloted ignition for methane, the major constituent in natural gas, occurs from a source providing 300 μJ of energy [115]. Sparks produced by each of the sources is well in excess of this and therefore the potential for spark ignition in such cases approaches 100%. Auto-ignition temperature of methane is 540°C [115]. Heated surfaces over which the vapor cloud could pass cannot produce this heating effect so auto-ignition of the natural gas cloud is not expected to occur. It should be noted that contaminants in the natural gas could lower the conditions for ignition from that of methane. This effect is not investigated. To compensate for this a low probability is assigned to the ignition potential for a lighted cigarette, even though experiments [167] have shown that it did not ignite a flammable methane-air vapor cloud of 7% by volume.

An automobile contains other potential ignition sources apart from the electrical system [167]. These sources include:

1. Flashback from the combustion chamber back into the carburetor.
2. Exhaust of gases still burning as occurs with backfiring.
3. Reaction inside a catalytic converter.
4. Friction between the tires and the road and between metal parts.

No empirical data exist at present for these ignition sources. Engineering judgment was used to assign a probability to the existence of such sources and the potential for igniting a flammable gas cloud. Only the combination of these other potential ignition sources is considered in the analysis.

Table 9.1 Probability Estimates for Applicable Ignition Sources

Ignition Source	**Probability of Source Activation**		**Ignition Potential**		**Probability of Contact With Cloud**		**Probability of Source Not Extinguished**	
	Del.	Imm.	Del.	Imm.	Del.	Imm.	Del.	Imm.
Traffic Light	1.0	0.5	0.24	0.24	0.8	0.05	1	1
Smoking	0.29	0.29	0.1	0.1	0.5	0.01	0.5	0.5
Lighter	0.14	0.14	1	1	0.5	0.01	1	1
Vehicle Electrics	1.0	0.2	0.06	0.06	1.0	0.5	1	1.0
Vehicle Other	0.5	0.5	1.0	1.0	0.5	0.1	1.0	0.5
Open Fires	0.07	0.07	1.0	1.0	0.08	0.02	1.0	1.0

9.3.2 Ignition Likelihood Results

A Fault Tree model similar to what is typically used to compute the top event in a multi-component system is used to estimate the likelihood of delayed and immediate ignition. The contribution of each source is represented by the probabilities computed from the events or category associated with each source from Table 9.1. occurring simultaneously. The possibility of simultaneous occurrence of ignition sources is

represented by “and” gates on the tree. The occurrence of any one of the source is sufficient to cause ignition of the vapor cloud. This is represented by “or” gates. The results for delayed ignition and immediate ignition are shown in Figures 9.3 and 9.4 respectively.

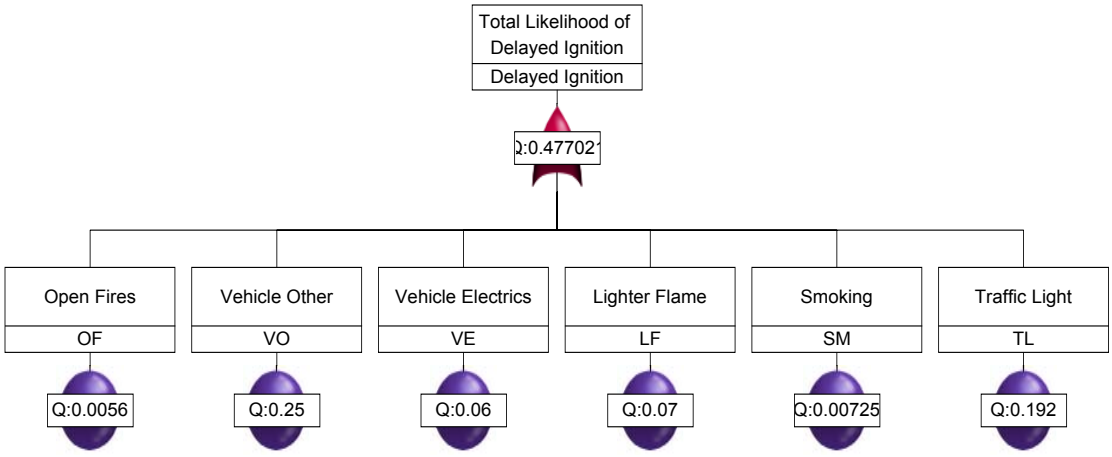

Figure 9.3 Likelihood of Delayed Ignition by All Relevant Sources

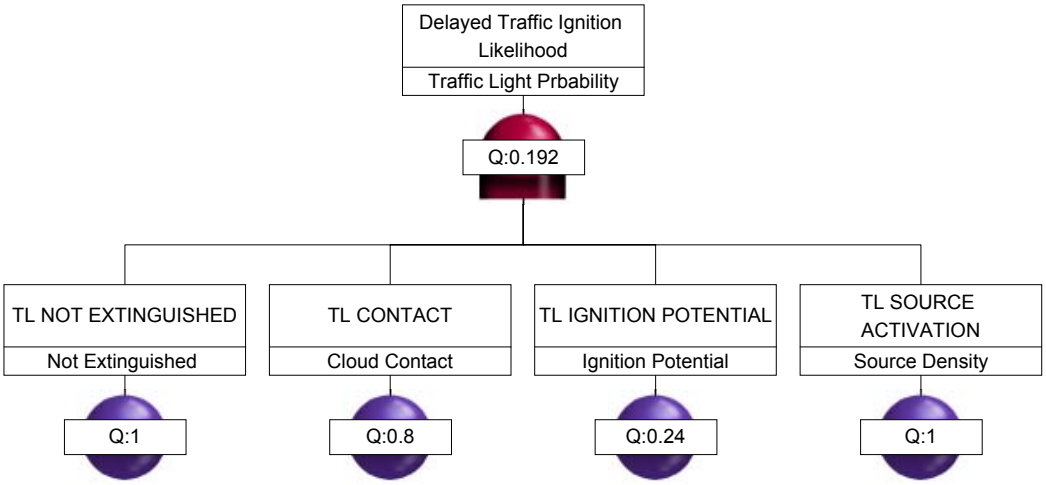

Figure 9.3.1 Likelihood of Ignition by Traffic Lights

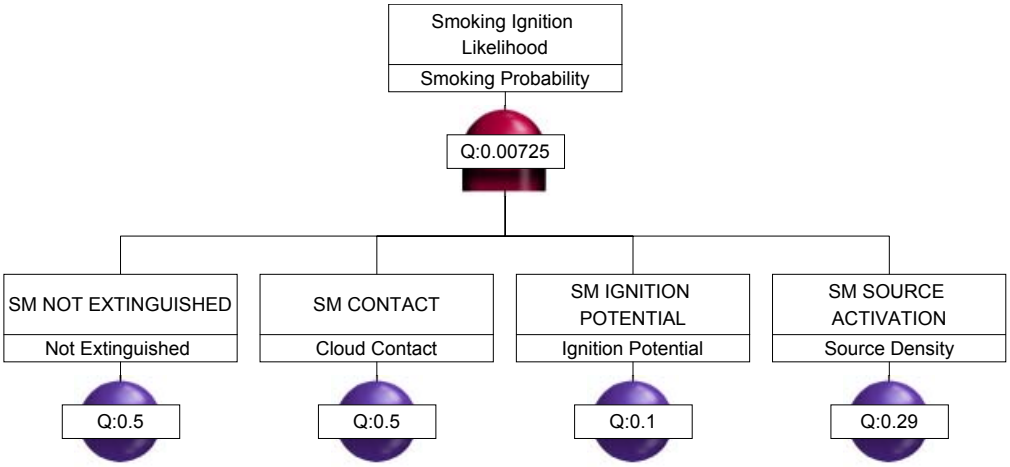

Figure 9.3.2 Likelihood of Delayed Ignition by Smoking

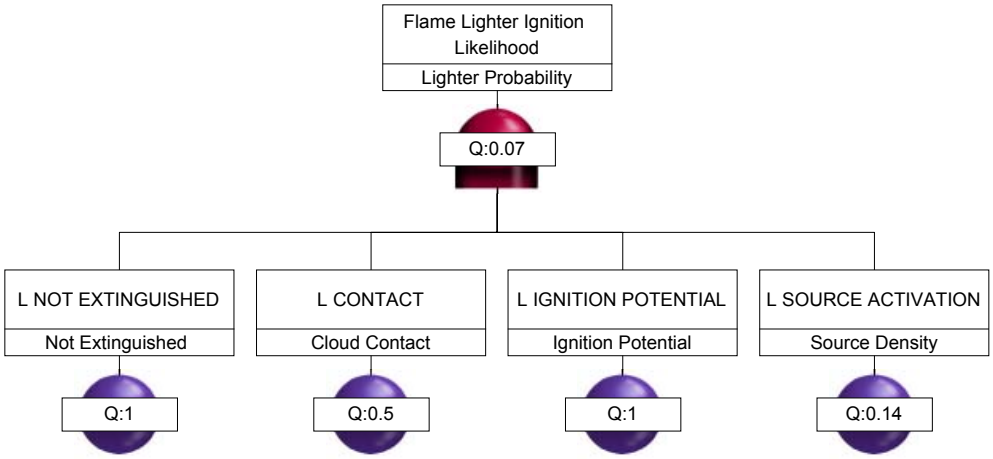

Figure 9.3.3 Likelihood of Delayed Ignition by Lighter Flame

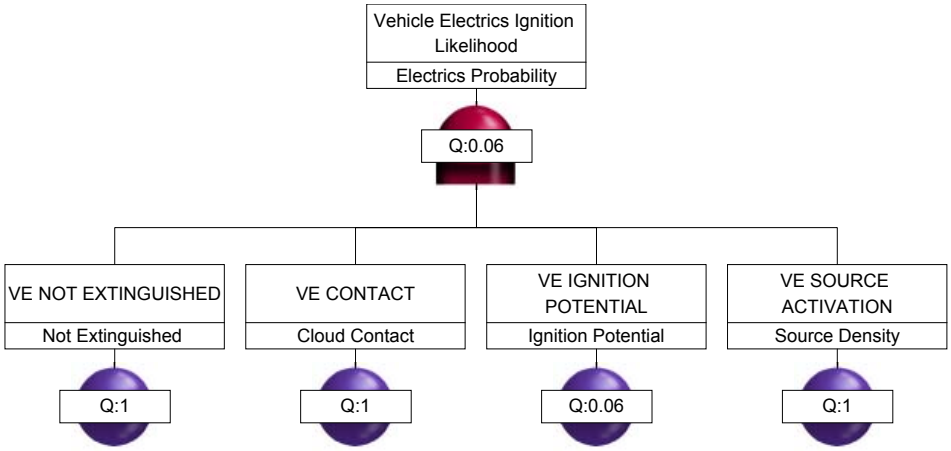

Figure 9.3.4 Likelihood of Delayed Ignition by Vehicle Electrics

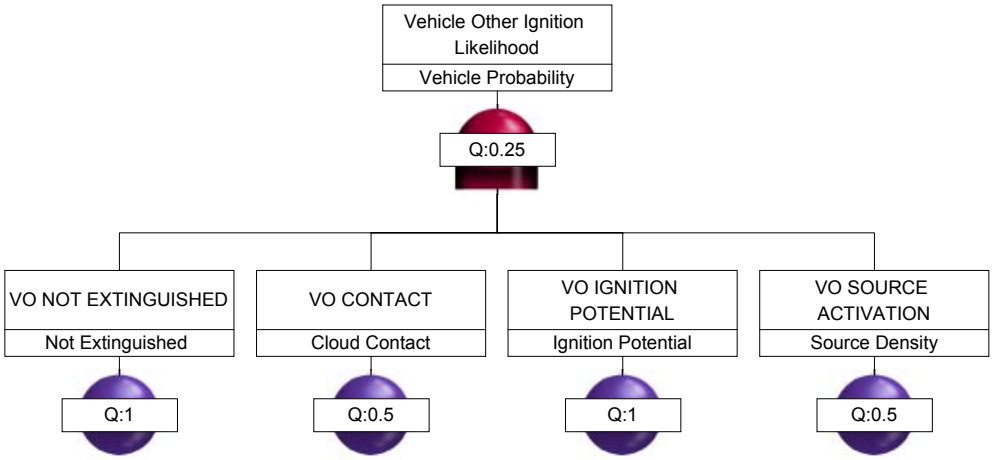

Figure 9.3.5 Likelihood of Delayed Ignition by Vehicle Other

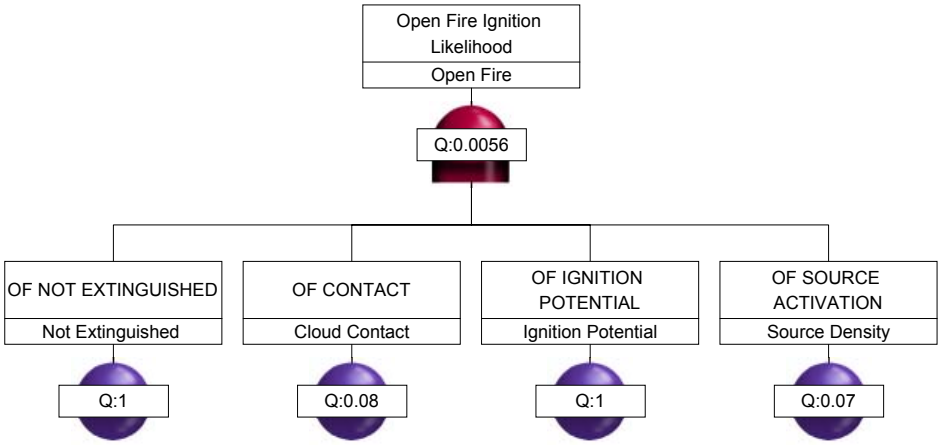

Figure 9.3.6 Likelihood of Delayed Ignition by Open Fire

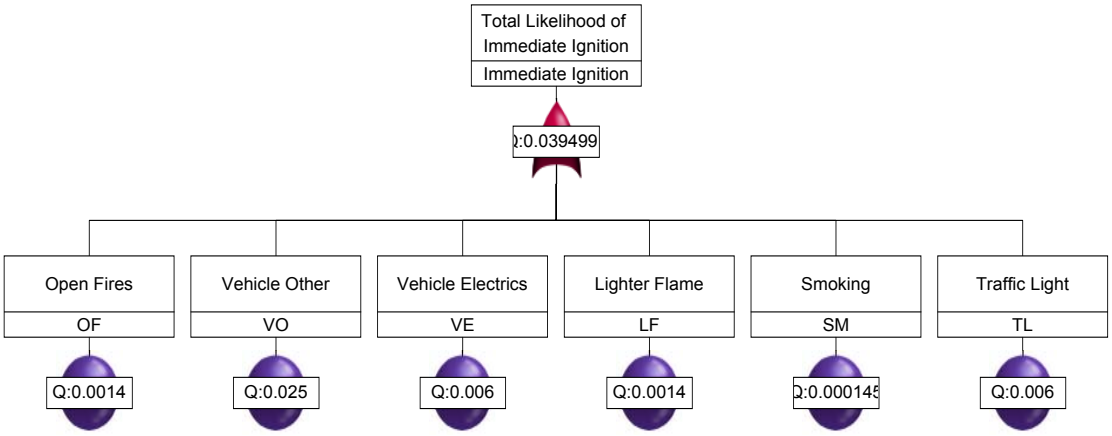

Figure 9.4 Likelihood of Immediate Ignition by All Relevant Sources

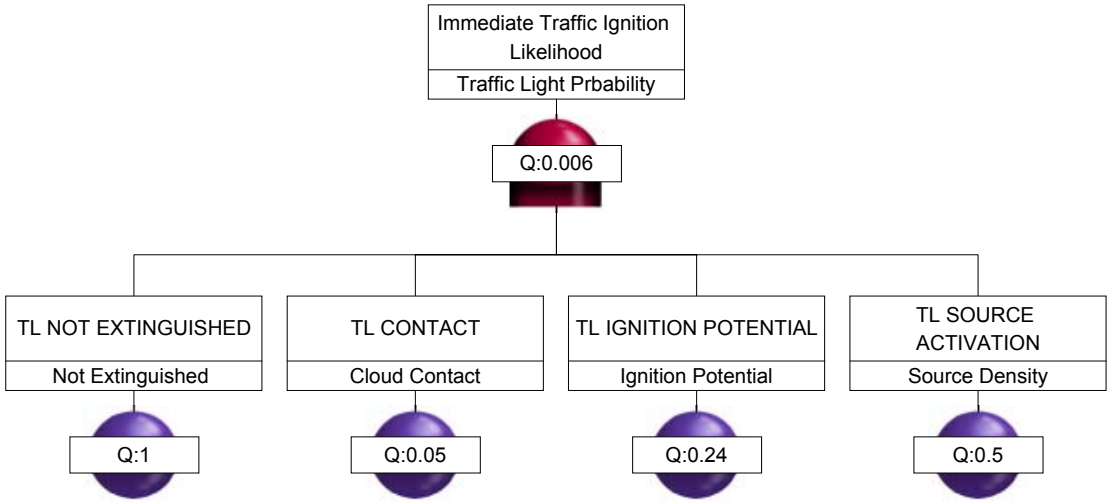

Figure 9.4.1 Likelihood of Immediate Ignition by Traffic Light

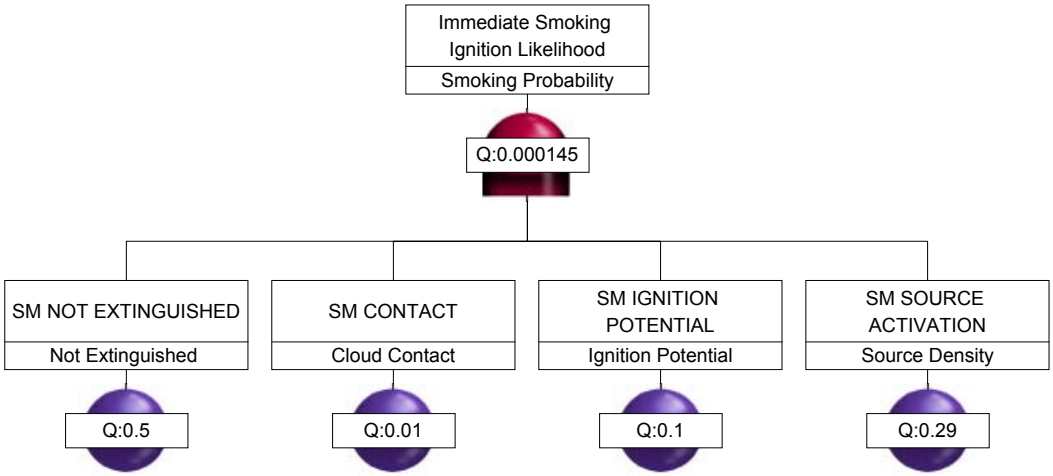

Figure 9.4.2 Likelihood of Immediate Ignition by Smoking

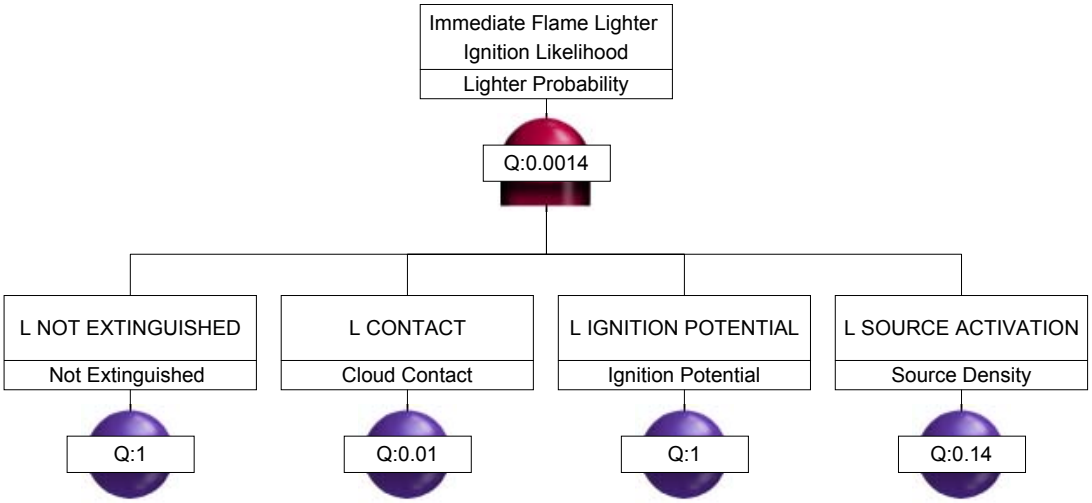

Figure 9.4.3 Likelihood of Immediate Ignition by Lighter Flame

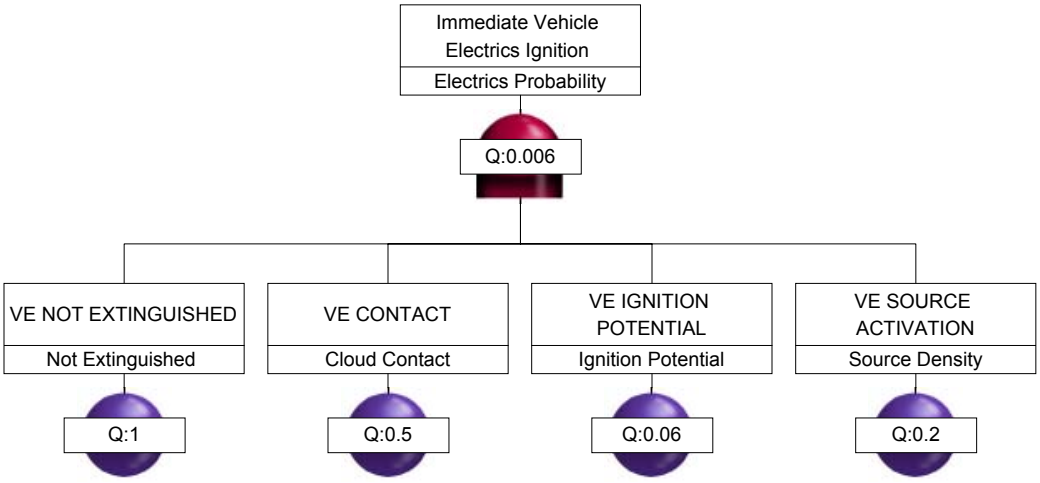

Figure 9.4.4 Likelihood of Immediate Ignition by Vehicle Electrics

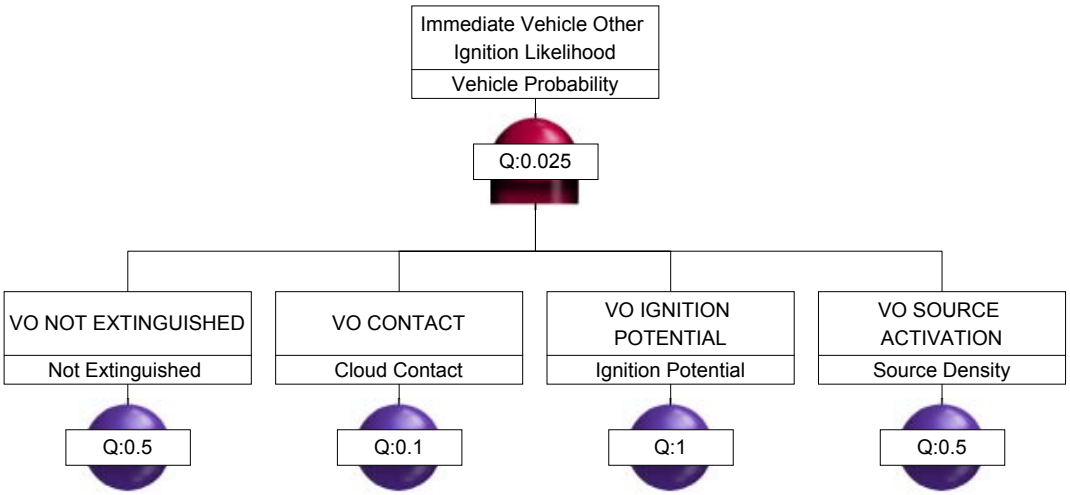

Figure 9.4.5 Likelihood of Immediate Ignition by Vehicle Other

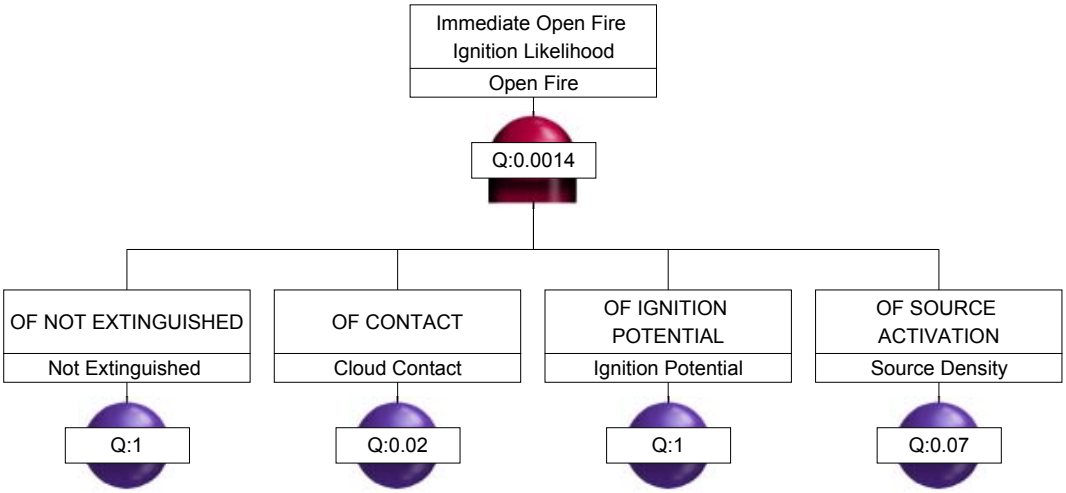

Figure 9.4.6 Likelihood of Immediate Ignition by Open Fires

9.4 Probability of Explosion of Natural Gas Vapor Cloud

The probability of a vapor cloud exploding depends on the weight of flammable vapor in the cloud [154], [159] and the mass of flammable vapor at which the explosion probability is 50%. In this analysis the latter is conservatively chosen to be 7.7 kg, even though bus natural gas explosions have been documented [1] with much less gas in the vapor cloud. The probability relationship may be expressed as [159]:

$$P_E = 0.5\left[1-\left\{1-\left(\exp^{-0.15\left\{\ln\left[\frac{W}{7.7}\right]\right\}^2}\right)\right\}^{1/2}\right] \qquad (9.2)$$

where,

P_E = Probability of vapor cloud explosion

W = kg, is the weight of flammable vapor in the cloud at concentrations above the LFL.

Current research has not identified significant differences in probability of explosion for jet, plume and puff releases of natural gas [159]. Equation 9.2 will therefore be applied to jet and puff discharge originating from a crack in a cylinder wall and catastrophic rupture respectively. The probability for each type of release will now be calculated.

9.4.1 Jet Release Explosion Probability

The volume of flammable vapor above the lower flammable limit in a jet, generated by release of natural gas near sonic velocity, from a crack in the wall of the cylinder is given by [167]:

$$W = 0.178 w^{1.5} \frac{T_a^{0.5}}{k^{0.75} T_0^{0.75} (LFM)^2 M^{1.25}} \tag{9.3}$$

where,

$$\begin{aligned} &w = 0.019 \text{ kg/s, rate of vapor flow} \\ &T_0 = 25\ ^\circ\text{C, initial vapor temperature} \\ &T_a = 24\ ^\circ\text{C, ambient air temperature} \\ &k = 1.307 \\ &LFL = 5.3\%, \text{ lower flammable limit volume fraction} \\ &M = 16.043, \text{ approximate molecular weight of natural gas} \end{aligned} \tag{9.4}$$

Substituting from Equation 9.4 into 9.3 and into 9.2 we get

$$W = 1.856 \text{x} 10^{-3} \text{ m}^3 \tag{9.5}$$

$$P_{E_{JET}} = 0.06 \tag{9.6}$$

9.4.2 Puff Release Explosion Probability

The volume of flammable vapor at concentrations above the lower flammable limit in a puff of natural gas generated by the rupture of a CNG cylinder or release by the pressure relief device, is given by [168]:

$$W = W_v \left[1 - \exp^{-\frac{0.36}{(LFL)^{0.6}}} \right] \tag{9.7}$$

where,

$$\begin{aligned} &W_v = 7.7 \text{ kg, the total initial mass of fuel released} \\ &LFL = 5.3\%, \text{ lower flammable limit volume fraction} \end{aligned} \tag{9.8}$$

Substituting from Equation 9.8 into 9.7 and 9.2 we get

$$W = 6.75 \text{ m}^3 \tag{9.9}$$

$$P_{E_{PUFF}} = 0.42 \tag{9.10}$$

9.5 Bus Location

The number of fatalities from each fire scenario depends on where the bus is located. Five locations are chosen for this analysis representing the full spectrum that a typical bus may be found in. The five vehicle fire locations chosen represents normal

usage. A probability factor, representing the expected length of time that a vehicle is expected to be in each location during normal use, is applied in order to normalize the use profile. The probability factor is therefore the unconditional probability that the bus could be in that location when the fire scenario contemplated is occurring. This allows determination of the expected fatality in each location. The locations and probability factors are:

- Garage or storage facility (0.5).
- Fueling station (0.06).
- Urban roadway (0.25).
- Sub-Urban roadway (0.17).
- Tunnel or Bridges (0.02).

9.6 Quantitative Risk Assessment Results

The consequence the fire for each gas release scenario was multiplied by the frequency of occurrence of gas release, with the likelihood of other event leading up to that fire scenario, to get the estimated number of fatalities. The total fire fatality risk is arrived at by summing the risk associated with each fire scenario.

The risk results are calculated based on:

$$\text{Risk}\left\{\frac{\text{consequence}}{\text{unit time}}\right\} = \text{Frequency}\left\{\frac{\text{combined gas release and fire event}}{\text{unit time}}\right\} \times \text{Magnitude}\left\{\frac{\text{condequences}}{\text{combined gas release and fire event}}\right\}$$

The computation was done using event sequence diagrams, with each gas release scenario becoming an initiating event. @ Risk and Precision Tree two codes in the Palisade suite of software [169] were used to perform the calculations. The Event Trees are shown in Figure 9.5. Table 9.2 summarizes the results.

Table 9.2 Quantitative Risk Results

RESULTS OF QUANTITATIVE RISK ASSESSMENT

Failure Scenario Leading to Fire/ Explosion and Fatality	**Passenger Mean Risk (Fatalities/ Bus/year)**	**N-Passenger Mean Risk (Fatalities/ Bus/year)**	**Mean Risk (Fatalities/ Bus/year)**	**Mean Risk (Fatalities/ 100 M Miles)**
Jet or Puff Release from through wall crack and rupture due to micro-crack originating on **inside** surface of cylinder.	5.61×10^{-4}	3.34×10^{-4}	8.95×10^{-4}	8.95
Jet or Puff Release from through wall crack and rupture due to micro-crack originating on **outside** surface of cylinder.	4.89×10^{-4}	2.91×10^{-4}	7.80×10^{-4}	8.13
Jet or Puff Release from through wall crack and rupture due to micro-crack originating in **transition region** or ends surface of cylinder.	3.47×10^{-4}	2.06×10^{-4}	5.53×10^{-4}	5.76
Total Mean Fire Fatality Risk	$\mathbf{1.40 \times 10^{-3}}$	$\mathbf{8.31 \times 10^{-4}}$	$\mathbf{2.23 \times 10^{-3}}$	**22.84**

** Assuming 9598 miles of travel per bus per year*

9.7 Uncertainty Analysis

The sources of uncertainty in the results of this study can be classified and characterized as follows:

- Typical bus used to represent all bus configurations, cylinder type and use profile (model/completeness uncertainty).
- Conservatism in the crack density in each cylinder manufactured.
- Initial crack size distribution and distribution parameter (model/parameter uncertainty).
- Model of crack propagation leading to failure (model uncertainty).
- Major fire scenarios considered (model/completeness uncertainty).
- Consequence modeling techniques used (model/ assumption uncertainty)
- Bus location during the development of a fire scenario.
- Integration of all scenarios to estimate total risk (model uncertainty)

While model uncertainties are important, due to lack of a sound model uncertainty estimation methodology, at this point only the uncertainty in estimating model parameters. Model uncertainties were accounted for by the conservatism used throughout the analysis in constructing the models.

Uncertainty in the frequency of occurrence of leakage and rupture of cylinders was evaluated by assuming a normal distribution of the frequency, with mean and standard deviations shown in Tables 7.1 – 7.3. The uncertainty in the likelihood that a gas release will be flammable was represented by a uniform distribution, with the limits

representing the probability of a jet or puff release of natural gas becoming flammable, at the lower and upper flammable limits of methane, based on Figure 9.2. The uncertainty that an explosion will accompany a fire when the gas is ignited was evaluated using a lognormal distribution based on the mass of fuel available and the mass of fuel, required for an explosion to occur. This is detailed in Section 9.4.

Uncertainty in the number of fatalities was represented by a lognormal distribution with a median value of half of the expected fatality calculated previously. An error factor of 6.3 was used representing the range of the worst case fatality scenario (0 - 40 fatalities in a secondary fireball scenario in urban areas), with a 90% confidence. Other methods such as for reducing the uncertainty in the initial crack distribution using Bayesian methods were discussed previously.

Propagation and combination of the uncertainties in the risk analysis were performed using the @ Risk code [169]. The propagation of the uncertainties relied on a Monte Carlo simulation with Latin Hypercube sampling [170]. The results of the uncertainty analysis are summarized in Table 9.3. Graphical representation of the risk for each initiating event is shown in Figures 9.5 – 9.7.

Table 9.3 Quantitative Risk Results

RESULTS OF QUANTITATIVE RISK ASSESSMENT

Failure Scenario Leading to Fire/ Explosion and Fatality	Mean Frequency of (Leakage/ Bus/year)	Mean Frequency of (Rupture/ Bus/year)	Risk 5% (Fatalities/ Bus/year)	Risk 95% (Fatalities/ Bus/year)
Jet or Puff Release from through wall crack and rupture due to micro-crack originating on **inside** surface of cylinder.	5.56×10^{-3}	3.34×10^{-4}	6.00×10^{-5}	3.10×10^{-3}
Jet or Puff Release from through wall crack and rupture due to micro-crack originating on **outside** surface of cylinder.	4.84×10^{-3}	2.98×10^{-4}	6.00×10^{-5}	2.73×10^{-3}
Jet or Puff Release from through wall crack and rupture due to micro-crack originating in **transition region** or ends surface of cylinder.	3.42×10^{-3}	2.21×10^{-4}	6.00×10^{-5}	3.00×10^{-3}
Total Mean Fire Fatality Risk			**1.18×10^{-4}**	**8.83×10^{-3}**

** Assuming 9598 miles of travel per bus per year*

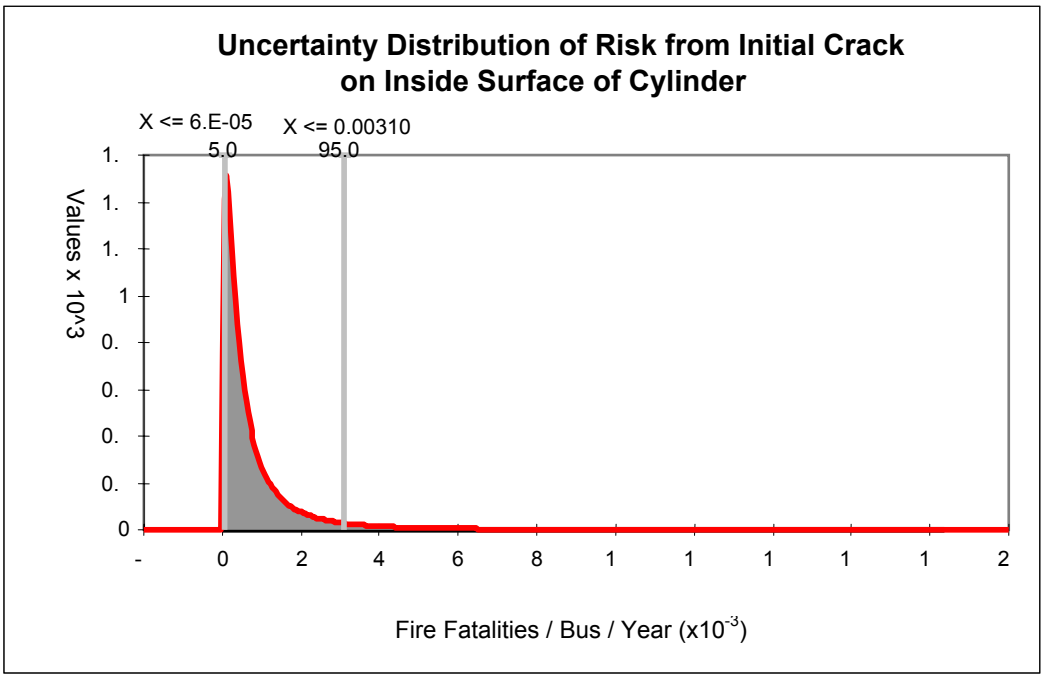

Figure 9.5 Risk Uncertainty Results for Initial Crack on Inside Surface

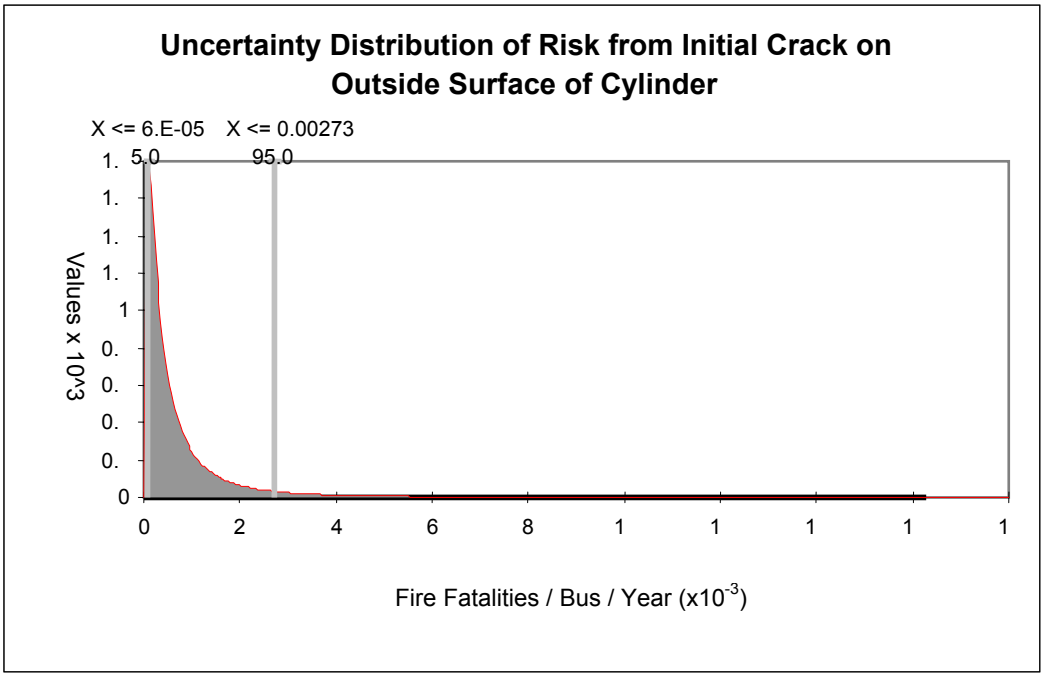

Figure 9.6 Risk Uncertainty Results for Initial Crack on Outside Surface

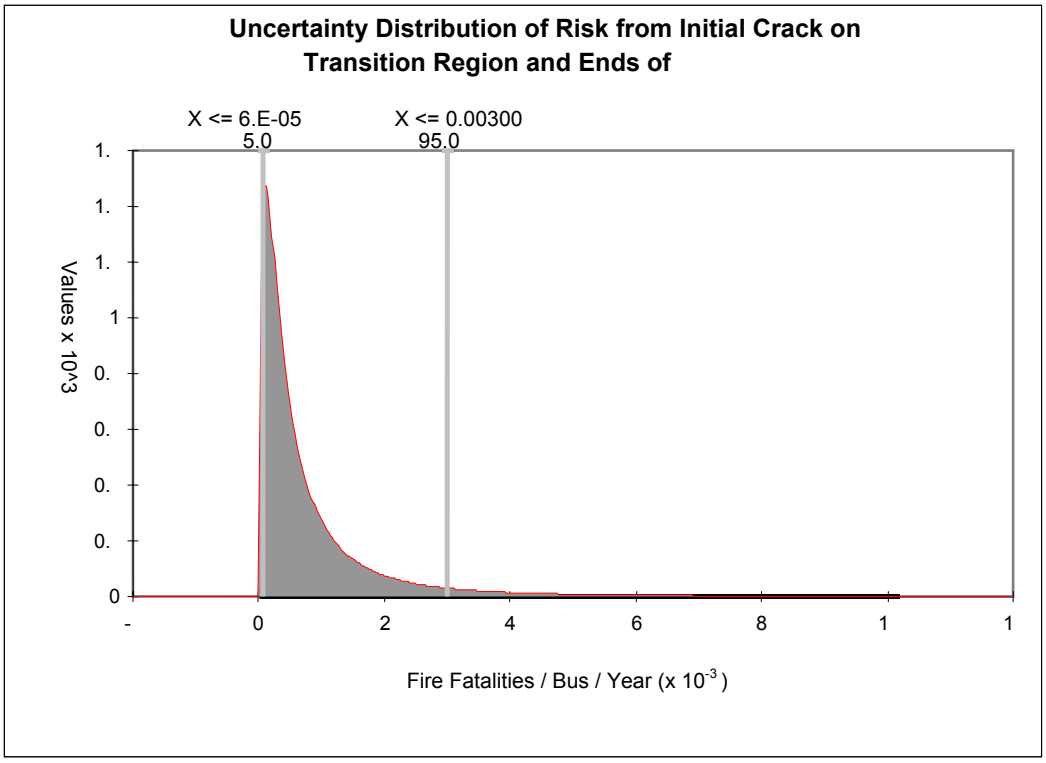

Figure 9.7 Risk Uncertainty Results for Initial Crack on Transition Surface

9.8 Discussions of Risk Results and Comparison with Diesel

9.8.1 Overall Risk Results

The projected mean fatalities from a typical bus due to cylinder failures from micro-cracks on the inside surface (the most likely scenario), resulting in an uncontained fire and explosion are 3.34×10^{-4}/bus/year. Considering school buses only, for the 1400 CNG school buses [171 - 173] in operation in the U.S. in year 2004, this would lead to a mean total risk value of approximately 0.46 deaths/year or a mean time to occurrence of two years. If all the existing buses were to be replaced with CNG buses, then the projected fatality would be 147 deaths/year.

The uncertainty in the risk results is dominated by the number of fatalities in each fire scenario. This is expected as the number of persons in each scenario is subject to significant variation. However using an error factor which would give between zero and forty fatalities in the worst case scenario for propagating the uncertainty in all fire events, the results are orders of magnitude close to the mean values estimated. The results are therefore a credible representation of the fire fatality risk of CNG buses.

It should be noted that some actual cases of CNG related explosions and fire from cylinder failures have been recorded. One such incident was reported in Houston, Texas [174] in 1998. In this case, gradual gas release and delayed ignition resulted in an explosion and a subsequent flash fire (no fatalities were reported). A CNG cylinder rupture as a result of accidental impact caused a fireball in Nassau County, NY [175] in 2001. Seven individuals were killed in a CNG bus explosion/fire in Tajikistan and four

in another accident in San Salvador [176 - 177] in 2001. As such, the evidence of some of the scenarios considered in this study has already been observed.

Comparing the historical data and the results of the analysis, the numbers of fatalities from CNG bus fires are low, or have not been reported to date in the U. S., this is only due to the small number of CNG buses in operation. Increasing the number of such buses will increase the expected number of fatalities due to fires and explosions.

9.8.2 Comparison with Diesel

Of the 448,000 school buses in operation in year 2004, the large majority of them were diesel powered [178 - 179]. The school buses travel approximately 4.3 billion miles per year [179]. An average of one hundred and thirty deaths per year is recorded of which approximately 10 are school bus passengers and none are directly related to the catastrophic fires due to use of the diesel fuel itself. This approximates to 3 fatalities (fire and non-fire causes) per 100-million miles for all, and 0.23 fatalities per 100-million miles for bus passengers. There are about 12,000 injuries (all causes) in these bus incidents [179].

At present, school buses consume all types of fuels, however, they are dominated by the diesel buses (over 95% were diesel in 2004) [173]. Accordingly, one can assume that the accident data discussed above can be viewed to a large extent as a representative of the diesel bus safety performance. Approximately 3 % of all fatalities are fire fatalities of which between 8% and 10%, are school bus passenger fatalities [179]. Accordingly, fire risk for diesel bus passengers is 0.0007 fatalities per 100-million miles of travel.

Also, considering all fire related fatalities (for bus passengers and others outside of the bus who are exposed to the fire), the fire risk for diesel buses would be 0.091 fatalities per 100-million miles.

Comparatively, based on the quantitative analysis done in this study, total mean fire risk for CNG buses is 23 per 100-million miles of operation. This would suggest that CNG school buses are subject to fire fatality risk by a factor of 250 larger than that of diesel powered buses.

According to this study 63 % of fire related fatalities in CNG buses are projected to be bus passengers. Estimated CNG bus passenger mean risk is 14.4 fatalities per 100-million miles vs. 23 per two-million miles for total estimated fatalities (bus passengers, other affected vehicle passengers, operators and pedestrians). Therefore, CNG bus passengers are estimated to carry a higher risk of explosion and fire fatality. Comparing the same experience for diesel bus passengers (i.e., 0.0007 fatalities per 100-million miles), CNG school bus passenger fire fatality risk is four orders of magnitude (20000) greater than that of diesel buses. Explosions due to detonation or deflagration of flammable vapor cloud within a bus are a major contributor to this increased risk, which is not expected to occur with diesel. With diesel buses fire is a secondary result of some accidents, and happens outside of the bus.

Corrosion-fatigue is a degradation process of the CNG cylinders. The small number of incidents recorded for CNG buses can be due in part to the small number of

such buses in operations and the fact that the average age of buses are well below the anticipated 15 years useful life. This is the reason that this study analytically developed the frequency of failure of CNG cylinders from the associated failure mechanisms, rather than relying on historical data. Similarly modeling the consequence of fires was done using the most current models of methane fire propagation. If all school buses are replaced by CNG buses, based on this research an increase in fire fatality is projected to occur.

9.9 Conclusions

This research has contributed to the body of knowledge on CNG vehicles by the following:

- Developing a probabilistic physics of failure model to compliment the existing deterministic model available [3 – 4]. This new model identifies important features of CNG cylinder crack propagation, where crack growth is dependent on cycling due to refilling. Additionally crack growth will not occur below a stress intensity factor of 12 ksi-in^2 and rate of crack growth will decrease above 14 – 15 ksi-in^2, due to crack tip blunting and the effect of plasticity at the crack tip.

- A method was developed for estimating the flow rate of natural gas from a through wall crack, using crack tip opening displacement methods from fracture mechanics. This enabled the calculation of release velocity and the propensity for sustaining a jet flame. The results were consistent with experimental

determination of maximum release velocity from a circular orifice for sustaining a jet flame.

- A tractable determination of the consequence of each fire scenario was accomplished but using analytical methods to estimate thermal and explosive outcomes from fire scenarios and their effects. The most current models for evaluating fireballs and unconfined vapor cloud fires were used.

- Fire fatality risk of CNG buses have been estimated for the first time, taking into account all the subsequent events required to develop a fire or explosion. An approximation of the uncertainty in the risk results has also been completed.

The results of this research have shown that CNG buses are more susceptible to major fires and explosions than diesel powered buses. The estimated fire risks for all fatalities are two orders of magnitude greater. Passengers risk is estimated to be higher than the overall estimated risk. Previous study of CNG bus risk using generic models and failure data underestimated the risk especially for passengers. This is mainly because of the approximate methods used to estimate the heat flux generated and the consequence of explosions ignored. The results using the physics of failure modeling and analytic analysis of fire scenarios is expected to be more accurate. Explosion effects are included in this detailed study which was not accounted for in the simplified approaches used previously to determine fire fatality risk. The results in this detailed analysis supports the conclusions arrived at in the previous analysis, as they are within the margins of error for the overall risk.

CHAPTER 10: RECOMMENDATIONS

To compare the results of CNG risk with other technologies, the risk assessment should add risk of non-fatal injuries in addition to fatalities from all the major sources of risk unique to this technology. For any policy decision making, the fire risk should be compensated for and properly characterized by integrating the safety risks of this study and the expected health and environmental benefits of using CNG powered school buses. The results from this analysis could be used in any such holistic risk assessment.

This research estimated the fire fatality risk as a result of thermal radiation and explosion effects, by developing an analytical model of the predominant failure mechanism, in estimating the frequency of release of natural gas due to a cylinder failure. Modeling of the dispersion and dynamics of resulting fires was done using the most current research in modeling of methane or natural gas fires. A number of simplifying assumptions were made in the computation procedures and various sources of uncertainty exist in the modeling exercise. Future research has to be conducted in analyzing the uncertainties and the sensitivity of the results to some of the assumptions. Specific recommendations to how the results may be improved are now itemized as follows:

- The frequency of the initiating events was computed for steel cylinders only. Similar models of the degradation process of all the other types of cylinders should be developed and used to calculate the risk. The overall risk would

then be estimated by weighting the proportion of cylinders of the different types that are found in the bus population.

- A generic initial crack size distribution was developed and used in estimating the number of cycles to failure. Data from the cylinder manufacturers should be used to estimate the initial crack depth distribution. Additionally the distribution of crack shapes (crack aspect ratio) should be determined and a joint distribution of crack depth and aspect ration be used in the analysis instead of the marginal crack depth distribution.

- The density of cracks in each section of the cylinder should be determined from actual data. This density can then be used to compute the probability of existence of a crack on the inside, outside and ends of each cylinder.

- Exponential and Poisson distributions were assumed for the crack size and occurrence in the cylinder, respectively. The validity of these distributions should be determined from actual data. The uncertainty in the risk results and sensitivity to using other distributions should be analyzed.

- Each crack was assumed to grow independently through the wall of the cylinder without any interaction or cracks coalescing. This is a conservative approach which should be relaxed and the likelihood cracks interacting and the effects on the frequency of failure be investigated.

- A fixed number of iterations and crack growth increments were implemented in the algorithm developed for computing the number of cycles to failure. Analysis of the sensitivity of the results to the number of iterations, and crack growth increments is imperative. A method of incorporating this uncertainty in the overall risk result has to be developed.

- The number of cycles to leakage or rupture was predicated on the assumed number of cycles of 15,000 during normal usage in estimated during a lifetime of ten to fifteen years. Uncertainty analysis should be performed on the risk result based on the use profile being different from the above assumption.

- Uncertainty of fracture toughness of cylinder material can have the most impact on the cycles to catastrophic failure by brittle rupture. The uncertainty in the fracture toughness is governed by the ductile to brittle transition temperature (DBTT) of the cylinder steels and the use profile of the buses. Sufficient data was not available to develop a distribution of the variation of K_{IC} with temperature. Additionally the temperature distribution of CNG buses has to be developed and the uncertainty of the frequency of rupture evaluated. This is an imperative as the buses may be operated in climates below DBTT.

- Ignition likelihoods were estimated from data [167] available on Boston, Massachusetts and its environments for a typical urban and sub-urban area.

The uncertainty of the availability of such ignition sources and their ability to ignite a flammable vapor cloud should be investigated, for other areas of the US where large populations of CNG buses are located.

- The number of fatality associated with each fire scenario was calculated based on the thermal radiation produced, explosive overpressure produced, explosion equivalent TNT mass and occupation of the exposure zones. Some attempt was made to reducing this uncertainty and quantifying its effect on the overall results. Further analysis is required for each individual scenario and its various outcomes. This analysis should focus on using other population and vehicle demographics in deriving the occupation of the exposure zones.

- The sensitivity of the overall result to each component in the risk model should be analyzed. Based on the result of this analysis further uncertainty analysis should be performed on the most sensitive components. In this way the bounds of uncertainty could be better characterized.

REFERENCES

1 Chamberlain, S., Modarres, M., Mowrer, F., "Compressed Natural Gas Bus Safety: A Qualitative and Quantitative Risk Assessment," Center for Technology Risk Studies, University of Maryland, May 2002.

2 American National Standard For Basic Requirements For Compressed Natural Gas Vehicle (NGV) Fuel Containers, ANSI/CSA NGV2 - 2000, Second Edition, 2000.

3 Hudak, S.J., Birring, A.S, Bartlett, M., Hanley, J.J., "Control of Corrosion Fatigue in NGV Fuel Cylinders," Southwest Research Institute, Gas Research Institute, Chicago, IL, 1989.

4 Hudak, S.J., Connolly, M.P., Roy, S., "Fracture Mechanics Analysis of NGV Fuel Cylinders, Part I: Steel Cylinders," Southwest Research Institute, Gas Research Institute, Chicago, IL, 1993.

5 Department of Transport, "DOT Cylinders Used for Equipment and Vehicle Fuel Systems – 85-5," Federal Register, Volume 50, No. 196, October 1986.

6 American Society of Mechanical Engineers, "Rules for Construction of Pressure Vessels," ASME Boiler and Pressure Vessel Code, Section VIII, Division I, 1980.

7 Bhuyan, G., Webster, C., "Fracture Performance of NGV Cylinder Designs," Powertech Labs Inc., Gas Research Institute, Chicago, IL, 1998.

8 Institute of Gas Technology, "Compressed Natural Gas Storage Optimization for Natural Gas Vehicles," Powertech Labs Inc., Gas Research Institute, Chicago, IL, December 1996.

9 Federal Specifications, RR – C – 901C, "Compressed Gas Cylinders," US Department of Transport, DOT 3AA, 2003.

10 ASTM E647, "Standard Test Methods for Measurement of Fatigue Crack Growth Rate," Annual Book of ASTM Standards, Volume 03.01, 2003.

11 Compressed Natural Gas Fuel Container Integrity, DOT Regulation, Federal Motor Vehicle Standard (FMVSS) No. 304, 1995.

12 Lyle, F.H., Burghard, H.C., George, E.P., "Effects of Natural Gas Quality on Corrosion of CNG Storage Cylinders – Phase I," Final Report under Contract No. 730-FFES-FUC-85, New York State Energy Research and Development Authority, Albany, NY, February 1989.

13 Lyle, F.F., Jr., "Evaluation of the Effects of Natural Gas Contaminants on Corrosion in Compressed Natural Gas Storage Systems – Phase II," Report No. ORNL/Sub/85-22025/1, Department of Energy Contract No. DE-AC05-84OK21400, Oak Ridge National Laboratory, Martin Marietta Energy Systems, Inc., Oak Ridge, TN, January 1989.

14 Bradshaw, F.J., Wheeler, C., Applied Material Research, Volume 5, p. 112, 1966.

15 ISO/DIS 11439: Gas Cylinders, "High Pressure Cylinder for the On-Board Storage of Natural Gas as a Fuel for Automotive Vehicles,".

16 Canadian Standards Association B51: Part 2, "High Pressure Cylinder for the On-Board Storage of Natural Gas as a Fuel for Automotive Vehicles, CSA B51-97, September 1997.

17 Proposed American Standard for Basic Requirements for Compressed Natural Gas Vehicle Fuel Container, July 1997.

18 NACE MR0175/ISO 15156-3, "Petroleum and Natural Gas Industries – Material for Use in H_2S-Containing Environments in Oil and Gas Production, NACE/ANSI/ISO, 2003.

19 Collins, J.A., Failure of Materials in Mechanical Design – Analysis, Prediction, Prevention, John Wiley & Sons, 1993.

20 Webster, C.T.L., Havelock, F., "Sulphide Stress Cracking Criteria for Steel NGV Cylinders. Topical Report, June 1991," Powertech Labs, Inc, Gas Research Institute, Chicago, IL, June 1991.

21 Barsom, J.M., "Effect of Cyclic-Stress Form on Corrosion-Fatigue Crack Propagation Below K_{ISCC} in a High-Yield-Strength Steel," Corrosion Fatigue: Chemistry, Mechanics, and Microstructure, *International Corrosion Conference Series,* Vol. NACE-2, National Association of Corrosion Engineers, Houston, TX, 1972.

22 Barsom, J.M., "Investigation of Sub-Critical Crack Propagation, Ph.D. Dissertation, University of Pittsburgh, 1969.

23 Barsom, J.M., "Corrosion Fatigue Crack Propagation Below K_{ISCC}," Journal of Engineering Fracture Mechanics, Volume 3, No. 1, July 1971.

24 Barsom, J.M., "Mechanism of Corrosion Fatigue Crack Propagation Below K_{ISCC}, International Journal of Fracture Mechanics, Volume 7, No. 2, June 1971.

25 Paris, P., Tada, H., Irwin, G., The Stress Analysis of Cracks Handbook, Second Edition, Paris Productions, Inc., St. Louis MO., 1985.

26 ASTM E647, "Standard Test Methods for Measurement of Fatigue Crack Growth Rate," Annual Book of ASTM Standards, Volume 03.01, 1992.

27 Barsom, J.M., Imhof, E.J., Rolfe, S.T., "Fatigue Crack Propagation in High Strength Steels," Journal of Engineering Fracture Mechanics, Volume 2, No. 4, June 1971.

28 Barsom, J.M., "Fatigue Crack Propagation in Steels of Various Yield Strength," Transactions of the ASME, Journal of Engineering for Industry, Volume 93, Series B, No. 4, November 1971.

29 Paris, P.C., Gomez, M.P., Anderson, W.E., "A Rational Analytic Theory of Fatigue," Trend Engineering, University of Washington, Volume 13, No. 1, p. 9 – 14, 1961.

30 Barsom, J.M., "The Dependence of Fatigue Crack Propagation on Strain Energy Release Rate and on Crack Opening Displacement," Damage Tolerance in Aircraft Structures, ASTM STP 486, ASME, May, 1971.

31 Chapman, O.J.V., "Simulation of Defects in Weld Construction", Reliability and Risk in Pressure Vessel and Piping, ASME PVP, Volume 251,p. 81-89, ASME, NY, 1993.

32 ASTM E647, "Standard Test Methods for Measurement of Fatigue Crack Growth Rate," Annual Book of ASTM Standards, Volume 03.01, 1990.

33 Cruse, T.A., et. al., Reliability-Based Mechanical Design, Marcel Dekker, Inc., NY, 1997.

34 Barsom, J.M., Rolfe, S.T., Fracture and Fatigue Control in Structures, Second Edition, Prentice-Hall, Englewood Cliffs, NJ, 1987.

35 Yagawa, G., Kitajima, Y., Ueda, H., "Three Dimensional Fully Plastic Solutions for Semi-Elliptical Surface Cracks," International Journal of Pressure Vessels and Piping, Volume 53, p. 457 – 510, 1993.

36 Foreman, R.G., Shivakumar, V., Newman, J.C., Piotrowski, S.M., Williams, L.C., "Development of the NASA/FLAGRO Computer Program," Fracture Mechanics: 18th Symposium, ASTM STP945, Philadelphia, PA, 1988, p. 781 – 803, 1983.

37 Bamford, W.H., Bush, A.J., "Fracture Behavior of Stainless Steel," Elastic-Plastic Fracture, p. 553 – 577, ASTM, Special Technical Publication No. 668, Philadelphia, PA, 1979.

38 James, L.A., "Some Questions Regarding the Interaction of Creep and Fatigue," Journal of Engineering Materials and Technology, ASME Paper 75-WA/Mat-6, ASME, 1975.

39 Hale, D.A., Jewett, Kass, J.N., "Fatigue Crack Growth Behavior of Four Structural Alloys in High Temperature High Purity Oxygenated Water", ASME Paper 79-PVP-104, ASME, NY, 1979.

40 Modarres, M., ENRE 650 - Accelerated Testing Course Notes, University of Maryland, 2001.

41 Ritchie, R.O., "Near-Threshold Fatigue Crack Propagation in Ultra-High Strength Steel: Influence of Load Ratio and Cyclic Strength," Journal of Engineering Materials and Technology, p. 195 – 204, 1977.

42 Paris, P.C., Bucci, R.J., Wessel, E.T., Clark, W.G., Mager, T.R., "Extensive Study of Low Fatigue Crack Growth Rates in A533 and A508 Steels," Stress Analysis and Growth of Cracks, ASTM Special Publication No. 513, p. 141 – 176, American Society of Testing and Materials, Philadelphia, PA, 1972.

43 Ritchie, R.O., "Influence of Microstructure on Near-Threshold Fatigue Crack Propagation in Ultra-High Strength Steel," Metal Science, p. 368 – 381, August/September, 1977.

44 Coke, R.J., Irving, P.E., Booth, G.S., Beevers, C.J., "The Slow Fatigue Crack Growth and Threshold Behavior of a Medium Carbon Alloy Steel in Air and Vacuum," Journal of Engineering Fracture Mechanics, Volume 7, p. 69 – 77, 1975.

45 Newman, J.C., Raju, I.S., "Stress-Intensity Factors for Internal Surface Cracks in Cylindrical Pressure Vessels," Journal of Pressure Vessel Technology, ASME Transactions, Volume 102, p. 342, 1980.

46 Newman, J.C., Raju, I.S., "Stress-Intensity Factors for Internal Surface Cracks in Cylindrical Pressure Vessels," Journal of Pressure Vessel Technology, ASME Transactions, Volume 104, p. 293, 1982.

47 Timoshenko, S., Strength of Materials, Advanced Theory and Problems, D. Van Nordstrom Company, NY, 1956.

48 Shah, R.C., "Stress Intensity Factors for Through and Part-Through Cracks Originating at Fastener Holes," Mechanics of Crack Growth, ASTM STP-590, p. 429 – 459, American Society of Testing and Materials, 1976.

49 Heliot, J., Labbens, R.C., Pellissier-Tanon, A., "Semi-Elliptical Cracks in the Meriodional Plane of a Cylinder Subject to Stress Gradients," Fracture Mechanics, ASTM STP-677, p. 341 – 364, American Society of Testing and

Materials, 1979.

50 Newman, J.C., Raju, I.S., "An Empirical Stress-Intensity Factor Equation for the Surface Crack," Engineering Fracture Mechanics, Volume 15, No. 1 – 2, p. 185 - 192, 1981.

51 Cruz, T.A., Besuner, P.M., "Residual Life Prediction for Surface Cracks in Complex Structural Details," Journal of Aircraft, Volume 12, No. 4, p. 369 – 375, 1975.

52 Besuner, P.M., "Residual Life Estimate for Structures with Partial Thickness Cracks," Mechanics of Crack Growth, p. 403 – 419, ASME Special Technical Publication No. 590., American Society of Testing and Materials, Philadelphia, PA, 1976.

53 Nair, P.I., "Fatigue Crack Growth Model for part-Through Flaw in Plates and Pipes," Journal of Engineering Materials and Technology, American Society of Mechanical Engineers, NY, 1978.

54 Rice, J.R., "A Path Independent Integral and the Approximate Analysis of Strain Concentrations by Notches and Cracks," Journal of Applied Mechanics, Volume 39, p. 379 – 386, 1968.

55 Begley, J.A., Landes, J.D., "The J-Integral as a Failure Criterion," Fracture Toughness, p. 1 – 23, ASTM Special Technical Publication No. 514, American Society of Testing and Materials, Philadelphia, PA, 1972.

56 Begley, J.A., Landes, J.D., "The Effect of Specimen Geometry on J_{IC}," Fracture Toughness, p. 24 – 39, ASTM Special Technical Publication No. 514, American Society of Testing and Materials, Philadelphia, PA, 1972.

57 Harris, D.O., "Probabilistic Analysis of Rupture in Reactor Coolant Piping," Probabilistic Analysis of Nuclear Reactor Safety, Volume 2, Paper II.7, Proceedings of Topical Meeting of the American Nuclear Society, Los Angeles, CA, May 1978.

58 Hutchinson, J.W., "Singular Behavior at the End of a Tensile Crack Tip in a Hardening Material," Journal of the Mechanics Physics of Solids, Volume 16, p. 13 – 31, 1968.

59 Rice, J.R., Rosengren, G.F., "Plane Strain Deformation Near a Crack Tip in a Power-Law Hardening Material," Journal of the Mechanics Physics of Solids, Volume 16, p. 1 – 12, 1968.

60 Anderson, T.L., Fracture Mechanics, Fundamentals and Applications, CRC Press, Boca Raton, FL, 1991.

61 Paris, P.C., Tada, H., Zahoor, A., Ernst, H., "The Theory of Instability of the Tearing Mode of Elastic-Plastic Crack Growth," Elastic-Plastic Fracture, p. 5 – 36, ASTM Special Technical Publication No. 668, American Society of Testing and Materials, Philadelphia, PA, 1979.

62 Kanninen, M.F., et. al., "Toward an Elastic-Plastic Fracture Mechanics Capability for Reactor Piping," Nuclear Engineering and Design, Volume 45, p. 117 – 134, 1978.

63 Standard Test Methods for J_{IC}, A Measure of Fracture Toughness, ASTM Standard E813-89, Annual Book of ASTM Standards, Part 3, American Society of Testing and Materials, Philadelphia, PA, 1990.

64 Dowling, A.R., Townley, C.H.A., "The Effects of Defects on Structural Failure: A Two Criteria Approach," International Journal of Pressure Vessels and Piping, Volume 3, p. 77 – 137, 1975.

65 Harrison, R.P., Loosemore, K., Milne, I., "Assessment of the Integrity of Structures Containing Defects," CEGB Report R/H/R6, Central Electricity Generating Board, United Kingdom, 1976.

66 Rana, M., et al, "Technical Basis for Flawed Cylinder Test Specification to Assure Adequate Fracture Resistance of ISO High Strength Steel Cylinder," Proceedings of the ASME PVP Conference, Montreal, Canada, 1996.

67 Bhuyan, G.S., "Fracture Performance of All Metal Gas Cylinders," Fatigue and Fracture, Proceedings of ASME PVP-Vol. 346, Volume 2, p. 263, American Society of Mechanical Engineers, 1997.

68 Horn, R.M, Kanninen, M.F., "Toward an Elastic-Plastic Fracture Mechanics Capability for Reactor Piping," Nuclear Engineering and Design, Volume 45, p. 117 – 134, 1978.

69 Harris, D.O., Lim, E.Y., Dedhia, D., "Probability of Pipe Fracture in the Primary Coolant Loop of a PWR Plant, Volume 5: Probabilistic Fracture Mechanics Analysis," US NRC Report NUREG/CR-2189, Volume 5, Washington, DC, 1981.

70 Kanninen, M.F., et. al., "Toward an Elastic-Plastic Fracture Mechanics Capability for Reactor Piping," Nuclear Engineering and Design, Volume 45, p. 117 – 134, 1978.

71 Lei, F., Assessment of Pressure Vessel Failure Due to Pressurized Thermal Shock With Consideration of Probabilistic-Deterministic Screening and Uncertainty Analysis, Ph.D. Dissertation, University of Maryland, College Park, MD, 2001.

72 Standard Test Methods for Plain-Strain Fracture Toughness of Metallic Materials, ASTM Standard E399-90, Annual Book of ASTM Standards, Part 3, American Society of Testing and Materials, Philadelphia, PA, 1990.

73 McCabe, D.E., "A Comparison of Weibull and β_{IC} Analyses of Transition Range Data," Fracture Twenty-Third Symposium, ASTM STP 1189, ASTM Special Technical Publication No. 1189, p. 80 – 94, American Society of Testing and Materials, Philadelphia, PA, 1993.

74 ISO/TR 1239-1-4, "Gas Cylinders: Refillable Seamless Steel – Performance Tests," ISO, December, 2001.

75 Barson, J.M., Rolfe, S.T., ASTM STP 466, ASTM Special Technical Publication No. 466, p. 281, American Society of Testing and Materials, Philadelphia, PA, 1970.

76 Rolfe, S.T., Novak, S.R., "Slow Bend KIC Testing of Medium-Strength High-Toughness Steels," Review of Developments in Plain Strain Fracture Toughness Testing, ASTM 463, American Society of Testing and Materials, Philadelphia, PA, 1970.

77 Horn, R.N., "The Growth and Stability of Stress Corrosion Cracks in Large Diameter BWR Piping," Report NEDC-24750-1, General Electric Company, San Jose, CA, November, 1979.

78 British Standard, "Transportable Gas Containers – Part 1. Specification for Seamless Steel Gas Containers Above 0.5 Liter Water Capacity," BS 5045: Part 1, 1982.

79 Minutes of CSA/NGV Joint Technical Meeting, NGV 2 Technical Advisory Group on Development of Standards on Natural Gas Vehicle and Hydrogen Vehicle Fuel Containers, Cleveland, OH, February, 2003.

80 Hudak, S.J., McClung, R.C., Bartlett, M.L., Fitzgerald, J.H., Russell, D.A., "A Comparison of Single-Cycle vs. Multi-Cycle Proof Testing Strategies, NASA Contractor Report 4318, George C. Marshall Space Flight Center, Huntsville, AL, 1990.

81 Chapman, O.J.V., "Simulation of Defects in Weld Construction", Reliability and Risk in Pressure Vessel and Piping, ASME PVP, Volume 251,p. 81-89, ASME, NY, 1993.

82 An Assessment of the Integrity of PWR Vessels, Report of a Study Group Chaired by W. Marshall, H.M. Stationary Office, 1976.

83 Wilson, S.A., "Estimating the Relative Probability of Pipe Severance by Fault Cause," General Electric Company Report GEAP-20615, Boiling Water

Reactor Systems Department, San Jose, CA, September 1974.

84 Becher, P.E., Pederson, A., "Application of Statistical Linear Fracture Mechanics to Pressure Vessel Reliability Analysis," Nuclear Engineering and Design, Volume 27, No. 3, p. 413 – 425, 1974.

85 Nilsson, F., "A Model for Fracture Mechanics Estimation of the Failure Probability of Reactor Pressure Vessel," Third International Conference on Pressure Vessel Technology, Part II, Materials and Fabrication, p. 593 – 601, American Society of Mechanical Engineers, NY, 1977.

86 Modarres, M., Kaminskiy, M., Kritvtsov, V., Reliability Engineering and Risk Analysis – A Practical Guide, Marcel Dekker, Inc., NY, 1999.

87 Kaplan, S., "On A Two-Stage Bayesian Procedure for Determining Failure Rates from Experimental Data," IEEE Transactions on Power Apparatus and Systems, Volume PAS-102, No. 1, January 1983.

88 Ayubb, B.M., McCuen, R.H., Probability, Statistics and Reliability for Engineers and Scientists, CRC Press Company, Washington, D.C., 2003.

89 Evans, M., Hastings, N., Peacock, B., Statistical Distributions, Third Edition, John Wiley and Sons, Inc., 2000.

90 Cramond, R., A Probabilistic Analysis of Structural Reliability Against Fatigue and Failure, Ph.D. Dissertation, University of Illinois, at Urbana, Champaign, 1974.

91 US Nuclear Regulatory Commission, Policy Issue Information, Secy2000-0140, 2000.

92 Harris, D.O., Fullwood, R.R., "An Analysis of the Relative Probability of Pipe Rupture at Various Locations in the Primary Cooling Loop of a Pressurized Water Reactor Including the Effects of a Periodic Inspection," Report SAI-001-PA, Science Applications, Inc., Palo Alto, CA, June 1976.

93 Harris, D.O., "An Analysis of the Relative Probability of Pipe Rupture at Various Locations in the Primary Cooling Loop of a Babcock and Wilcox 177 Fuel Assembly - Pressurized Water Reactor - Including the Effects of a Periodic Inspection," Report SAI-050-77-PA, Science Applications, Inc., Palo Alto, CA, September 1977.

94 Harris, D.O., "The Influence of Crack Growth Kinetics and Inspection on the Integrity of Sensitized BWR Piping Welds," Report EPRI NP-1163, Electric Power Research Institute, Palo Alto, CA, June 1979.

95 "Evaluation of PISC Trial Results," Report No. 5, Plate Inspection Steering Committee, May 1979.

96 Rummel, W.D., Hardy, G.L., Cooper, T.D., "Applications of NDE Reliability to Systems," Metals Handbook, Volume 17, Non-Destructive Evaluation and Quality Control, Ninth Edition, p. 674 – 688, ASM International, Metals Park, OH, 1989.

97 Akhtar, A., et al, "Integrity Assessment of All-Steel NGV Cylinders," GRI-92/0565, Powertech Labs, Inc., Gas Research Institute, Chicago, IL, 1992.

98 Foulds, J.R., Kennedy, E.L., "Bounding the Conservatism in Flaw-Related Variables for Pressure Vessel Integrity Analysis," Reliability and Risk in Pressure Vessels and Piping, ASME PVP, Volume 251, p. 67 – 74, ASME, New York, 1993.

99 Lehman, E.H., IEEE Transactions on Reliability, September 1963.

100 Mosley, A., ENRE 665 – Advanced Reliability Modeling Course Notes, University of Maryland, 2000.

101 Mosleh, A., Rasmuson, D.M., Marshall, F.M., "Guidelines on Modeling Common-Cause Failures in Probabilistic Risk Assessment," NUREG/CR-5485, INEEL/EXT-97-01327, US Nuclear Regulatory Commission, Washington, DC, June 1998.

102 Flannery, B.P., Press, W.H., Teukolsky, S.A., Vetterling, W.T., Numerical Recipes in C++ - The Art of Scientific Computing, Second Edition, Cambridge University Press, NY, NY, 2002.

103 Frost, N.E., Denton, K., "The Fatigue Strength of Butt Welded Joints in Low Alloy Structural Steel," British Welding Journal, Volume 14, No. 4, p. 156 – 161, April 1967.

104 Cramond, R. Jr., A Probabilistic Analysis of Structural Reliability Against Fatigue and Failure, Ph.D. Dissertation, University of Illinois, at Urbana, Champaign, 1974.

105 Kreyzig, E., Advanced Engineering Mathematics, John Wiley & Sons, 1995.

106 Assessment of Methane-Related Fuels for Automotive Fleet Vehicles, US Department of Energy Report DOE/CE/50179, Vol. 1-3, Aerospace Corp., El Segundo, California, 1982.

107 Summary Assessment of the Safety, Health, Environmental and System Risk of Alternative Fuels, Volpe National Transportation Systems Center, For U.S. DOT, 2001.

108 Comparative Analysis of the Environmental Impact of Alternative Transportation Fuels, Gas Research Institute Digest, V 12 # 4, 1983.

109 Guidelines for Chemical Process Quantitative Risk Analysis, Center for Chemical Process Safety, American Institute of Chemical Engineers, NY, NY, 1989.

110 Beuttner, K., "Effects of Extreme Heat and Cold on Human Skin, Part II – Surface Temperature, Pain and Heat Conductivity in Experiments with Radiant Heat," Journal of Applied Physics, Volume 3, p. 703, 1951.

111 Gayle, J.B., Bransford, J.W., "Size and Duration of Fireballs from Propellant Explosions," NASA Report TM X-53314, National Aeronautics and Space Administration, Huntsville, AL, 1965.

112 Hardee, H.C., Lee, D.O., "A Simple Heat Conduction Model for Skin Burns Resulting from an Incident Flux of Short Duration," Report SC-DC-714047, Sandia Laboratories, Albuquerque, NM, 1971.

113 The SFPE Handbook of Fire Protection Engineering, Second Edition, Society of Fire Protection Engineers, National Fire Protection Association, Quincy, MA, 1995.

114 Guidelines for Pressure-Relieving and Depressurizing Systems, API Recommended Practice 521, Second Edition, American Petroleum Institute, Washington, DC, 1982.

115 Quintiere, J.G., Draft Copy - Fundamentals of Fire Phenomena, Department of Fire Protection Engineering, University of Maryland, College Park, MD, 2003.

116 Hawthorn, W.R., Weddell, D.S., Hottell, H.C., "Mixing and Combustion of Turbulent Gas Jets," Proceedings of the 3rd International Combustion Symposium, p. 266 – 288, Combustion Institute, Pittsburgh, PA, 1949.

117 Fay, J.A., Lewis, D.H., "Unsteady Burning of Unconfined Fuel Vapor Clouds," Proceedings of the 16th International Combustion Symposium, p. 1397 - 1405, Combustion Institute, Pittsburgh, PA, 1976.

118 Raj, P.K., Emmons, H.W., "On the Burning of a Large Flammable Vapor Cloud," Proceedings of the Western and Central States Section Meeting, The Combustion Institute, San Antonio, TX, April 1975.

119 Baker, W.E., et al, Explosion Hazards and Evaluation, Elsevier, NY, 1983.

120 Shapiro, A.H., The Dynamics and Thermodynamics of Compressible Fluid Flow, The Ronald Press Company, NY, 1954

121 Hazard Analysis of Compressed Natural Gas Fueling Systems and Fueling Procedures Used at Retail Gasoline Service Station, GRI-95-05, The S.M. Stoller Corporation, Natural/Total Limited Liability Company, April 1995.

122 Courant, R., Friedrichs, K.O., Supersonic Flow and Shock Waves, Interscience Publishers, Inc., 1948

123 Anderson, T.L., Fracture Mechanics, Fundamentals and Applications, Second Edition, CRC Press, NY, NY, 1995.

124 Yuen, W.W., Tien, C.L., "Simple Calculations Scheme for the Luminous Flame Emissivity," Proceedings of the 17th International Combustion Symposium, p. 1481, Combustion Institute, Pittsburgh, PA, 1976.

125 Birch, A.D., Brown, D.R., Dodson, M.G., Thomas, J.R., "The Turbulent Concentration Field of a Methane Jet," Journal of Fluid Mechanics, Volume 88, Part 3, p. 431 – 449, 1978.

126 Thring, M.W., Newby, M.P., "Combustion Length of Enclosed Turbulent Jet Flames, Proceedings of the 4th International Combustion Symposium, p. 789 - 796, Combustion Institute, Pittsburgh, PA, 1953.

127 Lydersen, A.L., Fluid Flow and Heat Transfer, John Wiley & Sons, 1979.

128 Kalghatgi, G.T., "Blow-Out Stability of Gaseous Jet Diffusion Flames. Part I: In Still Air," Combustion Science and Technology, Volume 26, p. 233 – 239, 1981.

129 Kalghatgi, G.T., "Blow-Out Stability of Gaseous Jet Diffusion Flames. Part I: In Still Air," Combustion Science and Technology, Volume 26, p. 233 – 239, 1981.

130 Kalghatgi, G.T., "Blow-Out Stability of Gaseous Jet Diffusion Flames. Part I: In Still Air," Combustion Science and Technology, Volume 26, p. 233 – 239, 1981.

131 Hasegawa, K., Sato, K., "Experimental Investigation of the Unconfined Vapor Cloud Explosion of Hydrocarbons," Technical Memorandum of the Fire Research Institute, Volume 12, Japan, 1978.

132 Fay, J.A., Lewis, D.H., Desgroseilliers, J., "Radiation from Burning Hydrocarbon Clouds," Combustion Science and Technology, Volume 20, p. 141 – 151, 1979.

133 Lewis, D.H., The Combustion of Unconfined Vapor Clouds Burning in a Fireball Configuration, Ph.D. Dissertation, Massachusetts Institute of Technology, Cambridge, MA, 1977.

134 Hardee, H.C., Lee, D.O., Benedick, W.B., "Thermal Hazards from LNG Fireballs," Combustion Science and Technology, Volume 17, No. 189, 1978.

135 Markstein, G.H., "Radiative Energy Transfer from Turbulent Diffusion Flames," Combustion and Flames, Volume 27, No. 51, 1976.

136 Hottel, H.C., Sarofim, A.F., Radiative Transfer, McGraw Hill, 1967.

137 Lewis, B., von Elbe, G., Combustion, Flames and Explosion of Gases, 3rd Edition, Academic Press, San Diego, CA, 1987.

138 Prugh, R.W., "Evaluation of Unconfined Vapor Cloud Explosion Hazards," Proceedings of the International Conference on Vapor Cloud Modeling, American Institute of Chemical Engineers, NY, November 1987.

139 Murphy, M.J., Brown, S.T., Philips, D.B., "Extent of Indoor Flammable Plumes Resulting from CNG Bus Fuel System Leaks," Federal Transit Administration Technical Report, November 1991.

140 Preliminary Fire Safety Analysis of CNG-Fueled Vehicles, Mowrer F. W., Department of Fire Protection Engineering, University of Maryland, 2001

141 Raj, P.K., "An Analysis of Compressed Natural Gas Release from a High Pressure Cylinder," Technology and Management Systems, January 1994.

142 Raj., P.K., Gaumer, R.L., Dispersion of CNG Following a High-Pressure Release, US Department of Transport, Washington, DC, 1996.

143 Howard, M.D., Gattis, J.L., Large School Bus Design Vehicle Dimensions, Arkansas State Highway & Transportation Department, Little Rock, AR, 1998.

145 Raj, P.K., Emmons, H.W., "On the Burning of a Large Flammable Vapor Cloud," Proceedings of the Western and Central States Section Meeting, The Combustion Institute, San Antonio, TX, April 1975.

146 Sparrow, E.M., Cess, R.D., Radiation Heat Transfer, McGraw Hill Book Company, New York, 1978.

147 Raj, P.K., Emmons, H.W., "On the Burning of a Large Flammable Vapor Cloud," Proceedings of the Western and Central States Section Meeting, The Combustion Institute, San Antonio, TX, April 1975.

148 Steward, F.R., "Prediction of the Height of Turbulent Diffusion Buoyant Flames," Combustion Science and Technology, Volume 2, p. 203 – 212, 1970.

149 McGrattan, K.B., Forney, G.P., Floyd, J.E., Hostikka, S., Prasad, K., Fire Dynamics Simulator (Version 3) – Users Guide, National Institute of Standards and Technology, US Department of Commerce, 2002.

150 Baum, H.R., McGrattan, K.B., "Simulation of Large Industrial Outdoor Fires," Proceedings of 6th International Symposium for Fire Safety Science, p. 611 –

622, International Association for Fire Safety Science, Boston, MA, 2000.

151 Atreya, A., Agrawal, A., "Effects of Heat Loss on Diffusion Flames," Combustion and Flames, p. 372 – 382, 1998.

152 Decker, D.A., "An Analytic Method for Estimating Overpressure from Theoretical Atmospheric Explosions," Proceedings of the Annual Meeting of the National Fire Protection Association and Society of Fire Protection Engineers, May 1974.

153 Stull, D., Fundamentals of Fire and Explosion, AIChE Monograph Series 73, No. 10, American Institute of Chemical Engineers, NY, 1977.

154 Lees, F.P., Loss Prevention in the Process Industry, Butterworths, London, 1980.

155 Baker, W.E., et al, Explosion Hazards and Evaluation, Elsevier, NY, 1983.

156 Eichler, T.V., Napadensky, H.S., "Accidental Vapor Phase Explosion on Transportation Routes Near Nuclear Power Plants: US Nuclear Regulatory Commission, May 1978.

157 US Army, Structures to Resist Effects of Accidental Explosions. Technical Manual TM5-1300, Department of Army, Navy and Air Force, Washington, DC, 1969.

158 Brown, S.J., "Energy Release Protection for Pressurized Systems. Part II. Review of Studies into Impact/Terminal Ballistics," Applied Mechanics Reviews 39, p. 177 – 201, 1986.

159 Prugh, R.W., "Quantitative Evaluation of BLEVE Hazards," AIChE Loss Prevention Symposium, Paper 74e, AIChE Spring National Meeting, New Orleans, March 1988.

160 Guidelines for Chemical Process Quantitative Risk Analysis, Center for Chemical Process Safety, American Institute of Chemical Engineers, NY, NY, 1989.

161 Mehta, A.K., et al, "Measurement of Flammability and Burn Potential of Fabrics," Fuels Research Laboratory, Massachusetts Institute of Technology, Cambridge, MA, 1973.

162 Eisenberg, N.A., Lynch, C.J., Rausch, A.H., "Continued Development of the Vulnerability Model – Final Report," NTIS AD-A-044197, Springfield, VA, 1977.

163 Mudan, K.S., "Thermal Radiation hazards from Hydrocarbon Pool Fires," Proceedings of the Energy Combustion Science, Volume 10, p. 59 – 80, 1984.

164 Lees, F.P., Loss Prevention in the Process Industry, Butterworths, London, 1980.

165 Birch, A.D., Brown, D.R., Dodson, M.G., "Ignition Probabilities of a Natural Gas Jet," 18th International Symposium on Combustion, Combustion Institute, Pittsburgh, PA, 1981

166 Mudan, K., Gustafson, R.M., "Ignition Potential Distribution for Heavy Gas Plumes," Proceedings of the International Conference on Vapor Cloud Modeling, AIChE, NY, 1987.

167 Jeffreys, D.J., Moussa, N.A., Caron, R.N., Allan, D.S., Ignition Sources of LNG Vapor Clouds – GRI-80/0108, Arthur D. Little, Inc., Gas Research Institute, Chicago, IL, 1980 – 1981.

168 Van Buijtenen, C. J. P., "Calculation of the Amount of Gas in the Explosive Region of a Vapor Cloud," Journal of Hazardous materials, Volume 3, p. 209, 1980.

169 @Risk Reference Guide, Version 4.5, Palisade Corporation, NY, 2002.

170 Vose, D., Risk Analysis: A Quantitative Guide, John Wiley & Sons, 2000.

171 Analysis of US School Bus Population, Antares Group, Inc., 2003.

172 Alternative Fuel Data Center, US Department of Energy, www.afdc.doe.gov

173 Alternative Fueled Vehicle Fleet Survey, National Technical Information Service, 1999.

174 Summary Assessment of the Safety, Health, Environmental and System Risk of Alternative Fuels, Volpe National Transportation Systems Center, For U.S. DOT, 2001

175 Newsday, Newsday Inc., New York, NY, August 26, 2001.

176 ITAR News, ITAR-TASS News Agency, TASS, July 10, 2001.

177 A.P. World-Stream Associated Press, May 20, 2001.

178 Traffic Safety Facts 1999 - School Buses, NHTSA, 2000.

179 Fact Sheet - School Bus Safety, NHTSA, 2000.